



**This electronic thesis or dissertation has been  
downloaded from Explore Bristol Research,  
<http://research-information.bristol.ac.uk>**

*Author:*  
**Fushimi, Tatsuki**

*Title:*  
**Nonlinear Dynamics of Phased Array Levitators**

**General rights**

Access to the thesis is subject to the Creative Commons Attribution - NonCommercial-No Derivatives 4.0 International Public License. A copy of this may be found at <https://creativecommons.org/licenses/by-nc-nd/4.0/legalcode>. This license sets out your rights and the restrictions that apply to your access to the thesis so it is important you read this before proceeding.

**Take down policy**

Some pages of this thesis may have been removed for copyright restrictions prior to having it been deposited in Explore Bristol Research. However, if you have discovered material within the thesis that you consider to be unlawful e.g. breaches of copyright (either yours or that of a third party) or any other law, including but not limited to those relating to patent, trademark, confidentiality, data protection, obscenity, defamation, libel, then please contact [collections-metadata@bristol.ac.uk](mailto:collections-metadata@bristol.ac.uk) and include the following information in your message:

- Your contact details
- Bibliographic details for the item, including a URL
- An outline nature of the complaint

Your claim will be investigated and, where appropriate, the item in question will be removed from public view as soon as possible.



# **Nonlinear Dynamics of Phased Array Levitators**

**Tatsuki FUSHIMI**

Department of Mechanical Engineering  
University of Bristol

*A dissertation submitted to the University of Bristol  
in accordance with the requirements for award of the degree of  
Doctor of Philosophy in the Faculty of Engineering*

January 20, 2020

Word Count: 42,723





# Abstract

Acoustic levitation is a powerful method which enables objects to be levitated in mid-air using sound waves. The introduction of phased array levitator (PAL) has expanded the capability of acoustic levitation. The PAL allowed the levitated objects to be manipulated more dynamically in a three-dimensional field and opened up avenues for new applications of acoustic levitation. Whilst the interest in the acoustic levitation is high, the dynamic behaviour of the levitated spherical particles has not been explored in-depth, and a linear stiffness model of remains standard in the field.

Therefore, this thesis aims to understand the underlying dynamics of a particle levitated in a PAL, and thereby improve the positioning performance of the particle. A single-axis PAL with two opposed emitting arrays was utilised for this thesis, and a numerical model was developed to predict the acoustic radiation force inside the levitator. A one-dimensional dynamic model was constructed using the numerical model to simulate the dynamic motion of particle in the PAL, and it was experimentally validated. It was found that there are positioning inaccuracies in the PAL, and was found to affect the dynamic response of the system. The effects and implications of these inaccuracies were demonstrated via the development of numerical simulations, and calibration schemes were developed to minimise the effect of the deviation.

Both the numerical models and calibration methods in this thesis can be generalised to be applied to other forms of acoustic levitation, and the results presented here will lay the foundation for the current development of acoustic levitators. This case was confirmed by the application of the findings to the practical development of acoustophoretic volumetric display and will continue to aid the development of future application in the field of acoustic levitation.



# Author's declaration

I, Tatsuki FUSHIMI, declare that this dissertation was carried out in accordance with the requirements of the University's *Regulations and Code of Practice for Research Degree Programmes* and that it has not been submitted for any other academic award. Except where indicated by specific reference in the text, the work is the candidate's own work. Work done in collaboration with, or with the assistance of, others, is indicated as such. Any views expressed in the dissertation are those of the author.

SIGNED:

---

DATE:

---



## *Acknowledgements*

I would like to express my deepest gratitude to both of my supervisors, Professor Bruce W. Drinkwater and Dr. Thomas L. Hill for their supervision, insights and encouragements that I received throughout my degree. Their passions and enthusiasms to the research have inspired me to dive in and explore the unknowns in the research field. Their comments were always constructive, and helpful in identifying the points of improvements in my approach.

I would also like to extend my gratitude to Dr. Asier Marzo for his insights and for his help from the day one of my degree. The experimentation in this thesis was not possible without his acoustic levitation setup, and I would like to thank him for listening to my suggestions and consistently improving the setup. Asier encouraged me to look beyond the research field and his passion to promote the usage of the acoustic levitator across the field is a great inspiration for me.

I would like to thank Japanese Student Services Organization (JASSO) for sponsoring my PhD in the form of Student Exchange Support Program (Graduate Scholarship for Degree Seeking Students). I would also like to thank to Mr. Stephen Isles for manufacturing designed components in the Faculty of Engineering Workshop, and to Dr. Andrew Harrison for his supervision in the first year of the degree.

Finally, I would like to thank my family, friends and colleagues for their support and encouragement throughout my study. Your kind words brightened up my day, and encouraged me to move forward; even in the cloudy days.



# List of Publications and Contributions

## Journal Paper: Refereed

- Fushimi, T., Marzo, A., Drinkwater, B. W., & Hill, T. L. (2019). Acoustophoretic volumetric display using a fast-moving levitated particle. *Applied Physics Letters*, 115(6), 064101.
- Fushimi, T., Hill, T. L., Marzo, A., & Drinkwater, B. W. (2018). Nonlinear trapping stiffness of mid-air single-axis acoustic levitators. *Applied Physics Letters*, 113(3), 034102.

## Conference Paper:

- Fushimi, T., Marzo, A., Hill, T. L., & Drinkwater, B. W. (2018). Trajectory Optimization of Levitated Particles in Mid-air Ultrasonic Standing Wave Levitators. 2018 IEEE International Ultrasonics Symposium (IUS), 1–9.

## Conference Contributions:

- Fushimi, T., Marzo, A., Drinkwater, B. W., & Hill, T. L. (2019). Acoustophoretic volumetric display using a fast-moving levitated particle. The Rank Prize Funds Symposium on Parallels between acoustics and EM radiation in structured materials. Grasmere, United Kingdom 28 - 31st October 2019. (Invited Speaker)
- Marzo, A., Andrade, M. A. B., Fushimi, T., Hill, T. L. & Drinkwater, B. W. Holographic Acoustic Tweezers: Applications in Mid-air Assembly and Acoustophoretic Displays. in 2019 International Congress on Ultrasonics (2019). Bruges, Belgium 3-6th September 2019
- Marzo, A., Fushimi, T., Hill, T. L. & Drinkwater, B. W. Holographic Acoustic Tweezers: Future Applications in Medicine and Acoustophoretic Displays. in Optical Trapping and Optical Micromanipulation XVI (SPIE, the international society for optics and photonics, 2019). San Diego, California, United States 11-15th August 2019
- Fushimi, T., Marzo, A., Hill, T. L. & Drinkwater, B. W. Enhancing dynamic positioning performance inside mid-air acoustic levitator. 177th Meeting of the Acoustical Society of America. Louisville, Kentucky, United States 13-17th May 2019





# Contents

<b>Abstract</b>	<b>iii</b>
<b>Author's declaration</b>	<b>v</b>
<b>Declaration of Authorship</b>	<b>v</b>
<b>Acknowledgements</b>	<b>vii</b>
<b>List of Publications and Contributions</b>	<b>ix</b>
<b>Contents</b>	<b>xi</b>
<b>List of Figures</b>	<b>xv</b>
<b>List of Tables</b>	<b>xxiii</b>
<b>1 Introduction</b>	<b>1</b>
1.1 Research Motivation . . . . .	2
1.2 Thesis Outline . . . . .	3
<b>2 Literature Review</b>	<b>7</b>
2.1 Acoustic Radiation Force . . . . .	7
2.1.1 Non-zero Time Average . . . . .	7
2.1.2 Acoustic Radiation Force and Torque on Objects . . . . .	9
2.1.3 Gor'kov Potential . . . . .	10
Example: Calculation of Acoustic Radiation Force in Plane Standing	
Wave Field . . . . .	10
2.2 Types of Acoustic Levitators . . . . .	11
2.2.1 Classical Acoustic Levitator . . . . .	11
Single / Multi Axis Acoustic Levitator . . . . .	12
Near-field Levitator . . . . .	13
2.2.2 Phased Array Levitator . . . . .	17
Single / Multi Axis Levitator . . . . .	17
Single Beam Acoustic Levitator . . . . .	18
2.3 Dynamics of Acoustically Levitated Objects . . . . .	20
2.4 Applications of Acoustic Radiation Force . . . . .	21
2.4.1 Specimen Holding (Classical Levitator) . . . . .	21

2.4.2	Specimen Holding (PAL)	23
2.4.3	Additive Manufacturing	24
2.4.4	Contactless Production Line	24
2.4.5	Human Computer Interface (Display)	25
2.5	Nonlinear Behaviour of Dynamic System	25
2.6	Summary	27
<b>3</b>	<b>Acoustic Levitation of a Particle: Experimental Considerations and Simulations</b>	<b>29</b>
3.1	Introduction	29
3.2	Acoustic Levitator	30
3.2.1	Phased Array Levitator	30
	Single-Axis Phased Array Levitator	30
	Phase Calculation	31
	Levitator Controller	32
3.2.2	Particle	33
	Acoustic Levitation of Particle	34
3.2.3	Air Property Measurement	35
	Speed of Sound in Air	35
	Density of Air	36
	Viscosity of Air	36
3.3	Particle Position Tracker	37
3.3.1	Camera Setup	37
	Data Capture	38
	Calibration of Camera	39
	Identification of Particle Position	40
3.3.2	Location of Experiment	41
3.4	Formulation of Numerical Simulation	42
3.4.1	Huygens' Model	42
	Transducer Model	43
	Transducer Pressure Measurement	44
	Implementation of Huygens' Model in MATLAB	47
	Gor'kov Potential	49
3.5	Summary	51
<b>4</b>	<b>Dynamics of Mid-Air Single Axis PAL</b>	<b>53</b>
4.1	Introduction	53
4.2	Formulation of One-Dimensional Dynamic Model	54
4.2.1	Acoustic Radiation Force Profile	55
	Nonlinear Stiffness	57
	Linear Stiffness	58
4.3	Experimental Validation of Numerical Simulation	59
4.3.1	Setting up the Numerical Continuation Problem with COCO	60
4.3.2	Experimental Setup	61

4.4	Results . . . . .	62
4.5	Discussion . . . . .	64
4.6	Summary . . . . .	67
<b>5</b>	<b>Static Trajectory Calibration of Levitated Particles</b>	<b>69</b>
5.1	Introduction . . . . .	69
5.2	Static Equilibrium Points in an Acoustic Levitators: Numerical Approach . .	70
5.2.1	Experimental Observation of Equilibrium Points . . . . .	73
5.3	Exploring Causes of Static Deviation in Experimental System . . . . .	74
5.3.1	Scattering from Transducer Surfaces . . . . .	74
5.4	Static Trajectory Calibration Approach . . . . .	78
5.4.1	Offline Trajectory Calibration (2D) . . . . .	79
5.4.2	Online Trajectory Calibration (3D) . . . . .	80
	3D camera setup . . . . .	80
	Calibration Algorithm . . . . .	82
5.5	Summary . . . . .	85
<b>6</b>	<b>Acoustophoretic Volumetric Display</b>	<b>87</b>
6.1	Introduction . . . . .	87
6.2	Volumetric Display . . . . .	88
6.2.1	Illumination of the Particle . . . . .	89
6.2.2	Generation of Images . . . . .	90
	Vector Graphics Generation . . . . .	91
	Raster Screen Generation Process . . . . .	92
6.3	Dynamic Response of Particle in Large Displacement . . . . .	94
6.3.1	Dynamic Modelling . . . . .	96
6.3.2	Formulation of Hybrid Model . . . . .	97
6.4	Performance Limitation in Current Implementation . . . . .	99
6.4.1	Transducer Limitation . . . . .	100
6.5	Summary . . . . .	104
<b>7</b>	<b>Conclusions and future work</b>	<b>105</b>
7.1	Future Work . . . . .	106
7.1.1	Increasing the accuracy of the forward model . . . . .	106
7.1.2	Multi-particle dynamics . . . . .	107
7.1.3	Open / closed-loop controller . . . . .	107
7.1.4	Future of Acoustophoretic Volumetric Display (Transducer Limitation)	108
<b>A</b>	<b>Camera Holder</b>	<b>109</b>
<b>B</b>	<b>Calibration Probe Holder</b>	<b>115</b>
<b>C</b>	<b>Calibration Probe Extender</b>	<b>117</b>



# List of Figures

2.1	Boundary of acoustic radiation force calculation for (a) rigid object and (b) compressible object . . . . .	9
2.2	The class, subcategory, and types of mid-air acoustic levitator, and the underlying working principle for each levitator. $n = \{1, 2, 3, \dots\}$ is an integer. . . . .	12
2.3	Single-axis resonant acoustic levitator demonstrated by Whymark. Reprinted from [10] with the permission of Elsevier. . . . .	13
2.4	Non-resonant acoustic levitation of particles. Reprinted from [54], with the permission of AIP Publishing. . . . .	14
2.5	Squeeze film levitation using flexural travelling wave. Reprinted from [7], with the permission of Elsevier. . . . .	14
2.6	Acoustic streaming induced near-field acoustic levitation causes air between the clearance between the plates out. (a) Levitation of streaming induced levitation. Reprinted from [67], with the permission of Elsevier. (b) Modelled view of the setup, not to scale. . . . .	15
2.7	Near-field standing wave levitation. A standing wave forms between the transducer surface and the reflector. Reprinted with the permission from [68]. Copyright 2017, Acoustical Society of America. . . . .	16
2.8	Example of phased array acoustic levitator with 4 phased array configured for three-dimensional manipulation. Adapted from [72], licensed under CC BY 4.0. . . . .	17
2.9	The levitation of expanded polystyrene ball using single beam acoustic levitator. Adapted from [79], licensed under CC BY 4.0. . . . .	19
2.10	Applications of acoustic levitators in real-world. On the left hand side are applications that do not require particle to move, and on the right are dynamic applications. In a dynamic applications, the particle needs to be transported or controlled inside the levitator to achieve the target. . . . .	22
2.11	Levitation of blood sample during Raman spectroscopy. Reproduced from [115], with the permission of Royal Society of Chemistry. . . . .	22
2.12	Micro-manipulation device with electromagnetic coils and acoustic levitator. Reprinted from [19], with the permission of IEEE. © 2019 IEEE . . . . .	24
2.13	1D Acoustic radiation force of 1D plane wave standing wave, and linearly approximated acoustic radiation force (given gravity force is zero). . . . .	26

3.1	Examples of phased array configurations. (a) shows the single-axis PAL with flat surface, (b) shows the single-axis PAL with curved surface for focusing, and (c) shows the single-sided acoustic levitator with flat surface . . . . .	30
3.2	Transducer positions in the acoustic levitator. (a) shows the whole assembly view of the single-axis acoustic levitator, with the relative positions of the transducers. Reproduced from [28], with the permission of IEEE. (b) shows the detailed orientation and position of the transducers in each phased array. Reproduced from [27] with the permission of AIP Publishing. . . . .	31
3.3	Custom perspex holder for transducers and the transducer assembly [21]. The levitator is viewed from the y-z plane. . . . .	32
3.4	Acoustic levitator controller. The FPGA board is connected to the PC via Serial COM, and commands are packed into a vector of 1 by 66. It starts with 255 and ends with 254, and value between 0 to 127 is used to select the phase value for each transducers. Value 128 is reserved for turning off the transducer. . . . .	33
3.5	Overview of acoustically levitated EPS particle. (a) shows the particle position relative to the acoustic levitator, and (b) is a close up of the levitated particle. . . . .	34
3.6	A patch of cloth was utilised to insert particles into the node of the standing wave. After the insertion of particle, the particle position was checked visually using a ruler to confirm that the particle was in the correct node. . . .	35
3.7	Camera setup with a single-axis acoustic levitator and LED light with diffuser. The camera observes the particle movement in the y-z plane. . . . .	38
3.8	An example of a particle shillouette created by the diffused light source at the back of levitator. This method of identifying the particle is robust to changes in light settings, in comparison to setting up the LED light in the same side as the camera. . . . .	38
3.9	Experimental setup overview. (a) show the assembly of PointGrey camera and camera holder (b) The relative positioning of the camera, levitator, and LED light source. . . . .	39
3.10	The identification of the calibrator centre by the image recognition algorithm. (a) The diffused light from the LED source creates shillouette of the calibrator (b) Zoomed in view to the tip of the CMM-styli. The pixel to metre conversion rate is determined from here. . . . .	40
3.11	Assembly of CMM-stylus and its custom made holder. The CMM-Stylus has a ruby ball at the tip, and is used for the calibration procedure. Together with the custom made holder, the centre of the ruby ball is 40 mm away from the bottom of the holder. The notches on the holder are used to align the calibrator with the transducer array. . . . .	41

3.12	The sequence of particle identification algorithm. (a) The recorded image is loaded on to the MATLAB workspace memory. (b) The image is binarized with a threshold value. (c) Masking is applied to hide the boundaries of LED light, and therefore reduce the misdetection of particles. . . . .	42
3.13	Circle Hough Transform identifies the central position of the particle. (a) shows the relative position of the particle in the image and (b) is the close up version of the identified particle in (a). . . . .	42
3.14	Vibration level measurement on the passive vibration isolation table. The recording time was 10 minutes, and DFT was taken over the measured time domain acceleration signal. . . . .	43
3.15	Coordinate system of the numerical simulation. The global Cartesian coordinate $(x, y, z)$ has datum point at the centre of the acoustic levitator, and pressure contribution from each transducer is summed together to identify the total acoustic pressure field. The transducer position is offset from the global coordinate by $(x_{t,n}, y_{t,n}, z_{t,n})$ . . . . .	44
3.16	Comparison of the directivity function provided by the manufacturer specification sheet (Reproduced from [149]) and the piston source directivity function. . . . .	45
3.17	Experimental apparatus setup for the determination of the transducer power using pressure microphone. The microphone was incrementally moved in $z$ axis and the acoustic pressure (Pa) at distance $H$ was recorded. . . . .	45
3.18	Experimental plot of pressure amplitude of a single transducer as a function of inversed distance ( $r^{-1}$ ) . . . . .	46
3.19	Experiment demonstrating the linear relationship between the output pressure value and the voltage. The B&K microphone was fixed at a distance (20 mm), and the pressure value was recorded as the excitation voltage of the transducer was increased. . . . .	46
3.20	Phase assignments for the transducers in acoustic levitator and the red isosurface in the centre represents the resultant pressure field (Isosurface at 1000 Pa). . . . .	48
3.21	Qualitative assessment on the pressure field inside the acoustic levitation using dry ice. (a) shows the numerically predicted acoustic pressure field, and (b) shows the acoustic pressure field in the acoustic levitator visualised by the dry ice in the experimental apparatus. . . . .	48
3.22	The resultant Gor'kov potential ( $U$ ) calculated from the acoustic pressure field. As the original pressure field is a standing wave, the Gor'kov potential alternates between positive and negative over the distance. . . . .	49
3.23	Acoustic radiation force in $x$ axis, as calculated from the Gor'kov potential . .	50
3.24	Acoustic radiation force in $y$ axis, as calculated from the Gor'kov potential . .	50
3.25	Acoustic radiation force in $z$ axis, as calculated from the Gor'kov potential . .	50



4.1	Two types of single-axis standing wave levitators. (a) A Langevin horn transducer assembly with an opposed reflector, or a second transducer. (b) Two transducer arrays with phased delays or geometry designed to focus the acoustic waves at the centre. (c) Resultant central near-one-dimensional sinusoidal acoustic radiation force from both of the acoustic levitators. Reproduced from [27], with the permission of AIP Publishing . . . . .	54
4.2	The comparison of the linear (Stoke's Law) and nonlinear drag force (Massey). . . . .	56
4.3	The comparison of the directivity function as defined by the manufacturer's specification sheet [135], piston-source approximation, and the custom-directivity function fit generated by the MATLAB Curve Fitting App. . . . .	56
4.4	Simulated instantaneous pressure field generated by the acoustic levitator in YZ plane. Reproduced from [27], with the permission of AIP Publishing . . . . .	57
4.5	Simulated field generated by the acoustic levitator. (a) Pressure distribution across the central axis and (b) acoustic radiation force. Reproduced from [27], with the permission of AIP Publishing . . . . .	57
4.6	Force field shift by change in $z_p$ . It changes the position of the equilibrium point, and therefore applies force to the particle . . . . .	58
4.7	The change in linear stiffness value through each focal points. The value was normalised to the maximum value of the stiffness. . . . .	59
4.8	An example image, taken by the Photron FASTCAM camera. The red circle is the identified position of the particle, and the length scale is retrieved from the pixel-to-metre conversion rate using CMM-stylus. Reproduced from [27], with the permission of AIP Publishing. . . . .	62
4.9	Low pass filter used to remove the noise in the experimental data. The pass-band frequency was set at 100 Hz, and the stopband frequency was set at 150 Hz. . . . .	62
4.10	Comparison of the nonlinear stiffness model, experimental results and equivalent linear stiffness model with $A_{in} = 0.15$ mm. Reproduced from [27], with the permission of AIP Publishing . . . . .	63
4.11	Predicted response from the nonlinear model when excited at different amplitudes. Reproduced from [27], with the permission of AIP Publishing . . . . .	64
4.12	Predicted response from the linear stiffness model with the change in the excitation amplitude. The system shows amplitude dependence as the drag term is nonlinear. . . . .	65

4.13	The comparison of numerical and experimentally obtained results for period-doubling birurcations. (a) The numerical model predicts an unstable response from 82 to 86 Hz, the experimental results confirm the existence of this period-doubling (PD) bifurcation. The PD branch is part of a stable region, and the dotted part continues to an unstable PD branch. (b) Frequency spectrum of the signal denoted A and B in (a) from ‘Exp (Sweep Down)’. The dominant frequency at point B, where the period-doubling is occurring, is half that of the excitation frequency, whereas point A oscillates at the excitation frequency. Reproduced from [27], with the permission of AIP Publishing	65
4.14	Time domain signal of point A and B. Whilst the focal point is moved at a similar frequency, point A oscillates at 1:1 to the excitation frequency and point B oscillates at half the frequency and with greater amplitude. . . . .	66
5.1	A demonstration of the deviation of the particle trajectory deviating from the target trajectory. (a) shows the target trajectory that is in the shape of a hand-drawn letter, ‘S’. (b) shows the resultant trajectory taken by the particle in the experiment. Location deviation is particularly visible around the curves of the letter. Reproduced from [28], with the permission of IEEE. . . . .	70
5.2	Acoustic radiation force profile when driven at 18 V. (a) shows the $z$ axis force, and (b) shows the $y$ axis force. Reproduced from [28], with the permission of IEEE. . . . .	72
5.3	Quiver plot showing the relative position of the equilibrium point from the corresponding focal point in numerical simulation. As the particle reaches the either side of the acoustic levitator, the equilibrium point shifts inwards but the position of the focal point approximates the position of the particle in numerical simulation. Scale of quiver plot is 1:1 with the $x$ -axis and $y$ -axis of the graph. Reproduced from [28], with the permission of IEEE. . . . .	72
5.4	Quiver plot showing the relative position of the equilibrium point from the corresponding focal point in experiment. Scale of quiver plot is 1:1 with the $x$ -axis and $y$ -axis of the graph. Reproduced from [28], with the permission of IEEE. . . . .	73
5.5	The surface of Murata transducer. The surface has a spider-web shaped mesh, and cone shaped resonator and piezoelectric transducer is housed inside the transducer. . . . .	75
5.6	Schematic showing the principle behind simulation of scattering effect from the transducer surfaces. (a) Numerical simulation is formulated such that for the lower phased array the regions marked by ‘Acoustic Levitator’ and ‘Excess Field 1’ was calculated, and for lower phased array the regions marked by ‘Acoustic Levitator’ and ‘Excess Field 2’ was calculated. (b) It is memory intensive to evaluate all of the regions at the same time, therefore, region of interest was applied to reduce the load on memory. . . . .	75

5.7	Schematic showing the experimental apparatus for measuring the reflective coefficient of the phased array surface. The Murata transducer faces towards the hard surface, and B&K microphone was set up directly next to the transducer. The transducer was activated by a pulse from the signal generator, and the audio signal from microphone was recorded on an oscilloscope. The distance between the transducer/microphone to surface is 25 cm, and the speed of sound was $343 \text{ ms}^{-1}$ . . . . .	76
5.8	The signals as recorded by the oscilloscope. The top graph shows the input pulse into the transducer, and the bottom graph shows the recording of the signals from microphone. The signal between 0.5 and 1.5 ms is the emitted audio signal from the transducer, and the signal between 2 and 2.5 ms is the reflected echo from the surface. . . . .	77
5.9	Numerically predicted equilibrium points with the reflective coefficients included. The equilibrium points becomes shifted, but the shift is ordered and symmetrical around the axis. Scale of quiver plot is 1:1 with the $x$ -axis and $y$ -axis of the graph. . . . .	77
5.10	The comparison of the work flows in offline and online trajectory calibration scheme. (a) Offline trajectory calibration scheme processes the images off-site and applies the trajectory calibration as post processing, whilst (b) Online trajectory calibration scheme analyses the images on-site and fed back into the calibration loop. The on-site refers to processes performed during the experiment, and off-site refers to processes performed after the experiments. .	78
5.11	Evaluating the effectiveness of the calibration algorithm. (a) Comparison of the target circle trajectory (black), with calibration (blue dots) and without calibration (red dots). (b) RMS error (difference between target position and equilibrium position) of the path in the $x$ axis. (c) RMS error of the path in the $z$ axis. Reproduced from [28], with the permission of IEEE. . . . .	80
5.12	Application of the calibration algorithm on letters trajectory. The position of the target trajectory was normalised against the location of the letter to demonstrate the improvement. (a) Target trajectory in the hand-drawn shape of 'I', 'U', 'S' and 'E'. (b) Trajectory of the particle without calibration. (c) Trajectory of the particle with calibration. (d) Collection of pictures where the particle drew 'IEEE IUS' separately in each instances. Reproduced from [28], with the permission of IEEE. . . . .	81
5.13	Experimental setup for the measurement of the particle in 3D space. The camera assemblies are orthogonal to each other and was calibrated using the CMM-styli. . . . .	81
5.14	Accuracy of the particle positioning in 3D camera setup as determined by the calibration grid. . . . .	82
5.15	The target trajectory for performance measurement of 3D online calibrator. .	83
5.16	The averaged equilibrium points with and without online calibrator. . . . .	84

5.17	Wireframe Airplane Trajectory of paper plane in 3D. (a) - (c) shows the target trajectory of the wireframe plane as viewed from different angles and (d) - (e) shows the calibrated focal point trajectory. Reproduced from [29], with the permission of AIP Publishing. . . . .	84
6.1	Overall schematics for the proposed Acoustophoretic Volumetric Display (a) Concept diagram showing the experimental setup. (b) The volumetric display as seen by a human observer. Reproduced from [29], with the permission of AIP Publishing. . . . .	89
6.2	Light Intensity as Observed from Different Angles with DSLR camera. The light intensity of the particle was determined from the RGB value at the centre of the particle, and the change in the light intensity was determined by the change in the viewing angle. The LED is illuminated from the front side. Reproduced from [29], with the permission of AIP Publishing. . . . .	90
6.3	Examples of vector graphics rendered by the proposed system. (a) Circle with a radius of 3 mm, (b) Infinity symbol with a horizontal length of 5 mm, (c) Square with a side length of 5 mm. The rendering (drawing) frequency was gradually increased from 1, 5, to 10 Hz and the exposure time of recording camera for each picture is equal to the rendering frequency. Reproduced from [29], with the permission of AIP Publishing. . . . .	91
6.4	Rendered 3D vector graphics. (a)-(c) 3D wireframe volumetric image of an paper plane viewed from various angles (rendering time of 5 seconds). Reproduced from [29], with the permission of AIP Publishing. . . . .	91
6.5	Schematics showing the formulation of a raster screen. (a) An image is split into voxels and one particle will trace the trajectory shown in the arrow. The illuminated light will be varied as the particle changes the position (b) The resolution of the screen is limited by the radius of the circle, and it can be improved by the adding another sets of rows and columns between the original raster graphics trajectory. . . . .	92
6.6	Conversion from still image to volumetric display trajectory. Left image shows the original University of Bristol logo, and right image shows the converted results without subpixelation. Reproduced from [29], with the permission of AIP Publishing. . . . .	93
6.7	Calculation process for the subpixelated image. When the shaded crossover section is greater than 20 % of the area, the colour from the neighbouring colour will be used to calculate the colour for the pixel, C. . . . .	93
6.8	Conversion from still image to volumetric display trajectory. Left image shows the original University of Bristol logo, and right image shows the converted results with subpixelation. Reproduced from [29], with the permission of AIP Publishing. . . . .	93

6.9	Examples of raster graphics generated by the acoustophoretic display device. (a) Overview of the raster graphics with the acoustic levitator (rendering time $T_r = 20$ s), (b) zoomed in version of (a) as seen from the front, (c) an example of an image of a stop sign ( $T_r = 20$ s). Reproduced from [29], with the permission of AIP Publishing. . . . .	94
6.10	The experimental results showing the particle response by vertical focal point oscillation (with different amplitude and frequency of trap oscillation). (a) shows the experimental $z$ -axis error, in terms of the absolute difference between the oscillation amplitude of the trap and response amplitude of the particle ( $E_A$ ), (b) shows the experimental $y$ -axis oscillation, (c) shows the ratio between the $y$ -axis response frequency and the $z$ -axis input frequency ( $F_R$ ). Reproduced from [29], with the permission of AIP Publishing. . . . .	95
6.11	Simulation of the Dynamic Response using a Huygens' Model and the Gor'kov acoustic radiation force model. Reproduced from [29], with the permission of AIP Publishing. . . . .	97
6.12	The equilibrium point of the particle as focal point is scanned across $z_f = 0.03$ to $0.05$ m. . . . .	98
6.13	Comparison of experimental and hybrid simulated response to a vertical focal point oscillation of varying amplitude and frequency. (a) shows the experimental $z$ -axis error, in terms of the absolute difference between the oscillation amplitude of the trap and response amplitude of the particle ( $E_A$ ), (b) shows the experimental $y$ -axis oscillation, (c) shows the ratio between the $y$ -axis response frequency and the $z$ -axis input frequency ( $F_R$ ), (d)-(f) show the numerically simulated $z$ -axis error, $y$ -axis error, and $y$ -axis frequency ratio using the hybrid model, respectively. Reproduced from [29], with the permission of AIP Publishing. . . . .	99
6.14	Particle ejection limits for different applied voltages showing that voltage does not significantly affect the ejection frequency of the particle. The experiment for each amplitude starts as a low frequency of oscillation and proceeds until the particle is ejected. Reproduced from [29], with the permission of AIP Publishing. . . . .	101
6.15	Time domain response (received voltage is proportion to acoustic pressure) for different rates of change of phase. The voltage-time domain signal was Hilbert transformed to identify the amplitude of voltage at instantaneous point. . . . .	102
6.16	Comparison of transducer model and experimental output. Reproduced from [29], with the permission of AIP Publishing. . . . .	103
6.17	Comparison of experimental result and transducer with wider bandwidth. Reproduced from [29], with the permission of AIP Publishing. . . . .	103
C.1	Experimental setup for the measurement of the particle in 3D space. The camera assemblies are orthogonal to each other and was calibrated using the CMM-styli. . . . .	117

# List of Tables

- 3.1 Measured particle properties. Each particle was given an unique identifica-  
tion number, and each particle was stored in an individual glass container to  
prevent deformation, and mix up. . . . . 34
- 3.2 Tables of constants for speed of sound calculation as listed on Cramer.  
Reprinted with permission from [143]. Copyright 1993, Acoustic Society of  
America. . . . . 36
- 3.3 Table of air viscosity with varying temperature. Reproduced from [144]. . . . 37
  
- 6.1 Example showing the variability of the ejection frequency of particle from the  
acoustic trap. Reproduced from [29], with the permission of AIP Publishing. . 100



# Chapter 1 Introduction

The vibration of matter occurs at every level, from the smallest scale of subatomic particles and atoms to large solid structures such as bridges and buildings, to fluids. One of the most familiar vibrations for humans in daily lives is sound: the vibrations that travel through media such as air. Sounds surround us, and we interact with them in various ways. For example, many biological species use sounds to communicate and alert each other, and the early human civilisation also created musical instruments and devices for communication and entertainment.

Thus, it was natural for humans to keep exploiting the mechanisms of sound for the benefit of human society, and acoustics (the study on the properties of sound) is an active field of research in both natural and applied science. From the late 19th century to the early 20th century, scientists began to realise that sound could be used to generate remote forces, called the acoustic radiation forces [1–5]. Such force has a large potential to benefit human society further, and can be utilised to achieve stable levitation of objects in mid-air.

An acoustic radiation force can be generated in many ways, and various methods have been proposed over the last century such as resonant, non-resonant single-axis classical levitators, resonant chambers, and near-field system such as squeeze film and acoustic streaming-based levitators [6–12]. These levitators allow levitation of a wide range of objects in various shapes and mass and were utilised as specimen holders in various applications. For example, NASA utilised acoustic levitators to hold liquid droplets inside the space shuttle in the 80s and 90s [13, 14], and Argonne National Laboratory studied amorphization of molecular liquids of pharmaceutical drugs using an acoustic levitator [15] in 2011. For applications as a specimen holder; the stability of the levitated particle plays a significant role in the accuracy of the analysis. It is common for these acoustic levitators to be placed in an open environment where air current and thermal fluctuation induced by the heating of electronics may result in random oscillation of the particle. As the ability of the levitator to adjust its position in these early form of levitators were limited, it was challenging to implement systems that minimise random oscillation of a levitated particle.

This problem may finally be addressed by the introduction of a phased array levitator (PAL). A phased array is an array of transducers which utilises the interference property of the waves to generate or steer the field, and Ochiai et al. were the first to demonstrate a PAL with 1140 ultrasonic transducers to achieve dexterous manipulation of particles in mid-air. In the following year, Marzo et al. achieved the first single sided acoustic levitation in mid-air, and it has brought new application as a display and additive manufacturing method.



## 1.1 Research Motivation

In 2017, Marzo et al. published an open-source acoustic levitation system, “TinyLev” [16] and this allowed a wide range of researchers to utilise static acoustic levitator for their research [17–20]. Marzo et al. further published “Ultrairno”; the open-sourced version of PAL in 2018 [21] and some researchers are already beginning to utilise the published phased array into their research [22]. Therefore, we can easily imagine that “Ultrairno” will similarly invite and encourage researchers across the field to develop further applications of acoustic levitation with a PAL. Current applications [20, 23], along with desired future applications [24, 25], of a PAL already demands a high particle velocity and precise particle positioning and understanding the dynamics of acoustic levitation is critical in determining the performance, characteristics and limitations of the system. In addition, whilst it is possible to formulate a system that minimises the particle oscillations without the full knowledge of the dynamics (such as minimal control synthesis [26]): it is highly desirable to have a good understanding of the system to formulate a control system.

The dynamics of acoustic levitation has been investigated in some acoustic levitators such as resonant-chamber and near-field levitation. However, the dynamics of levitated solid particles in air using a PAL has not yet been investigated. While the most similar system to a PAL is a classical single-axis acoustic levitator; the dynamics of a levitated particle in this system is not explored in-depth, despite it being one of the most commonly utilised acoustic levitators in the field. The linear stiffness model is still a widely accepted method in the acoustic levitation, but its limitation and the range of applicability have not yet been identified [12].

Therefore this thesis aims to identify the underlying dynamics of a levitated solid particle in a PAL and improve the dynamic positioning performance of the PAL. This will lay the foundation for the development of a control system for a static application such as specimen holder, and as the basis of numerical simulation for the future application of a dynamic acoustic levitator. In order to achieve this aim, the objectives of the thesis were set to:

- Construct numerical forward model which can predict that acoustic pressure field inside the acoustic levitator, and thereby the acoustic radiation force.
- Construct a one-dimensional dynamic model of a particle levitated inside a PAL and explore the range of validity of the ‘linear stiffness model’ in acoustic levitation.
- Design and establish experimental apparatus and set up to accurately track the position of the levitated particle, and therefore the dynamic response of the system.
- Validate a one-dimensional dynamic model against experimentally obtained data and identify and hypothesise the limitations in the dynamic model.
- Develop hybrid dynamic models which quantitatively and qualitatively demonstrates the validity of the proposed hypothesis.
- Develop a trajectory calibration scheme to improve the static trajectory of the particle.

- Apply the findings above to the development of a novel application of acoustic levitation: an acoustophoretic volumetric display.

## 1.2 Thesis Outline

### Chapter 2

In § 2, a review of the published literature is presented. The literature review covers the acoustic radiation force, the types of acoustic levitators, dynamics of levitated objects, applications of the levitators and the implications of nonlinear responses in systems.

### Chapter 3

In § 3, the experimental consideration and numerical simulation of the acoustically levitated particle are introduced. Specifically, the PAL that is utilised throughout the rest of the thesis is introduced, and its method of controlling the position of the particle will be described in full. An equivalent setup is numerically simulated using MATLAB, and the methods of obtaining the empirical values for the numerical simulation will also be described. Furthermore, the particle tracking system which is also utilised throughout the thesis is introduced, and its setup, calibration and the method of extracting the particle position from still images is described.

The experimental setup was developed in collaboration with Dr. Asier Marzo from UpnaLab in Universidad Pública de Navarra in Spain, and the acoustic levitators shown in this thesis, together with the FPGA controller is the work of Dr. Marzo. The numerical simulation, particle tracking system (with setup and calibration scheme), and other experiments described in this Chapter are the work of the author, whilst components such as Appendix A-B were designed by the author and manufactured by Mr. Stephen Isles in the Faculty of Engineering Workshop.

### Chapter 4

In § 4, a one-dimensional dynamic model of the levitated particle is introduced, and the underlying forces in the system are described. The acoustic radiation forces are described in terms of the linear and nonlinear stiffness equation, and the validity of the linear stiffness model is tested. The governing equations are introduced and the method of predicting the system response using the numerical continuation toolbox, COCO is described, and the responses using linear and nonlinear stiffness models are determined. The results are compared against experimentally obtained data, and nonlinear stiffness model is found to be in an excellent match with the experimental results. The nonlinear stiffness model is further utilised to predict the softening behaviour of the system, and the occurrences of period-doubling bifurcations are also predicted. The experiment was repeated again in the vicinity of the predicted point in the numerical simulation, and the occurrences of the period-doubling bifurcation in the acoustic levitator are experimentally confirmed.

The work presented in this chapter was published in *Applied Physics Letters* as “Nonlinear trapping stiffness of mid-air single-axis acoustic levitators” [27] and texts and figures were reproduced from [27] with the permission of AIP Publishing. The author led the development of the numerical simulation, executed experiments, analysed and discussed the results from the numerical simulation and experimental results.

## **Chapter 5**

In § 5, experimental observations demonstrate that the trajectory of the particle is offset from the desired path. The cause of this deviation is attributed to the shift in the static equilibrium points that were not numerically predicted. The static equilibrium point shift was quantified, and its significance was identified. The sources of the static deviation were hypothesised, and one of the hypotheses (reflection from the phased array) was explored in detail. A numerical simulation which replicates the effect in the hypothesis was developed and was qualitatively validated. A calibration scheme was then developed to compensate for the shift of the equilibrium points and was implemented in both a 2D and 3D field. The effectiveness of the calibration scheme was quantitatively and qualitatively demonstrated.

This work was presented in ‘IEEE International Ultrasonics Symposium 2018’, in the format of oral, poster, and conference paper as “Trajectory Optimization of Levitated Particles in Mid-air Ultrasonic Standing Wave Levitators” (IEEE IUS 2018 Best Student Paper in Physical Acoustics group) [28] and published in *Applied Physics Letters* as “Acoustophoretic volumetric displays using a fast-moving levitated particle” [29]. Texts and figures in this chapter are reproduced with the permission of IEEE and AIP Publishing. The contributions of the author were to lead the identification and quantification of the static deviation in the experimental setup, the development of reflection included acoustic pressure simulation and the development of the calibration scheme for the trajectory improvements.

## **Chapter 6**

In § 6, the findings from the previous chapters are applied in the development of a new application as a free-space volumetric display, and the sources of the performance degradation in the proposed system were identified. The concept of the volumetric display along with the setup for the proof-of-concept device is described in full. Two modes of display, vector and raster graphics are described, and its differences are highlighted. The static trajectory calibration procedure used in § 5 is utilised to improve the rendered quality of the volumetric display. A significant horizontal movement of the particle was observed, which was not predicted via numerical simulation, and a hypothesis was developed that the static deviations has initiated horizontal movements. A hybrid model which incorporates the static deviation into the dynamic simulations was proposed, and its validity was quantitatively and qualitatively demonstrated. Furthermore, the current limitations of the system are determined with potential solutions to each limitation.

This work was published in *Applied Physics Letters* as “Acoustophoretic volumetric displays using a fast-moving levitated particle” [29]. This work was carried out using the computational facilities of the Advanced Computing Research Centre, University of Bristol - <http://www.bris.ac.uk/acrc/>. The texts and figures in this chapter are reproduced with the permission of AIP Publishing. The contents in this chapter were also presented in ‘Rank Prize Funds Symposium on the Parallels between acoustics and EM radiation in structured materials’ as “Acoustophoretic volumetric displays using a fast-moving levitated particle” (Early Career Researcher Best Paper Award). The idea of “Acoustophoretic Volumetric Display” was proposed by Dr. Asier Marzo, and the proof-of-concept device (acoustic levitator, RGB LED light controller) was developed by Dr. Marzo. The author contributed to identify the sources of the image quality degradation through experimentation, designed specific trajectories for vector and raster graphics, experimentally demonstrated the feasibility of the prototype, calibrated the static trajectory, and proposed and developed the hybrid dynamic model.



# Chapter 2 Literature Review

In this chapter:

- The method of calculating acoustic radiation force is reviewed, starting from the physical origin of radiation pressure.
- Gor'kov potential is introduced with an example calculation for a simple 1D planar standing wave system.
- Various methods of generating acoustic radiation force are introduced and categorised into either classical and phased array acoustic levitators.
- Literature on the dynamic behaviour of acoustically levitated objects is reviewed.
- Demonstrated and proposed applications of acoustic levitators are reviewed, with a specific focus on PAL.
- Relevance and importance of understanding nonlinear dynamic behaviour in the dynamic system are reviewed.

## 2.1 Acoustic Radiation Force

When a particle is located in an acoustic field; the acoustic radiation force could be exerted to the particle. This acoustic radiation force is generated through the interaction of sound and particle and it can be generated both in liquids and gas. This force arises by considering the non-zero time averaged pressure field, and the concept of radiation pressure will be first introduced.

### 2.1.1 Non-zero Time Average

The majority of the acoustic problems are solved in a linear domain, and three physical equations are required to describe the motion of fluid when it is assumed to be inviscid and non-heat conductive. The first equation is the exact continuity equation [30],

$$\frac{\partial \rho}{\partial t} + \nabla \cdot (\rho \mathbf{v}) = 0 \quad (2.1)$$

where  $\mathbf{v}$ ,  $\rho$  are velocity vector, and density respectively. The second equation is the Euler's equation [12, 30]

$$\rho \left[ \frac{\partial \mathbf{v}}{\partial t} + (\mathbf{v} \cdot \nabla) \mathbf{v} \right] = -\nabla p \quad (2.2)$$

and finally:

$$p = p(\rho) \quad (2.3)$$

which expresses the pressure in terms of the fluid density. In the absence of acoustic waves, the field is static ( $v_0 = 0$ ) and has constant pressure ( $p_0$ ), and density ( $\rho_0$ ). When a wave propagates in the fluid medium, the total field ( $p, v, \rho$ ) is a summation of the unperturbed field ( $p_0, v_0, \rho_0$ ) and a first-order perturbation ( $p_1, v_1, \rho_1$ ) in a linear acoustic sense. However, it requires the consideration of nonlinear terms to evaluate the effect of acoustic radiation force [31]. Thus, the second-order effect ( $p_2, v_2, \rho_2$ ) is included in the calculation [12, 32]:

$$\rho = \rho_0 + \rho_1 + \rho_2 \quad (2.4)$$

$$v = v_1 + v_2 \quad (2.5)$$

$$p = p_0 + p_1 + p_2 \quad (2.6)$$

By substituting equation 2.4-2.6 to Euler's equation in 2.2:

$$\nabla p_2 = -\rho_0 \frac{\partial v_2}{\partial t} - \rho_1 \frac{\partial v_1}{\partial t} - \rho_0 (v_1 \cdot \nabla) v_1 \quad (2.7)$$

will be obtained by only keeping the second order terms [12]. As the acoustophoretic motion is the result of radiation force averaged over a full oscillation cycle; only the time average of the full oscillation period ( $\tau$ ) needs to be studied [32]:

$$\langle X \rangle = \frac{1}{\tau} \int_0^\tau X(t) dt \quad (2.8)$$

The time averaged, second-order acoustic pressure,  $\langle p_2 \rangle$  in the inviscid bulk fluid is then [12]:

$$\nabla \langle p_2 \rangle = -\rho_0 \left\langle \frac{\partial v_2}{\partial t} \right\rangle - \left\langle \rho_1 \frac{\partial v_1}{\partial t} \right\rangle - \rho_0 \langle (v_1 \cdot \nabla) v_1 \rangle \quad (2.9)$$

The first term on the right hand side of equation 2.9 is zero due to the fact that “second-order velocity is periodic for a time-harmonic field, and its decomposition in Fourier series results in a sum of sinusoidal waves and a constant. The time average of these sinusoidal waves and the time derivatives of the constant are both zero” [12]. By utilising the linearised version of Euler's equation in Equation 2.2 [30]:

$$\rho_0 \frac{\partial v_1}{\partial t} = -\nabla p_1 \quad (2.10)$$

and substituting 2.10 together with identities  $p_1 = c_0^2 \rho_1$ ,  $\nabla(p_1^2) = 2p_1 \nabla p_1$ , and  $\nabla(v_1 \cdot v_1) = 2(v_1 \cdot \nabla) v_1$  to Equation 2.9 [12, 32]:

$$\langle p_2 \rangle = \frac{1}{2\rho_0 c_0^2} \langle p_1^2 \rangle - \frac{\rho_0}{2} \langle v_1 \cdot v_1 \rangle \quad (2.11)$$

This equation is the governing second order time-averaged acoustic radiation pressure.

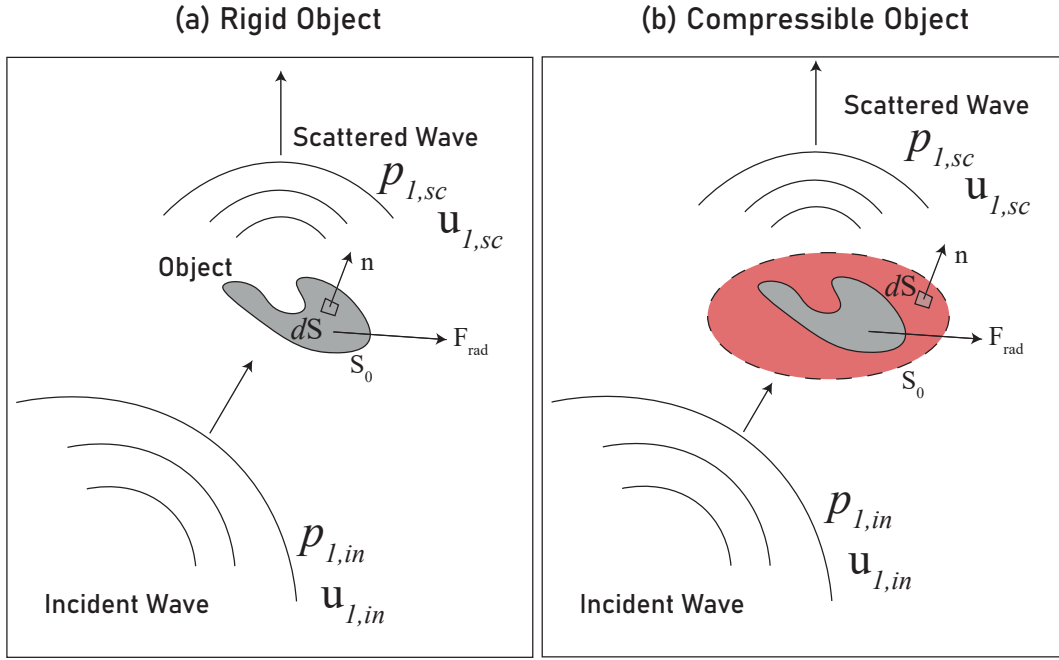


FIG. 2.1. Boundary of acoustic radiation force calculation for (a) rigid object and (b) compressible object

### 2.1.2 Acoustic Radiation Force and Torque on Objects

The acoustic radiation force acting on a rigid object of arbitrary shape and size can then be calculated by taking the surface integral around the levitated object. The method of calculating the acoustic radiation force depends on the boundary of the object as illustrated in Fig. 2.1. For a rigid objects in a fixed position, the surface integral of second order time-average acoustic radiation pressure around the object, as shown in Fig. 2.1 (a) [12, 33]:

$$F_{rad} = - \int_{S_0} \langle p_2 \rangle \mathbf{n} dS \quad (2.12)$$

where  $\mathbf{n}$  is the normal vector,  $S$  is the surface of the object. On the other hand, if the object is compressible and the object surface can move, the acoustic radiation force is evaluated by taking a surface integral in the vicinity of the object as shown in Fig. 2.1 (b) [32, 34]:

$$F_{rad} = - \int_{S_0} \langle p_2 \rangle \mathbf{n} dS - \int_{S_0} \rho_0 \langle (\mathbf{n} \cdot \mathbf{v}_1) \mathbf{v}_1 \rangle dS \quad (2.13)$$

Along with acoustic radiation force, acoustic radiation torque is applied to the object, and Maidanik derived a general expression for acoustic radiation torque in 1958 [35] using the conservation of linear momentum, similarly to the derivation method of acoustic radiation force by Westervelt [36]:

$$T_{rad} = \rho_0 \int_{S(R)} dS \cdot \langle \mathbf{r} \times \mathbf{u} \rangle \quad (2.14)$$

where the integral is taken over the surface  $S(R)$ ,  $\mathbf{u}$  and  $\mathbf{r}$  are the fluid velocity, and position vector, respectively. The evaluation of the acoustic radiation torque is important for stability



analysis when the object is not spherically symmetric [9, 37, 38], or when acoustic vortex is used for levitation [39].

### 2.1.3 Gor'kov Potential

Whilst these formulation allows us to effectively evaluate acoustic radiation force: it requires calculation of both the incidental and scattered wave from the object and it can be cumbersome. Thus, one of the most commonly utilised expression to evaluate acoustic radiation force is Gor'kov potential, which is valid for a spherical particle immersed in an ideal fluid and has radius much smaller than the wavelength ( $r \ll \lambda$ ) [40]. The acoustic radiation force ( $\mathbf{F}_{rad}$ ) is calculated from Gor'kov potential  $U_{rad}$ :

$$\mathbf{F}_{rad} = -\nabla U_{rad} \quad (2.15)$$

$$U_{rad} = \frac{4\pi}{3} r^3 \left[ \frac{f_1 \kappa_0 \langle p_{1,in}^2 \rangle}{2} - \frac{3f_2 \rho_0 \langle v_{1,in}^2 \rangle}{4} \right] \quad (2.16)$$

where  $f_1 = 1 - \frac{\kappa_p}{\kappa_0}$ ,  $f_2 = \frac{2(\tilde{\rho}-1)}{2\tilde{\rho}+1}$ , and  $\tilde{\rho} = \frac{\rho_p}{\rho_0}$ .  $\rho$  is density,  $\kappa = \frac{1}{\rho c}$  is compressibility with  $c$  being the speed of sound,  $p_{1,in}$  and  $v_{1,in}$  are incident pressure and velocity fields, respectively. Subscript 0 represents the properties of the fluid medium and  $p$  of the particle [32, 40]. Therefore, this Gor'kov potential only needs to evaluate  $p_{1,in}$  and  $v_{1,in}$  which can be calculated easily without utilising finite element model or complex analytical solutions.

#### Example: Calculation of Acoustic Radiation Force in Plane Standing Wave Field

Here an example of evaluating acoustic radiation force in a 1D plane standing wave field in  $z$  axis is demonstrated. The pressure field in the 1D planar standing wave is expressed by [32]:

$$p_{1,in} = p_0 \cos(\omega t) \cos(kz) \quad (2.17)$$

where  $p_0$ ,  $\omega$ ,  $k = \frac{\omega}{c_0}$  are pressure amplitude, angular frequency, and the wave number, respectively.

The velocity field,  $v_1$  is evaluated by:

$$v_{1,in} = \left| \nabla \left( \frac{p_{1,in}}{\rho_0 \omega i} \right) \right| \quad (2.18)$$

Therefore using 2.17:

$$v_{1,in} = \frac{p_0}{\rho_0 c_0} \cos(\omega t) \sin(kz) \hat{k} \quad (2.19)$$

Using the identities,  $\langle \cos^2(\omega t) \rangle = \langle \sin^2(\omega t) \rangle = \frac{1}{2}$  [32]:

$$\langle p_{1,in}^2 \rangle = \frac{p_0^2}{2} \cos^2(kz) \quad (2.20)$$

and

$$\langle v_{1,in} \cdot v_{1,in} \rangle = \left( \frac{p_0}{\rho_0 c_0} \right)^2 \frac{1}{2} \sin^2(kz) \quad (2.21)$$

By substituting 2.20 and 2.21 to 2.16:

$$U_{rad} = \pi r^3 \kappa_0 p_0^2 \left( \frac{f_1}{3} \cos^2(kz) - \frac{f_2}{2} \sin^2(kz) \right) \quad (2.22)$$

The acoustic radiation force is then:

$$F_{rad,z} = -\delta_z U_{rad} = 4\pi\Phi(\tilde{\kappa}, \tilde{\rho})kr^3 E_{ac} \sin(2kz) \quad (2.23)$$

where  $E_{ac} = \frac{p_0^2}{4\rho_0 c_0^2}$  is the acoustic energy density, and  $\Phi(\tilde{\kappa}, \tilde{\rho}) = \frac{1}{3} \left[ \frac{5\tilde{\rho}-2}{2\tilde{\rho}+1} - \tilde{\kappa} \right]$  is the acoustophoretic contrast factor. Acoustophoretic contrast factor determines where the submerged particle settles in the acoustic wave. If the contrast factor is smaller than 0, it goes to the anti-node, and if the contrast factor is larger than 0, the particle settles to the node of the pressure field. For the case of particle levitated in air, the majority of the object is considered to be hard in comparison to air: making the contrast factor positive, and particle settles to the node of the field.

## 2.2 Types of Acoustic Levitators

Various methods of generating acoustic radiation force has been proposed by many reserachers and “Kundt’s tube”, one of the most classical demonstration device in acoustics for standing wave is also an acoustic levitator. The demonstration of Kundt’s tube usually consists of a clear tube with a speaker attached at the end, and the standing wave is visualised with fine powders/particles [1]. These particles accumulate at the nodes of the standing wave and light objects can be levitated using this method [41]. However, the first levitation of objects with acoustic radiation forces is credited to Bücks & Müller in 1933 [4] who demonstrated the levitation of alcohol droplets using vibrating quartz and a reflector. The droplets were used as a means to visualise the position of the nodes and to determine the oscillation frequency of the quartz accurately.

Since then, many researchers worked on the development of acoustic levitators, and the current mid-air acoustic levitator can broadly be classified to two types of category, as shown in Fig. 2.2. The acoustic levitators can be categorised into ‘Classical’ and ‘Phased Array’ levitators (PAL). The classical acoustic levitators referred to here are mid-air acoustic levitator designed prior to 2014, and usually utilises a ‘bolt clamped Langevin transducer’ to generate an acoustic pressure field. On the other hand, PAL is constructed by an array of off-the-shelf low power transducers and uses the phase difference between each transducers to generate acoustic pressure field by using the constructive/destructive interference property of the wave.

### 2.2.1 Classical Acoustic Levitator

A classical acoustic levitator can further be classified into single/multi axis and near-field levitators. A single / multi axis levitator usually consists of a combination of the transducer

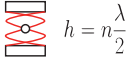
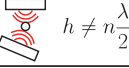





Category	Subcategory / Type		Diagram	Underlying Principle
Classical Acoustic Levitator	Single / Multi Axis	Resonant	 $h = n \frac{\lambda}{2}$	Standing wave caused by multiple reverberating waves.
		Non Resonant	 $h \neq n \frac{\lambda}{2}$	Reflected wave is limited to primary reflection.
	Near-Field	Squeeze Film		Cushioning effect caused by squeezed film.
		Acoustic Streaming		Acoustic streaming pushes the air from the space.
		Standing Wave		Standing wave forms between the object and transducer.
Phased Array Levitator	Single / Multi Axis			Phase from each transducer is adjusted to create acoustic trap.
	Single Beam			Achieves single sided levitation by forming twin, vortex, or bottle trap.

FIG. 2.2. The class, subcategory, and types of mid-air acoustic levitator, and the underlying working principle for each levitator.  $n = \{1, 2, 3, \dots\}$  is an integer.

and a reflector, or; two opposed transducers, whereas, the levitator itself acts as a reflector in near-field levitator.

### Single / Multi Axis Acoustic Levitator

A single / multi axis acoustic levitator can further be classified into a resonant and non-resonant system. The resonance state refers to the volume between the transducers and reflectors, and the resonant levitator is achieved by the superposition of multiple ‘reflected’ waves in between the transducer and reflector. The distance between the two needs to be finely adjusted to match the resonance mode of the cavity (for a plane standing wave, the distance between the two components needs to be an integer multiple of a half wavelength) [42] for ‘resonant single-axis acoustic levitator’. The resonant single-axis acoustic levitator, as shown in Fig. 2.3 is one of the earliest design of single-axis acoustic levitator [10, 43, 44], and it is advantageous in a case where a strong acoustic radiation force is required. The resonance of the volume allows a heavy object to be levitated in space. For example, resonant single-axis levitator can levitate high-density material such as liquid mercury or iridium, which is very challenging in non-resonant single-axis acoustic levitator [8]. A multi-axis acoustic levitator is constructed using multiple Langevin transducers enabling multi-axis manipulation. Multi-axis manipulation with 21 Langevin transducers was demonstrated by Foresti et al. in 2013 [23]. Whilst the transducers are aligned in a format of an array, it is not a phased array as only the amplitude of the voltage was modulated to achieve transportation. Another example of multi-axis levitator was demonstrated by Hong et al. where the acoustic vortex generated by 6 Langevin transducers was utilised to levitate particles [45]. Furthermore,

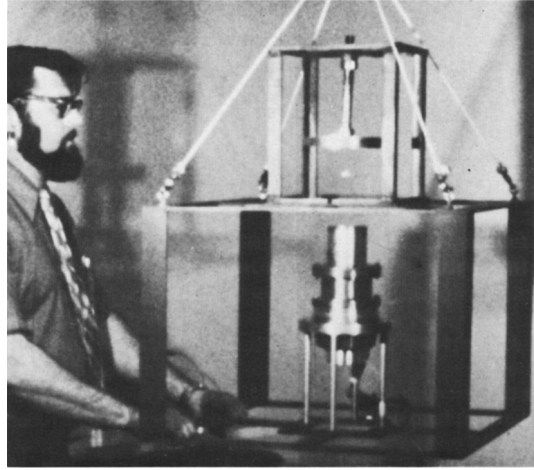


FIG. 2.3. Single-axis resonant acoustic levitator demonstrated by Whymark. Reprinted from [10] with the permission of Elsevier.

Clough et al. and Sracic et al. demonstrated two-axis and three-axis acoustic levitators using 4 and 6 Langevin transducers, respectively; improving the stability of the levitated particle in mid-air [46, 47].

A close variant of resonant single / multi axis levitator is a closed resonant chamber which was extensively developed by NASA and their collaborators for use on various space missions [48–52]. A closed resonant chamber utilises the resonance of the chamber to levitate objects. The levitator developed by NASA Jet Propulsion Lab (JPL) utilised three ‘commercial speaker drivers’ [53] and the speakers generated audible frequency acoustic waves (100-4000 Hz for levitators described by JPL [53]). Experiments utilising a closed resonant chamber was performed in Space Shuttle missions STS-50 and STS-51-B in 1992 and 1985, respectively [13, 14]. The experiment was conducted by Wang in STS-51-B, and Trinh in STS-50 and they contributed significantly to understand the liquid droplet rotation and oscillation using acoustic levitation [48–52]. The dynamics involved with the closed resonant chamber was also investigated by Rudnick & Barmatz in 1990 [11] and their contributions will be described in § 2.3.

On the other hand, a ‘non-resonant’ levitation is achieved by the superposition of two or more counter-propagating waves, and the distance between the transducer and reflector/transducer does not need to be fixed with an integer number of half wavelengths. Rey proposed the development of non-resonant acoustic levitator in 1978 [55], but it was not until 2007 when Kozuka et al. demonstrated that a set of two transducers can levitate particles without having resonant volume [56]. Similarly, Andrade et al. demonstrated a non-resonant levitator (Fig. 2.4) with a concave reflector and transducer in 2015 [54].

### **Near-field Levitator**

The configuration of the near-field levitator is very similar to the resonant single-axis acoustic levitator. However, the levitated object itself acts as a reflector in a near-field acoustic levitator, and the object levitates at the near field of the transducer. According to Hansen,

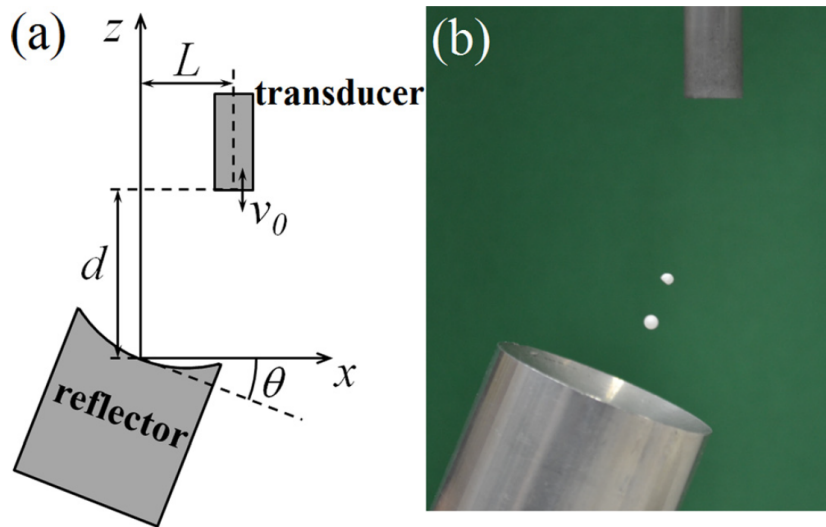


FIG. 2.4. Non-resonant acoustic levitation of particles. Reprinted from [54], with the permission of AIP Publishing.

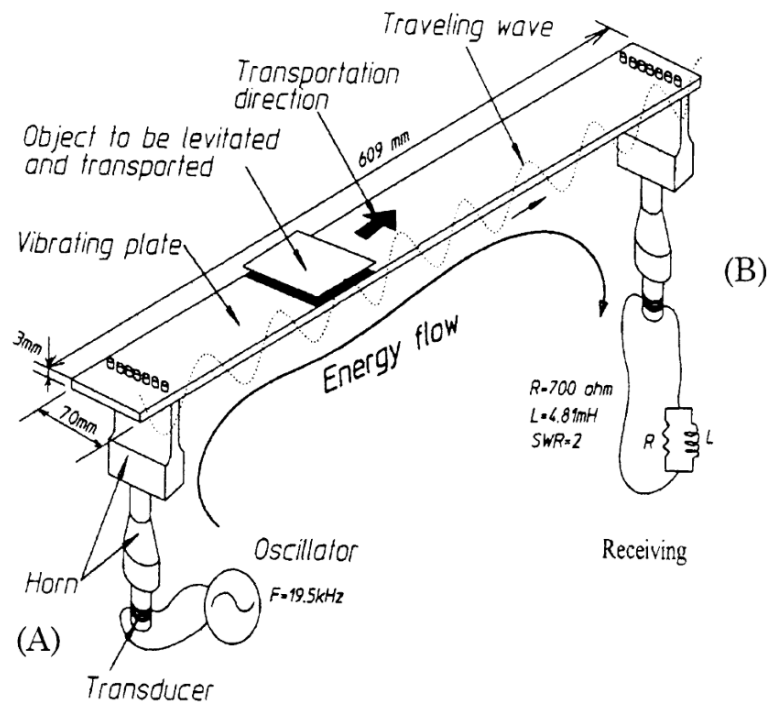


FIG. 2.5. Squeeze film levitation using flexural travelling wave. Reprinted from [7], with the permission of Elsevier.

the near-field is the “region close to a source where the sound pressure and acoustic particle velocity are not in phase” and it is limited to region within “a wavelength of the sound or equal to three times the largest dimension of the sound source” [57]. There are three types of near-field acoustic levitation, and those are squeeze film, acoustic streaming, and standing wave.

**Squeeze Film levitation** The near-field levitation that utilises squeeze film levitation in mid-air was first published by Hashimoto et al. [58] in 1995. The squeeze film levitation is classified as acoustic levitation as the levitation is achieved by “time-averaged pressure higher than surrounding” and this time-averaged pressure is generated by the vibrating surface squeezing “the compressible fluid that occupies the clearance between the planes” [59]. Using this method, Hashimoto et al. levitated objects ranging from 0.0076 to 0.1049 kg using a longitudinal vibration mode at the distance of 20 to 500 micrometre [58]. Similarly, Hashimoto et al. demonstrated that flexural vibration (where the vertical displacement of the plate is uniform along the horizontal axis, but oscillatory in the vertical axis) of a rectangular plate can also be utilised to achieve levitation [6]. The rectangular plate had dimensions of 695 mm by 220 mm and a Langevin transducer was attached at one end of the rectangular plate. It was demonstrated experimentally that, for a stable levitation on flexural vibration mode, the specimen needs to be longer than  $1.5\lambda$  of the flexural vibration mode.

The non-contact transportation of objects was also demonstrated using squeeze-film levitation through the generation of a flexural travelling wave along vibrating plates [60], as shown in Fig. 2.5. Here, two Langevin transducers were attached at both ends of the plate and one transducer generated whilst the other was set to absorb it. A velocity of  $0.7\text{ ms}^{-1}$  was reported by the authors, and the change in the thickness of plate induced change in the displacement amplitude of the plates. Many authors have since developed and analysed various types of squeeze-film levitator [7, 59, 61–64] and recent advances enabled researchers to levitate non-planar objects such as spheres [65] and cylindrical objects [66].

**Acoustic Streaming** Near field levitation with acoustic streaming is achieved by generating acoustic streaming in the clearance between the object and transducer surface. This causes the air to be carried out from the space between the two surfaces: generating time-averaged pressure in the gap, and object is attracted by atmospheric pressure [67]. For exam-

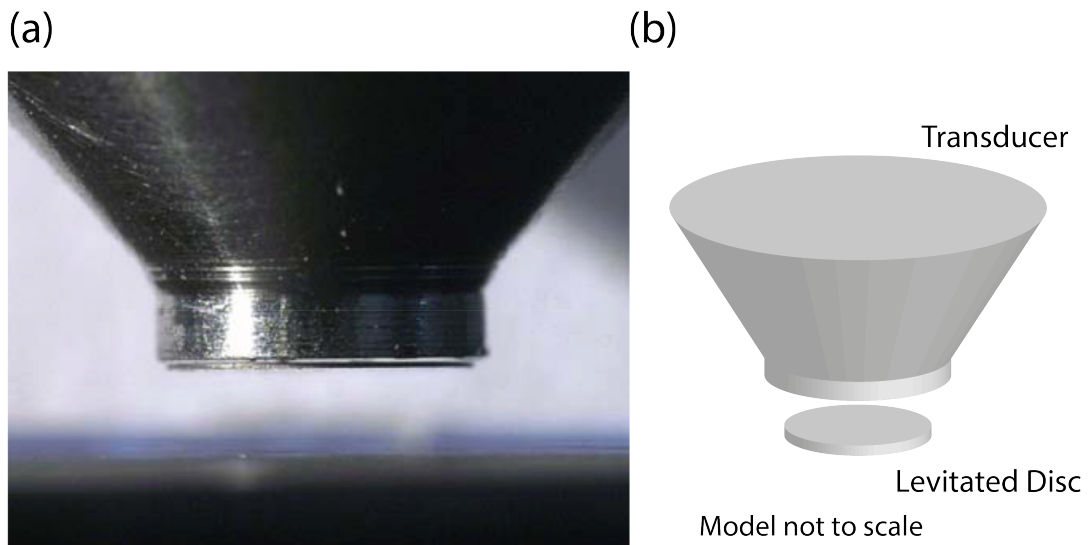


FIG. 2.6. Acoustic streaming induced near-field acoustic levitation causes air between the clearance between the plates out. (a) Levitation of streaming induced levitation. Reprinted from [67], with the permission of Elsevier. (b) Modelled view of the setup, not to scale.

ple, Takasaki et al. demonstrated that a disk with a diameter of 2-4 mm with a thickness of 0.05 mm can be levitated at the distance of 30-50 micrometre using Langevin type transducer with the resonance frequency of 21 kHz, as shown in Fig. 2.6. In contrary to the near-field acoustic levitation where a large object is required for levitation; the inverted near-field acoustic levitator requires the objects to be small in order to achieve successful levitation [12].

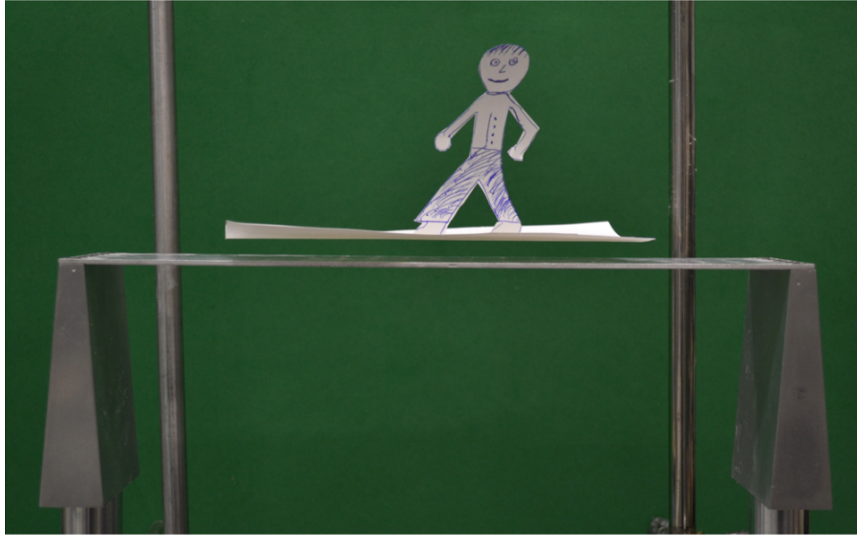


FIG. 2.7. Near-field standing wave levitation. A standing wave forms between the transducer surface and the reflector. Reprinted with the permission from [68]. Copyright 2017, Acoustical Society of America.

**Standing Wave** This levitation method can levitate objects larger than the wavelength by generating a standing wave between the transducer and the reflector. The clearance between the transducer and reflector is at the state of resonance, and acoustic radiation force on the object is “substantially increased” at that point [12]. This was first observed by Clair in 1941 [69], but the application to the acoustic levitator in mid-air was first published by Why-mark [10] in 1975 where a brass disc with a diameter of 5 cm was levitated at a distance of half-wavelength from the transducer. This near-field standing wave acoustic levitation was studied in detail by Zhao & Wallaschek in 2011 and demonstrated the levitation of compact disc (CD) in air. More recently, Andrade et al. demonstrated the stable levitation of large polystyrene ball (with a diameter of 50 mm) [70] using three Langevin transducers with 25 kHz. The transducers were aligned such that the surface the sphere is approximately  $\frac{\lambda}{2}$  from the surface of the transducers, and as the transducer is aligned to be geometrically centred: it generates vertical and axially convergent acoustic radiation force. In 2017, Andrade et. al. also demonstrated acoustic levitation of a curved paper (27.7 by 71 mm) with mass of 2.3 gram using a flexural vibration of the rectangular plate [68], as shown in Fig. 2.7. It was levitated near  $\frac{\lambda}{2}$  from the surface of the transducers and demonstrated that the curved surface of the paper could provide horizontally convergent force for stability.

### 2.2.2 Phased Array Levitator

Phased array levitator (PAL) is the latest method of achieving acoustic levitation, and utilises an array of low-cost parking sensors to generate an acoustic pressure field. Whilst driving one Langevin transducer requires a high-power amplification (typically a magnitude of  $10^2$  Watts), the power consumption of phased array (with all transducers combined) are typically an order of magnitude less, at  $10^0$  -  $10^1$  Watts [71].

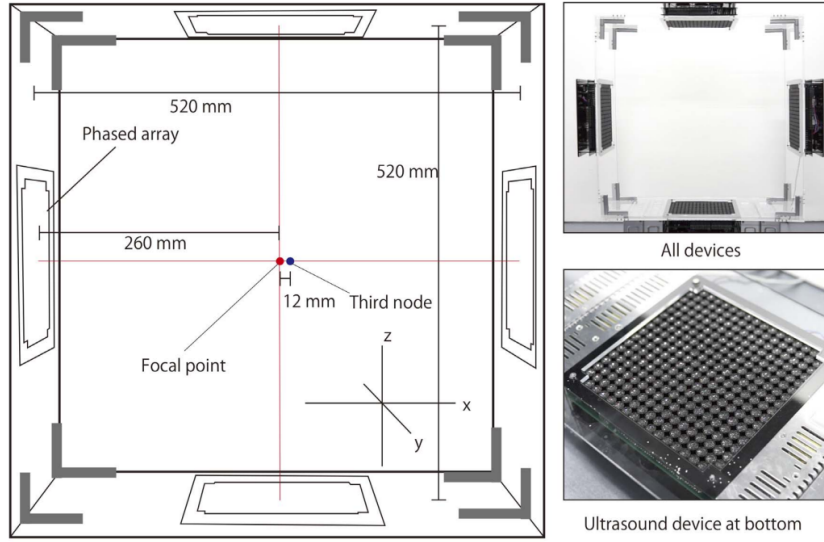


FIG. 2.8. Example of phased array acoustic levitator with 4 phased array configured for three-dimensional manipulation. Adapted from [72], licensed under CC BY 4.0.

### Single / Multi Axis Levitator

Here, it is defined that the single and multi axis levitator for PAL is distinguished by the configuration of the levitator and not the ability for a particle to move in multi-dimensional movement. Therefore, a levitator is called a single-axis levitator when the pair of phased arrays or reflector is configured in one single axis. On the other hand, when additional phased-array was placed orthogonal to the original one, it will be referred to as multi-axis PAL. It is also generally assumed that the single / multi axis levitator is a ‘non-resonant’ acoustic levitator as it does not usually require the separation distance between the phased-array or reflector to be an integer multiple of wavelength constant, as in classical resonant acoustic levitators, and the reflection from the transducer surfaces are considered minimal in majority of the cases.

One of the first mid-air PAL was published by Ochiai et al. in 2014 which had 4 phased arrays set up as shown in Fig. 2.8. This type of acoustic levitator is assumed to be a non-resonant multi-axis levitator, and only the incident wave from the transducer is considered during the manipulation. The setup demonstrated by Ochiai et al. was operated by an FPGA board, which can simultaneously emit signals to each transducer with different phases. By specifying the focal point of the transducer array and thus modulating the phase of each transducer, it enabled dynamic manipulation of the particles. The authors demonstrated levitation



of an expanded-polystyrene ball with radius up to 2.0 mm, and simultaneous trapping of the particle was also demonstrated.

In 2017, Marzo et al. published a single-axis acoustic levitator, ‘TinyLev’ on an open-access basis [16]. TinyLev could be considered to be a simplified PAL with a fixed phases, and uses the geometry of the levitator to focus the field. This simplified the electronics of the levitators, and it can be operated using a commercially available micro-controller board; making the setup affordable (approximately 60 GBP in total) and can easily be built at home [73]. More recently, Marzo et al. published ‘Ultrairno’, an open-source phased array system which allows multiple transducers to be controlled similarly to Ochiai et al. [72]. The methods of manufacturing the phased array levitator that is utilised throughout this thesis is also publicly available in ‘Ultrairno’.

The single-axis PAL can also be achieved with a combination of phased array and a reflector; similarly to Langevin transducer system. Using this method, Watanabe et al. [74] and Andrade et al. [75] demonstrated the contactless transportation of the liquid droplets. Contrary to Foresti et al. [23], the liquid droplets were transported by manipulating the phase, and not the amplitude of the transducers. In 2019, Inoue et al. demonstrated the levitation of a larger than wavelength object, using two opposing phased arrays, each with 996 transducers [38]. The stable levitation of a  $3.5\lambda$  diameter sphere, and a rectangular octrahedron with side length of  $5.9\lambda$  were demonstrated by the authors. Moreover, the dynamic capability of the acoustic levitator to manipulate particle is increasing every year, and most recently, Marzo & Drinkwater demonstrated “Holographic acoustic tweezer” which achieved up to 27 simultaneous manipulation of particles using standing wave levitator with two phased array, each with 256 transducers [76].

### Single Beam Acoustic Levitator

Single-beam acoustic levitation is often referred to as ‘acoustic tweezers’, and it is inspired by the works of Noble Laureate, Ashkin on optical tweezers in the late 20th Century [77, 78]. The first single-beam acoustic levitation was demonstrated using an underwater transducer by Lee et al. in 2009 [77]. Lee et al. utilised a press focused 30 MHz single-element transducer to trap liquid droplets and only generated horizontal acoustic radiation force (the liquid droplet was placed under an acoustically transparent membrane, and the buoyancy of the droplet provided vertical force). In 2016, Baresch et al. published the first single-beam acoustic trap in water which can provide both vertical and horizontal acoustic radiation force [78]. It was achieved by utilising an ultrasonic emitter (1.15 MHz) with 127 elements, and it generated a focused acoustical vortex with a topological charge of -1. The first single-beam acoustic levitation of particle in the air was achieved by Marzo et al. in 2015 [79], as shown in Fig. 2.9. Marzo et al. utilised optimisation algorithms to obtain the optimal acoustic field that can achieve stable levitation of object. The optimisation function was defined to maximise the Laplacian of the Gor’kov potential and minimise the modulus of the pressure:

$$O(\phi^1, \dots, \phi^j) = w_p |p| - w_x U_{xx} - w_y U_{yy} - w_z U_{zz} \quad (2.24)$$

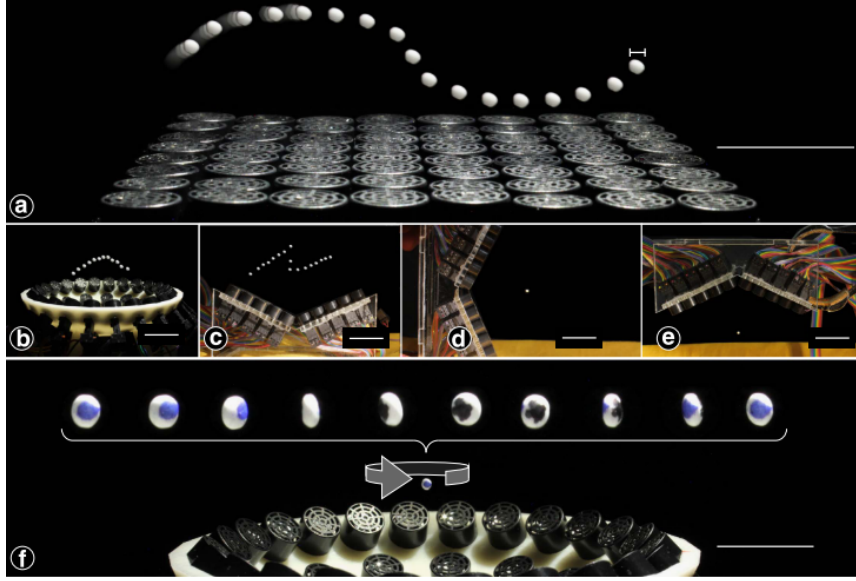


FIG. 2.9. The levitation of expanded polystyrene ball using single beam acoustic levitator. Adapted from [79], licensed under CC BY 4.0.

where  $\phi^j$ ,  $U$  and  $w$  represents phase of each transducer, Laplacian of Gor'kov potential and weighting constants, respectively and subscripts,  $p$ ,  $x$ ,  $y$  and  $z$  represent the pressure, and direction in Cartesian axes, respectively. By varying the weighting constants, the optimisation function will converge to different acoustic traps, and Marzo et al. identified that there exists three types of acoustic trap which can stably levitate the particle in their setup (i.e. twin, vortex and bottle trap). It was demonstrated that the position of the particle can be manipulated by summing the phase required to focus at a point (focal point) and the acoustic lens:

$$\phi = \phi_{lens} + \phi_{focal} \quad (2.25)$$

where  $\phi_{lens}$  and  $\phi_{focal}$  are the phase distribution on the transducer array required for generating acoustic lens and focal point, respectively. This method of identifying the phase distribution required to achieve stable levitation at a given point, can be applied not only in the single-sided acoustic levitator but in any other variant of PAL [21]. Marzo et al. also achieved the levitation of particles larger than the wavelength (diameter of  $1.88\lambda$ ) using single-beam acoustic levitator by utilising acoustic vortices [39]. The acoustic vortex was generated using a PAL consisting of 192 transducers, and the stability of the particle was obtained by switching between the clock-wise and anti-clockwise vortex at a constant time step.

Whilst the particle manipulation is predominantly achieved by the manipulation of phase at the side of transducer array, the manipulation of phase can also be achieved by using acoustic metamaterials. An acoustic metamaterial is defined by a property that “achieves effects not found in nature as means to address long-standing engineering challenges in acoustics” [80]. The context and forms of metamaterial may differ amongst the applications of acoustics but in the field of acoustic levitation, it is used most frequently to manipulate the phase of the acoustic pressure field emitted by acoustic transducers.

For example, Franklin et al. [81] and Melde et al. [82] demonstrated an acoustic lens which physically attached itself to the acoustic transducers, and the phase of propagating acoustic wave was varied by changing the thickness of the acoustic lens. Memoli et al. similarly demonstrated the manipulation of acoustic waves in air in 2017 using ‘metamaterial bricks’ where the phase delay was achieved by guiding the wave through geometrical features in the bricks [83]. More recently, the metamaterial bricks were adapted to ‘bend’ the acoustic pressure field [84], and levitated an EPS particle above a large obstacle.

### 2.3 Dynamics of Acoustically Levitated Objects

Since the first demonstration of acoustic levitation, the behaviour of objects levitated under the influence of acoustic radiation force has been studied in detail by many researchers. There are a number of studies on the dynamics of levitated liquid droplets, ranging from the study of the internal flow of acoustically levitated droplets [85] to the droplet shape oscillation [48, 49, 74, 86, 87]. The dynamics of near-field levitated objects has also been investigated by Ilsar & Bucher in 2017 [88], and a feedback controller have also been implemented by Ilsar et al. [89] in the same year.

Some of the earliest studies in the instability of solid particles was published by Rudnick & Barmatz in 1990 for a resonant chamber based acoustic levitator [11]. In a resonant chamber, the presence of the levitated particle generates a shift in the resonance frequency, arising in a velocity-dependent acoustic radiation force. With the increase in velocity, the acoustic radiation force acts as a negative damping force and causes an instability of the particle. In 2019, Andrade et al. demonstrated the occurrence of particle instability experimentally and showed that the particle instability can occur within resonant ‘single-axis’ classical acoustic levitator [44].

In 2005, Aboobaker et al. modelled the movement of particles in acoustic manipulator in liquids with flow field [90]. The primary acoustic radiation force, along with the secondary acoustic radiation force was also calculated in multi-particle settings, and the particle trajectory was predicted under such settings. Xie & Vaneeste similarly solved the dynamics of particle under the influence of acoustic radiation force from the first principles in 2014 [91]. They demonstrated that the acoustically manipulated particle in a plane standing wave in the liquid is driven by acoustic radiation pressure, Basset force, inertia (with added mass) and viscous drag:

$$(M + M')\ddot{x} = F_{rad,lin} + F_{drag} + F_{Basset} \quad (2.26)$$

where  $M'$  is the added mass,  $F_{rad,lin}$  is the linearised acoustic radiation force,  $F_{drag}$  is the viscous drag, and  $F_{Basset}$  is a force caused by the “temporal delay in boundary layer development as the relative velocity changes with time” and “the value of the Basset force depends on the acceleration history up to the present time” [92]. However, it is considered to be negligible in gas-particle flow [93]. Thus, Basset force is not considered in the acoustic levitation system where a solid particle is levitated in mid-air [11, 44, 88, 94]. The relevancy of each

force was discussed by Xie & Vaneeste, considering the different regime of dynamics, and the governing equations of dynamics were discussed in detail for fluids.

In 2012, Foresti et al. studied the stability of levitated spherical and ellipsoidal particles in various viscosity, and demonstrated that the stability of the levitated particle is dependent on the sign of radial acoustic radiation force [95]. In 2014, Pérez et al. experimentally studied the dynamics of the acoustically levitated sphere in ‘single-axis’ classical acoustic levitator [96]. The dynamics of the levitated particle in mid air was considered as:

$$m\ddot{x} = -b_2\dot{x}|x| - b_1\dot{x} - kx - mg \quad (2.27)$$

where  $kx$  is the linearised acoustic radiation force (using Hooke’s Law of linear spring stiffness),  $mg$  is the gravitational force, and  $b_1$  and  $b_2$  are constants for linear/nonlinear damping [96]. These constants were experimentally obtained, but no clear justifications were made regarding the usage of quadratic damping in the system.

In 2017, Hong et al. investigated the dynamics of a water droplet levitated in a multi-axis classical levitator, with assumption that “the gradient of the force-distance curve near the array centre is near-linear” and “object-trap system to be a simple mass-spring oscillator” [45].

## 2.4 Applications of Acoustic Radiation Force

The acoustic radiation force has found use in a wide range of applications from chemistry, biology, to human-computer interactions. One of the most popular branch of acoustic manipulation has been in the liquid-based acoustic manipulators. Particle manipulation in liquid has been studied extensively [81, 82, 97–102] and has been applied to as a “lab-on-a-chip” device. Lab-on-a-chip is “a class of device that integrates and automates multiple laboratory techniques into a system that fits on a chip” [103], and some functions are already investigated by many researchers as particle separators, filters and as patterning devices [104–111]. Moreover, near-field acoustic levitators have found applications as an ultrasonic motor [7], a contactless stage [112], a clutch [113] and a bearing [114]. However, in this section, the application of ‘resonant’ classical acoustic levitator and PAL in mid-air will be discussed. As shown in Fig. 2.10, the applications of acoustic levitator can be put on a scale from static to dynamic, and the applications in the dynamic regime are beginning to be made possible with the usage of PAL.

### 2.4.1 Specimen Holding (Classical Levitator)

Since the demonstration by Bücks & Müller [4] in 1933, acoustic levitators have continued to be utilised as a specimen holder. As previously mentioned, NASA-funded research contributed significantly to the development of the acoustic levitator at its initiation and used ‘resonant chamber’ classical acoustic levitator in space shuttle missions [49]. On these missions, the resonant chamber was utilised to hold specimen inside the space shuttle, and allowed the investigation of the “surface tension-dominated equilibrium shapes of rotating drops” with

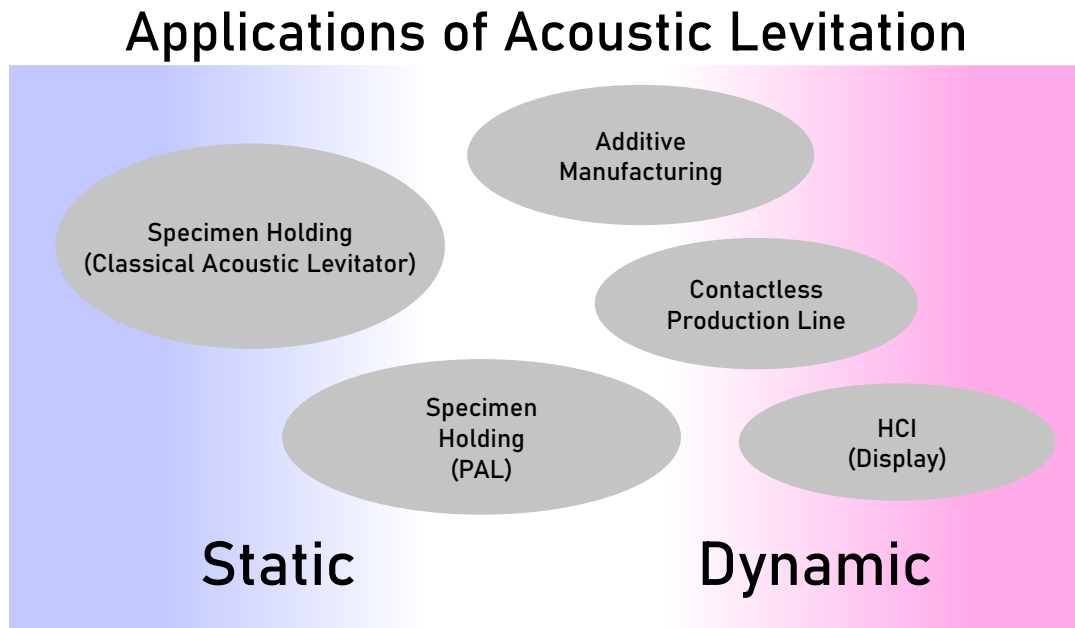


FIG. 2.10. Applications of acoustic levitators in real-world. On the left hand side are applications that do not require particle to move, and on the right are dynamic applications. In a dynamic applications, the particle needs to be transported or controlled inside the levitator to achieve the target.

reduced gravitational acceleration [49]. In addition, Trinh & Hsu proposed a method of utilising acoustic levitators to measure density using the ‘linear spring’ assumption of the acoustic levitator [51]. Classical acoustic levitators have also been utilised by biologists to analyse the blood samples. Puskar et al. demonstrated “Raman acoustic levitation spectroscopy of red blood cells” in 2007 [115] with a ‘single-axis’ resonant classical acoustic levitator as shown in Fig. 2.11, and Hosseinzadeh et al. analysed the shape oscillation of blood samples

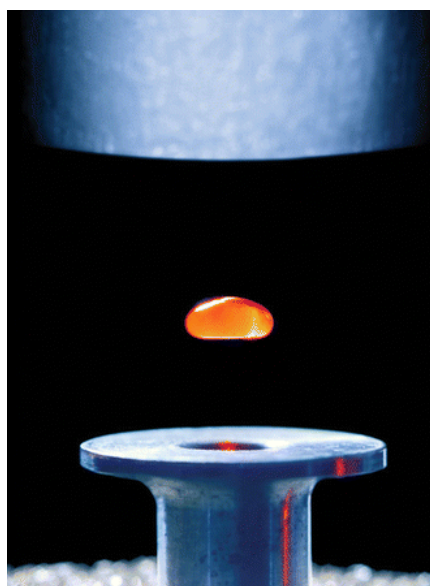


FIG. 2.11. Levitation of blood sample during Raman spectroscopy. Reproduced from [115], with the permission of Royal Society of Chemistry.

in 2018 [116]. Moreover, Argonne National Laboratory studied amorphilization of molecular liquids of pharmaceutical drugs using single-axis resonant acoustic levitator [15] in 2011, and Tsujino & Tomizaki utilised 'single-axis' resonant classical acoustic levitator to hold the specimen in place during X-ray protein crystallography [117]. Bierstedt et al. utilised the levitator to confine laser-induced plasmas in air [118]. In 2013, Foresti et al. developed "contactless multidrop manipulator" using an array of Langevin transducers [23]. The input voltage into each transducer was varied to shift each droplet from one transducer to another, and stable levitation of multiple near-spherical droplets with a volume of 0.1 to 10 microlitre was demonstrated. Moreover, the authors demonstrated the merging of two droplets of the water droplets and demonstrated DNA transfection in mid-air.

### 2.4.2 Specimen Holding (PAL)

Since the publication of 'TinyLev' in 2017 [16], it is beginning to replace single-axis classical acoustic levitator as a specimen holder and Morris et al. utilised acoustic levitation during the macromolecular crystallography with X-ray [17]. Whilst a classical acoustic levitator can provide sufficient forces to hold the specimen in mid-air, it is "complex to set up accurately" [17] and TinyLev offers significant simplification of the system. Moreover, as TinyLev utilises less power than the classical acoustic levitator; samples receive negligible heating, and thus free from excessive evaporation [71].

Moreover, Yurduseven et al. characterised 340 GHz Imaging radar using acoustically levitated water droplets [18] in 2019. If the target is suspended using a rigid object during the measurement of point-spread-function (PSF); the "reconstructed PSF pattern includes not only the contribution of the point scatterer but also the objects that are used to suspend the point scatterer at its position" [18]. By suspending the target in mid-air using acoustic levitation, the scattering from the 'holder' will be removed and can achieve better analysis on the scattering pattern.

Acoustic levitation enables the levitation of objects without being limited by the physical properties, and it is one of the strongest points of acoustic levitation in comparison to the other forms of levitation such as magnetic, optical, or electrostatic methods. Works by Cox et al. [37] and Inoue et al. [38] demonstrate methods of levitating objects of non-spherical geometry with more flexibility than previously achieved and the ability to manipulate particles for acoustic levitators are continuing to improve.

The application of 'Ultrano' [18] with individual control of transducers may allow these researchers to automate the specimen handling process, suppress unwanted oscillation by air current or thermal fluctuations during the analysis, and may further allow new studies using acoustic levitation. For example, Ultrano may allow doppler effect of droplets in new radar system (similarly to Yurduseven et al. [18]) by moving the droplets away or towards the radar.

The automation of specimen handling has already been studied by Andrade et al. [75] and Watanabe et al. [74] in 2018; demonstrating the contactless transportation and merging of

droplets using 40 kHz ultrasonic phased array and suggested potential application in the field of biology, analytical chemistry and pharmacy.

### 2.4.3 Additive Manufacturing

The ability to merge and combine objects in mid-air enables the generation of physical objects in space, and there are on-going studies on using this ability to develop additive manufacturing methods or new human-computer interfaces (HCI). For example, in 2014, Harkness & Goldschmid of “The Boeing Company” filed a patent on “free-form spatial 3-D printing using part levitation” in 2014 where they suggested a component could be fabricated by an additive manufacturing process whilst being levitated in air [24]. Similarly, Ryan et al. of “Siemens Energy, Inc.” filed a patent on the “Acoustic manipulation and laser processing of particle for repair and manufacture of metallic components” in 2016 [25]. Melde et al. has achieved such ‘acoustic fabrication’ using acoustic manipulation; however, it is in a liquid-based system and buoyancy of the particle assists favourably to ease the process of acoustic fabrication. The assembly system in mid-air have not yet been realised (or not publicly available to the best of author’s knowledge); these patents from the manufacturing sector demonstrate the interest of the industry in the application of acoustic levitation in additive manufacturing.

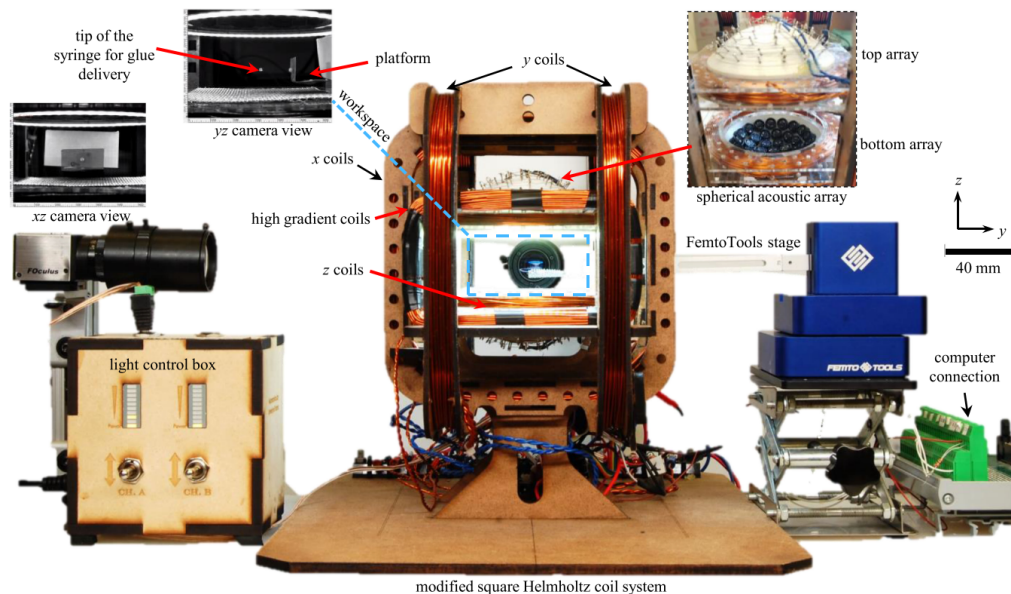


FIG. 2.12. Micro-manipulation device with electromagnetic coils and acoustic levitator. Reprinted from [19], with the permission of IEEE. © 2019 IEEE

### 2.4.4 Contactless Production Line

A similar but different application is to utilise PAL in a contactless production line. In this application, multiple components are assembled by levitating and controlling the orientation of each component. One of the first micro-assembly line in a mid-air acoustic levitator was developed by Youssefi & Diller who demonstrated a hybrid device of electromagnetic coil

and TinyLev, as shown in Fig. 2.12 [19]. In the device, the levitation was achieved by the acoustic levitator, and the orientation of the components was controlled by magnetic forces. Assembly of “Inuksuk figure” with a dimension of 3 by 3 mm was demonstrated by authors by glueing seven components together in mid-air.

### 2.4.5 Human Computer Interface (Display)

Whilst additive manufacturing aims to generate a component by bonding multiple particles together, the application of acoustic levitation in HCI promotes reconfigurability of the generated shape. The position and the movement of the particle are utilised to transmit information, and one of the first attempts using the acoustic levitator was demonstrated by Ochiai et al. [119] in 2014. Ochiai et al. levitated particles in a multi-axis PAL and shapes (e.g. letters, star) were outlined by levitated particles. In 2016, Sahoo et al. demonstrated a proof-of-concept device for “a mid-air display based on the electrostatic rotation of levitated Janus objects” [120]. Multiple particles were levitated in a grid pattern with PAL, and the colour painted on the particle was utilised to represent information. Moreover, Uno et al. levitated an assembly of coil and LED light using acoustic levitation [121] and utilised the movement of the assembly to transmit information. Similarly, Freeman et al. and Bachynskyi et al. demonstrated ‘Point-and-Shake’ [122] and ‘LeviCursor’ [123] respectively in 2018, which highlights the interest from the computer science field in utilising the movement of the particle as the feedback to the human inputs.

Most recently, ‘Holographic Acoustic Tweezer (HAT)’ [76] was developed by Marzo & Drinkwater; enabling the simultaneous control of multiple particles using PAL. Up to 27 particles were controlled simultaneously, and the minimum distance of separation achieved by the authors was  $1.4\lambda$  between each particle. This minimum separation distance demonstrates the challenge in creating re-configurable particle clusters; as it is limited by the Rayleigh criterion [3] and the close proximity of two focal points distorts the pressure field.

## 2.5 Nonlinear Behaviour of Dynamic System

Oscillation is unavoidable in many systems, and structures which did not properly consider the vibrational characteristic in design could perform poorly [124] or fail in a catastrophic manner [125]. Determining how these oscillation occur in acoustic levitation can be critical as the ability to control the position or velocity of the particle depends on how well the dynamic system is understood. As mentioned in § 2.3, the linear assumption on the dynamics of acoustic levitators remain popular model, and utilises the linearity of the acoustic radiation force at the vicinity of the equilibrium point to linearise the force field. For example, for an acoustic radiation force in 1D plane standing wave field, the acoustic radiation force has a sinusoidal profile as demonstrated by 2.23 and Fig. 2.13 shows the acoustic radiation force as calculated by 2.23. Here, parameters were assumed to be  $4\pi\Phi(\tilde{\kappa}, \tilde{\rho})kr^3 = 1$ ,  $k = \frac{2\pi f}{c_0}$  where  $f = 40000\text{Hz}$  and  $c_0 = 340\text{m s}^{-1}$ , and gravitational force were set to zero for simplicity. In such a simplified case, the equilibrium point of the levitated particle is at the origin of the



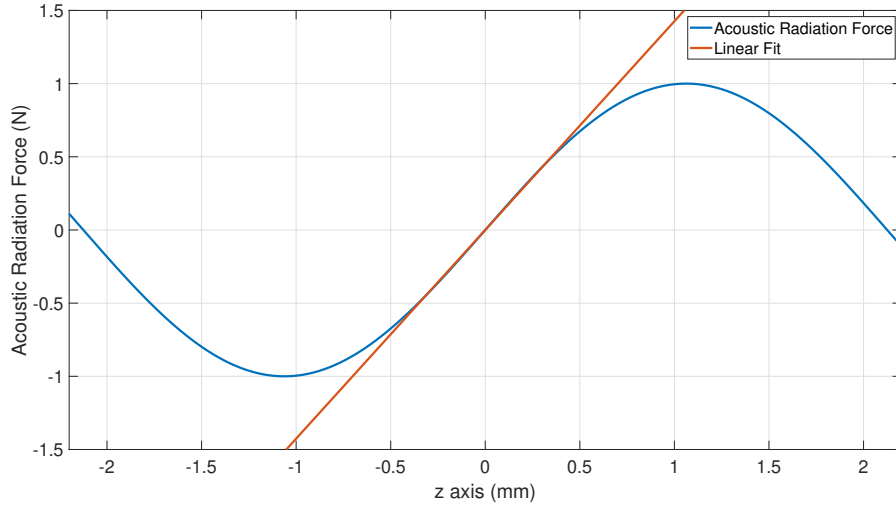


FIG. 2.13. 1D Acoustic radiation force of 1D plane wave standing wave, and linearly approximated acoustic radiation force (given gravity force is zero).

graph, and a linear fit was taken at the vicinity of the equilibrium point. Using the Hooke's law, the gradient of the linearised acoustic radiation force in Fig. 2.13 gives the stiffness of the 'spring', and can be used to determine the resonance frequency and the frequency response function of the system (given damping force is also linear) by taking the Laplace transform [126]. However, as the PAL is beginning to be utilised in a dynamic applications, the assumption that the particle stays at the vicinity of the equilibrium point is beginning to not hold true. As the particle begin to move in a larger displacement inside the acoustic trap, it will inevitably reach the regions where the linear assumption in Fig. 2.13 does not hold. As the result, the dynamic equation of interest begins to take the form of:

$$\dot{x} = F(t, x, p), \quad t \in [T_0, T_0 + T] \quad (2.28)$$

where  $T_0$ ,  $T$ ,  $x$ ,  $F$  and  $p$  are initial time, time interval length, a vector of state variables, nonlinear function and vector of problem parameters, respectively. This equation cannot be solved by simply taking the Laplace transform of the system, and will require more advanced methods to analyse the response of the system.

One of the most commonly utilised methods of analysing nonlinear system is 'numerical continuation'. Numerical continuation method is a numerical method which allows investigation of the behaviour of a dynamic system as a function of problem parameters [127]. It analyses the dynamic equation by perturbing the initial solution using the problem parameters and applies descent method such as Newton's method to reach the next solution assuming that the solution is in the close vicinity of initial solution [128]. The problem parameters can be from the frequency of oscillation, stiffness constants on nonlinear spring to the damping coefficients; and numerical continuation can efficiently determine the system responses. There is a number of the toolbox which can perform numerical continuation, such as MATCONT [129], COCO [130], and AUTO [131]. Numerical continuation is "more

efficient than direct time-integration techniques” such as ODE solvers, as “the steady-state solutions are sought directly, rather than relying on transient settling times” [132]. Numerical continuation is a powerful tool; however, it is not perfect for all dynamic analysis. One of the potential drawbacks is that it requires the solution to be periodic. Thus, for system with non-periodic solution, such as torus, analysis will require additional consideration.

Many of these toolboxes have in-built functions to identify the location of bifurcations and follow the branch of bifurcation. The bifurcation is the point at which the system changes its behaviour as the parameters are varied [133], and identifying the occurrences of these bifurcations can offer critical insights into the characteristics of the investigated system. This is because the “bifurcations can occur only when a system is structurally unstable” [134]. There are several types of bifurcations, and examples include but not limited to; pitchfork, saddle-node, symmetry-breaking, cyclic-fold, and period-doubling bifurcations. Bifurcations such as pitchfork and saddle-node bifurcations are associated with the bifurcation of the equilibrium points. These responses are often seen in a system such as buckling of beams where there is symmetry in the physical problem [135]. Considering these bifurcations are critical in ‘morphing winglets’ for aerospace applications where bistable composites are developed to transform the shape of the plate by the change in state [133, 136].

On the other hand, symmetry-breaking, cyclic-fold and period-doubling bifurcations are associated with the bifurcations of periodic solutions. Period-doubling bifurcations; in particular, occur frequently as “precursors to chaos” [134] and are of interest by many researchers in wide-range of field from astrophysics [137, 138], biology [139, 140] to chemistry [141]. The details on how these nonlinear responses may affect the performance of acoustic levitation system will be described in the later section of this thesis.

## 2.6 Summary

In this literature review, wide range of literature from the the physical origin of acoustic radiation to the applications of acoustic levitation were reviewed. The method of calculating acoustic radiation force is reviewed and the Gor’kov potential which allows acoustic radiation force to be evaluated for a spherical object with radius significantly smaller than the wavelength was introduced. In addition, an example of evaluating acoustic radiation force for a simple 1D planar standing wave was also demonstrated.

Various types of acoustic levitation system were reviewed, and the various methods of generating acoustic radiation force were introduced. In particular, two categories, classical and phased array acoustic levitators, were introduced. PAL allows the particle to be manipulated in three-dimensional space by varying the phases sent to each transducer and it can be achieved both by single/multi axis or single-beam methods. The PAL is generally considered to be a non-resonant acoustic levitator, as it does not require the separation distance between the phased array to be any specific constant length, and reflection from each surface is considered minimal.

The literature on the study of the dynamic behaviour of the objects levitated in acoustic levitator was also reviewed, and there exists no study on the dynamics of levitated particles in PAL. This is due to the fact that PAL was only introduced in 2014. The closest variant of PAL is single-axis acoustic levitator; however, the dynamics are not explored in-depth, and the study utilises a ‘linear mass-spring-damper’ model. The linear spring model remains a popular model in the field [12], but the extent to which this model is valid has not been studied in-depth, and applicability to PAL has not been studied.

The PAL are beginning to be utilised in various applications such as contactless production lines, and human-computer interfaces (displays) and it has promising future as additive manufacturing devices and contactless production lines. These proposed and demonstrated applications in the literature already demand high positioning accuracy and the speed of the levitated particles, and demonstrates the importance of understanding the dynamics of particles levitated in PAL.

# Chapter 3 Acoustic Levitation of a Particle: Experimental Considerations and Simulations

In this chapter:

- The single-axis acoustic levitator which is utilised throughout the thesis is introduced.
- The method of calculating necessary phased delays for each transducer is demonstrated.
- The setup and calibration method of the optical cameras are described.
- The tracking and identification method of the particle's position are described.
- The acoustic pressure field inside the levitator is modelled using Huygens' principle.
- The experiments to obtain empirical values in numerical simulation is described.
- The method of calculating acoustic radiation force with Gor'kov potential is described.

## 3.1 Introduction

This chapter aims to introduce the working principle of the phased array levitator (PAL), the tracking method of the particle inside the levitator and the formulation of numerical simulation methods. As described in the literature review, in recent years, the acoustic levitators have gained the ability to manipulate objects more freely by the introduction of the PAL. Ochiai et al. published three-dimensional mid-air acoustic manipulation using a PAL [72] in 2014, a single-sided acoustic levitator was achieved by Marzo et al. [79] in 2015, and PAL has been made open-source by Marzo et al. [21] in 2018. The acoustic field inside the levitators is varied by changing the phases of each transducer, and that allows particles to be controlled freely inside the levitator. Developing an experimental setup that allows the determination of the particle behaviour and numerical models that allow quantitative prediction of the response of the system is a paradigm to the future application that utilises acoustic levitation system.

As such an experimental setup is unique system; bespoke experimental apparatus was designed to accurately determine the behaviour of the particles inside the acoustic levitator using optical cameras, and numerical models were developed to allow quantitative analysis of the system, using empirically derived values. The setup of the experimental apparatus; along with the method of deriving the empirical values will be explained in detail.

## 3.2 Acoustic Levitator

### 3.2.1 Phased Array Levitator

The acoustic levitator used in the experiments is a PAL that can change the position of the focal point by varying the phase sent to each transducer. Some examples of the PAL are as shown in Fig. 3.1. Each configuration in Fig. 3.1 have unique feature and the single-axis PAL with a flat surface in Fig. 3.1 (a) is the most basic form the phased array acoustic levitator. This configuration of flat arrays is a typical setup in the field, and different implementation exists with varying number of transducer elements [21, 72, 75, 123]. On the other hand, the single-axis PAL with a curved surface in Fig. 3.1 (b) is designed such that the transducers are geometrically focused to the centre of the acoustic levitator: increasing the pressure amplitude at the point of focus. Thus, it can achieve higher magnitude of acoustic radiation force with the same number of transducers and a stable transportation of liquid/solid over distances were demonstrated by Vi et al. [142]. Fig. 3.1 (c) on the other hand, is a single-sided acoustic levitator which can manipulate the particle position from one-side. As a single-sided levitator does not have another transducer arrays or reflector; it allows generation of pressure field that is not bound by standing wave [79]. The single-axis acoustic levitator with a flat surface in Fig. 3.1 (a) was selected as the target of the analysis as this levitator is the most common setup that is applicable to wide range of researchers in the field.

#### Single-Axis Phased Array Levitator

A single-axis PAL, with two sets of 30 ultrasonic transducers that are running at 40 kHz, was used for the experiment. 40kHz transducers are most available ultrasonic transducers that are predominantly utilised by the automobile industry as parking sensors, and the availability in the market and the high-frequency characteristic that is inaudible to humans render it preferable for a system that requires the generation of a high-intensity acoustic field. The two sets of phased array were placed such that they opposes each other as shown in Fig. 3.2 (a) with a separation distance of 80 mm, and the phased array was arranged as shown in Fig. 3.2

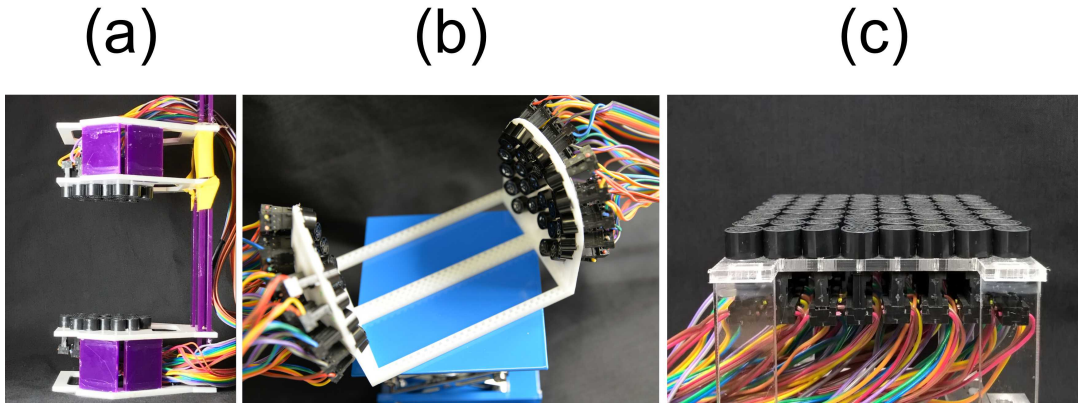


FIG. 3.1. Examples of phased array configurations. (a) shows the single-axis PAL with flat surface, (b) shows the single-axis PAL with curved surface for focusing, and (c) shows the single-sided acoustic levitator with flat surface

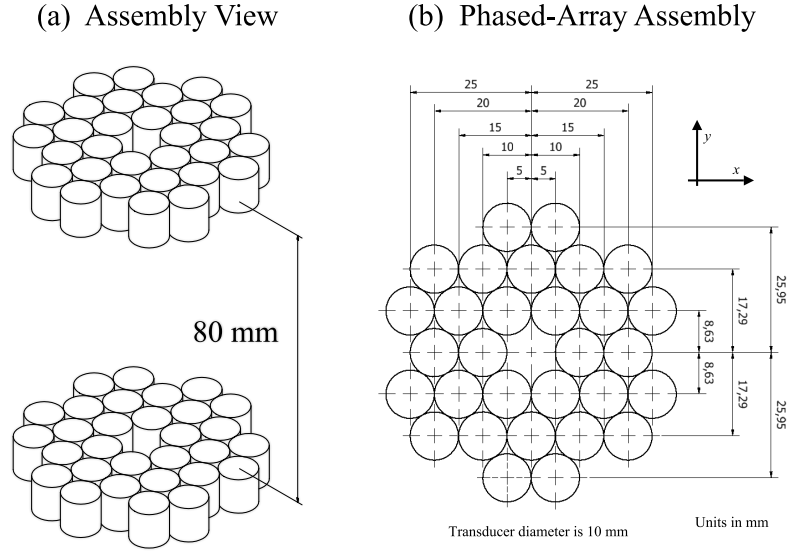


FIG. 3.2. Transducer positions in the acoustic levitator. (a) shows the whole assembly view of the single-axis acoustic levitator, with the relative positions of the transducers. Reproduced from [28], with the permission of IEEE. (b) shows the detailed orientation and position of the transducers in each phased array. Reproduced from [27] with the permission of AIP Publishing.

(b). This configuration with 60 transducers was selected via the process of optimisation: the transducer number should be less than 64 transducers (limited by hardware controller) and achieve some symmetry across an axis. Each transducer was wired via 16-way flat ribbon wire connectors [21] and was connected to a controller that transmitted an individual signal to each transducer via female MOLEX connector. The further details and methods of constructing this particular PAL are available in [21]. The transducers were housed in a customised perspex holder as shown in Fig. 3.3 [21].

### Phase Calculation

The focal point specifies the levitation point of a particle in a levitator ( $\mathbf{x}_f = (x_f, y_f, z_f)$ ) of the phased array. In order to achieve stable levitation at this focal point, the phase-delay on each transducer is calculated using:

$$\phi_{focal,n} = \phi_{focus} + \phi_{lens} \quad (3.1)$$

where  $\phi_{focus} = -\frac{2\pi f_0}{c_0} (|\mathbf{x}_{t,n} - \mathbf{x}_f| - |\mathbf{x}_f|)$  and  $\mathbf{x}_{t,n}$  is the position of the  $n$ th transducer ( $x_{t,n}, y_{t,n}, z_{t,n}$ ). The focusing delay is calculated by first setting the point of zero delay at the origin of the acoustic levitator (i.e. (0, 0) m). The time of flight of acoustic wave from the origin to the focal point is  $\frac{1}{c_0} |\mathbf{x}_f|$ . The time of flight from the transducer to the focal point is  $\frac{1}{c_0} |\mathbf{x}_{t,n} - \mathbf{x}_f|$ . The required phase delay is then the difference between the two time of flight ( $(|\mathbf{x}_{t,n} - \mathbf{x}_f| - |\mathbf{x}_f|)$ ), multiplied by the frequency of the acoustic wave ( $\frac{2\pi f_0}{c_0} (|\mathbf{x}_{t,n} - \mathbf{x}_f| - |\mathbf{x}_f|)$ ).

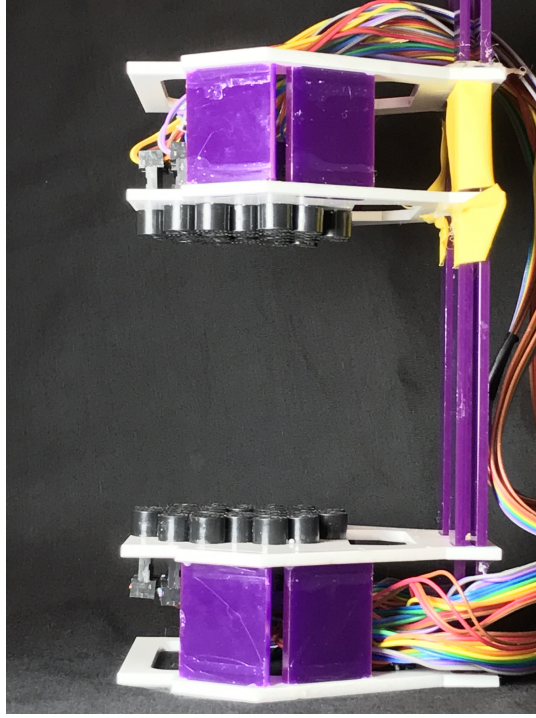


FIG. 3.3. Custom perspex holder for transducers and the transducer assembly [21]. The levitator is viewed from the y-z plane.

The datum point for all the coordinates is placed from the surface of the centre of the lower phased array.  $\phi_{lens}$  is an acoustic lens delay that could be applied to each transducer to achieve different types of acoustic pressure field such as twin trap, bottle trap, or vortex trap [79]. In the single-axis acoustic levitator, stable traps can be generated without the usage of the lens. However, a ‘standing wave’ trap can be applied to the PAL such that the pressure node of the standing wave matched with the focal point. This acoustic trap is achieved by setting  $\phi_{lens} = 0$  for lower phased array, and  $\phi_{lens} = \pi$  for the upper phased array.

### Levitator Controller

Excitation signals to the transducer were generated by an FPGA board (ALTERA CoreEp4C-E6), which generates 64 square waves in parallel with individual control of phase on each channel. The details of the signal generation method in FPGA (field-programable gate array) board is available in Marzo et al. [21]; however, a general schematic of the levitator controller is as shown in Fig. 3.4. The FPGA board is connected to the PC via USB UART (universal asynchronous receiver-transmitter) cable and utilises serial communication protocol to communicate with the FPGA board. The command to the FPGA board is packaged into a vector of 1 by 66. The first and the last slots of the command vector are reserved for number 255 and 254, which signifies the beginning and the end of the serial communication for FPGA board. The transducer is ordered to turn off when the value of 128 is received.  $S_{\phi,n}$  is an integer in the range of 0 to 127 and are used to specify the phase of the levitator (from 0 to  $2\pi$ ) with phase resolution of  $\frac{\pi}{64}$ . The input phase specification,  $S_{\phi,n}$  is then slotted into the corresponding part of the command vector. The baud rate for the serial communication is 1.5

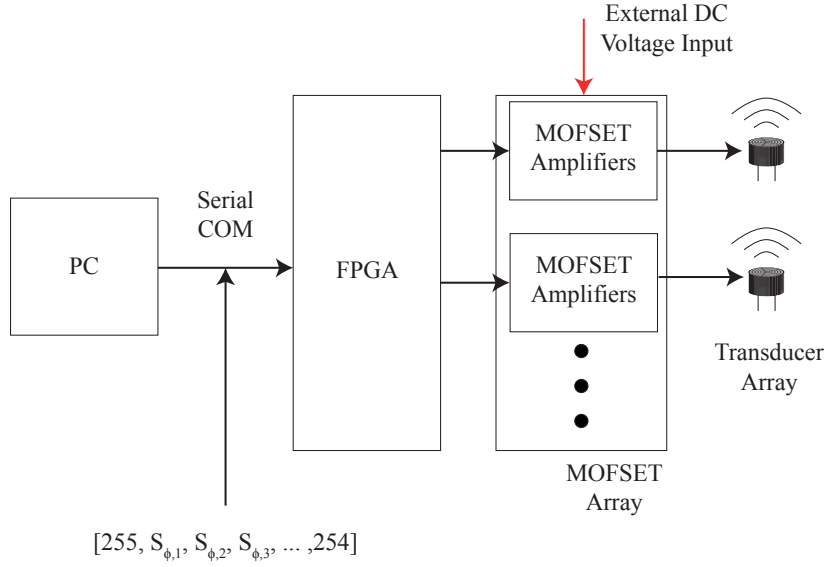


FIG. 3.4. Acoustic levitator controller. The FPGA board is connected to the PC via Serial COM, and commands are packed into a vector of 1 by 66. It starts with 255 and ends with 254, and value between 0 to 127 is used to select the phase value for each transducers. Value 128 is reserved for turning off the transducer.

MBaud and can update the FPGA board at 1200 Hz. The generated signal is then amplified by a set of MOSFET driver arrays (TC4427a) which using the external DC power supply (RS Pro IPS 303DD) amplifies the signal up to 18 V.

### 3.2.2 Particle

The particles used in the levitation experiments in the single-axis acoustic levitator are Expanded Polystyrene (EPS). The EPS particles were purchased in bulk, and each particle has a different radius and mass. Therefore, the particles used in the experiments were sampled, isolated, and labeled clearly to improve the accuracy of the physical model in numerical simulation. The mass of the particle ( $m$ ) was measured using a microbalance (Sartorius MC5) with a resolution of 0.001 mg. The radius of the particle was digitally measured by taking a picture of the particle and comparing it to a datum radius from CMM-stylus (Renishaw A-5000-7806). In general, the radius of the particle was in the range of  $0.5 \leq r \leq 0.8$  mm, and the measurements of mass and radius were used to calculate the density of the particle:

$$\rho_p = \frac{m}{V} = \frac{3m}{4\pi r^3} \quad (3.2)$$

and had density in the range of  $30 \leq \rho_p \leq 50 \text{ kg m}^{-3}$ . The detailed information of the particle that was used in the experiment will be made available where appropriate in the corresponding section. An example list of the particle properties is as shown in TABLE 3.1. EPS particles were assumed to be spherical, and the particle was checked for signs of indentation or damage before the experiment. Any particle that has been mixed up, damaged, or indicate unusual behaviour (such as spinning) was disqualified from the experiment. Moreover,



residual EPS particles without labels were removed from the room before the experiment. Performing this step eased the identification of the particle after the sudden ejection of the particle from the levitator and reduced the required number of particle samples.

Particle Number	Mass ( $\pm 0.001$ ) mg	Radius ( $\pm 0.000003$ ) m	Density ( $\text{kg m}^{-3}$ )
AB01	0.063	0.000711	41.7
AB02	0.065	0.000750	36.6
AB03	0.037	0.000585	44.2
AB04	0.050	0.000657	42.1
AB05	0.052	0.000693	37.3
AB06	0.050	0.000660	41.4
AB07	0.043	0.000630	41.1
AB08	0.059	0.000726	37.0
AB09	0.068	0.000807	31.0
AB10	0.059	0.000705	40.2

TABLE 3.1: Measured particle properties. Each particle was given an unique identification number, and each particle was stored in an individual glass container to prevent deformation, and mix up.

### Acoustic Levitation of Particle

The levitation of the EPS particle in the single-axis acoustic levitator is as demonstrated in Fig. 3.5 (a), and Fig. 3.5 (b) shows the close-up on the levitated particle. The particle is released on a patch of cloth as shown in Fig. 3.6 and placed into the pressure trap generated by the acoustic levitator. As there exist multiple nodes where particles can levitate itself stably inside the single-axis PAL; a visual inspection with a ruler was performed prior to any experiment to ensure the particle was entrapped in the appropriate node.

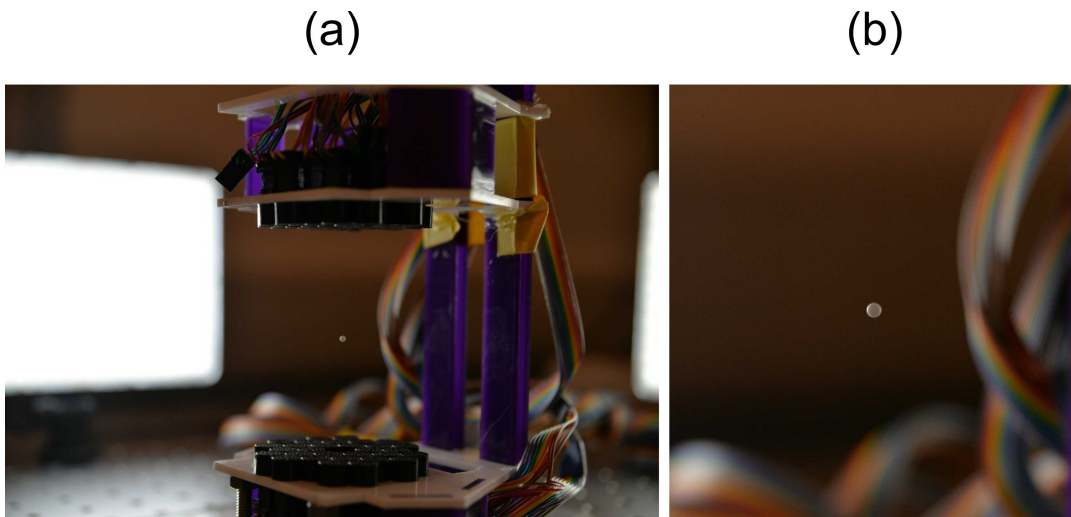


FIG. 3.5. Overview of acoustically levitated EPS particle. (a) shows the particle position relative to the acoustic levitator, and (b) is a close up of the levitated particle.



FIG. 3.6. A patch of cloth was utilised to insert particles into the node of the standing wave. After the insertion of particle, the particle position was checked visually using a ruler to confirm that the particle was in the correct node.

#### 3.2.3 Air Property Measurement

At the beginning of the experiment, the air temperature ( $T_c$ ) in Celsius, humidity ( $h$ ) in fraction and atmospheric pressure ( $p_a$ ) in Pa were recorded using an environmental monitor, “BlueMaestro Pebble” (BlueMaestro (UK), PEB001WHITE) that can record temperature, humidity, dew point and atmospheric pressure. The recorded measurement was used to determine the speed of sound ( $c_0$ ), density ( $\rho_0$ ) and viscosity ( $\nu_0$ ) of the air. These parameters were used for the phase calculations during the experiments, and in numerical simulations.

##### Speed of Sound in Air

The speed of sound in air was determined using the formulation by Cramer [143]:

$$c_0 = a_0 + a_1 T_c + a_2 T_c^2 + (a_3 + a_4 T_c + a_5 T_c^2) X_w + (a_6 + a_7 T_c + a_8 T_c^2) p_a + (a_9 + a_{10} T_c + a_{11} T_c^2) X_c + a_{12} X_w^2 + a_{13} p_a^2 + a_{14} X_c^2 + a_{15} X_w p_a X_c \quad (3.3)$$

where  $T_c$ ,  $X_w$ , and  $X_c = 0.0004$  are temperature in Celsius, water vapour mole fraction, and carbon dioxide mole fraction. The values for constants  $a_0$  to  $a_{15}$  are as listed in TABLE 3.2. The water vapour mole fraction,  $X_w$  is calculated by:

$$X_w = \frac{h E_h p_{sv}}{p_a} \quad (3.4)$$

where  $E_h = 1.0062 + 3.15 \times 10^{-8} p_a + 5.6 \times 10^{-7} T_c^2$  is an enhancement factor and  $p_{sv}$  is the saturation vapour pressure of water in air [143]:

$$p_{sv} = e^{1.2811805 \times 10^{-5} T^2 - 1.9509874 \times 10^{-2} T + 34.04926034 - \frac{6.3536311 \times 10^3}{T}} \quad (3.5)$$

Constants	Values
$a_0$	331.5024
$a_1$	0.603055
$a_2$	-0.000528
$a_3$	51.471935
$a_4$	0.1495874
$a_5$	-0.000782
$a_6$	$-1.82 \times 10^{-7}$
$a_7$	$3.73 \times 10^{-8}$
$a_8$	$-2.93 \times 10^{-10}$
$a_9$	-85.20931
$a_{10}$	-0.228525
$a_{11}$	$5.91 \times 10^{-5}$
$a_{12}$	-2.835149
$a_{13}$	$-2.15 \times 10^{-13}$
$a_{14}$	29.179762
$a_{15}$	0.000486

TABLE 3.2: Tables of constants for speed of sound calculation as listed on Cramer. Reprinted with permission from [143]. Copyright 1993, Acoustic Society of America.

where  $T$  is the temperature  $T_c$  in Kelvin.

### Density of Air

The density of air was determined by evaluating the humidity of the air recorded. Firstly, the saturation pressure of water ( $p_{w,s}$ ) was spline interpolated using the ‘saturated water and steam’ table in Rogers & Mayhew [144]. The partial pressure of water vapour in moist air is [145]:

$$p_w = p_{w,s}h \quad (3.6)$$

The humidity ratio is then [146]:

$$X_s = 0.62198 \frac{p_w}{p_a - p_w} \quad (3.7)$$

The density of air is [147]:

$$\rho_0 = \frac{\frac{p_a}{R_a T} (1 + X_s)}{\left(1 + X_s \frac{R_w}{R_a}\right)} \quad (3.8)$$

where  $R_a = 286.9$  and  $R_w = 461.5$  are individual gas constant in air and water vapour, respectively.

### Viscosity of Air

The viscosity of air in comparison to the temperature [144] is as shown in TABLE 3.3, and values were spline interpolated from these values.

Temperature (K)	$\mu \times 10^{-5} (\text{kg}(\text{ms})^{-1})$
200	1.329
225	1.467
250	1.599
275	1.725
300	1.846
325	1.962
350	2.075

TABLE 3.3: Table of air viscosity with varying temperature. Reproduced from [144].

### 3.3 Particle Position Tracker

#### 3.3.1 Camera Setup

The position of the particle was determined using either the commercial high-speed camera (Photron FASTCAM SA-Z Type 2100K-M-32GB with Tokina AT-X Pro macro 100 F2.8 D lens) or a USB camera (FLIR PointGrey Chameleon 3, with an SV-5014H lens). The PointGrey camera has the advantage of being able to control the system via MATLAB Image Acquisition Toolbox and enables the automation of the experiment along with the acoustic levitator controller. It can record up to 500 FPS but with limited region of interest (ROI), and MATLAB implementation of PointGrey camera is limited to 150 FPS regardless of the image resolution. On the other hand, the Photron camera can record up to 21,000 FPS and offers better high-speed imaging capability than PointGrey camera. The manufacturer's proprietary software was utilised for the control of the camera, and manual operation and export of images were required.

In each instance, the camera is set up in parallel to the  $y$ - $z$  plane of single-axis acoustic levitator, as shown in Fig. 3.7 with an LED light source (10.5 Watts, width = 170 mm, height = 120 mm) placed at the back of the single-axis acoustic levitator with a diffuser. The diffused light source generates a silhouette on the side of the camera when a particle is levitated as shown in Fig. 3.8 and eases the identification of particle in images. The  $y$ - $z$  plane of the acoustic levitator was chosen as the obstruction of the view was minimal. Alternative methods such as the usage of Laser Doppler Vibrometer (LDV) are possible. However, the optical method of obtaining the particle position/response is a non-invasive method of observing levitated objects in acoustic levitator and are accepted methods by various authors [42, 48, 85].

The Photron SA-Z camera was placed on a tripod for stability, and a customised camera holder was designed for PointGrey camera as shown in Appendix A. The assembly of the camera holder is as shown in Fig. 3.9 (a), the height of the camera is adjustable such that it is suitable for a different variation of acoustic levitator. Fig. 3.9 (b) is the experimental implementation of the apparatus setup as shown in Fig. 3.7.

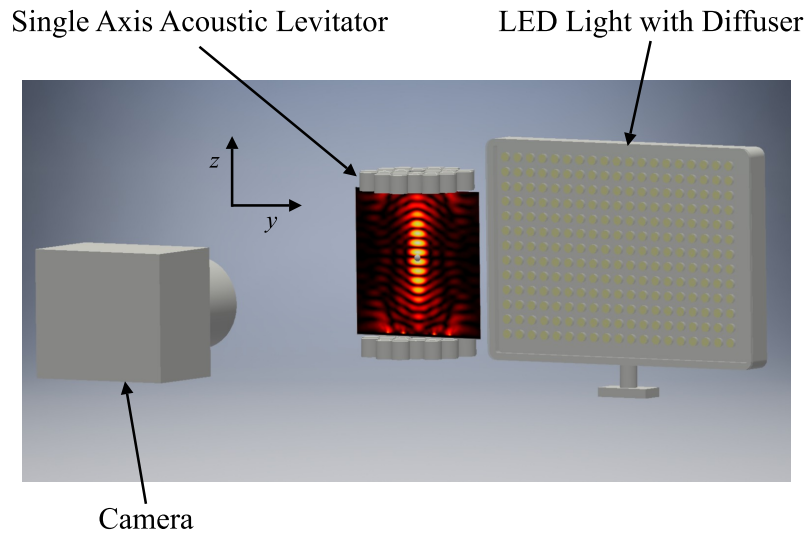


FIG. 3.7. Camera setup with a single-axis acoustic levitator and LED light with diffuser. The camera observes the particle movement in the  $y$ - $z$  plane.

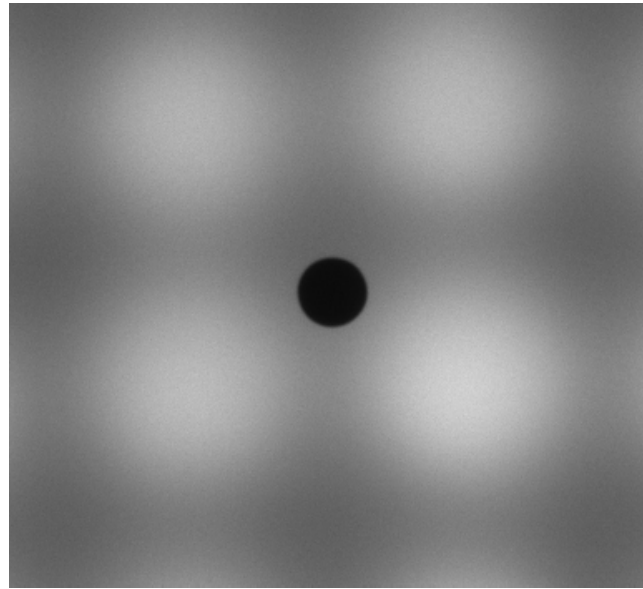


FIG. 3.8. An example of a particle silhouette created by the diffused light source at the back of levitator. This method of identifying the particle is robust to changes in light settings, in comparison to setting up the LED light in the same side as the camera.

### Data Capture

The Photron SA-Z camera was connected to a PC via Ethernet cable, and camera settings, and the data capture was commanded via a proprietary software (Photron FASTCAM Viewer 3). The camera was set up to record at 1000 frames per second, and the footage of the experiment was downloaded from the camera and saved on local hard-disk as static images with meta-data.

MATLAB Image acquisition toolbox and proprietary software (PointGrey FlyCapture 2)

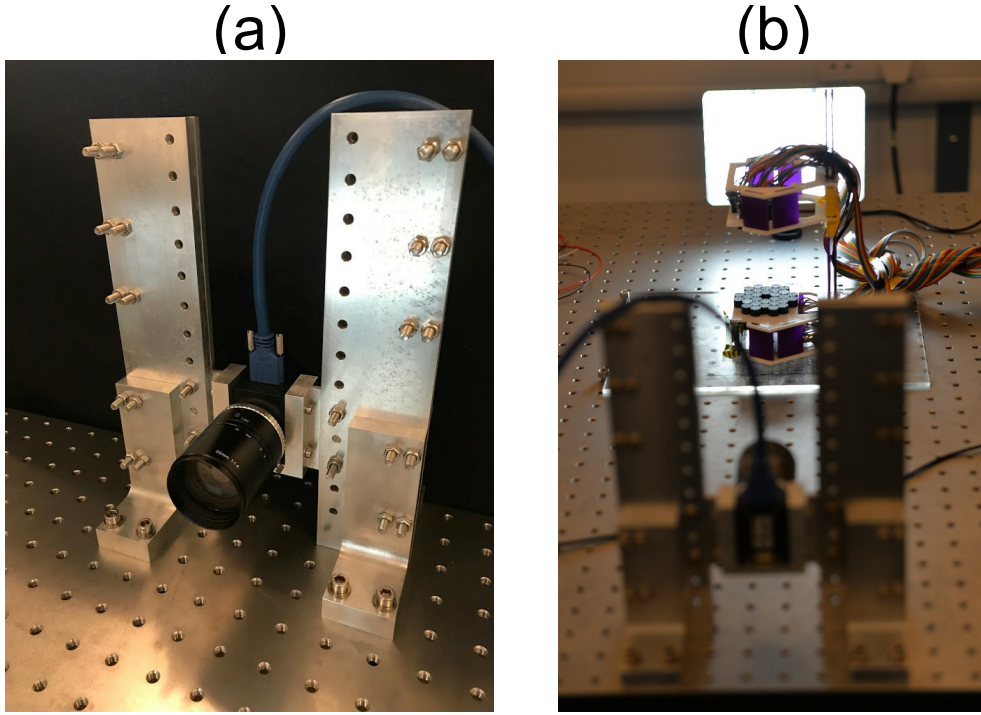


FIG. 3.9. Experimental setup overview. (a) show the assembly of PointGrey camera and camera holder (b) The relative positioning of the camera, levitator, and LED light source.

were used in conjunction to control and capture images from PointGrey camera, and the connection with PC was established via USB 3.0. For individual pictures, ‘getsnapshot’ function of MATLAB Image Data Acquisition Toolbox was utilised. The recorded footage of the experiment may be stored as static images for post-processing.

For a high-speed recording, a manual trigger was set for the PointGrey camera, and the desired FPS was set using manual frame rate mode. The software trigger was fired to start the recording of the footage, and when the recording was finished, the images were extracted using the ‘getdata’ function. The data size of the loaded images is approximately 500 MB when recorded at 150 FPS for 10 seconds. In some experiments, storing all the footage from the camera was difficult due to the volume of data. In such instances, the data was processed on-site, and raw-data was disposed. Both PointGrey and Photron SA-Z camera are monochromatic, and the resolution of the image were 1280 by 1024 pixels and 896 by 896 pixels for PointGrey and Photron camera, respectively.

#### Calibration of Camera

The cameras used in the experiment were checked for radial distortion using a MATLAB camera calibration toolbox and checkboard pattern. Approximately 20 images were captured using the camera with randomly oriented patterns, and it was identified that for both cameras, the radial distortion was minimal (0.1 to 0.2 pixel, in the range of  $0.3$  to  $0.6 \times 10^{-5}$  m). The datum point and the pixel to metre conversion rate were determined using a CMM-stylus (Renishaw A-5000-7806), that was attached to a custom made CMM-stylus holder as shown

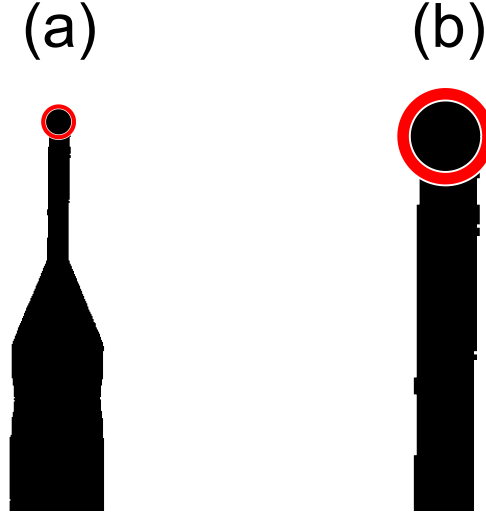


FIG. 3.10. The identification of the calibrator centre by the image recognition algorithm. (a) The diffused light from the LED source creates shillouette of the calibrator (b) Zoomed in view to the tip of the CMM-styli. The pixel to metre conversion rate is determined from here.

in Appendix B. The holder was manually placed at the centre of the acoustic levitator. Using the Circle Hough transform in the MATLAB Image Processing Toolbox, the radius of the ruby ball ( $R_{pix}$ ) at the tip of the CMM-styli in the image was determined, as shown in Fig. 3.10 (a), and (b). As the radius of the ruby ball ( $R_{ruby} = 0.5 \text{ mm}$ ) is known, the pixel to metre conversion rate ( $I_{pix2m}$ ) was determined by:

$$I_{pix2m} = \frac{R_{ruby}}{R_{pix}} \quad (3.9)$$

The centre of the ruby ball is used as the datum point ( $x_d$ ) in the image, and if the custom-made holder was used: the centre of the calibrator will be at  $x_{d,offset} = (0, 0.040) \text{ m}$ . The calibration was performed regularly, and the datum point is subject to the ability of the user to be able to place at the correct position. However, the CMM-styli holder was designed with notches to ease the alignment along with the transducer phased array and reduce variability in the position of a datum point, as shown in Fig. 3.11.

### Identification of Particle Position

The particle position was determined by using MATLAB Image Processing Toolbox. The captured images were loaded sequentially to MATLAB using ‘imread’ function to the MATLAB workspace memory, and an example of such images is as shown in Fig. 3.12 (a). The loaded image is then binarised using ‘imbinarize’ (Otsu’s method [148]) with threshold of 0.2 to 0.3, as shown in Fig. 3.12 (b). This process of binarisation is necessary for utilising the Circle Hough Transform and converts the light intensity level encoded in 8-bit signal to 0 and 1. As this process introduces noise from the background as shown in Fig. 3.12 (b),



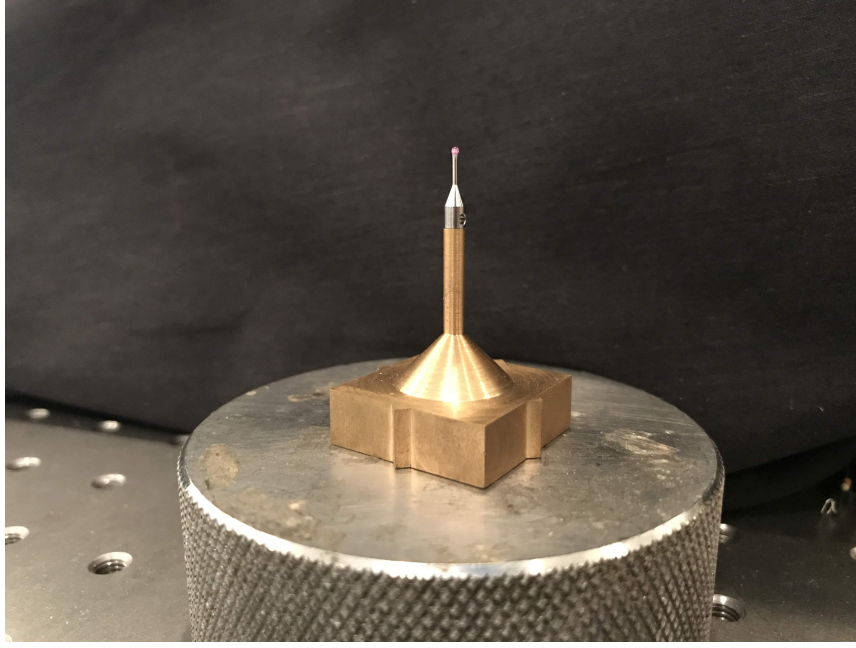


FIG. 3.11. Assembly of CMM-stylus and its custom made holder. The CMM-Stylus has a ruby ball at the tip, and is used for the calibration procedure. Together with the custom made holder, the centre of the ruby ball is 40 mm away from the bottom of the holder. The notches on the holder are used to align the calibrator with the transducer array.

appropriate maskings were applied by converting the regions to zeros, as shown in Fig. 3.12 (c) to reduce misdetection of particle. Lastly, the Circle Hough Transform was applied via the MATLAB Image Processing Toolbox function, ‘imfindcircles’, as shown in Fig. 3.13 (a). Fig. 3.13 (b) shows the close-up of the identified particle, and demonstrates that the image processing software can correctly identify the position of the particle. The function outputs the central position of the particle ( $\mathbf{x}_{pix}$ ) and by using the previously determined datum point ( $\mathbf{x}_d$ ); the particle position in Cartesian coordinate ( $\mathbf{x}_{pos}$ ) is determined:

$$\mathbf{x}_{pos} = \mathbf{x}_{d,offset} + I_{pix2m}(\mathbf{x}_d - \mathbf{x}_{pix}) \quad (3.10)$$

#### 3.3.2 Location of Experiment

All experiment was conducted in a closed-chamber (width = 4.3 m, height = 2.4 m, length = 2.4 m), and the acoustic levitator was placed on top of a passive vibration isolation table (Thorlabs PFH90150-8). The chamber is a Faraday cage (Type S501) manufactured by ETS-Lindgren Oy, and the physical isolation minimised the random displacement of the particle via external disturbances such as physical vibrations, air current, and thermal fluctuations. The vibration level on the passive vibration table was measured using the accelerometer on iPhone 7 MN8Y2B/A with “MATLAB Mobile” and recorded for 10 minutes with a sampling frequency of 100 Hz. The vibration level from the measurement is as shown in Fig. 3.14 and demonstrates that the physical vibration noise from the surrounding environment is minimal (the sensor bias causes the peak at  $< 0.5$  Hz in Fig. 3.14). Moreover, the air current inside



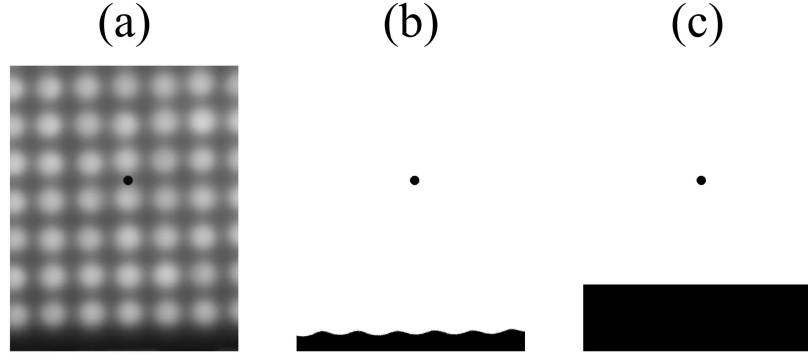


FIG. 3.12. The sequence of particle identification algorithm. (a) The recorded image is loaded on to the MATLAB workspace memory. (b) The image is binarized with a threshold value. (c) Masking is applied to hide the boundaries of LED light, and therefore reduce the misdetection of particles.

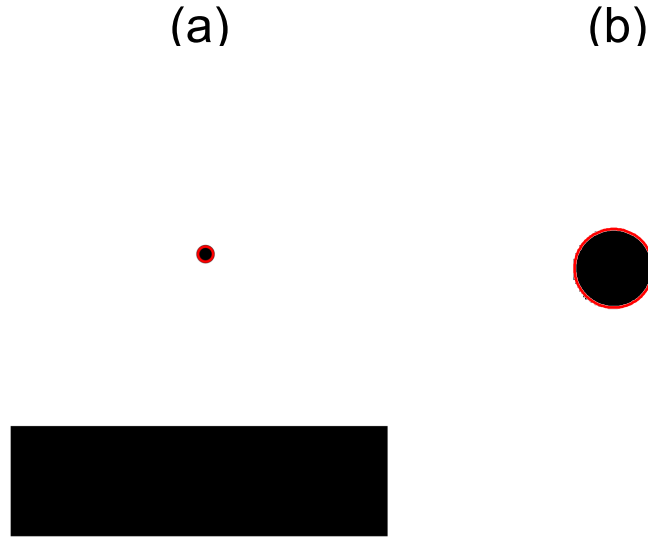


FIG. 3.13. Circle Hough Transform identifies the central position of the particle. (a) shows the relative position of the particle in the image and (b) is the close up version of the identified particle in (a).

the chamber and outside the chamber in general laboratory area was measured using Wind-Sonic Ultrasonic Wind Sensor (Gill Instruments Limited, Option 1) over 45 min period. The standard deviation in wind velocity were  $0.004$  and  $0.0219 \text{ ms}^{-1}$  for inside and outside the chamber, respectively and confirms that the air currents are minimal inside the experiment chamber.

### 3.4 Formulation of Numerical Simulation

#### 3.4.1 Huygens' Model

The numerical model of the single-axis PAL was developed in MATLAB. The linear superposition property of the pressure field was utilised, and the pressure field in the acoustic

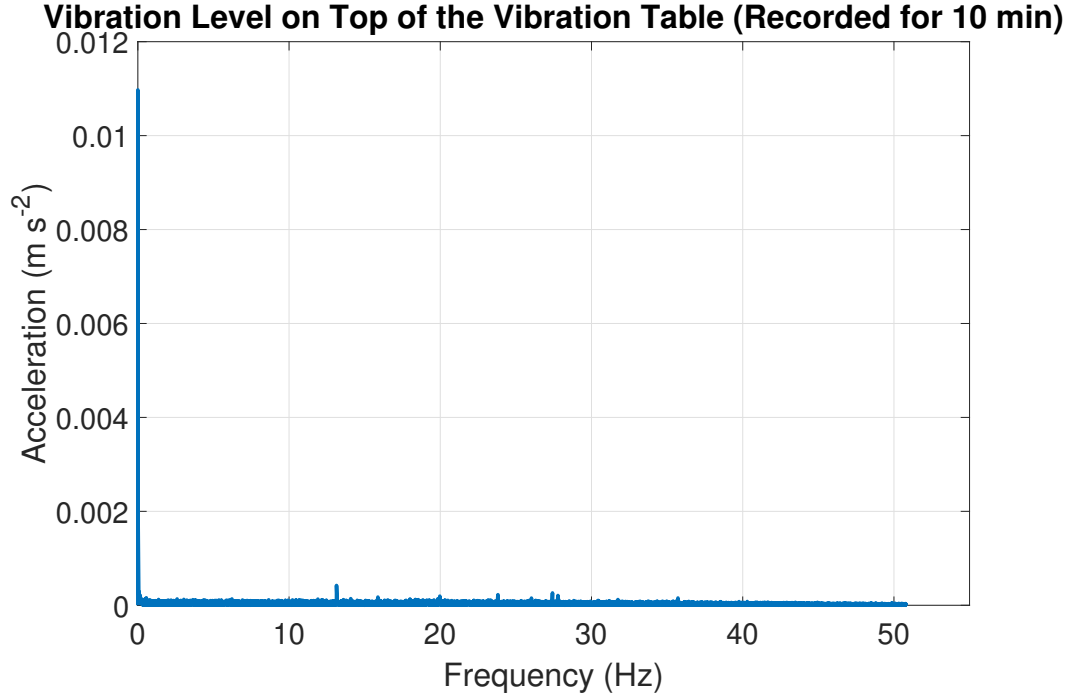


FIG. 3.14. Vibration level measurement on the passive vibration isolation table. The recording time was 10 minutes, and DFT was taken over the measured time domain acceleration signal.

levitator is determined by the summation of the pressure contribution from each transducers ( $p_{t,n}$ ) in the acoustic levitator:

$$p_{in} = \sum_n^N p_{t,n} \quad (3.11)$$

where  $n$  is the number of the transducer element and  $N$  is the total number of transducers in the acoustic levitator. The linear superposition property will be referred to as Huygens' principle in this thesis from here on.

### Transducer Model

Transducers in the single-axis PAL were assumed to emit a spherical wave [22, 75, 79] and all of the transducers were Murata MA40S4S. The transducers were approximated as a 'circular piston source' in the far-field, as shown in Fig. 3.15. The spherical wave emitted from the source is a function of the radial distance ( $r_{t,n}$ ), angle ( $\theta_n$ ) [30]:

$$p_{t,n}(r_{t,n}, \theta_n) = \frac{P_0}{r_{t,n}} D_f(\theta_n) e^{j(-kr_{t,n} + \phi_{focal,n})} \quad (3.12)$$

where  $P_0$  is the transducer power,  $D_f(\theta_n)$  is a directivity function and  $k = \frac{\omega}{c_0}$  is a wave number.  $\omega = 2\pi f_0$  is the angular frequency of the transducer ( $f_0 = 40$  kHz). The radial distance ( $r$ ) is determined by:

$$r_{t,n} = |\mathbf{x} - \mathbf{x}_{t,n}| = \sqrt{(x - x_{t,n})^2 + (y - y_{t,n})^2 + (z - z_{t,n})^2} \quad (3.13)$$

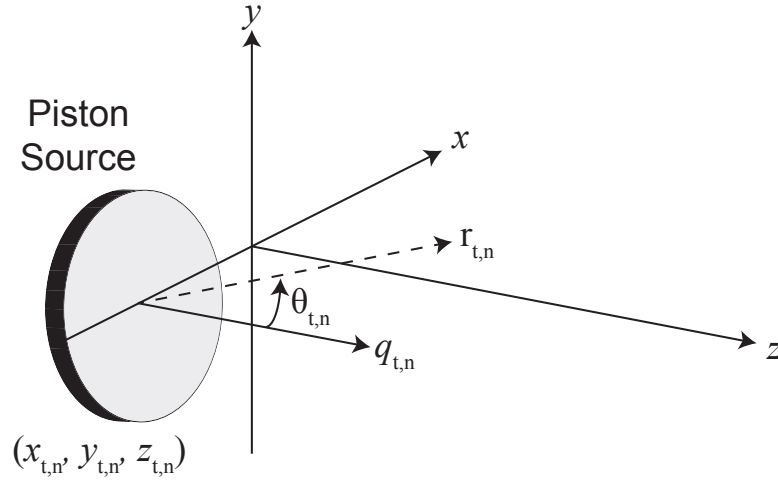


FIG. 3.15. Coordinate system of the numerical simulation. The global Cartesian coordinate  $(x, y, z)$  has datum point at the centre of the acoustic levitator, and pressure contribution from each transducer is summed together to identify the total acoustic pressure field. The transducer position is offset from the global coordinate by  $(x_{t,n}, y_{t,n}, z_{t,n})$

The far-field directivity function for the piston source is [30]:

$$D_f(\theta_n) = \frac{2J_1(\chi)}{\chi} \quad (3.14)$$

where  $J_1$  is the Bessel function of the first kind of order 1,  $\chi = ka \sin(\theta_n)$  where the transducer radius  $a = 0.0045$  m. The comparison of the directivity function in the manufacturer's transducer specification sheet [149], and the piston source directivity function is as shown in the Fig. 3.16.

### Transducer Pressure Measurement

The transducer output pressure was measured experimentally by setting up a Murata transducer and a pressure microphone (B & K Type 4138-A-015) as shown in Fig. 3.17. The transducer was driven by the FPGA board and the pressure microphone was placed along the central axis of the transducer. Thus, the height from the surface of the transducer ( $H$ ) is equal to the radial distance ( $r$ ) and it was varied in the range of  $20 \leq r \leq 50$  with an increment of 5 mm. The acoustic pressure is measured at the tip of the microphone and the peak-to-peak measurement ( $V_{pk-pk}$ ) of the voltage output from the microphone was monitored via an oscilloscope. As the microphone is calibrated to have a linear relationship between the voltage signal to pressure, the recorded peak-to-peak measurement was then converted to pressure ( $P_{pk-pk}$ ) using conversion rate ( $I_{v2p} = 0.64 \text{ mV Pa}^{-1}$ )

$$P_{pk-pk} = \frac{V_{pk-pk}}{I_{v2p}} \quad (3.15)$$

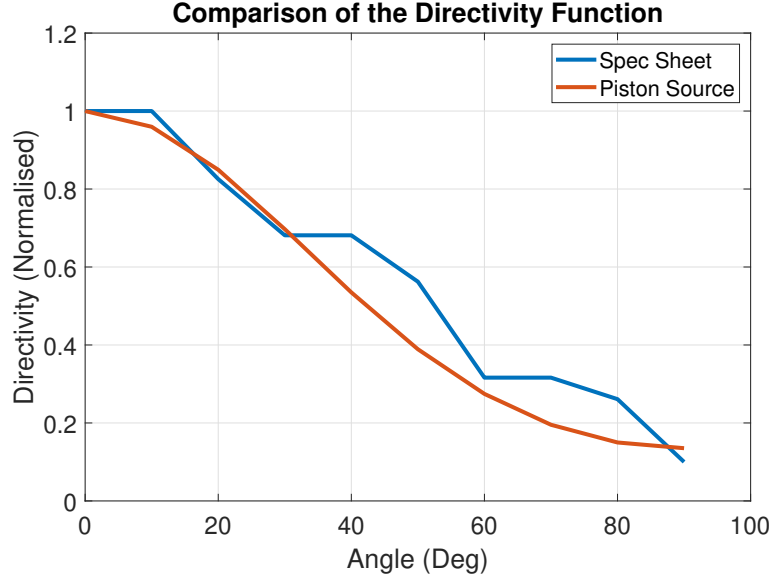


FIG. 3.16. Comparison of the directivity function provided by the manufacturer specification sheet (Reproduced from [149]) and the piston source directivity function.

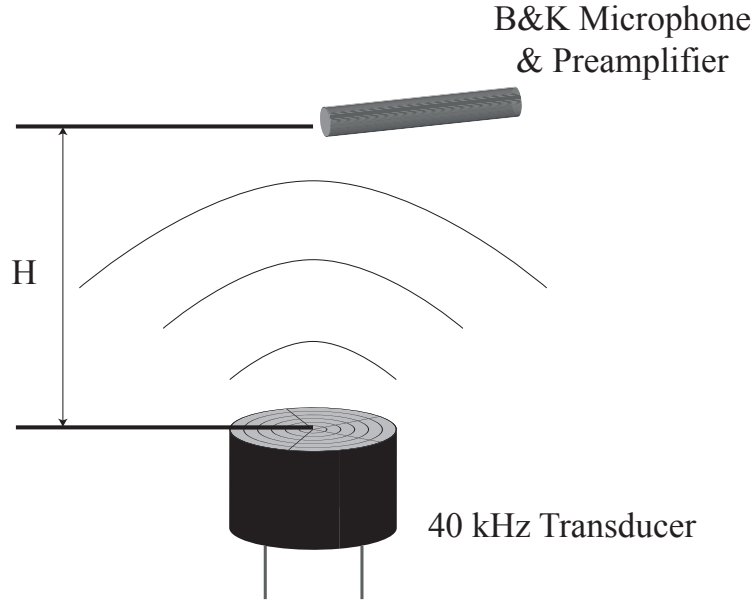


FIG. 3.17. Experimental apparatus setup for the determination of the transducer power using pressure microphone. The microphone was incrementally moved in  $z$  axis and the acoustic pressure (Pa) at distance  $H$  was recorded.

Assuming the acoustic wave is sinusoidal, the amplitude of the acoustic signal is then:

$$P_{amp} = \frac{P_{pk-pk}}{2} \quad (3.16)$$

The transducer power is then the gradient of the linear fit ( $p = P_0 \left( \frac{1}{r} \right) + b$ ). For example for a transducer in Fig. 3.18, the line of best fit was  $y = 3.1508x + 16.79$  with  $R^2 = 0.989$ , and the  $P_0$  for this particular instance was the gradient of this linear fit,  $3.15 \text{ Pa m}^{-1}$  at 17 V.

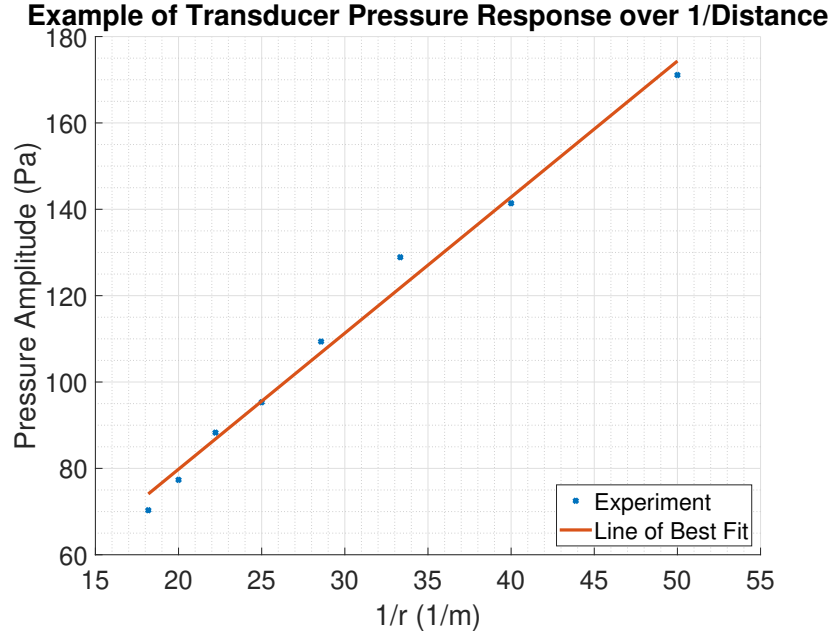


FIG. 3.18. Experimental plot of pressure amplitude of a single transducer as a function of inversed distance ( $r^{-1}$ )

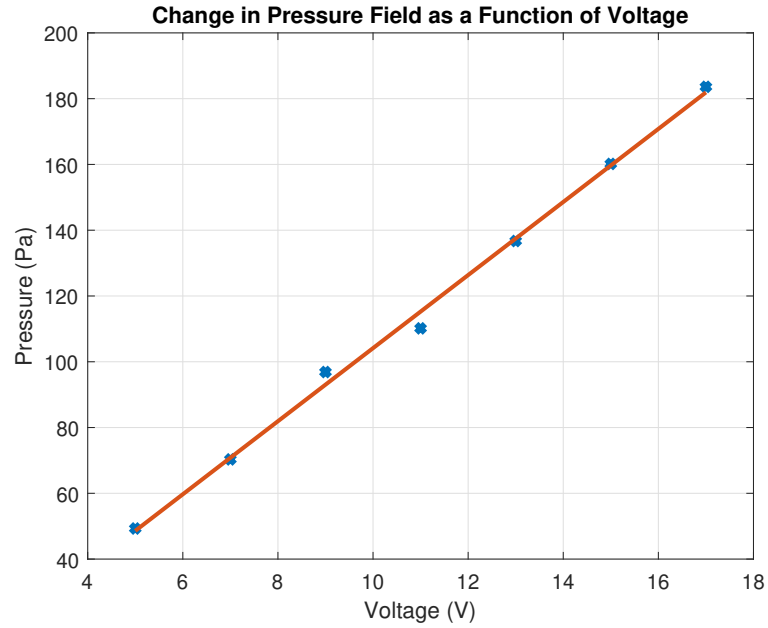


FIG. 3.19. Experiment demonstrating the linear relationship between the output pressure value and the voltage. The B&K microphone was fixed at a distance (20 mm), and the pressure value was recorded as the excitation voltage of the transducer was increased.

The transducer power coefficient per voltage ( $P_0^V = \frac{P_0}{V} = 0.186 \text{ Pa m}^{-1} \text{ V}^{-1}$ ) [150] was then determined and the average value of  $P_0^V$  was taken over 10 Murata transducers. The mean  $P_0^V$  was  $0.181 \text{ Pa m}^{-1} \text{ V}^{-1}$  with the standard deviation of 0.013. This measurement of  $P_0^V$  matches with the previous independent measurement [150]. The transducer power coefficient per voltage takes advantage of the fact that the Murata MA40S4S have a linear relationship

between the voltage and output pressure level, and allows a good approximation of transducer power from the operating voltage. Fig. 3.19 demonstrates such linear approximation of the transducer within the operating regime; where pressure value is read at a constant distance (20 mm) away from the transducer as the voltage was increased.

#### Implementation of Huygens' Model in MATLAB

The numerical model was formulated in a Cartesian coordinate system  $(x, y, z)$  and used the centre of the lower phased array of single-axis acoustic levitator as the datum point of the coordinate system, similarly to the experimental setup. The field was discretized into a regular interval, with minimum of  $x_{step} = \frac{\lambda}{60}$  in each axis. The angle from the transducer to an arbitrary position in the levitator is determined by:

$$\theta_n = \cos^{-1} \left( \frac{(\mathbf{x} - \mathbf{x}_{t,n}) \cdot \mathbf{q}_{t,n}}{|\mathbf{x} - \mathbf{x}_{t,n}| \cdot |\mathbf{q}_{t,n}|} \right) \quad (3.17)$$

where  $\mathbf{q}_{t,n}$  a unit vector representing the direction for which the transducer is facing relative to the datum point. For example, the transducers have  $\mathbf{q}_{t,n} = (0, 0, 1)$  and  $\mathbf{q}_{t,n} = (0, 0, -1)$  for lower and upper phased array, respectively. This formulation is particularly useful when the transducer is positioned on a circular curvature. In order to maximise the efficiency of the numerical simulation where the focal point of the levitator is continuously changing, equation 3.12 was split into two sections:

$$p_{t,n} = p_{1,n} \times \Phi_{focal,n} \quad (3.18)$$

where  $p_{1,n} = \frac{P_0}{r_{t,n}} D_f(\theta_n) e^{-jkr_{t,n}}$  and  $\Phi_{focal,n} = e^{j\phi_{focal,n}}$ . The raw pressure field ( $p_{1,n}$ ) was pre-calculated and stored in memory, and when the focal point changes, the necessary phase delay was imposed via  $\Phi_{focal,n}$ . The phase delay for the acoustic levitator when the focal point is set to  $\mathbf{x}_f = (0, 0, 0.040)$  m is as shown in Fig. 3.20. The red isosurface in the Fig. 3.20 represents the isosurface of equal pressure. The qualitative agreement of the pressure field calculated in Fig. 3.20 was obtained by exposing the acoustic pressure trap to a piece of dry ice. The water vapour generated by the dry ice is briefly trapped inside the acoustic levitator and visualises the acoustic traps inside the levitator. The results are as shown in Fig. 3.21 (a) and (b), where (a) shows the acoustic pressure field as predicted by the numerical simulation and (b) shows the pressure field as visualised by the dry ice. The comparison shows that the position of the pressure nodes and anti-nodes as predicted by the numerical simulation matches the experiment, and qualitatively confirms the validity of the numerical model.

More quantitative measurements can be made via the measurement using a pressure microphone. The B&K microphone was utilised to scan the pressure field inside the acoustic levitator. The maximum pressure value obtained in the field as the pressure microphone was scanned  $\pm 1$  cm with an increment of 2 mm from the focal point  $(0, 0, 0.04)$  m in  $z$  axis was  $\approx 1700$  Pa; approximately matching the results shown in Fig. 3.21. The mismatch in the pressure amplitude is due to the scattering from the pressure microphone where the width of the microphone (3.18 mm) is comparable to the wavelength of the field (8.6 mm) [79,

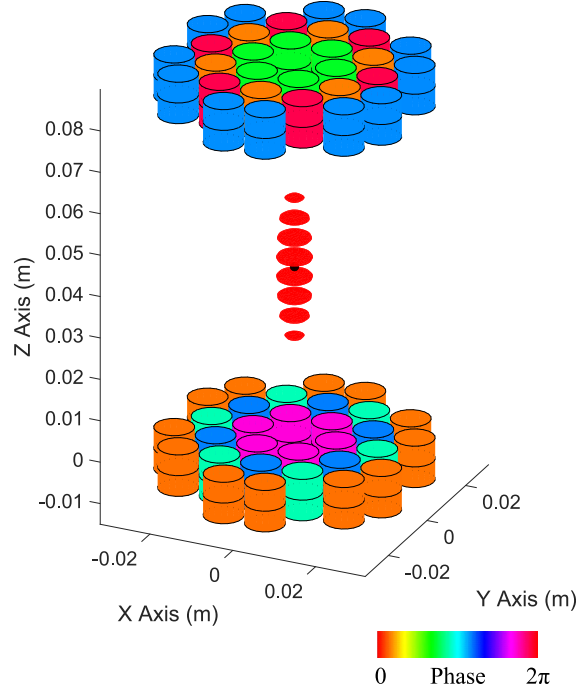


FIG. 3.20. Phase assignments for the transducers in acoustic levitator and the red isosurface in the centre represents the resultant pressure field (Isosurface at 1000 Pa).

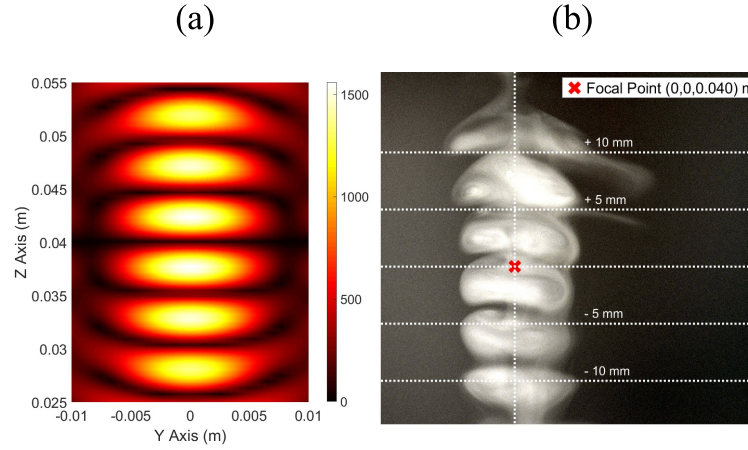


FIG. 3.21. Qualitative assessment on the pressure field inside the acoustic levitation using dry ice. (a) shows the numerically predicted acoustic pressure field, and (b) shows the acoustic pressure field in the acoustic levitator visualised by the dry ice in the experimental apparatus.

84]. However, the good qualitative agreement, along with reasonable quantitative agreement suggests that the numerical simulation can predict the acoustic pressure field inside the levitator. There exist alternative methods to measure acoustic pressure field inside the levitator

with minimal effects, such as Laser Doppler Vibrometer [151], or Schlieren Imaging [104]: however, they require more advanced equipment, training, and calibrations.

#### Gor'kov Potential

Acoustic radiation force generated by the acoustic levitator was evaluated using the Gor'kov potential as described in § 2.1.3 [40]:

$$U_{rad} = \frac{4\pi}{3} r^3 \left[ \frac{f_1 \kappa_0 \langle p_{in}^2 \rangle}{2} - \frac{3f_2 \rho_0 \langle v_{in}^2 \rangle}{4} \right] \quad (3.19)$$

where  $f_1 = 1 - \frac{\kappa_p}{\kappa_0}$ ,  $f_2 = \frac{2(\tilde{\rho}-1)}{2\tilde{\rho}+1}$ , and  $\tilde{\rho} = \frac{\rho_p}{\rho_0}$ .  $\rho$  is density,  $\kappa = \frac{1}{\rho c}$  is compressibility with  $c$  being the speed of sound,  $p_{in}$  and  $v_{in}$  are incident pressure and velocity fields, respectively. Subscript 0 represents the properties of the fluid medium and  $p$  of the particle [32, 40]. The pressure input,  $p_{in}$  is determined from equation 3.11, and the velocity field is [32]:

$$v_{in} = \left| \nabla \left( \frac{p_{in}}{\rho_0 \omega i} \right) \right| \quad (3.20)$$

The gradient of the field was evaluated using the native MATLAB function, ‘gradient’, however, MEX-function (‘DGradient’) developed by Jan Simon [152] was utilised in instances where an increase in the processing capability was required [152]. The pressure field from the Fig. 3.20 was used to evaluate an example of an Gor'kov potential in an acoustic levitator, and the resultant Gor'kov potential is as shown in Fig. 3.22. The acoustic radiation force is

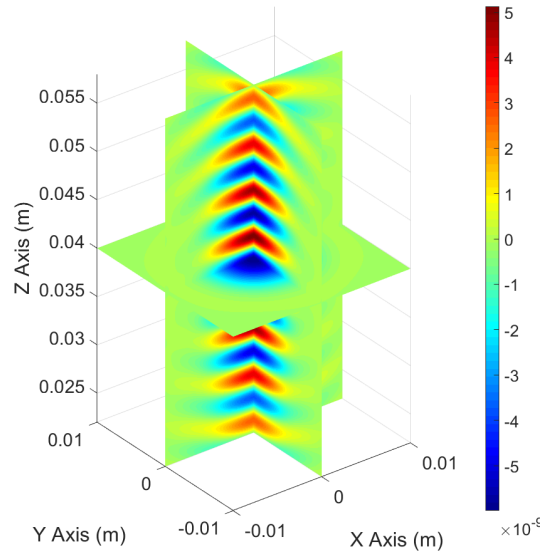


FIG. 3.22. The resultant Gor'kov potential ( $U$ ) calculated from the acoustic pressure field. As the original pressure field is a standing wave, the Gor'kov potential alternates between positive and negative over the distance.

then calculated by taking the gradient of the Gor'kov potential:

$$\mathbf{F}_{rad} = (F_{rad,x}, F_{rad,y}, F_{rad,z}) = -\nabla U_{rad} \quad (3.21)$$



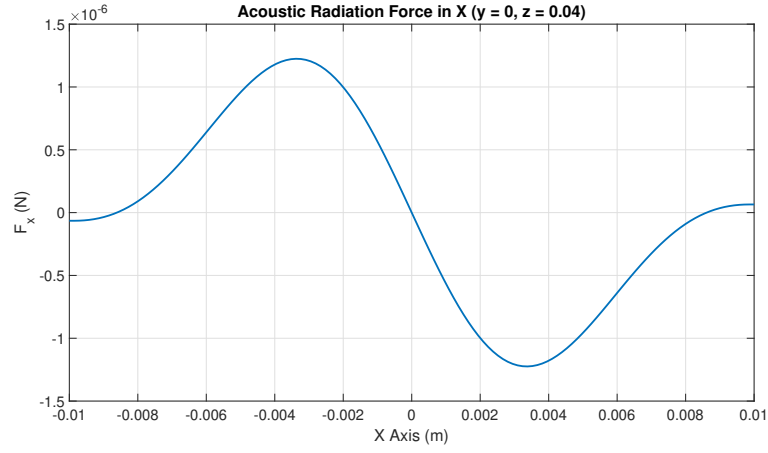


FIG. 3.23. Acoustic radiation force in  $x$  axis, as calculated from the Gor'kov potential

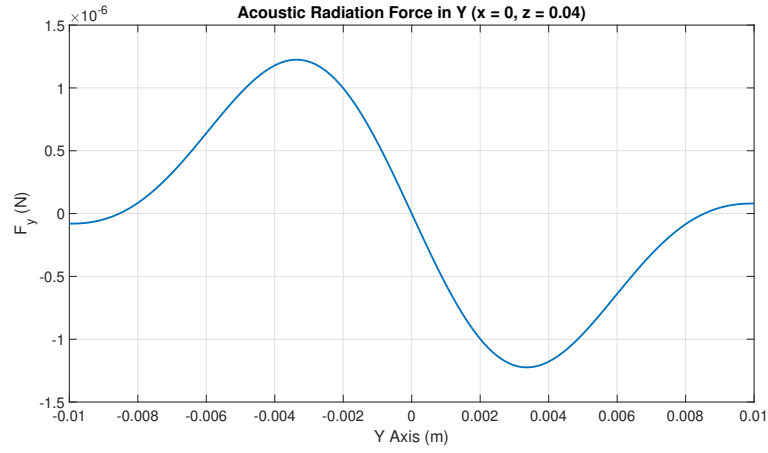


FIG. 3.24. Acoustic radiation force in  $y$  axis, as calculated from the Gor'kov potential

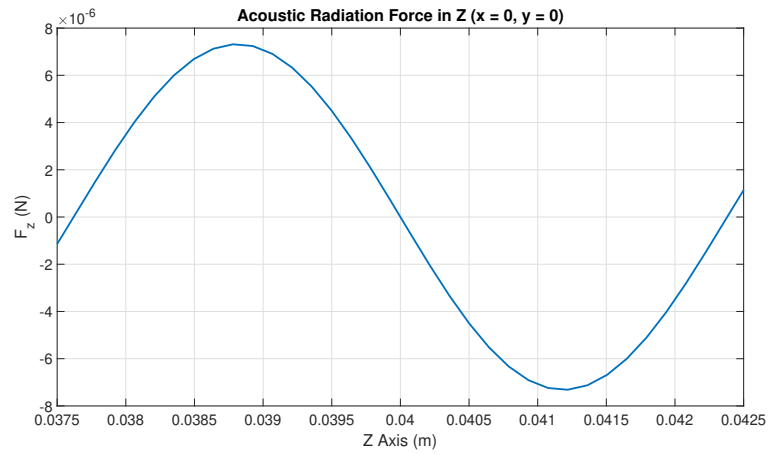


FIG. 3.25. Acoustic radiation force in  $z$  axis, as calculated from the Gor'kov potential

The resultant acoustic radiation force in  $x$ ,  $y$ , and  $z$  axis are as shown in Fig. 3.23, 3.24, and 3.25, respectively. These figures confirm that the acoustic trap generated by the acoustic levitator is a stable trap, as the forces in all directions are convergent. The validity of the numerical model is confirmed via the dynamic response of the particles suspended in the acoustic levitator in § 4.

## 3.5 Summary

The single-axis PAL has been introduced from the transducer array arrangement to the levitator controller. The stable levitation of EPS particle has been demonstrated with the described system, and the method of obtaining empirical constants for particle and air property was described. A tracking system for the acoustically levitated particle was described, and bespoke components were manufactured where necessary to facilitate calibration and robust measurements.

Moreover, the method of numerically simulating the pressure field inside the acoustic levitator was introduced with empirically obtained constants, and its validity was confirmed via experiments. The pressure field was then used to determine the acoustic radiation force using Gor'kov potential.

The work presented here will form the basis of the analysis on the dynamic response of the acoustic levitator, and its effect on future applications of acoustic levitation.



# Chapter 4 Dynamics of Mid-Air

## Single Axis PAL

In this chapter:

- A one-dimensional dynamics of levitated particle is introduced.
- Acoustic radiation force is approximated in a linear and nonlinear stiffness function.
- Numerical continuation toolbox, COCO is introduced.
- Numerical models were validated against the experimentally obtained results.
- Softening behaviour of the system is demonstrated.
- Occurrences of period-doubling bifurcation was numerically predicted, and was validated experimentally.

### 4.1 Introduction

The common model of the statics and dynamics of the particles levitated in an acoustic levitator has been linear mass-spring oscillators [12]. This model follows from the small displacement assumption and the fact that the majority of the acoustic levitators have a sinusoidal acoustic radiation force profile [9, 153] when acoustic fields are generated with a Langevin horn transducer, and another opposed Langevin horn transducer or reflector as in Fig. 4.1. As demonstrated in Fig. 3.23 to 3.25, the PAL used in this thesis can similarly create acoustic radiation force with a near-sinusoidal force profile in the vicinity of the equilibrium points (Fig. 4.1 (b)), with the added advantage of being able to adjust this force and hence move the particle to arbitrary positions. Therefore, both Langevin horn based and phased array based single-axis PAL have the same working principle of having a standing wave and hence sinusoidal acoustic radiation force around the equilibrium (Fig. 4.1 (c)).

Acoustic levitators have a broad range of applications in non-contact transportation and as a processing method for pharmaceutical, biological or chemical applications [15, 23, 97, 108, 117, 154]. The behaviour of the levitated objects has been of interest in all classes of acoustic levitator [11, 88, 95]. The chaotic shape dynamics of bubbles and droplets inside acoustic levitators are well documented [155, 156] and the translational oscillation of these deformable samples has been studied in the past, often with damping forces neglected [9, 51, 157]. Pérez et al. [96] devised an experimental approach to determine the dynamics of solid particles in a single-axis classical acoustic levitator and demonstrated the fit of quadratic damping terms in a dynamic model. Jia et al. analyzed the dynamic response of micro-particles in liquids

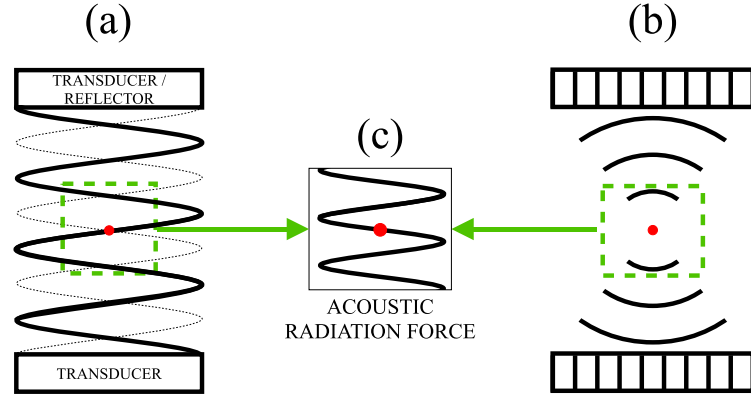


FIG. 4.1. Two types of single-axis standing wave levitators. (a) A Langevin horn transducer assembly with an opposed reflector, or a second transducer. (b) Two transducer arrays with phased delays or geometry designed to focus the acoustic waves at the centre. (c) Resultant central near-one-dimensional sinusoidal acoustic radiation force from both of the acoustic levitators. Reproduced from [27], with the permission of AIP Publishing

to show the effects of acoustic streaming and hydrodynamic forces on particles [158] and Andrade et al. [151] pointed out that the particle may exhibit nonlinear behaviours similar to a Duffing oscillator (nonlinear oscillator with damping and nonlinear elasticity [135]). However, whilst the popular model of linear spring-mass-oscillator is applied frequently [45, 91, 96, 159, 160], its effect on the dynamics of solid particles suspended inside a standing wave levitator in mid-air has not yet been fully explored. The linear spring models are applicable only in the case that the movement of the suspended particle is small [12], and the boundary at which small displacement assumption is no longer valid have not yet been determined: the lack of understanding of the translational dynamics of the levitated samples hinders the development of future applications.

In this chapter, a nonlinear dynamic model for the restoring forces inside a single-axis PAL will be presented. This model accurately predicts various nonlinear dynamic phenomena such as amplitude-dependence, multiple solutions, and period-doubling bifurcations. These responses were observed experimentally and found to be in excellent agreement with the model predictions, whereas previous linear spring models by definition, fail to predict these phenomena.

## 4.2 Formulation of One-Dimensional Dynamic Model

The single-axis PAL utilised in the experiments described in this thesis is composed of 60 Murata transducer phased array system and is described in § 3.2.1. An assumption was made that the acoustic transducers instantly emits the acoustic pressure wave with the requested phased delays and associated dynamics on particle is slow in comparison to the emission of the acoustic waves. Moreover, the system was assumed to be a single degree of freedom

oscillator when oscillated in  $z$ -axis. The particle radius was  $r = 0.71$  mm, with density  $\rho_0 = 34.0 \text{ kg m}^{-3}$ . This particle is small in comparison to the wavelength (8.6 mm) of the acoustic wave, and the Gor'kov potential is assumed to be applicable [32]. Moreover, as the particle is levitated in mid-air; added mass effect or history forces in viscous media is assumed to be negligible in this case and acoustic streaming was assumed to be zero.

Using the above assumptions, the force balance on the levitated particle in  $z$ -axis is then:

$$m\ddot{z} = (F_{rad,z} + F_{grav}) + F_{drag} \quad (4.1)$$

where  $m = \frac{4}{3}\pi r^3 \rho_p$  is the mass of the particle, and  $F_{rad,z}$  is acoustic radiation force in  $z$ . The difference in system responses between the linear and nonlinear stiffness will be determined by changes in this term, and will be described in detail in § 4.2.1.  $F_{grav} = -mg$  is gravitational force, and  $F_{drag}$  is the drag force by air. The drag force is calculated as [161, 162]:

$$F_{drag} = -\frac{1}{2}C_d \frac{\pi}{4}(2r)^2 \rho_0 |\dot{z}| \dot{z} \quad (4.2)$$

where  $\rho_0$  is the density of air. In a liquid based acoustic manipulation, the Reynolds number in the system maybe considered sufficiently low to assume it as a linear drag force (Stoke's law) [163]:

$$C_d = \frac{24}{\text{Re}} \quad (4.3)$$

where  $\text{Re} = \frac{2r|\dot{z}|\rho_0}{\mu}$  is the Reynolds number and  $\mu$  signifies the viscosity of the medium. However, Stoke's law is only valid for Reynolds number less than 0.1 [162], and in the air-based acoustic levitator the velocity of the particle is in the range of  $10^{-1}$ - $10^{-2} \text{ ms}^{-1}$  [72, 79, 123]. In this range of velocity, the usage of nonlinear damping coefficient [161, 162] is more suitable:

$$C_d = \frac{24}{\text{Re}} \sqrt{1 + \frac{3}{16}\text{Re}} \quad (4.4)$$

This damping coefficient is applicable up to  $\text{Re} \leq 100$  [161]. The comparison of the linear and nonlinear drag force is as shown in Fig. 4.2 and it is clear that beyond  $\pm 0.05 \text{ ms}^{-1}$ , the linear drag force is invalid as the expected velocity is at least a magnitude higher. As the coefficient of drag in 4.4 contains inverse of velocity, which goes to infinity when the velocity is zero, the drag force was set to zero when stationary.

### 4.2.1 Acoustic Radiation Force Profile

The acoustic radiation force in the single-axis acoustic levitator is evaluated using the MATLAB numerical simulation as described in § 3.4. The transducer coefficient of  $P_0 = 0.904 \text{ Pa}$  was utilised as the levitator was driven at 5 V (see § 3.4.1) and  $\pm 7$  mm of the field around the focal point was evaluated with field discretization of  $\frac{\lambda}{90}$ , which makes a vector with length of 147 in each dimension. The directivity function of the transducer was evaluated using a

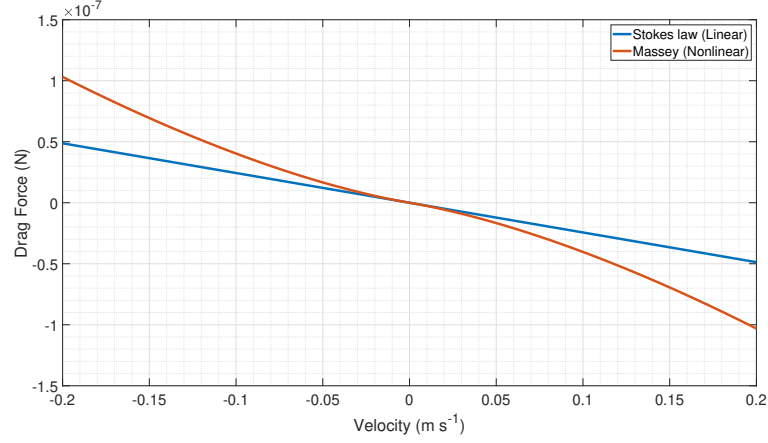


FIG. 4.2. The comparison of the linear (Stoke's Law) and nonlinear drag force (Massey).

function:

$$D_f(\theta_n) = 1 \quad \text{for } -0.175 < \theta_n < 0.175 \quad (4.5)$$

and

$$D_f(\theta_n) = 0.907 \sin(0.999\theta + 1.57) + 0.0882 \sin(3.98\theta + 1.57) + 0.0474 \sin(12.2\theta - 1.57) + 0.0575 \sin(8.22\theta + 1.57) \quad (4.6)$$

otherwise. This formulation was obtained by fitting a curve to the values of directivity measurements from the product specification of Murata MA40S4S [149], using MATLAB Curve Fitting App. The customised directivity function had a profile as shown in Fig. 4.3.

The pressure field generated by the acoustic levitator is symmetrical around the  $z$ -axis, and

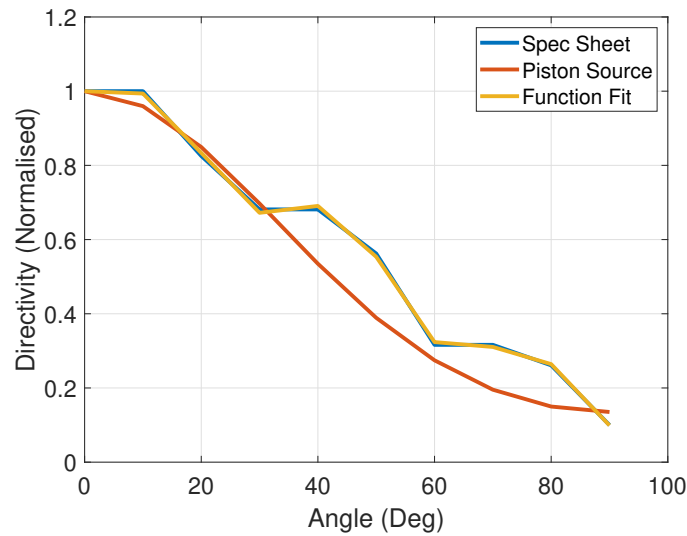


FIG. 4.3. The comparison of the directivity function as defined by the manufacturer's specification sheet [135], piston-source approximation, and the custom-directivity function fit generated by the MATLAB Curve Fitting App.

its instantaneous pressure field distribution in XZ and YZ planes are as shown in Fig. 4.4 (a) and (b), respectively. The resultant acoustic pressure field along the  $z$  axis when  $x = 0$  and  $y = 0$  is as shown in Fig. 4.5 (a), and the resultant acoustic radiation force profile over the distance is as shown in Fig. 4.5 (b).

#### Nonlinear Stiffness

In order to demonstrate the applicability of the analysis performed on the single-axis PAL to the other single-axis acoustic levitators such as Langevin transducer based systems, a sinusoidal function was approximated in the vicinity of the equilibrium point. The ‘fit’ function

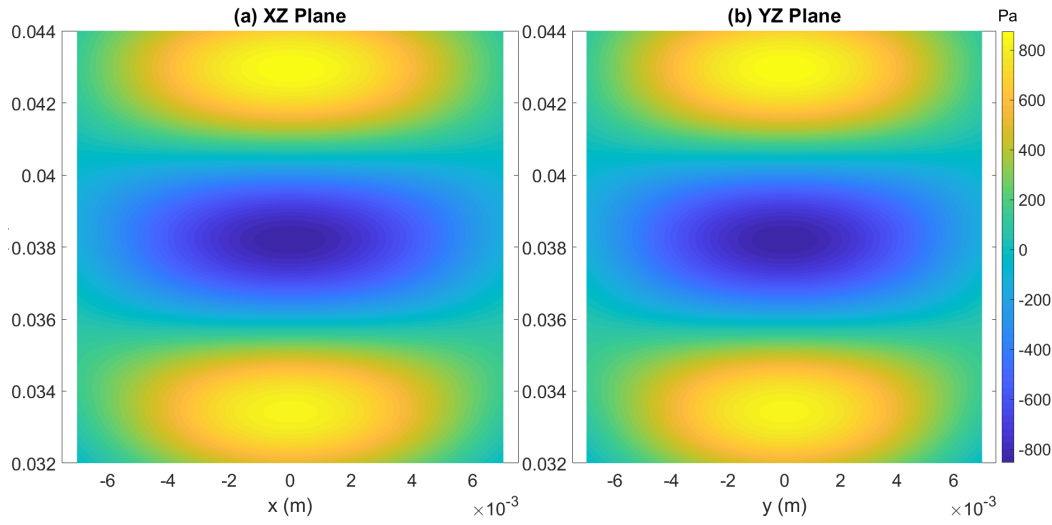


FIG. 4.4. Simulated instantaneous pressure field generated by the acoustic levitator in YZ plane. Reproduced from [27], with the permission of AIP Publishing

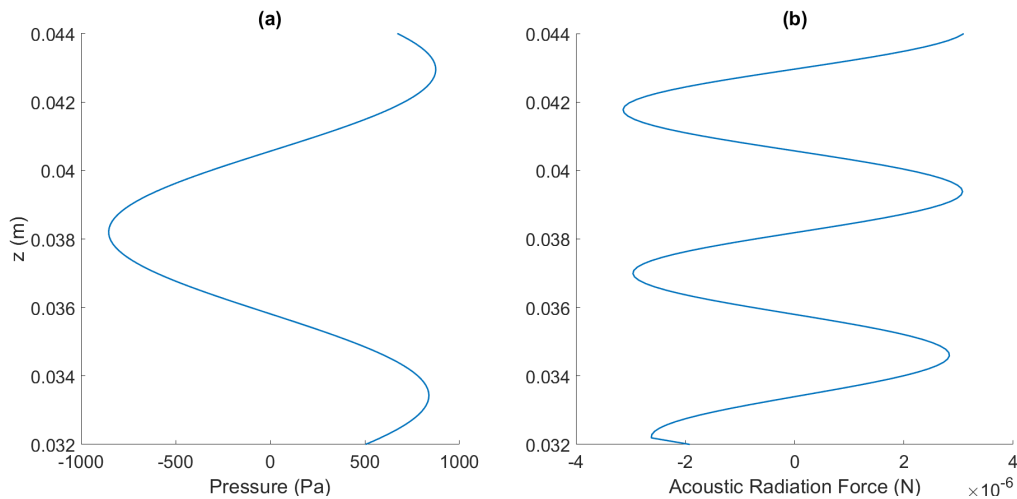


FIG. 4.5. Simulated field generated by the acoustic levitator. (a) Pressure distribution across the central axis and (b) acoustic radiation force. Reproduced from [27], with the permission of AIP Publishing



of MATLAB was applied to the acoustic radiation force profile with function in the form:

$$F_{rad} = \alpha \sin(\beta(z - z_p)) \quad (4.7)$$

where  $z_p$  is the input excitation via shift in the focal point and  $\alpha$  and  $\beta$  were identified as  $-3.06 \times 10^{-6} \text{ N}$  and  $1315 \text{ m}^{-1}$  respectively (by taking the average of the values over the evaluated range of focal points). The change in  $z_p$  will initiate change in the equilibrium point of the field as shown in Fig. 4.6 and will result in applying force to the particle. The minimum  $R^2$  value for 4.7 was 0.998 for the range of  $z - z_p$  and demonstrates the validity of the sinusoidal approximation on the acoustic radiation force profile. The approximation of the acoustic radiation force as a sinusoidal force also allows a significant improvement in the computational efficiency, in comparison to the direct calculation of acoustic radiation force as shown in § 3.4.1 or interpolating the values from lookup tables.

### Linear Stiffness

The linear stiffness model of the acoustic levitation system utilised the formulation given by Hooke's law and approximated the acoustic radiation force as a linear spring in the vicinity of the equilibrium point:

$$F_{rad,L} = -K_L(z - z_p) \quad (4.8)$$

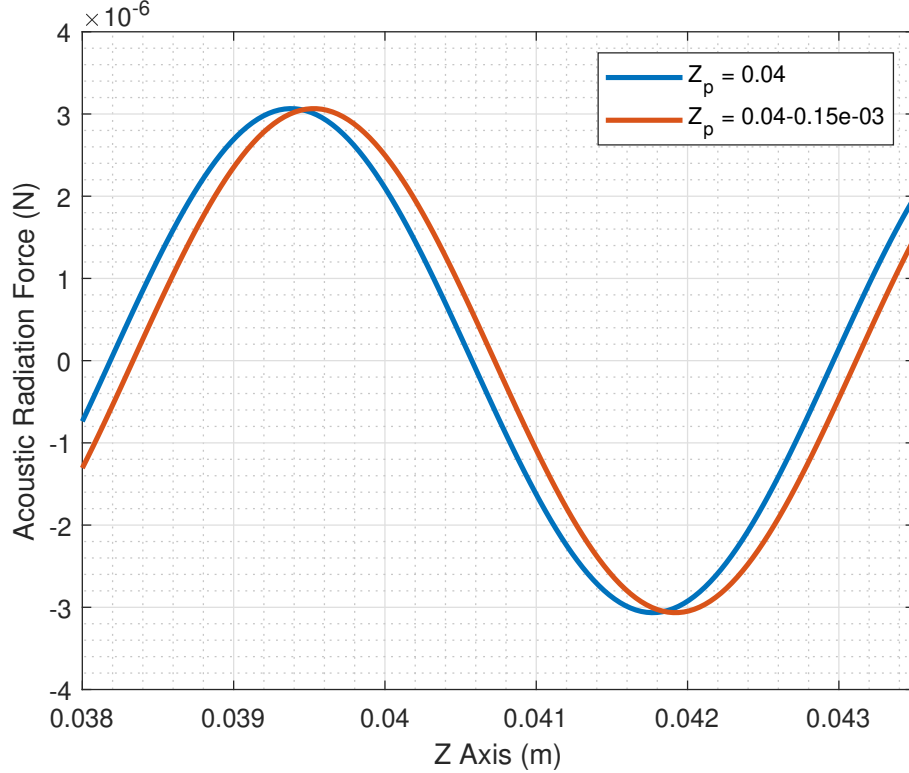


FIG. 4.6. Force field shift by change in  $z_p$ . It changes the position of the equilibrium point, and therefore applies force to the particle

where  $K_L$  is the linear stiffness around the equilibrium point. The equilibrium point at the focal point was identified by the force balance between the acoustic radiation force and the gravitational force. The linear stiffness was identified by taking the derivative of acoustic radiation force:

$$K_L = \frac{dF_{rad}}{dz} = \alpha\beta \cos(\beta(z - z_p)) \quad (4.9)$$

and was calculated from the sinusoidal approximation. As shown in the Fig. 4.7, the linear spring stiffness is invariant across the field (maximum differences in this range was 0.08 %). Therefore the average value of the linear stiffness value  $K_L$  was taken over the field to determine the average of linear stiffness which was  $0.003974 \text{ N m}^{-1}$ . This invariance in stiffness may give illusion that the linear stiffness is applicable in the dynamic simulation.

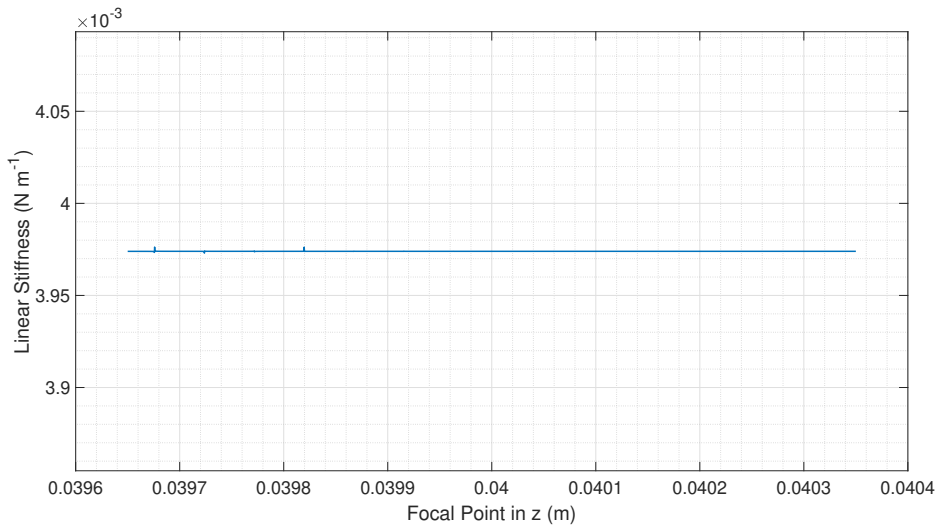


FIG. 4.7. The change in linear stiffness value through each focal points. The value was normalised to the maximum value of the stiffness.

### 4.3 Experimental Validation of Numerical Simulation

The dynamics of the levitation system can be explored by approaches such as the random excitation, sine-sweep, or a stepped sine-sweep [164], and the validity of the numerical model can be confirmed by comparing the frequency response function of the experimental results and numerical model. The determination of frequency response function usually involves the measurement of the system response by the change in the excitation frequency, and responses need to be identified for a wide range of frequency. Sine-sweeping is one of the frequently employed techniques, both in the experiment and numerical simulation. The force balance in the 4.1 is an ordinary differential equation (ODE), and the sine-sweeping can be implemented numerically using ODE solvers by moving the focal point with a sinusoidal function ( $z_p = z_o + A_{in} \sin(2\pi\Omega t)$ ) at a constant frequency ( $\Omega$ ), z-axis offset ( $z_o$ ) and amplitude ( $A_{in}$ ). Whilst a typical ODE solver can accurately determine the response of the system: the solver cannot recognise the existence of bifurcation branches or follow the branch when it exists.

This problem can be overcome by utilising a numerical continuation algorithm. Numerical continuation is widely employed in the field of nonlinear dynamics [127], and it can be used to compute periodic solutions, determine their stability, identify and follow bifurcations in the given responses [165]. These solutions may be considered accurate to within the tolerances of the numerical solver, and 4.1 was solved using numerical continuation software “Continuation Core and Toolboxes” (COCO, version “coco\_2016Feb10”) in MATLAB [130, 165]. COCO was selected as it is compatible with MATLAB, and its functionality has been tested independently by multiple authors [166–170].

#### 4.3.1 Setting up the Numerical Continuation Problem with COCO

Firstly the state space representation of 4.1 was formulated:

$$\begin{pmatrix} \dot{z}_1 \\ \dot{z}_2 \end{pmatrix} = \begin{pmatrix} z_2 \\ \frac{1}{m} (F_{drag}(z_2) + [F_{rad}(z_1) + F_{grav}]) \end{pmatrix} \quad (4.10)$$

where  $z_1 = z$  and  $z_2 = \dot{z}$ . A function handle which contains this 4.10 was coded in MATLAB. 4.10 is for a nonlinear stiffness model and for a linear stiffness model: the forces inside the square brackets are replaced by 4.8.

There are three programs in COCO, and they are ‘Periodic Orbit’ (PO), ‘Equilibrium Point’ (EP), and ‘Trajectory Collocation’ (COLL) toolboxes. The system response was predicted using the PO toolbox (which internally uses COLL toolbox), and specifically, ‘ode\_isol2po’ function was utilised. ‘ode\_isol2po’ starts the continuation of periodic orbits from initial guesses, and takes initial guesses,  $t_g$  and  $x_g$ , continuation parameters, the initial value of continuation parameters, and the evaluation range of the continuation parameters as the inputs to the continuation toolbox. For the system, it is common to set one of the continuation parameters as the input excitation frequency ( $\Omega$ ).

The initial guess of the periodic orbit can be obtained by utilising an ODE solver and solving for the time domain, position, and velocity information over one period ( $T = \frac{1}{\Omega}$ ). Specifically, the ODE45 solver (based on an explicit Runge-Kutta (4,5) formula) in MATLAB was selected [171] and the function handle of 4.10 and initial guess of position (initial focal point) and velocity (initially stationary) were fed into the ODE solver. In order to avoid the transient effects, the initial 300 cycles of the ODE solver were ignored, and one cycle length of time-domain signal and position/velocity signal was kept as the initial guess for the numerical continuation (note that ODE solver is only used for the initial guess, and does not need to be employed again when the excitation frequency changes).

The function handles of 4.10 can be implemented in two different forms, autonomous and non-autonomous function. The difference between the autonomous and non-autonomous functions is the time dependence of the functions. Whilst both autonomous and non-autonomous function will yield the same answer, the reduction of the number of variables in the system function was desired. Therefore, the function handles of 4.10 was formulated as a non-autonomous function. As COCO by default, “does not recognize that the

orbit period must equal an integer multiple of” the frequency [172]: the glueing function (‘coco\_add\_glue’) on COCO was utilised to force the interval length to equal the period length of the excitation frequency,  $\Omega$ .

The output solution of a system from COCO can be stable or unstable, and the difference between stable and unstable response is identified via the Floquet multipliers of the periodic orbit. Floquet multipliers are the eigenvalues of the linearized Poincaré map, and “the closed loop is linearly stable if and only if  $|\lambda_j| < 1$ ” for all values of eigenvalues [135]. COCO offers a function which outputs the Floquet multiplier of the solution, and the unstable orbits were identified and marked accordingly. Moreover, the COCO function ‘ode\_isol2po’ has the ability to identify the location and the type of bifurcations. There are various types of bifurcations, such as Hopf, Torus, Fold, and Period-Doubling (PD) bifurcations and detecting the occurrence of these bifurcations allows further understanding of the system.

#### 4.3.2 Experimental Setup

In order to conduct an experimental verification of the proposed dynamic model, the acoustic levitator was set up as described in § 3.3. Unlike, the numerical model, it is experimentally difficult to force a system to converge into a steady-state. Therefore, a stepped-sine approach was utilised to identify the frequency response function of the system. The focal point was moved sinusoidally at a fixed frequency for 40 cycles with a fixed input excitation amplitude ( $A_{in}$ ), and the excitation frequency was gradually increased or decreased until it reached the target frequency. When the excitation frequency reached the target frequency, the particle was allowed to settle into a steady state (i.e. for 10 seconds) and then the movement of the particle was captured by a high-speed camera (Photron FASTCAM SA-Z Type 2100K-M-32GB) at 1001 Hz for  $\approx 1$  second. The vertical dynamic manipulation of the focal point was transmitted from the computer to the acoustic levitator driver board at 700 Hz via a UART serial communication line operating at 500 kbauds. The driver board was made of an FPGA board (ALTERA CoreEp4CE6) which generates 60 independent square waves with a phase resolution of  $\phi = \frac{\pi}{64}$ , as described in § 3.2.

At the beginning of the experiment, the atmospheric properties were measured (using method described in § 3.2.3) and at 21.3°C: the values of air density ( $\rho_a$ ), viscosity ( $\mu$ ) and speed of sound ( $c_0$ ) were  $1.19 \text{ kg m}^{-3}$ ,  $1.82 \times 10^{-5} \text{ kg (ms)}^{-1}$ , and  $344 \text{ m s}^{-1}$ , respectively. The camera was calibrated accordingly using a CMM-stylus (Renishaw A-5000-7806) to find the pixel-to-metre conversion ( $3.29 \times 10^{-5} \text{ m pix}^{-1}$ ). The pixel-to-metre conversion rate was then used in a post-process stage where the high-speed camera data was processed by the MATLAB image analysis package to determine the centre of the levitated particle. An example of the image taken by the Photron camera, and the identification of the particle is as shown in Fig. 4.8.

The particle position signal was then passed through a low-pass filter to remove noise from the experiment. The low-pass filter was designed using MATLAB DSP System Toolbox. The sampling frequency was set at 1001 Hz, with passband frequency and stopband frequency set

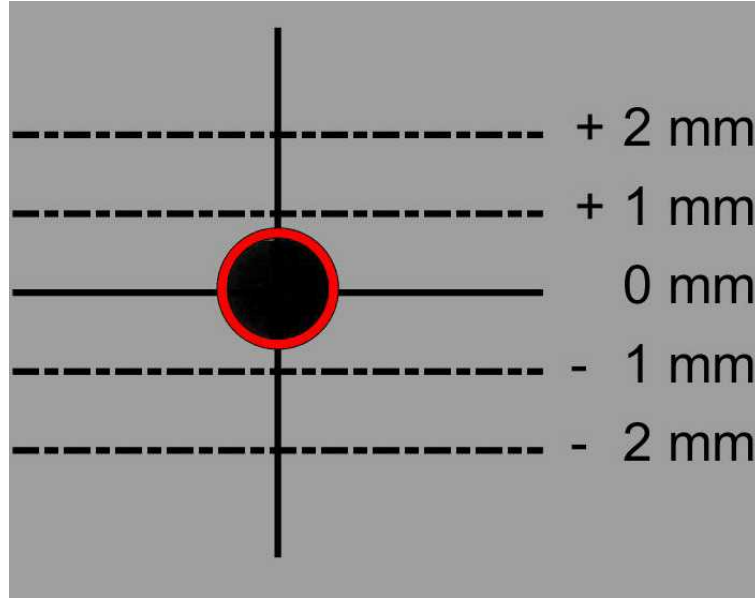


FIG. 4.8. An example image, taken by the Photoron FASTCAM camera. The red circle is the identified position of the particle, and the length scale is retrieved from the pixel-to-metre conversion rate using CMM-stylus. Reproduced from [27], with the permission of AIP Publishing.

at 100 and 150 Hz, respectively. The generated filter has a frequency response function, as shown in Fig. 4.9. The response amplitude of oscillation of the particle was then determined by taking the peak-to-peak difference of the filtered signal.

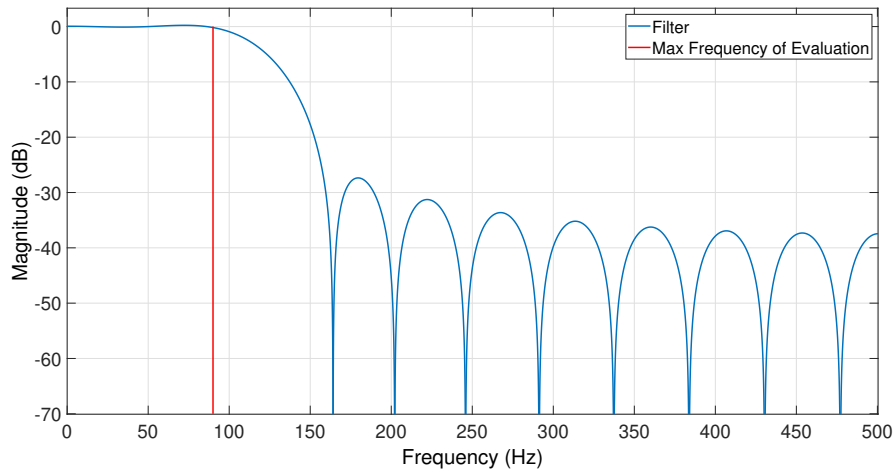


FIG. 4.9. Low pass filter used to remove the noise in the experimental data. The passband frequency was set at 100 Hz, and the stopband frequency was set at 150 Hz.

## 4.4 Results

Fig. 4.10 shows the comparison of both numerical models (linear and nonlinear stiffness) and experimental results for excitation amplitude of  $A_{in} = 0.15$  mm. A peak response amplitude of  $A_{out} = 2.58$  mm was predicted by the linear stiffness model with a symmetrical response

around the resonance. There are significant differences between this linear model and the experimental results even for a relatively small excitation amplitude of  $A_{in} = 0.15$  mm (or  $1.74\%\lambda$ ). This is also small in comparison to the width of the Gor'kov potential, which is 4.8 mm ( $A_{in} = 0.15$  mm is 3.13% of the width of the local Gor'kov potential minima). If the peak amplitude of the experiment and the linear stiffness model was compared at this point, it might suggest that the drag force of the numerical model differ by a factor of  $\approx 2$ .

However, by retaining the nonlinearity of the acoustic radiation force in the model: the nonlinear stiffness model correctly predicts the response of the system with a significantly greater accuracy of  $R^2 = 0.998$  between model and experiment. Despite the small oscillation amplitude, the peak frequency predicted by the linear and nonlinear stiffness models differ by  $\approx 18$  Hz, highlighting the difference between the two models.

In addition, the stepped-sine sweep was performed from low to high frequency (sweep up) and high to low frequency (sweep down), as shown in Fig. 4.10. The differences between the up and the down sweep demonstrate that multiple stable solutions exist for certain forcing frequencies - a feature that is not seen in linear systems. Experimentally measuring the complete stable portion of the branch on the downwards sweep (between 25 Hz and 34 Hz) is challenging, as the basin of attraction of the stable response typically decreases as it approaches a fold bifurcation [173]. The red curve in Fig. 4.10 represents unstable solutions where the aforementioned Floquet multiplier has a value greater than 1. The instability of the solution does not signify that the solution does not exist; however, it is more difficult to measure it experimentally, without employing a specific control strategy [174].

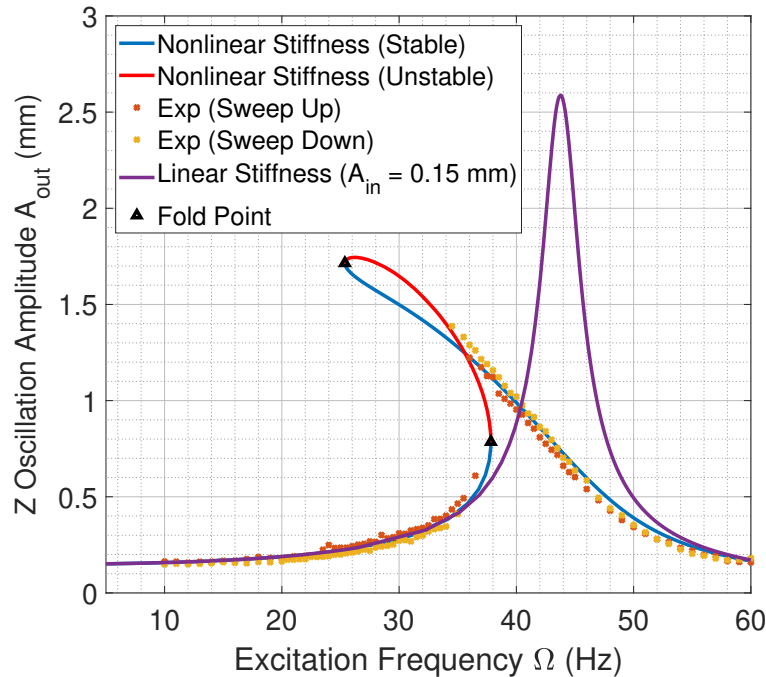


FIG. 4.10. Comparison of the nonlinear stiffness model, experimental results and equivalent linear stiffness model with  $A_{in} = 0.15$  mm. Reproduced from [27], with the permission of AIP Publishing

## 4.5 Discussion

With the accuracy of the numerical model is confirmed; the model is used to predict the responses of the system as the amplitude of the excitation sweep increased. The responses for different excitation amplitudes  $A_{in} = 0.10, 0.15$ , and  $0.20$  mm were solved and are shown in Fig. 4.11.

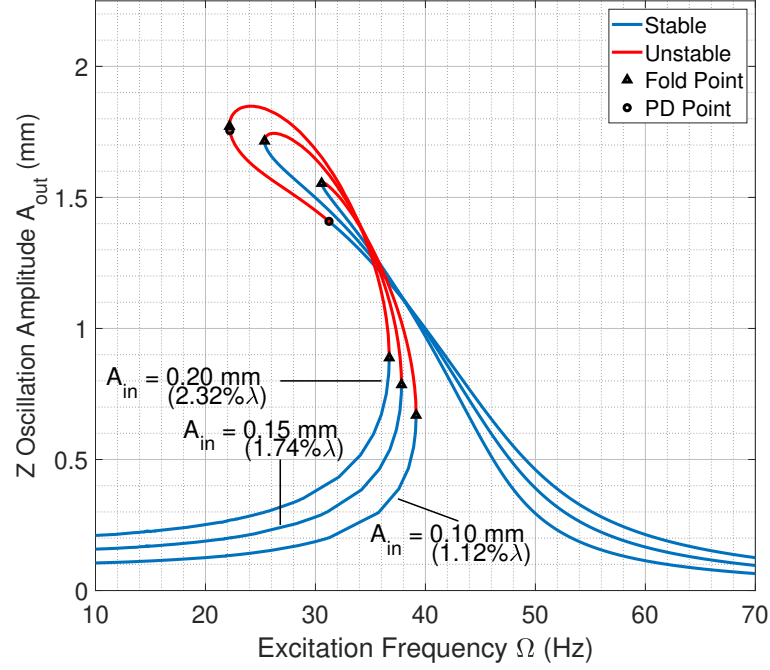


FIG. 4.11. Predicted response from the nonlinear model when excited at different amplitudes. Reproduced from [27], with the permission of AIP Publishing

Whilst the change in the amplitude is small (0.05 mm) in comparison to the wavelength ( $\lambda = 8.6$  mm), the response of the system varies significantly. Since the resonance frequency decreases with amplitude, the system is considered to be a ‘softening’ system [133]. The response becomes more symmetrical and approaches the linear spring model as the excitation amplitude decreases. This is caused by the reduction in the response amplitude of particle oscillation, which begins to match the condition for a linear assumption. Whilst the oscillation amplitude for the acoustic trap are in the range of 1.12 to 2.32 % of the wavelength, the response is not symmetrical and for the linear assumption to hold true; it needs to have significantly smaller perturbation than those evaluated here.

The linear stiffness model contains nonlinear damping terms, due to the drag forces, and therefore also exhibits amplitude dependence, as shown in Fig. 4.12. However, the resonant frequency is independent of the excitation amplitude and hence still exhibits a characteristic symmetrical frequency response.

For large excitation amplitudes (i.e.  $A_{in} \geq 0.2$  mm), a period-doubling (PD) bifurcation occurs near an excitation frequency of 80 Hz. For example, when the excitation amplitude is increased to  $A_{in} = 0.35$  mm, an unstable region emerges between 82 and 86 Hz as shown in

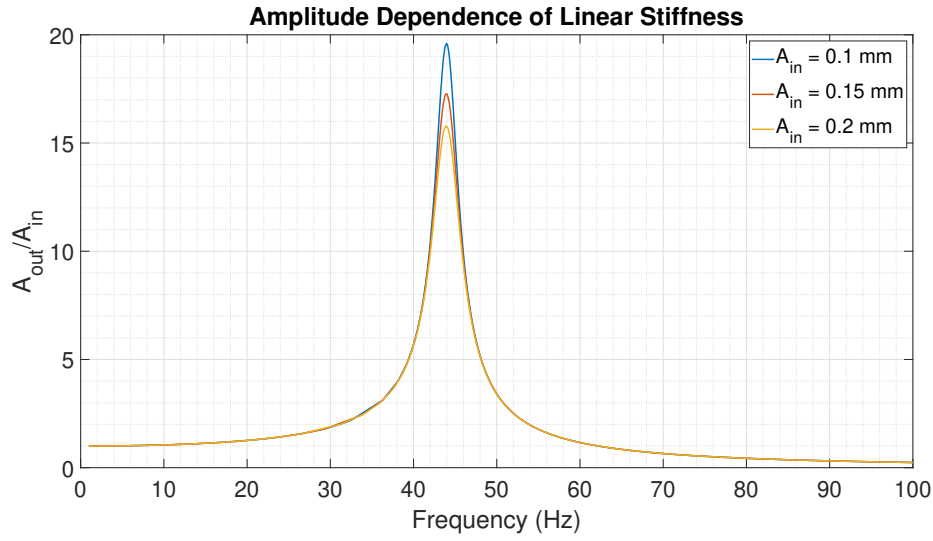


FIG. 4.12. Predicted response from the linear stiffness model with the change in the excitation amplitude. The system shows amplitude dependence as the drag term is nonlinear.

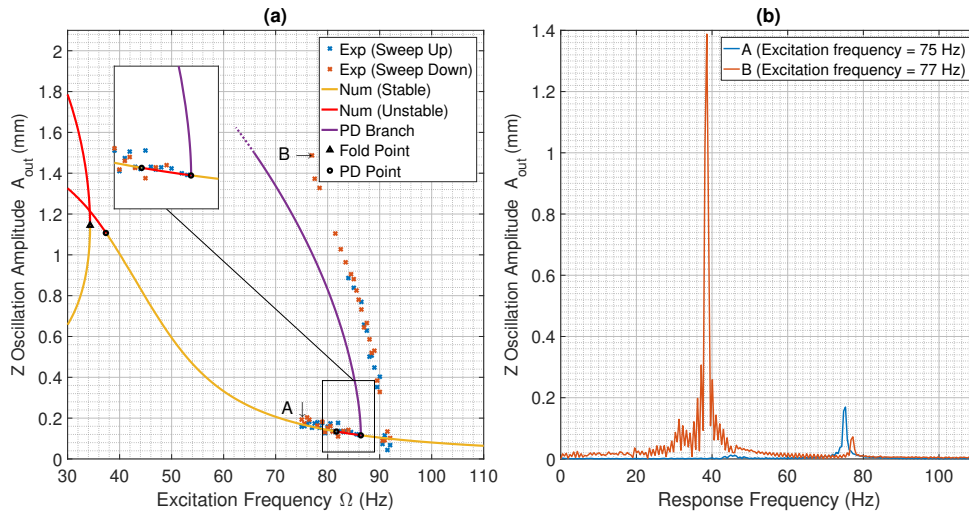


FIG. 4.13. The comparison of numerical and experimentally obtained results for period-doubling biruncations. (a) The numerical model predicts an unstable response from 82 to 86 Hz, the experimental results confirm the existence of this period-doubling (PD) bifurcation. The PD branch is part of a stable region, and the dotted part continues to an unstable PD branch. (b) Frequency spectrum of the signal denoted A and B in (a) from ‘Exp (Sweep Down)’. The dominant frequency at point B, where the period-doubling is occurring, is half that of the excitation frequency, whereas point A oscillates at the excitation frequency.

Reproduced from [27], with the permission of AIP Publishing



Fig. 4.13 (a). A period-doubling bifurcation marks the point at which the response of the system switches to a new behaviour with a period that is twice that of the original response [135]. This leads to a loss of stability of the single-period solutions (represented by the red line), and an emergence of a new set of double-period solutions (purple line) for the response, shown in Fig. 4.13 (a). The existence of this period-doubling bifurcation was confirmed by repeating the same experimental procedure with an excitation amplitude of  $A_{in} = 0.35$  mm.

The experimental results are as shown in orange and blue dots in Fig. 4.13 (a) and the response amplitude increases up to  $A_{out} = 1.49$  mm in the frequency range between 90 Hz and 77 Hz. The experimentally obtained results are offset from the predicted period-doubling branch by  $\approx 4$  Hz. However, the results show the same qualitative behaviour, verifying the existence of the PD bifurcation and resulting behaviour. The frequency domain response of the signal for the points denoted A and B from ‘Exp (Sweep Down)’ on Fig. 4.13 (a) were measured and are shown in Fig. 4.13 (b). As the result of the period-doubling behaviour, the dominant response frequency is at half of the excitation frequency, confirming the occurrence of a period-doubling bifurcation, as demonstrated in Fig. 4.14.

Furthermore, period-doubling bifurcations may also occur at lower excitation frequencies. For example, period-doubling bifurcations are predicted to occur at 37 Hz in Fig. 4.13 (a) and around 31 Hz for  $A_{in} = 0.20$  mm in Fig. 4.11. The experimental confirmation of the low frequency period-doubling bifurcation has not yet been achieved, due to the high amplitude of the response. However, this indicates that more complex dynamics are possible and further investigation of the nonlinear dynamics of acoustic levitators is needed.

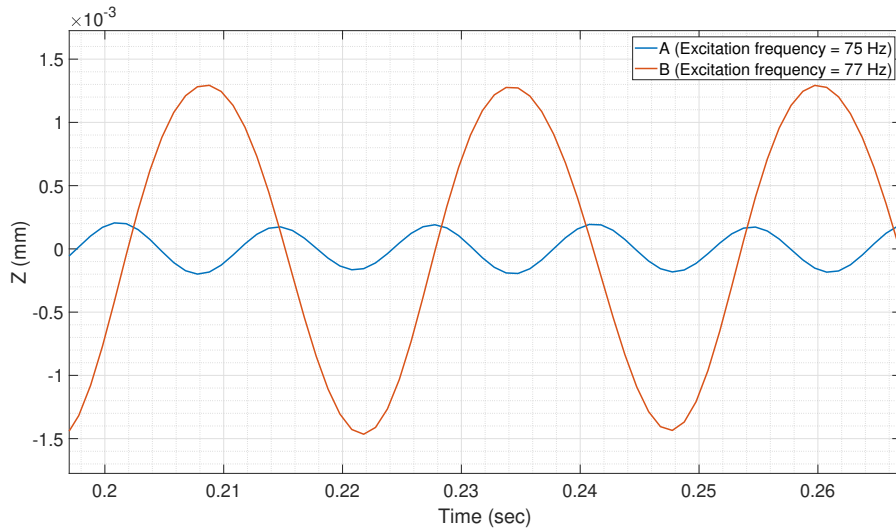


FIG. 4.14. Time domain signal of point A and B. Whilst the focal point is moved at a similar frequency, point A oscillates at 1:1 to the excitation frequency and point B oscillates at half the frequency and with greater amplitude.

## 4.6 Summary

In conclusion, the single degree-of-freedom nonlinear model of a solid particle trapped inside a mid-air single-axis PAL was developed and validated experimentally. The model assumed that the dynamics of the transducer (the change in phase) is faster than the dynamics of the levitated particle, and was assumed to be a single-degree of freedom system. The occurrence of nonlinear softening behaviour, as well as period-doubling bifurcations were predicted and verified. These behaviours were only predicted by the nonlinear stiffness model, highlighting the importance of the nonlinear model. The period doubling bifurcation is often the beginning of chaotic behaviour in many dynamic systems, and further studies may reveal this dynamic complexity in single-axis levitators. The characteristic sinusoidal restoring force of the acoustic levitator was found to cause these nonlinear responses. and this new model enables the dynamic instabilities of trapped particles to be accurately predicted, thereby benefiting contactless transportation and manipulation applications. The publication of this results has increased the awareness on the importance of considering the nonlinear stiffness, and is beginning to be considered in recent publications [75, 94, 175].



# Chapter 5 Static Trajectory

## Calibration of Levitated Particles

In this chapter:

- The shift of equilibrium points was experimentally observed.
- The source of the equilibrium points shift were hypothesised, and one of the hypothesis was selected for further study.
- A numerical model which demonstrate the hypothesis was developed, and qualitatively validated.
- The 2D particle tracking system was expanded to enable 3D particle tracking.
- Calibration method for improving the particle trajectory was developed in 2D and 3D, and its effectiveness was demonstrated quantitatively and qualitatively.

### 5.1 Introduction

This chapter introduces the method of improving the accuracy by which a particle is moved inside an acoustic levitator. The positioning accuracy by which the acoustic levitation system can place the object at specified points plays a fundamental role in the future applications of the acoustic levitators. As mentioned in the literature review, “The Boeing Company” filed a patent to fabricate objects whilst being levitated in air [24]. It is easy to imagine that the accuracy with which the part is being levitated would have a significant effect on the quality of the fabricated components.

Moreover, an emerging application of mid-air acoustic levitation is the creation of visual displays in which the particles represent information [72] such as 3D trajectories [176]. In ‘JOLED’, a screen made of acoustically levitated dielectric particles can be flipped individually between binary colours using an electric field [120]. More recently, Uno et al. proposed ‘Luciola’, a semi-spherical particle embedded with an LED and a coil that was acoustically levitated and lit up via wireless powering [121]. In these displays, the particle is held in mid-air and moved to the target position by refocusing a standing wave with a phased array, and the particle serves as a voxel (i. e. a 3D equivalent to a pixel in a 2D display).

In § 4, the nonlinear behaviour of a particle in an acoustic levitator was explored by analysing its frequency response function when subject to rapid movement of the trapping point. Whilst an excellent match between the numerical and experimental simulation was observed; the particle was only manipulated over the sub-millimetre scale. For the applications mentioned

above, objects need to move at a significantly longer distance (e.g. centimetre scale). However, even for a relatively simple case with levitation of one spherical particle, it was found to be non-trivial to follow desired paths on this larger scale. For example, if a particle is set to follow a trajectory as shown in Fig. 5.1 (a) in the centimetre range using the single-axis acoustic levitator described in § 3 and 4; the resultant path of the particle is clearly not identical to the target, as shown in Fig. 5.1 (b).

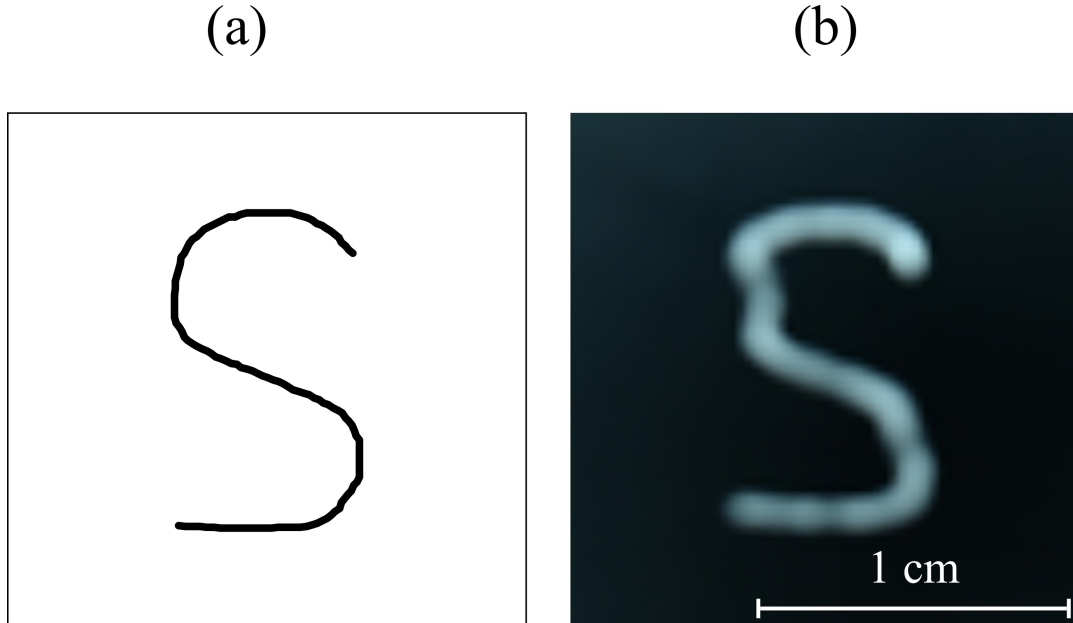


FIG. 5.1. A demonstration of the deviation of the particle trajectory deviating from the target trajectory. (a) shows the target trajectory that is in the shape of a hand-drawn letter, 'S'. (b) shows the resultant trajectory taken by the particle in the experiment. Location deviation is particularly visible around the curves of the letter. Reproduced from [28], with the permission of IEEE.

One potential solution to improve positioning accuracy is to utilise a control system. The implementation of an appropriate control system for the PAL could be expected to reduce the error between the target and actual particle position. However, it is technically challenging to track a millimetric sized particle in mid-air at the required frame rate. Thus, this thesis explores calibration of the trajectory as a solution, using experimental observations to correct for deviations in particle trajectory. The calibrated trajectory that follows from this process is expected to be valid for when the particle is moving at a low velocity.

## 5.2 Static Equilibrium Points in an Acoustic Levitators: Numerical Approach

The static equilibrium point is the position at which a particle in an acoustic levitator rests after steady state. The method of determining the numerical equilibrium points was briefly discussed in § 4.2.1, and involves the force balance between the acoustic radiation force and the gravitational force. For the method described in § 4.2.1, the acoustic radiation force was approximated as a sinusoidal force profile and hence identifying the point at which the

acoustic radiation force balances with gravitational force was relatively simple. However, obtaining a function that fits the acoustic radiation force field become more challenging with the increase in number of dimensions. Therefore, the equilibrium points were identified by implementing optimisation algorithms, and for the identification of the equilibrium points in a three-dimensional field, the optimisation problem was formulated as:

$$\arg \min_{\{x,y,z,f_y,f_z\} \in \mathbb{R}} \sqrt{F_{rad,x}(x,y,z,f_y,f_z)^2 + F_{rad,y}(x,y,z,f_y,f_z)^2 + (F_{rad,z}(x,y,z,f_y,f_z) + F_{grav})^2} \quad (5.1)$$

where  $F_{rad}$  is acoustic radiation force in  $x$ ,  $y$ , and  $z$ , ( $f_y$ ,  $f_z$ ) are focal points of the trap. Firstly, 2-D manipulation was considered and so the focal point was only changed in  $y$  and  $z$  axis with  $f_x = 0$ . In order to confirm that the movement in  $x$  can be approximated to be negligible, the numerical simulation was formulated in 3-D. For the single-axis PAL, the acoustic radiation force can be identified via the numerical simulation method as described in § 3. In the numerical simulation, the analytical formulation of the piston-source was utilised for the directivity function, the ‘standing wave lens’ was utilised for the transducer phase calculation (i.e.  $\phi_t = 0$  for the lower phased array and  $\phi_t = \pi$  for the upper phased array) and the transducer output ( $P_0$ ) was  $3.38 \text{ Pa m}^{-1}$  for the driven voltage of 18 V. The region of simulation was set to  $\pm 1 \text{ cm}$  from the centre of the levitator,  $(0,0,0.04) \text{ m}$  and the field was discretised with  $\frac{\lambda}{40}$ . The optimisation scheme for 5.1 was formulated using the constrained nonlinear multi-variable optimiser, ‘fmincon’ on MATLAB. The initial guess was set as:

$$\mathbf{x}_{guess} = [x_f, y_f, z_f] \quad (5.2)$$

and the search region was constrained to the region of simulation which were  $-0.01 \leq x \leq 0.01$ ,  $-0.01 \leq y \leq 0.01$ , and  $0.03 \leq z \leq 0.05 \text{ m}$ . Fig. 5.2 shows an example of the simulated acoustic radiation force when the focal point was set to  $\mathbf{x}_f = (0,0,0.040) \text{ m}$  and the identified equilibrium point of the particle ( $r = 0.78 \text{ mm}$ ,  $m = 0.079 \text{ mg}$ ) in the field using the optimisation algorithm. This equilibrium point identification process was repeated in a grid pattern within the working volume of the acoustic levitator (i.e.  $\pm 1 \text{ cm}$  from the centre of the acoustic levitator in the  $y$ - $z$  plane). Fig. 5.3 shows a quiver plot of the relative position of the equilibrium points from the specified focal point. In all cases, the position of the equilibrium point is close to the focal point, and the field is ordered with an RMS value of  $0.11 \text{ mm}$  and  $0.013 \text{ mm}$  between the focal point and equilibrium point in  $y$  and  $z$ , respectively. As the focal point reaches the sides of acoustic levitator, the equilibrium points shift towards the centre of the levitator. This shift is thought to be caused by the directivity of the transducers, as their ability to focus decreases towards the edge of the transducer array. Whilst the optimisation scheme was performed with the  $x$  axis forces considered; the particle movement in the  $x$  axis was negligible (mean  $x$  axis equilibrium point =  $1.62 \times 10^{-5} \text{ m}$  with standard deviation of  $3.72 \times 10^{-6} \text{ m}$ ) in numerical simulation, as hypothesized early in this section.

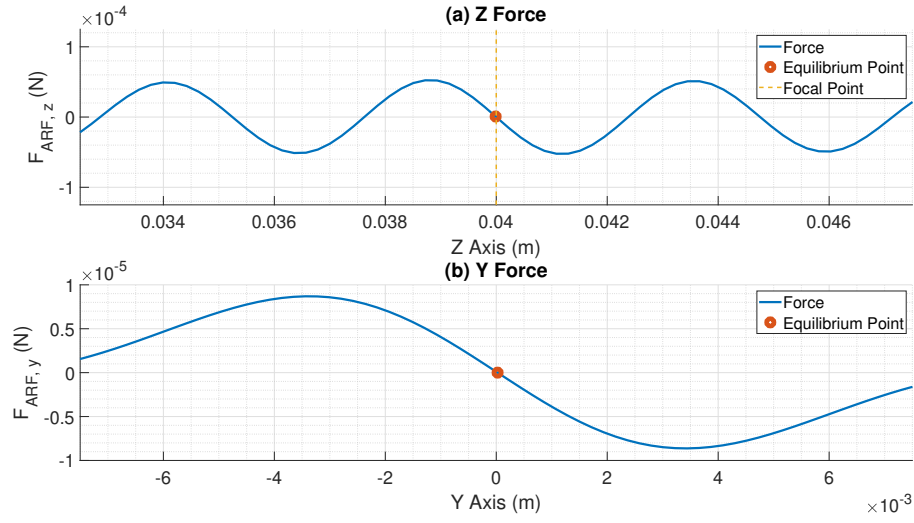


FIG. 5.2. Acoustic radiation force profile when driven at 18 V. (a) shows the  $z$  axis force, and (b) shows the  $y$  axis force. Reproduced from [28], with the permission of IEEE.

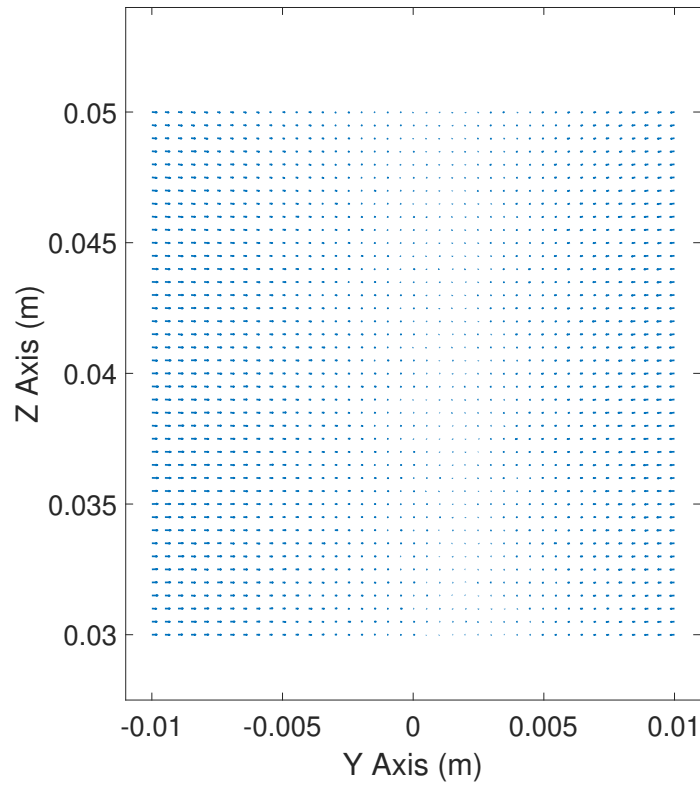


FIG. 5.3. Quiver plot showing the relative position of the equilibrium point from the corresponding focal point in numerical simulation. As the particle reaches the either side of the acoustic levitator, the equilibrium point shifts inwards but the position of the focal point approximates the position of the particle in numerical simulation. Scale of quiver plot is 1:1 with the  $x$ -axis and  $y$ -axis of the graph. Reproduced from [28], with the permission of IEEE.

### 5.2.1 Experimental Observation of Equilibrium Points

The experimental equilibrium points were determined using the particle tracking system as described in § 3.3. Specifically, a PointGrey camera (PointGrey Chameleon 3, with an SV-5014H lens) was used, and the experimentally obtained results of equilibrium point shifts are as shown in Fig. 5.4. The surveyed area is  $\pm 1$  cm from the centre of the acoustic levitator, i.e.  $(0, 0.04)$  m with an increment of 0.5 mm both in  $y$  and  $z$  axis (total of 1681 survey points). The experiment was repeated three times to obtain the average value. The duration of the experiment is approximately 2 hours, and the equilibrium point field obtained from the experiment is considered to be valid as long as the configuration of the experiment has not been changed.”. The deviation of the equilibrium points is more significant than predicted

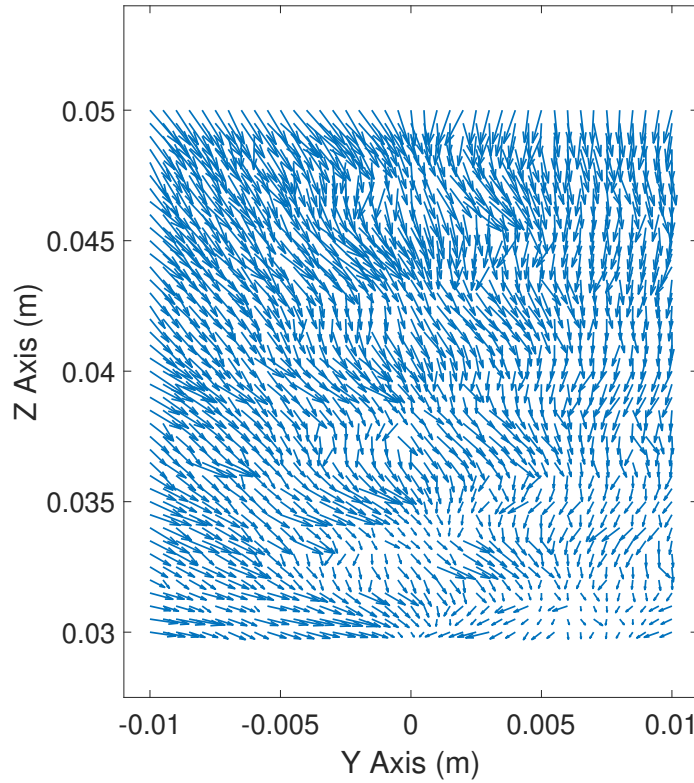


FIG. 5.4. Quiver plot showing the relative position of the equilibrium point from the corresponding focal point in experiment. Scale of quiver plot is 1:1 with the  $x$ -axis and  $y$ -axis of the graph. Reproduced from [28], with the permission of IEEE.

by the numerical simulation and the RMS value between the focal points, and equilibrium points is 0.57 mm and 0.83 mm in  $y$  and  $z$ , respectively. It can be seen that both the direction and magnitude of the experimentally measured deviation varies spatially. This equilibrium point shift is a repeatable phenomenon; not caused by random vibration or air current, and the global standard deviation in the raw equilibrium point is 0.17 and 0.02 mm in  $y$  and  $z$  axis, respectively. Given that the minimum RMS error is 0.57 mm; the grid increment of 0.5 mm may be considered as the coarsest grid increments possible, however, further testing is required to test how coarse the grid increments can be. On the other hand, it is possible to



only take one measurement of the field (and not take average) to reduce the survey time and achieve reasonable measurement of the equilibrium point field.

### 5.3 Exploring Causes of Static Deviation in Experimental System

The deviation of equilibrium point from the focal point is not unique to this particular setup of acoustic levitator, and multiple authors have reported the occurrences of the static deviation in their acoustic levitators. One of the earliest records of the inaccuracy of the positioning of a levitated particle was reported by Seah et al. [177] who identified that when a particle was moved around in a circular orbit, it settles to repeatable but offset position (average positional error of  $\pm 0.43$  mm). More recently, Prisbrey & Raeymaekers reported similar particle position inaccuracies when a particle is manipulated by a single-axis PAL (the maximum pattern error was 31.3% of the wavelength (approx. 2.71 mm, given  $\lambda = 8.65$  mm)) [22]. Moreover, Inoue et al. reported the inaccuracy of the particle positioning in single-axis PAL with sphere larger than wavelength [38].

Whilst, the existence of the equilibrium point shifts were known in the field, the significance of the static deviation of equilibrium points throughout the working volume has not been demonstrated. The exact cause of these deviations has not yet been identified and remains as an open problem. Previous studies suggest scattering from the transducers surface, temperature variations, nonlinear acoustics effects, inaccuracies in the positions of the transducers' as well as manufacturing variations between the transducer as potential contributing factors. The scattering from the transducer surfaces was considered to be the most prominent cause of the deviation of the equilibrium points. This is due to the fact that the transducer surfaces are facing each other and reflected wave could re-vibrate inside the acoustic levitator. In order to test this hypothesis, the implementation of the reflections from the transducer surfaces will be attempted to identify whether the cause of the static equilibrium point can be attributed to the reflections from the nearby surfaces.

#### 5.3.1 Scattering from Transducer Surfaces

In order to determine the effects of the scattering from the transducer surfaces, a numerical simulation was developed, based on model as described in § 3.4.1. Modelling the surface of the Murata transducer, as shown in Fig. 5.5 is a challenging task. There is a spider-web shaped mesh with thickness of approximately 1 mm on the surface of the transducer, and there is a hollow space between the mesh and the piezoelectric material. Acoustic waves can scatter from any part of the transducer, and waves could be expected to exist and interact with the levitation. Modelling such scatter in finite element analysis simulation is difficult and time-consuming; thus, the transducer surface was assumed to be a simple flat surface. This was achieved by modelling the acoustic field as shown in the schematic in FIG 5.6 (a). As an example of the process, the scattered pressure field from the lower phased array will be considered. The lower phased array will emit acoustic pressure waves from the bottom of the region marked by 'Acoustic Levitator' towards to top side of the levitator. It is then

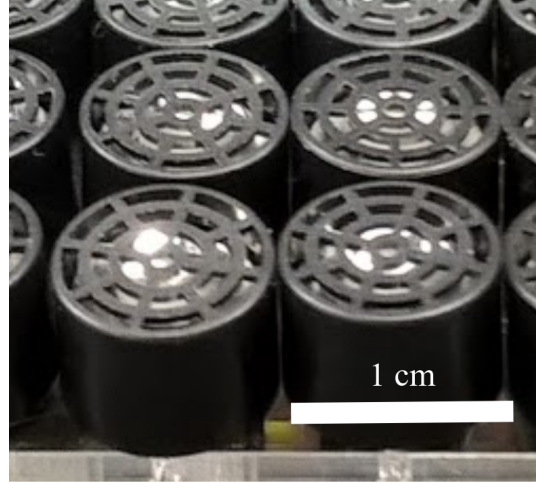


FIG. 5.5. The surface of Murata transducer. The surface has a spider-web shaped mesh, and cone shaped resonator and piezoelectric transducer is housed inside the transducer.

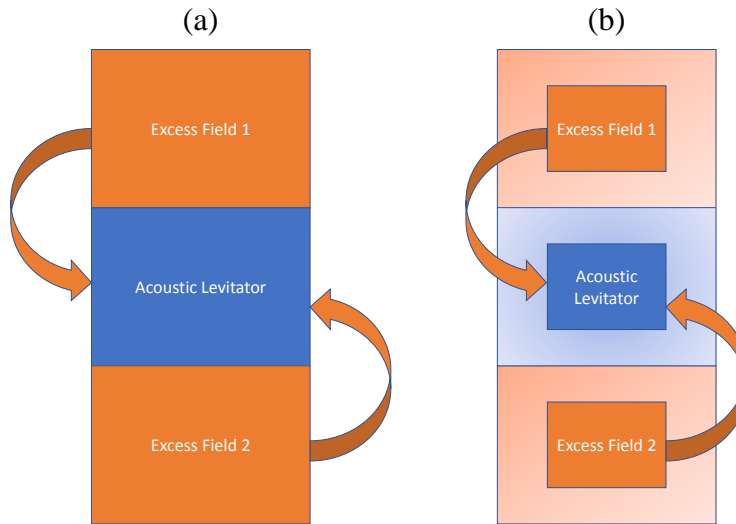


FIG. 5.6. Schematic showing the principle behind simulation of scattering effect from the transducer surfaces. (a) Numerical simulation is formulated such that for the lower phased array the regions marked by 'Acoustic Levitator' and 'Excess Field 1' was calculated, and for lower phased array the regions marked by 'Acoustic Levitator' and 'Excess Field 2' was calculated. (b) It is memory intensive to evaluate all of the regions at the same time, therefore, region of interest was applied to reduce the load on memory.

assumed that for the acoustic pressure wave will surpass the upper phased array, and continue travelling in the region marked by 'Excess Field 1'. This 'Excess Field 1' is then flipped and summed with the 'Acoustic Levitator' region and emulates the effect of the perfectly reflected wave under the assumption of Huygens' Principle. This process was repeated for the all transducers in the phased array. Whilst it is possible to implement Fig. 5.6 (a) in the numerical simulation, it uses an extensive amount of memory in the computer. Therefore, the region of interest ( $\pm 3$  mm from the focal point in  $x$ ,  $y$  and  $z$ ) was applied as shown in Fig. 5.6 (b).

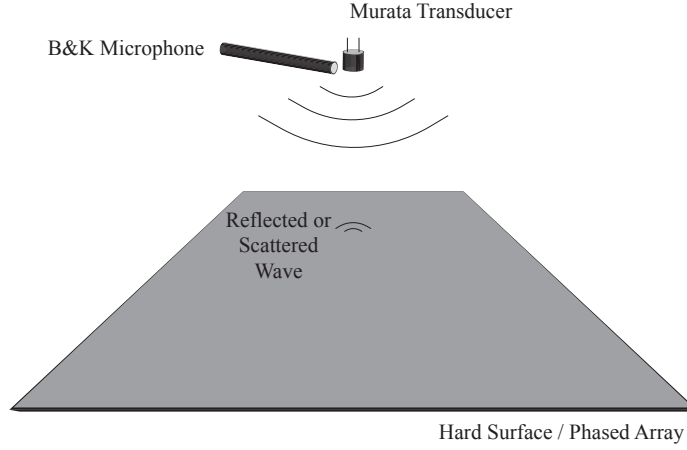


FIG. 5.7. Schematic showing the experimental apparatus for measuring the reflective coefficient of the phased array surface. The Murata transducer faces towards the hard surface, and B&K microphone was set up directly next to the transducer. The transducer was activated by a pulse from the signal generator, and the audio signal from microphone was recorded on an oscilloscope. The distance between the transducer/microphone to surface is 25 cm, and the speed of sound was  $343 \text{ m s}^{-1}$ .

In order to simulate the scattering surface, the reflection coefficient of the phased array surface needed to be identified. Therefore, a microphone was set up as shown in the Fig. 5.7. The transducer was used to emit a pulse of 40 kHz using a signal generator (Agilent 33220A 20 MHz function / Arbitrary Waveform Generator) and was set up such that it faces a surface. The microphone signal and the generated pulse was recorded using an oscilloscope (KEYSIGHT InfiniVision DSOX2024A), and the recorded signal was exported to a PC. The recording sequence was triggered using the trigger signal from the signal generator when the pulse was sent to the transducer, and the microphone and the transducer were 25 cm away from the surface.

The experiment was conducted twice using two different surfaces, a hard scattering surface (perspex sheet), and a phased array transducer surface on Fig. 5.5. The transducer surface in Fig. 5.5 is from the 8x8 single-sided acoustic levitator with a flat surface, as shown in Fig. 3.1 (c). This surface was utilised as the access to the transducer surface on the single-axis acoustic levitator with 60 transducers were limited (the propagation field is not free-space) and secondary scattering from other surface was undesirable. The result is as shown in Fig. 5.8, and the signal of interest is the scattered acoustic signal at 2-2.5 ms from the microphone. The maximum amplitude of the signal was taken from the audio signals with hard scattering surface (perspex),  $A_{per}$  and transducer array,  $A_t$ . The reflection coefficient of the transducer array is then:

$$R_{coef} = \frac{A_t}{A_{per}} = 0.348 \quad (5.3)$$

The empirically obtained reflection coefficient value is then fed into the numerical simulation of Fig. 5.6. The reflection wave from the transducer surface was treated as another input

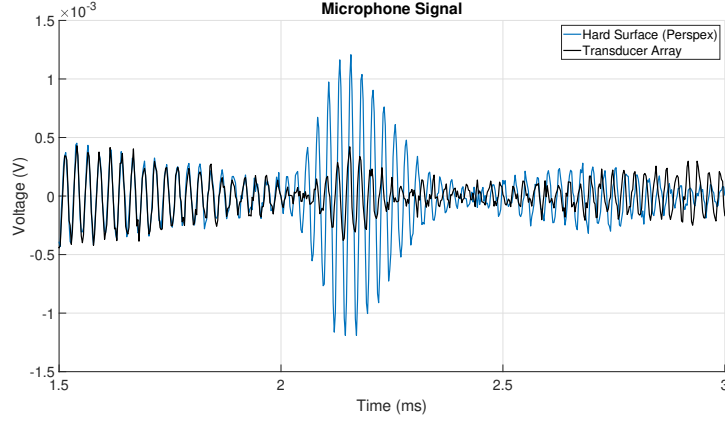


FIG. 5.8. The signals as recorded by the oscilloscope. The top graph shows the input pulse into the transducer, and the bottom graph shows the recording of the signals from microphone. The signal between 0.5 and 1.5 ms is the emitted audio signal from the transducer, and the signal between 2 and 2.5 ms is the reflected echo from the surface.

pressure field in the Gor'kov potential and the superimposed fields were utilised to calculate the acoustic radiation force. The static equilibrium point with the reflection coefficient included is as shown in Fig. 5.9. By the inclusion of the reflection from the transducer arrays, the equilibrium point shifts around in the space, beginning to resemble the equilibrium point shifts from the experimentally obtained results (Fig. 5.4). However, the direction of the shifts are ordered and the magnitude of movement do not match that of the experimental results. Therefore, whilst the inclusion of the reflection does hint the cause of static deviation: the simple flat-surface reflection modelled here does not fully explain the cause of the static

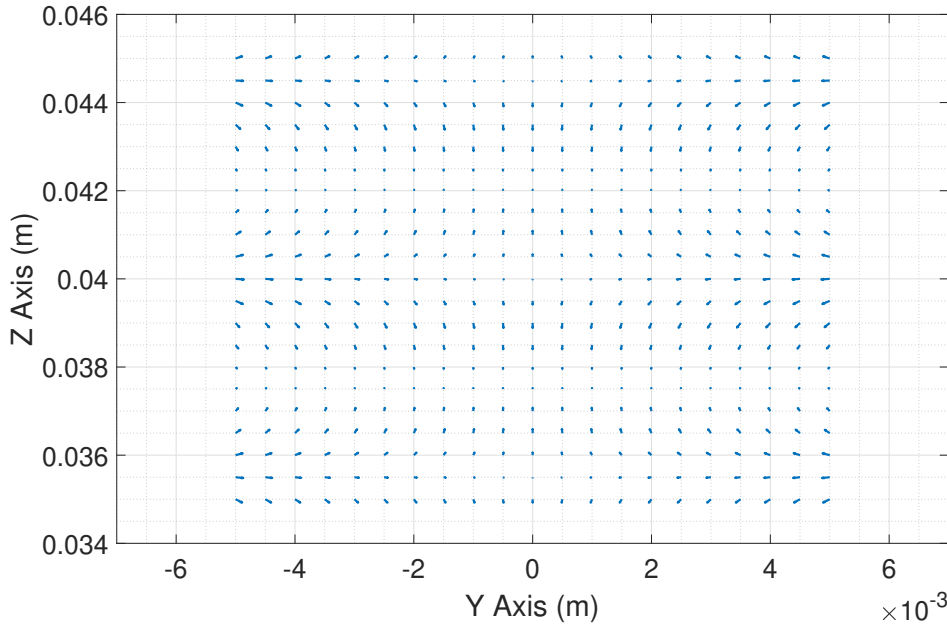


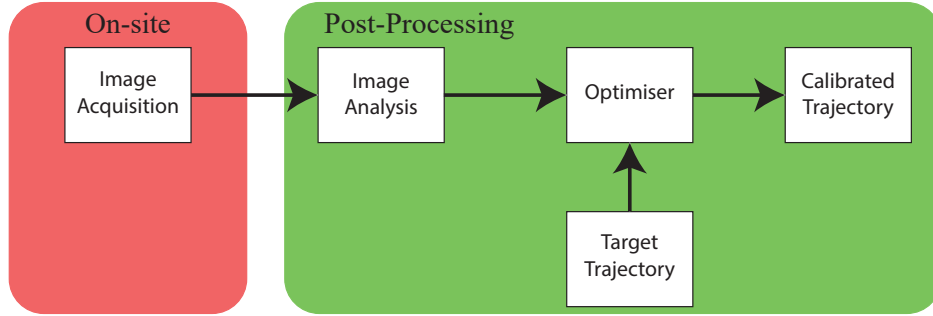
FIG. 5.9. Numerically predicted equilibrium points with the reflective coefficients included. The equilibrium points becomes shifted, but the shift is ordered and symmetrical around the axis. Scale of quiver plot is 1:1 with the  $x$ -axis and  $y$ -axis of the graph.

deviation.

The reflective surface scattering model can be improved further by using the matrix method as demonstrated by Andrade et al. [75, 178]. The region of the reflectors can be defined with better resolution, and angle-dependent terms could be implemented by modifying the matrix method. However, adding further complexity to the numerical simulation is likely to decrease the computational efficiency. Further investigation into temperature variations, nonlinear acoustic effects (e.g. generation of higher harmonics from strong acoustic pressure field [151]) may yield explanation into the cause of static deviation and it can be achieved by implementing computational fluid dynamics simulation which can consider thermo-viscous effect or nonlinear acoustics. However, such study is beyond the scope of this work.

## 5.4 Static Trajectory Calibration Approach

(a) Offline Trajectory Calibration



(b) Online Trajectory Calibration

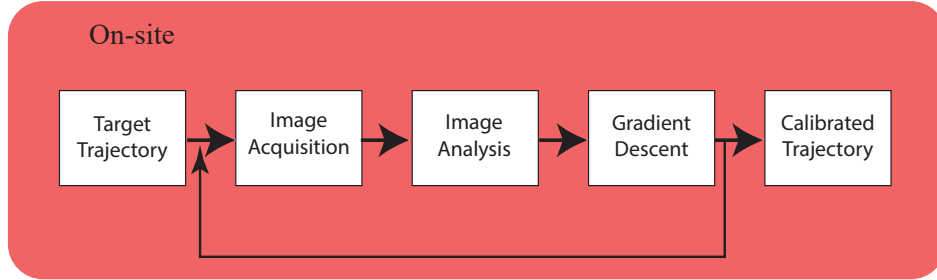


FIG. 5.10. The comparison of the work flows in offline and online trajectory calibration scheme. (a) Offline trajectory calibration scheme processes the images off-site and applies the trajectory calibration as post processing, whilst (b) Online trajectory calibration scheme analyses the images on-site and fed back into the calibration loop. The on-site refers to processes performed during the experiment, and off-site refers to processes performed after the experiments.

Therefore, a method of obtaining an accurate trajectory using the experimentally obtained equilibrium points was devised to adjust the focal points of the model such that the equilibrium points are where it is expected to be and bypass the need to model the effects accurately. This method of using experimental equilibrium points to improve the trajectory was initially proposed by Seah et al. [177], but here, we demonstrate the method of calibrating the trajectory, both in online and offline using the experimentally obtained equilibrium points. The

difference between the online and offline trajectory calibration process lies in where the calibration scheme is applied, as shown in Fig. 5.10. The offline trajectory calibration algorithm allows the user to calibrate trajectory for various cases from one recording; however, equilibrium points need to be recorded at each point in the working volume. Therefore, it becomes impractical when the particle is displaced in a wide range ( $\pm 3$  cm) or when the particle is moved in three-dimensional space. The online calibration was developed to calibrate the trajectory during the experiment, such that the recording of the large working volume is not required.

##### 5.4.1 Offline Trajectory Calibration (2D)

The offline trajectory calibration is based on the experimentally obtained equilibrium position data, as shown in Fig. 5.4. In order to achieve target position at each point of the trajectory, the new calibrated focal points were found by minimising:

$$\arg \min_{\{\mathbf{x}_T, \mathbf{x}_e\} \in \mathcal{R}} |\mathbf{x}_T - \mathbf{x}_e| \quad (5.4)$$

where  $\mathbf{x}_T = (y_T, z_T)$  is the target position and  $\mathbf{x}_e = (y_e, z_e) = F(\mathbf{x}_f)$  is the equilibrium position. Equilibrium points are functions of the focal points,  $\mathbf{x}_f = (y_f, z_f)$ . Using the focal points as the initial guess, the equilibrium points for the given focal points were interpolated (spline) from experimental data, and the optimisation function was evaluated for each set of focal points. The calibration algorithm used nonlinear optimiser, ‘fmincon’ on MATLAB to find the suitable set of focal points where its equilibrium points are close to the target particle position and the process was repeated for each step of the trajectory. As highlighted in Fig. 5.10 (a), the advantage of using this offline trajectory calibration is that once the equilibrium point field is surveyed experimentally, the trajectory of any shape can be calibrated as long as the particle stays within the surveyed volume.

The effectiveness of the offline calibrator was evaluated by setting the particle to follow a circular trajectory, as shown in Fig. 5.11. In each point of the trajectory, the equilibrium points were recorded after allowing the particle to settle (waiting time = 2 seconds). Without any calibration, the particle position is offset both in the horizontal ( $y$ ) and vertical ( $z$ ) directions and the trajectory is not circular. The RMS between target position and particle position is as shown in Fig. 5.11 b) and c), and it is 0.51 and 0.79 mm in  $y$  and  $z$ , respectively. Alternatively, the maximum pattern error of the path ( $E_{pat}$ , mean distance between the user specified and experimentally obtained particle locations, normalized by the wavelength of the field  $\lambda = 8.6$  mm as defined in [22]) is  $E_{pat} = 17.3\%$ . The blue dots in Fig. 5.11 show the particle position after the application of the calibration algorithm, which has significantly improved. The RMS value for  $y$  and  $z$  are 0.11 and 0.030 mm, respectively and the maximum  $E_{pat} = 3.4\%$ . The calibration algorithm has reduced the RMS error by 79.0% and 96.3% in  $y$  and  $z$ , respectively or 80.4% for maximum  $E_{pat}$ .

The calibration of the equilibrium points remains effective as long as the focal point movement is slow ( $\approx 1$  cm s<sup>-1</sup>). A camera (NIKON D610) was set up similarly to Fig. 3.7 and the

trajectories in the shape of the letters, ‘I’, ‘E’, ‘U’ and ‘S’ were sent to the levitator, as shown in Fig. 5.12 (a). The camera recorded the trajectory of the particle by setting the exposure time of the camera to 4 seconds. The particle trajectory for the letter shapes without calibration is as shown in Fig. 5.12 (b), and the trajectory after the application of the calibration algorithm is as shown in Fig. 5.12 (c).

### 5.4.2 Online Trajectory Calibration (3D)

The static equilibrium point shifts were also observed not only in the  $y$ - $z$  plane but also in the  $x$ - $z$  plane. As discussed above, applying the same offline trajectory calibration scheme to three-dimensional space is time-consuming. Therefore, an online trajectory calibration scheme was developed to analyse the particle position on the spot and determine the suitable sets of the focal point that achieves the target trajectory during the experiment.

#### 3D camera setup

The 3D camera was established by adding another camera assembly orthogonal to the  $y$ - $z$  plane camera in Fig. 3.9. The set up is as demonstrated in Fig. 5.13, and an additional LED backlight with diffuser was placed accordingly behind the acoustic levitator. The accuracy of the 3D camera was confirmed using the CMM-stylus holder and grid pattern, as shown in Fig. C.1. The grid pattern consists of 9 imprints of the base of the CMM-stylus holder in Fig. 3.11, and was displaced by  $\pm 1$  cm in both  $x$  and  $y$  directions. Instead of the CMM-stylus, a steel ball with a radius of 7 mm was balanced on top of the CMM-stylus holder. As the radius of the target is larger, it eases the detection of the change in radius when the sphere was displaced in 3D space. The positioning accuracy in the  $z$  axis was evaluated by attaching

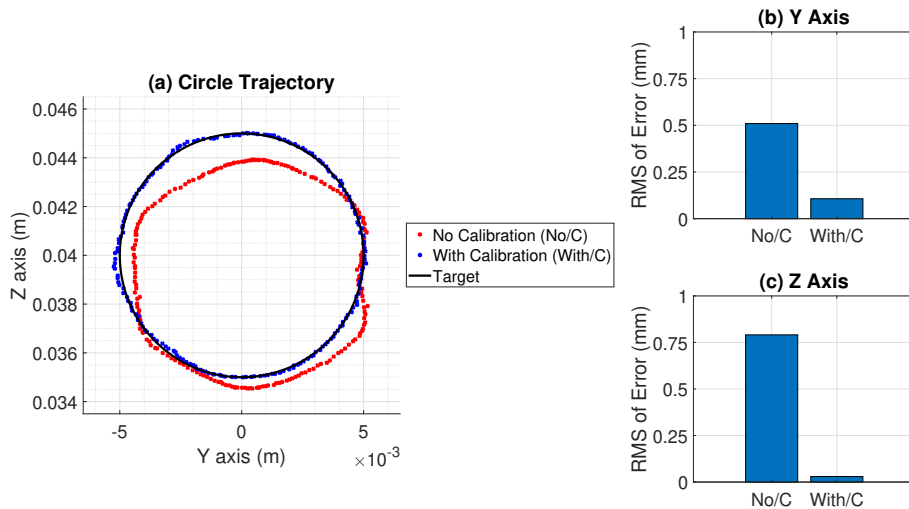


FIG. 5.11. Evaluating the effectiveness of the calibration algorithm. (a) Comparison of the target circle trajectory (black), with calibration (blue dots) and without calibration (red dots). (b) RMS error (difference between target position and equilibrium position) of the path in the  $x$  axis. (c) RMS error of the path in the  $z$  axis. Reproduced from [28], with the permission of IEEE.

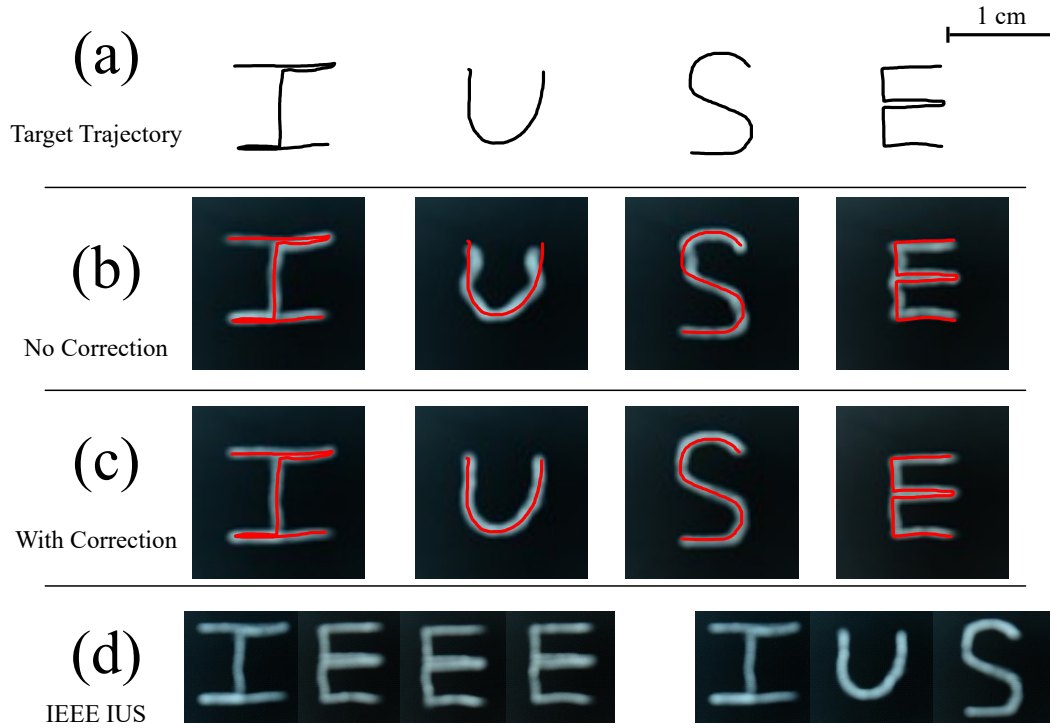


FIG. 5.12. Application of the calibration algorithm on letters trajectory. The position of the target trajectory was normalised against the location of the letter to demonstrate the improvement. (a) Target trajectory in the hand-drawn shape of 'I', 'U', 'S' and 'E'. (b) Trajectory of the particle without calibration. (c) Trajectory of the particle with calibration. (d) Collection of pictures where the particle drew 'IEEE IUS' separately in each instances. Reproduced from [28], with the permission of IEEE.

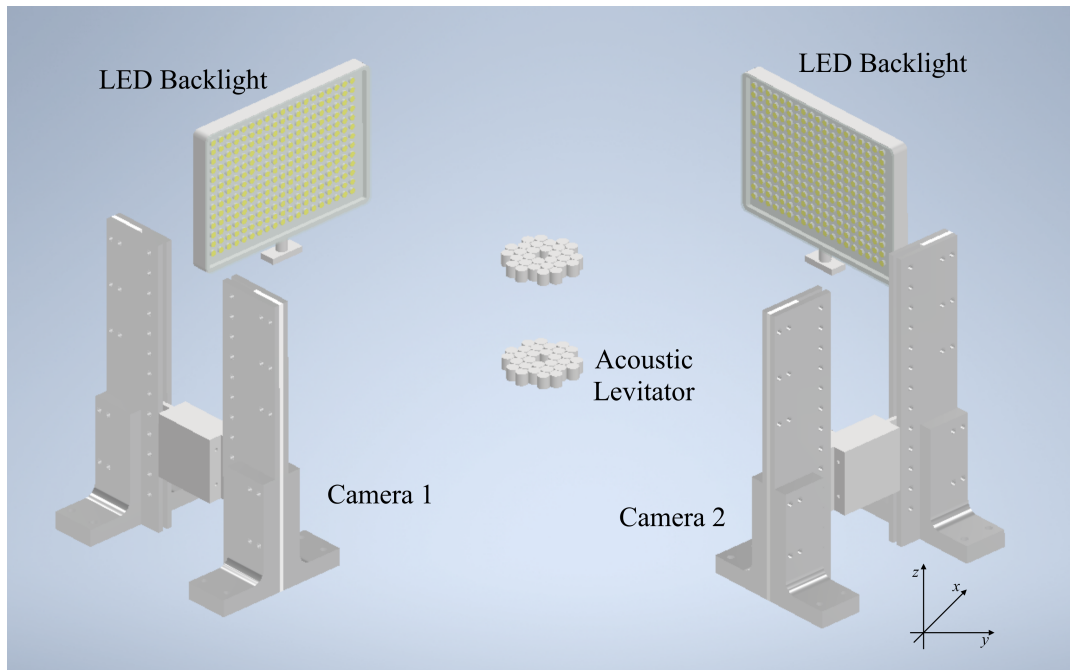


FIG. 5.13. Experimental setup for the measurement of the particle in 3D space. The camera assemblies are orthogonal to each other and was calibrated using the CMM-styli.



or removing the CMM-stylus extender, as shown in Appendix C. Camera 1 recorded the position of the particle in  $x$  axis, and camera 2 recorded the position in  $y$  and  $z$  axis.

The results are as shown in Fig. 5.14 and the camera was calibrated using the radius of the stylus at position number 14, which is the centre of the movement in  $x$ ,  $y$ , and  $z$  directions. Moving the CMM-stylus holder in  $x$  and  $y$  axis causes the radius of the stylus to fluctuate by  $\pm 2\%$  of the radius, the position of the ball is captured accurately within the working volume. The standard deviation of error in  $x$ ,  $y$  and  $z$  axis were 0.24, 0.29, and 0.24 mm, respectively. This method of testing the accuracy of 3D measurement is limited by the ability of the holder to be placed in the correct position; however, it demonstrates that the set up as shown in Fig. 5.13 can determine the particle position in the acoustic levitator with good accuracy and precision without utilising complex algorithms (e.g. data fusion, stereo vision).

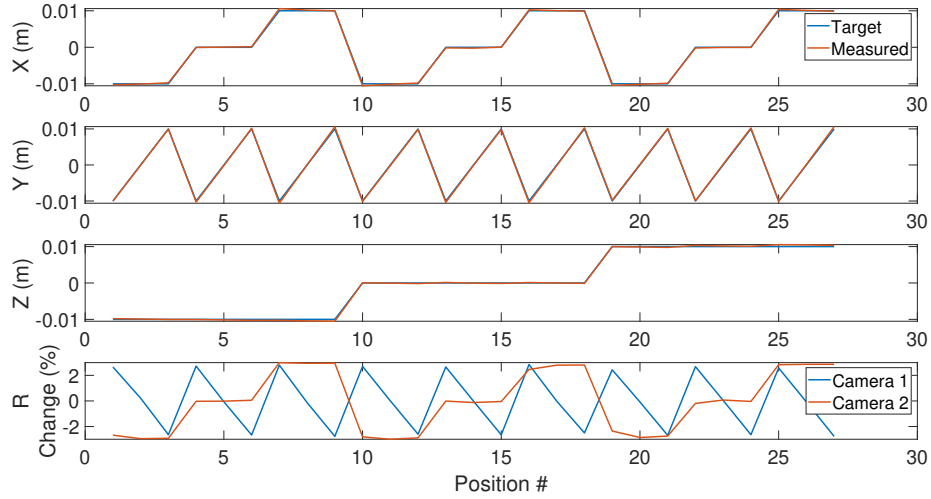


FIG. 5.14. Accuracy of the particle positioning in 3D camera setup as determined by the calibration grid.

### Calibration Algorithm

The online trajectory calibration was formulated using Newton's method:

$$u = \bar{u} + \hat{u} \quad (5.5)$$

where  $u$  is the desired solution,  $\bar{u}$  is the guess and  $\hat{u}$  is the correction term.

$$f(\bar{u} + \hat{u}) \approx f(\bar{u}) + f'(\bar{u})(\hat{u}) \quad (5.6)$$

where  $f$  is the equilibrium point function of focal points  $u$ . However, this does not include the target equilibrium point,  $T$ . The target is to:

$$T - f(\bar{u} + \hat{u}) = 0 \quad (5.7)$$

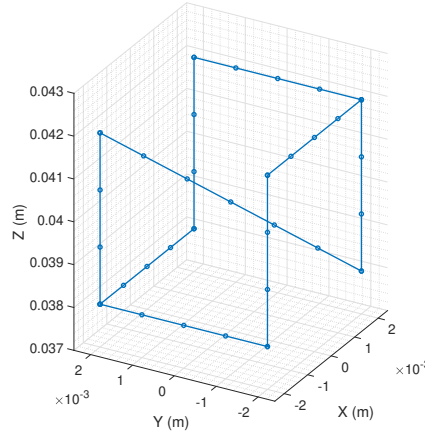


FIG. 5.15. The target trajectory for performance measurement of 3D online calibrator.

Therefore the correction factor needed is then:

$$\hat{u} = -[f'(\bar{u})]^{-1}(T - f(\bar{u})) \quad (5.8)$$

As the  $u$  is a  $1 \times 3$  vector,  $f'(\bar{u})$  is a Jacobian:

$$[f'(\bar{u})]^{-1} = \begin{pmatrix} \frac{\delta x_e}{\delta u_1} & \frac{\delta x_e}{\delta u_2} & \frac{\delta x_e}{\delta u_3} \\ \frac{\delta y_e}{\delta u_1} & \frac{\delta y_e}{\delta u_2} & \frac{\delta y_e}{\delta u_3} \\ \frac{\delta z_e}{\delta u_1} & \frac{\delta z_e}{\delta u_2} & \frac{\delta z_e}{\delta u_3} \end{pmatrix} \quad (5.9)$$

where  $x_e$ ,  $y_e$ , and  $z_e$  are equilibrium point in each Cartesian axis. The gradient e.g.  $\frac{\delta x_e}{\delta u_1}$  was determined by experimentally perturbing the focal point by a small increment,  $h$ :

$$\frac{\delta x_e}{\delta u_1} = \frac{f(x_e + h) - f(x_e - h)}{2h} \quad (5.10)$$

Therefore for each correction step, seven images were recorded to evaluate the correction factor,  $\hat{u}$ . Whilst, single two-point estimation using  $\frac{f(x_e + h) - f(x_e - h)}{h}$  can reduce the number of images taken and therefore the time of calibration; it was found experimentally more stable to utilise symmetric difference quotient method in 5.10. For each step of the trajectory, the calibration was continued until the error between the target trajectory point and the particle position was less than finish criteria. The finish criteria ( $C_f$ ) was based on the pixel to the metre conversion rate of the cameras, and it was set to:

$$C_f = 1.5I_{pix2m}\sqrt{3} \quad (5.11)$$

This value was obtained via process of iteration where a compromise between the accuracy and the duration of the calibration process for each step was made. If the calibrator was found to overshoot the target point by the addition of the correction term, a damping factor of 0.5 was applied to the correction factor to encourage solutions to converge. The improvements of the positioning accuracy gained by the online calibration was measured by repeating a

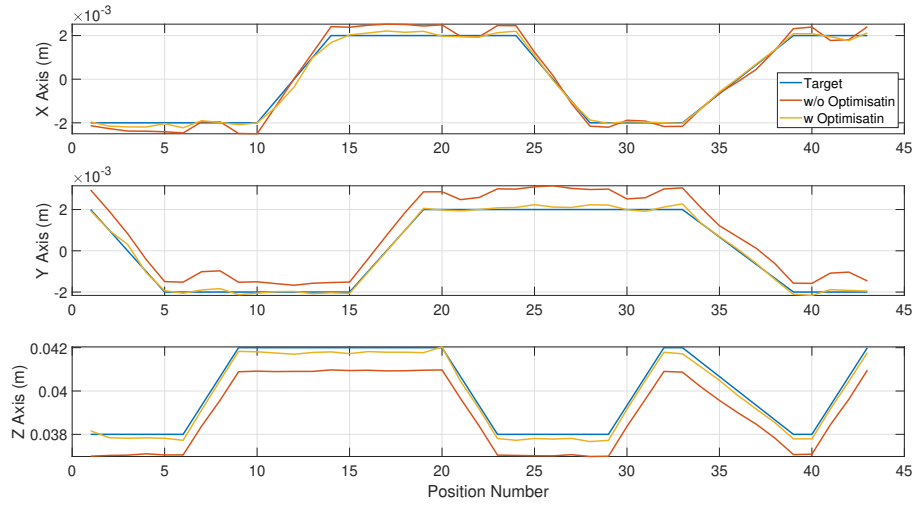


FIG. 5.16. The averaged equilibrium points with and without online calibrator.

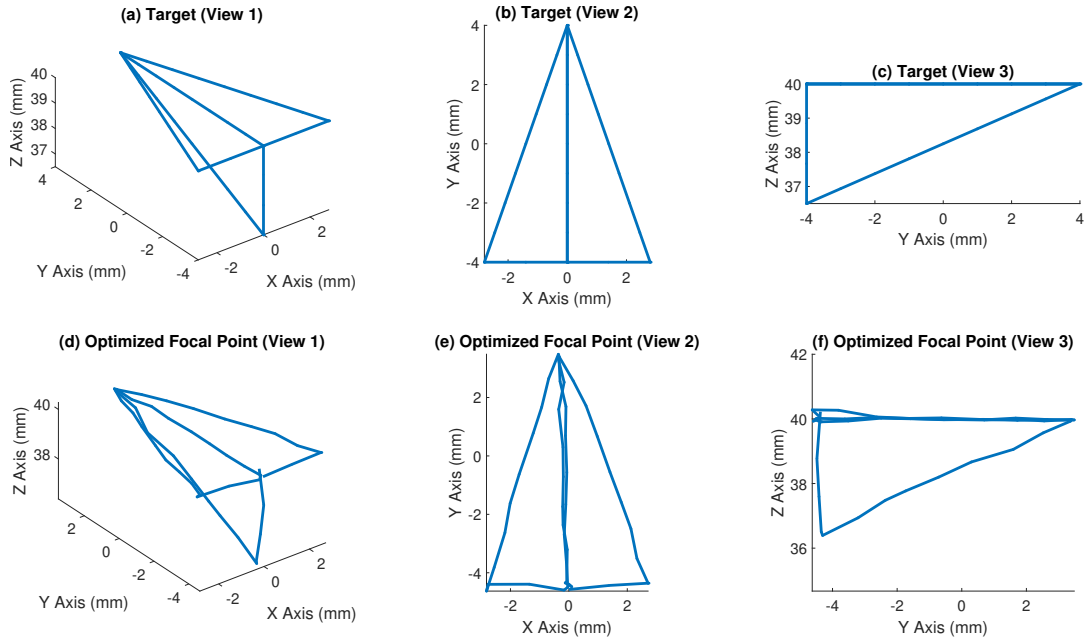


FIG. 5.17. Wireframe Airplane Trajectory of paper plane in 3D. (a) - (c) shows the target trajectory of the wireframe plane as viewed from different angles and (d) - (e) shows the calibrated focal point trajectory. Reproduced from [29], with the permission of AIP Publishing.

similar experiment to Fig. 5.11. A 3D trajectory as shown in Fig. 5.15 was set as the target, and the positioning accuracy was compared before and after the application of calibration algorithm.

The equilibrium position with and without calibration was measured using the 3D camera setup, and three samples were taken for the average. The resultant average equilibrium points for each target points are as shown in Fig. 5.16. The RMS error for trajectory without calibration are 0.309, 0.769, 1.01 mm for  $x$ ,  $y$  and  $z$  axis respectively. On the other hand, the calibrated trajectory has successfully reduced the RMS error down to 0.136, 0.114, and

0.210 in  $x$ ,  $y$  and  $z$  axis respectively. This is an effective reduction of RMS error by 55.9, 85.2, and 79.3 % in  $x$ ,  $y$  and  $z$  axis respectively, and demonstrates the effectiveness of the online calibrator.

The developed calibrator was further tested with a 3D trajectory in the shape of a paper plane, as shown in Fig. 5.17 (a)-(c). The required focal point trajectory to achieve the shape was determined using the online calibrator, and its results are as shown in Fig. 5.17 (d)-(e). A qualitative demonstration of the 3D trajectory will be demonstrated in § 6. If the offline calibrator for in § 5.4.1 was expanded to 3D dimensions, the process of acquiring the equilibrium point will increase polynomially, and is estimated to take longer than 24 hours to collect the data. In comparison, this process of 3D calibration takes about 2 hours to complete, and saves significant amount of time. The online calibration method is advantageous when there is only one trajectory to be outlined, however, if multiple trajectory needs to be calibrated (as in § 6); the offline optimisation may become more advantageous.

## 5.5 Summary

In conclusion, the significance of the static equilibrium point shifts in the acoustic levitators has been demonstrated via experimental determination of the static equilibrium points. A numerical simulation which utilises an empirically obtained reflection coefficient was developed, and whilst the shift was partially attributed to the reflection from the transducer surfaces; it is not sufficient to fully explain the shift. This static equilibrium deviation is reported by multiple authors across the field but its significance throughout the working volume of the acoustic levitator have not yet been reported. Two calibration schemes, which improve the particle trajectory inside the acoustic levitator, were developed. These online and offline trajectory calibration schemes were proposed to suit the dimensions of the trajectory, and each calibration algorithms improve the trajectory using experimental observations. For offline trajectory calibration, it was demonstrated that it can reduce the RMS error from 0.51 and 0.79 mm to 0.11 and 0.03 mm in  $y$  and  $z$  axis respectively, via the application of offline trajectory calibration scheme. As for online calibration, the RMS error was reduced from 0.309, 0.769 and 1.01 mm to 0.136, 0.114 and 0.210 mm in  $x$ ,  $y$  and  $z$  axis respectively. These calibration algorithms are generalised such that they can be applied to different configurations of acoustic levitator and not limited to single-axis PAL. Moreover, they can also be applied in the case where the levitated object is not spherical or where multiple particles are levitated simultaneously. The trajectory calibration for non-spherical object may be more challenging in comparison to the calibration on spherical objects: the orientation of the objects also need to be considered as part of calibration.

Whilst the calibration scheme is effective for a particle travelling at a slow velocity, the inertia of the particle starts to affect the trajectory as the particle is driven at a faster velocity. Previous work in § 4 has demonstrated the complexity of the particle's dynamic behaviour with a small perturbation in a PAL. The combined dynamics, together with unmodelled effects described in this chapter highlights the challenges and complexity of calibrating the

particle trajectory for higher velocities. The effects of increasing velocity on the particle will be further explored in the next chapter where application of acoustic levitator is proposed and its limitation identified.

# Chapter 6 Acoustophoretic Volumetric Display

In this chapter:

- A novel application of acoustic levitation as a free-space volumetric display is introduced.
- The apparatus and setup of the proof-of-concept device is described.
- The two modes of display; vector and raster graphics are demonstrated.
- The static trajectory calibration method was applied to both vector and raster graphics to improve the quality of the rendered image.
- Unwanted horizontal movement of the particle was observed experimentally when particle was excited in a large amplitude.
- Experimental observation suggested that static deviation was the cause of unwanted horizontal movement.
- A hybrid dynamic model which incorporates the dynamic model from § 4 and experimentally obtained static deviation is developed to quantitatively and qualitatively validate the hypothesis.
- Current limitations in the system are determined, and its solutions proposed.

## 6.1 Introduction

Since the study of radiation pressure by Rayleigh at the beginning of the 20th century [2, 179] acoustic levitation has been utilised in a wide range of applications [15, 23, 97, 108, 117, 154]. As briefly described in the § 5, one of the proposed applications of acoustic levitation in mid-air was the acoustic levitators as a display device. Ochiai et al. showed crosses and uniform 2D grids made out of levitating particles and utilised projector to project images to the grids of particles [72]. Sahoo et al. presented a screen made of levitated dielectric particles that can be flipped individually using an electric field [120]. Uno et al. demonstrated the levitation of an LED to draw images in the air using long exposure shots [121]. Marzo & Drinkwater controlled multiple particles (up to 27) independently to create different 3D shapes [76]. However, these approaches can only render a coarse object in mid-air and it was challenging to increase the spatial resolution of these display.

Recently, Smalley et al. presented the concept of a photophoretic-trap based volumetric display (OTD: Optical Trap Display) [180]. An OTD has significant advantages compared to holograms or light-field displays since it renders images that can be observed from different

angles without clipping [180]. In the OTD, a micrometric particle is held in mid-air and displaced, at high-speed (max  $1.8\text{ ms}^{-1}$ ), by an invisible photophoretic trap, induced with a laser [180, 181]. The levitated particle is simultaneously illuminated by a visible light source, and traces the volumetric image in the working volume. The scattering light from the different position in space forms a visible afterimage for the users. This image can be directly observed without wearing any device and from different perspectives. Hence this demonstrated that a photophoretic-trap based systems could render precise images of centimetre scale in mid-air. However, the OTD has significant disadvantages, such as requiring high-power lasers and providing a limited display volume. Similarly, electrostatic-trap based volumetric displays were demonstrated by Berthelot & Bonod [182]. In this concept, a micrometric charged particle was levitated and moved by a set of electrodes with varying electrostatic charges. This electrostatic trap is not as hazardous as a laser system, but the rendered images were on the scale of a micrometre.

Here, the concept of an acoustophoretic volumetric display is presented. Similarly to Electrostatic [182] and Photophoretic [183] volumetric displays, a levitated particle was displaced rapidly whilst being illuminated to create 3D shapes. However, this holding and displacement of the particle were achieved using acoustic radiation forces (i.e. acoustophoresis). Acoustophoretic traps generated by high frequency ultrasound waves are thought to be safe for humans and there is no agreed standard exposure to ultrasound (particularly at 40 kHz) [184], however there already exists commercial system (such as Ultrahaptics[185] and SonicEnergy [186]) which utilises similar level of pressure amplitude (approximately 150-160 dB) at the focal point). These precedents demonstrate that these ultrasonic devices are appropriate for public use. In addition, ultrasonic levitators are simpler to manufacture (i.e. a simple acoustic levitator can be manufactured from low-cost off-the-shelf components and used at home [21, 150]), and its work space can be as large as half a meter [38, 72].

## 6.2 Volumetric Display

A volumetric display is a device that “permits the generation, absorption, or scattering of visible radiation from a set of localized and specified regions within a physical volume” [187]. A ‘free-space display’ is a type of volumetric display that operates in mid-air and does not have barriers between the user and the images [183].

Fig. 6.1 (a) shows an overview of the acoustophoretic-trap free-space volumetric display developed in this thesis. The volumetric image is constructed by a series of voxels that are created when the particle reaches a particular position at a given time and is illuminated by an RGB LED. Therefore, a 3D graphic is represented as a sequence of particle positions  $((x, y, z))$  and RGB values (represented as an 8-bit signal for each RGB channel). The selected colours and the phase distributions on the phased array required for that instance of time are calculated accordingly and its commands are sent to RGB LED and PAL, respectively. The array-based ultrasonic levitator device is controlled by an FPGA board (ALTERA CoreEp4CE6) which is connected to a PC via UART serial communication (1.5 Mbauds), and

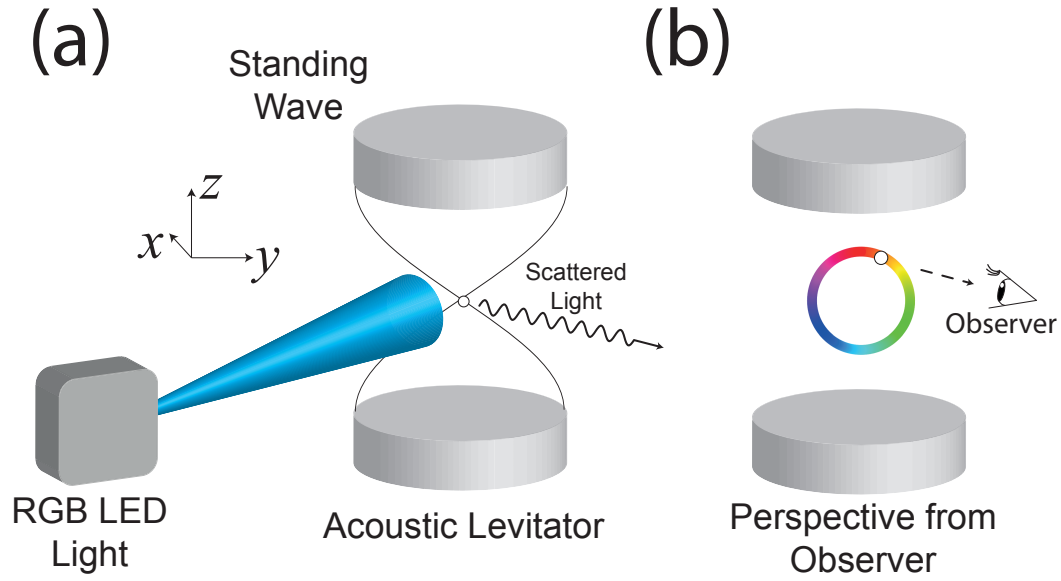


FIG. 6.1. Overall schematics for the proposed Acoustophoretic Volumetric Display (a) Concept diagram showing the experimental setup. (b) The volumetric display as seen by a human observer. Reproduced from [29], with the permission of AIP Publishing.

produces 60 channels of square-waves each controllable with  $\pi/64$  rad phase resolution [21], as described in § 3.2.1. The generated square waves from FPGA board were amplified to 9 volts using MOFSET drivers (TTC4427a) and external DC power supply (RS Pro IPS 303DD). These amplified signals are sent to 60 ultrasonic transducers (Murata MA40S4S) arranged as two opposed arrays, each of 30 transducers. Signals are generated to focus the array at the trap position (see § 3.2.1), and this creates an acoustic trap that a small Expanded Polystyrene (EPS) particle with a diameter of  $\approx 1.5$  mm can be levitated. Particle in variety of size may be levitated inside the levitator, however, the particle needs to be significantly smaller than wavelength for Gor'kov potential to hold true. On the other hand, very small particles ( $< 0.5$  mm) are often swept out of traps [37]. The operational region of the display can be approximated by the size of the employed single-axis acoustic levitator ( $4 \times 5 \times 8$  cm). The RGB LED light was fixed to a holder, and was located on the side of the acoustic levitator. The LED illumination will scatter off the particle and give colour to each voxel of the 3D path graphics. When the particle moves sufficiently fast while it is being illuminated, it generates a continuous 3D path due to the persistence of vision effect, as shown in Fig. 6.1 (b).

### 6.2.1 Illumination of the Particle

In this implementation of an acoustophoretic volumetric display, one RGB LED has been utilised for the illumination and an example of the particle levitated in mid-air with the illumination from the RGB light as shown in Fig. 6.2. The image was taken with DSLR camera (Nikon D610) with approximately same distance from various angles, and the location of



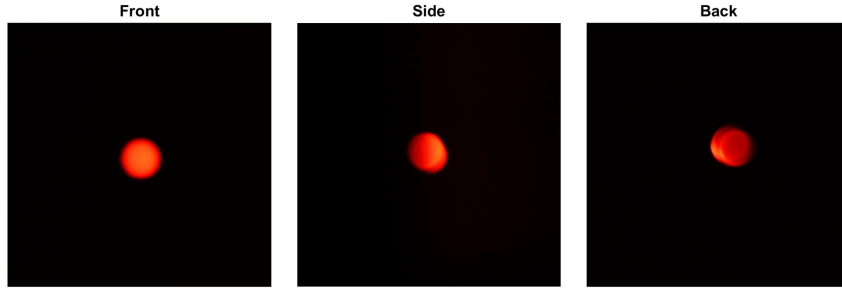


FIG. 6.2. Light Intensity as Observed from Different Angles with DSLR camera. The light intensity of the particle was determined from the RGB value at the centre of the particle, and the change in the light intensity was determined by the change in the viewing angle. The LED is illuminated from the front side. Reproduced from [29], with the permission of AIP Publishing.

LED light source was fixed. The RGB colour values at the centre of the particle was extracted, and the light intensity were calculated by:

$$I = \frac{1}{3}(R + G + B) \quad (6.1)$$

The measured light intensity was 128, 91, and 61 for the front, side and back, respectively. This is a reduction of the light intensity by 71.5 % and 48.0 % for “front to side” and “front to back”, respectively and demonstrates that the display can be viewed from a wide range of angles with one single LED illumination. The visibility from a full 360 degrees can be ensured by increasing the number of light sources around the levitator. Advanced illumination techniques, such as a light source that accurately tracks the position of the particle, may be employed to further improve the contrast and clarity of the displayed image.

### 6.2.2 Generation of Images

The developed acoustophoretic volumetric display was used to display images, and two methods, vector and raster graphics were utilised to render the images in space. The difference between the vector and raster graphics is the significance of the trajectory in the transmission of the visual information. For raster graphics, the display functions similarly to normal computer screens, and the particle will be moved to outline a 2D screen in mid-air. Normal computer screen changes the colour of each pixels to represent different images, and in the volumetric display; the colour of voxel will be changed to transmit different information. On the contrary, in the vector graphics, the trajectory itself is the primary information (e.g. circle, triangle, square) and the colour on the vector graphics is supplementary to the trajectory.

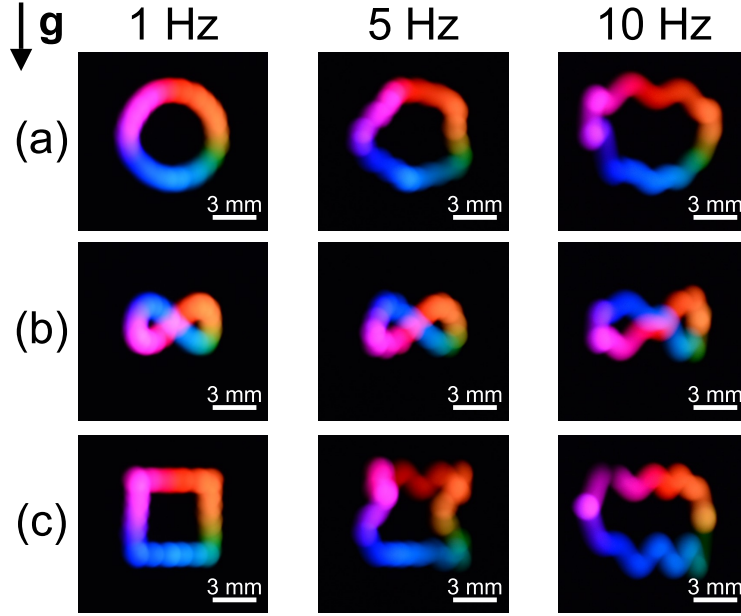


FIG. 6.3. Examples of vector graphics rendered by the proposed system. (a) Circle with a radius of 3 mm, (b) Infinity symbol with a horizontal length of 5 mm, (c) Square with a side length of 5 mm. The rendering (drawing) frequency was gradually increased from 1, 5, to 10 Hz and the exposure time of recording camera for each picture is equal to the rendering frequency. Reproduced from [29], with the permission of AIP Publishing.

### Vector Graphics Generation

Some examples of the vector generated graphics are shown in Fig. 6.3 (a) - (c), in the shape of a circle, infinity symbol, and square. These trajectories were calibrated using the offline 2D calibration method as described in § 5.4.1, and utilised the static equilibrium point to obtain the suitable trajectory. At the lowest frequency (1 Hz) the target shapes are formed as specified via static calibration, however as the frequency increases to 5 and 10 Hz; the image gets deformed. The oscillation in the picture involves relatively slow oscillation (from the trajectory) and unwanted fast oscillation (the particle oscillating in the acoustic trap). Vector graphics with a three-dimensional trajectory was also demonstrated, and the calibrated wire-frame plane trajectory in § 5.4.2 was generated. Fig. 6.4 is the resultant 3D trajectory with the online calibration scheme and qualitatively demonstrates the functioning of the online trajectory calibration. The minimum rendering time of the trajectory for it to be visible by



FIG. 6.4. Rendered 3D vector graphics. (a)-(c) 3D wireframe volumetric image of an paper plane viewed from various angles (rendering time of 5 seconds). Reproduced from [29], with the permission of AIP Publishing.

naked eye is around 10 Hz, and Fig. 6.3 demonstrates that it is possible to render the shape at the required time scale. However, the ability for acoustophoretic volumetric display to render objects in real-time highly depends on the size and complexity of the rendering object.

### Raster Screen Generation Process

#### EPS Particle

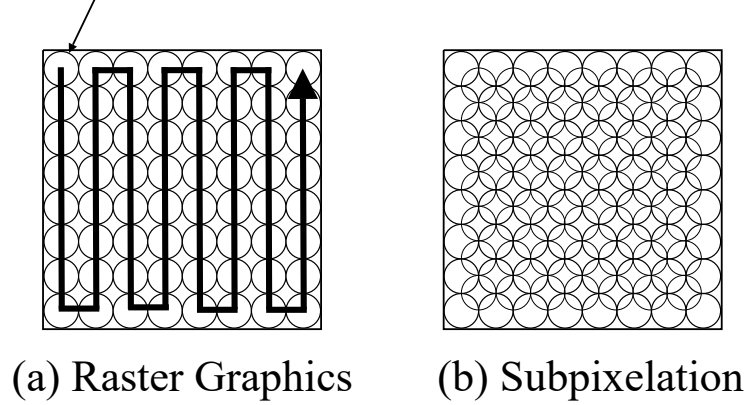


FIG. 6.5. Schematics showing the formulation of a raster screen. (a) An image is split into voxels and one particle will trace the trajectory shown in the arrow. The illuminated light will be varied as the particle changes the position (b) The resolution of the screen is limited by the radius of the circle, and it can be improved by the adding another sets of rows and columns between the original raster graphics trajectory.

In raster screen graphics, the particle is moved to generate a 2D plane of the screen in mid-air. Therefore, the first step of the raster screen-generation was to define the dimensions of the screen, and therefore the screen resolution. For example, if the screen size was set as 24 by 24 mm, the default screen resolution is 34 by 34 voxel, given that the particle was packed in a format as shown in Fig. 6.5 (a) with the radius of the particle being 0.7 mm. The colour information for each voxel can be obtained by using a static image file as an input. Fig. 6.6 shows an example of the image conversion from the static image to voxel position and colour information. Here the resolution of the University of Bristol logo image was reduced to 34 by 34 pixel and each voxel was assigned corresponding colour information. Whilst the conversion scheme works, the visibility of the logo is poor. Therefore, a subpixelation strategy, as demonstrated in Fig. 6.5 (b) was employed. Subpixelation was achieved by layering extra sets of rows and columns between the raster graphics generated for the non-subpixelated images. The colour for each voxel in the subpixelated scheme is determined from the pixel RGB colour from the neighbouring points, and the RMS of each RGB code was taken as demonstrated in Fig. 6.7. The results of conversion scheme with the subpixelation is as shown in Fig. 6.8, and the improvement is clearly visible with the implementation of the subpixelation. The trajectory of the raster screen was calibrated using the 2D offline calibration scheme as described in § 5.4.1 and a DSLR camera (Nikon D610) was setup with a tripod and a remote trigger. A fixed shutter speed was employed for the recording of the image, with the exposure time matching the rendering speed. The results are as shown in Fig. 6.9 (a)-(c). The recorded

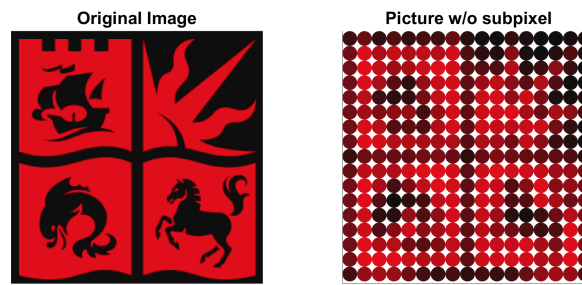


FIG. 6.6. Conversion from still image to volumetric display trajectory. Left image shows the original University of Bristol logo, and right image shows the converted results without subpixelation. Reproduced from [29], with the permission of AIP Publishing.

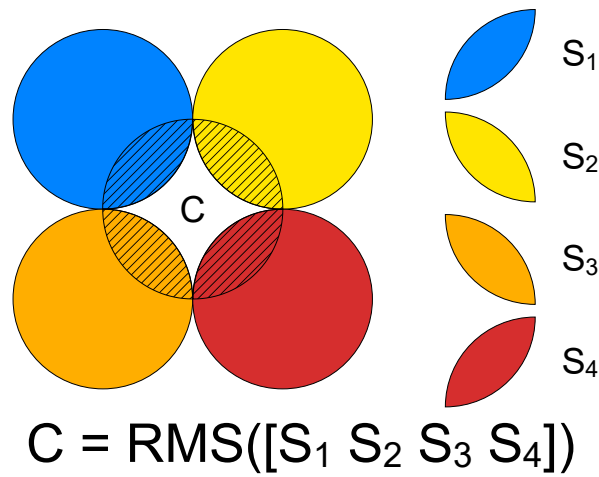


FIG. 6.7. Calculation process for the subpixelated image. When the shaded crossover section is greater than 20 % of the area, the colour from the neighbouring colour will be used to calculate the colour for the pixel, C.

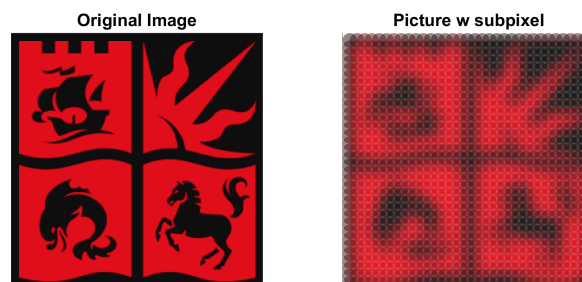


FIG. 6.8. Conversion from still image to volumetric display trajectory. Left image shows the original University of Bristol logo, and right image shows the converted results with subpixelation. Reproduced from [29], with the permission of AIP Publishing.

images are stored as JPG files, and no digital enhancement has been applied to Fig. 6.9 apart from cropping. The dimensions of the images for Fig. 6.9 (a)-(c) are 23.1 by 23.1 mm.

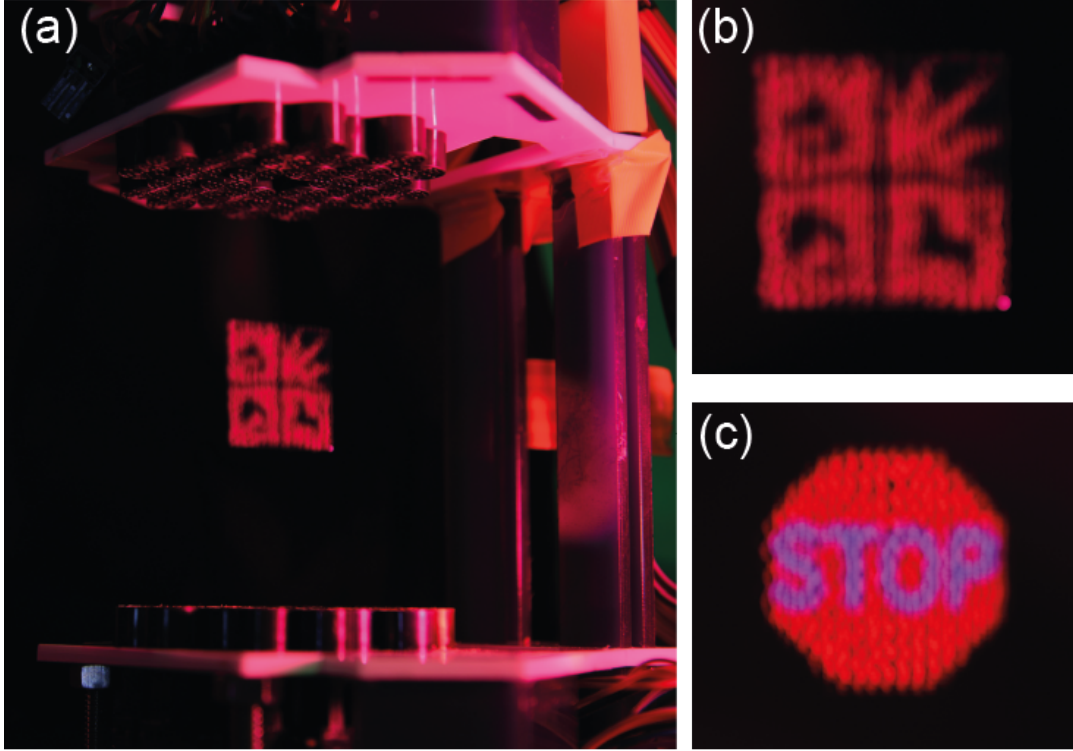


FIG. 6.9. Examples of raster graphics generated by the acoustophoretic display device. (a) Overview of the raster graphics with the acoustic levitator (rendering time  $T_r = 20$  s), (b) zoomed in version of (a) as seen from the front, (c) an example of an image of a stop sign ( $T_r = 20$  s). Reproduced from [29], with the permission of AIP Publishing.

### 6.3 Dynamic Response of Particle in Large Displacement

Although this static calibration significantly increases the image quality [28], the results in Fig. 6.3 demonstrate that this calibration decreases in effectiveness as the speed of the particle increases. Open-loop control or dynamic calibration of the trajectory was considered, however, it is inherently difficult due to the nonlinear dynamics of particles inside an acoustic levitator, as demonstrated in § 4. The distance travelled by the particle is significantly larger than dynamics studied at the scale of § 4, and therefore, the dynamic response of the levitated particle was investigated again.

To characterise the dynamics of the particle in the display with large displacement, the focal point was oscillated vertically along the  $z$ -axis with varying amplitude in the range of  $0.5 \text{ mm} \leq A_{in} \leq 10 \text{ mm}$  with an increment of  $0.5 \text{ mm}$  and a frequency ranging from  $2$  to  $35 \text{ Hz}$  with increments of  $1.0 \text{ Hz}$ . The oscillation frequency of the trap was increased gradually before maintaining a constant frequency for  $10$  seconds to take steady-state measurements. At each frequency step, the particle motion was recorded at  $150 \text{ FPS}$  using the same experimental setup as for the static equilibrium point experiment in § 5. This frame rate was considered sufficient for experiment as the frame rate is five times larger than the highest oscillation frequency ( $30 \text{ Hz}$ ); beyond the Nyquist frequency. The footage of the particle movement was analysed using MATLAB Image Processing Toolbox, and the particle's centre coordinates were extracted using the Hough Circle Transform.

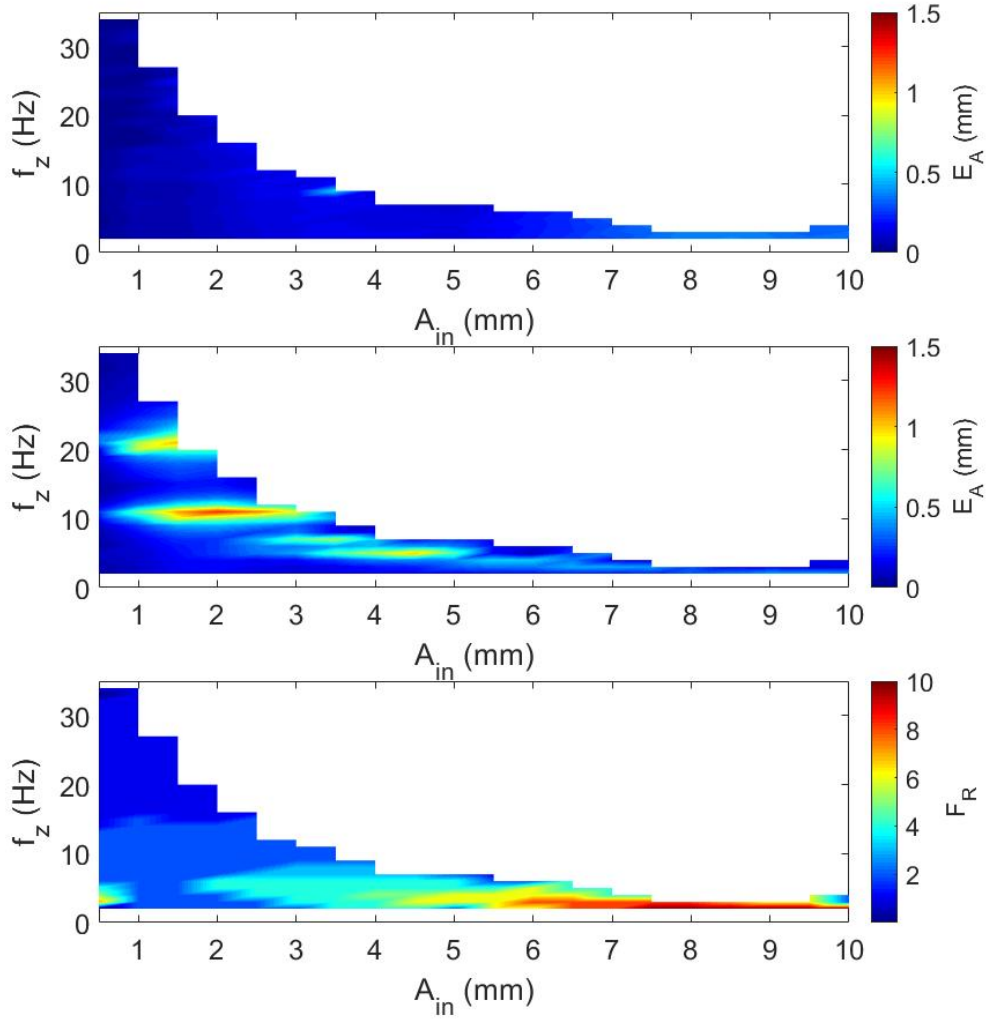


FIG. 6.10. The experimental results showing the particle response by vertical focal point oscillation (with different amplitude and frequency of trap oscillation). (a) shows the experimental  $z$ -axis error, in terms of the absolute difference between the oscillation amplitude of the trap and response amplitude of the particle ( $E_A$ ), (b) shows the experimental  $y$ -axis oscillation, (c) shows the ratio between the  $y$ -axis response frequency and the  $z$ -axis input frequency ( $F_R$ ). Reproduced from [29], with the permission of AIP Publishing.

The amplitude and frequency were then extracted in post-processing using the methods described in § 3 and experimental results are shown in Fig. 6.10 (a)-(c), represented in terms of the  $z$ - and  $y$ -axis amplitude error and  $y$ -axis frequency ratio ( $F_R = f_P/f_z$ , where  $f_P$  is the principal frequency of oscillation in the  $y$ -direction, identified via DFT analysis, and  $f_z$  is the input  $z$  axis oscillation frequency). This frequency ratio visualises the shift in the frequency of oscillation in response to the amplitude of oscillation. The amplitude error is the absolute difference between the oscillation amplitude of the trap and the response amplitude:

$$E_A = |A_{in} - A_{out}| \quad (6.2)$$

where  $A_{out}$  is the response amplitude of the response particle oscillation.

From Fig. 6.10 (a), it is clear that when the trap is oscillated at an amplitude ( $A_{in}$ ), the response amplitude of the particle closely matches. This is because the oscillation frequency has not yet reached the resonant frequency of the particle in trap (the resonance frequency is  $> 30$  Hz when the driving voltage is 9 V). The maximum acceleration value observed in the  $z$  axis in Fig. 6.10 (a) was  $30.0\text{ms}^{-2}$ , and the maximum velocity observed in the PAL was  $0.67\text{ms}^{-1}$ . On the other hand, Fig. 6.10 (b) shows that there are significant horizontal oscillations in the  $y$  axis around  $A_{in} = 2$  mm with 10 and 20 Hz.

### 6.3.1 Dynamic Modelling

These above occurrence of unwanted horizontal ( $y$ -axis) movement when the trap is moved vertically is not desirable for the purpose of volumetric display, as it makes the particle move diagonally in space. Thus, this horizontal movement needs to be eliminated to achieve a high fidelity acoustophoretic display. In order to identify the source of the off-axis movement of the particle in the experiment, the 1-D dynamic model from § 4 was extended to 2D to predict the dynamic response of the particle. Here, the formulation was expanded to predict particle movement in  $y$ - $z$  plane in Fig. 6.10, assuming that the oscillation in  $x$  axis is negligible is and the state space representation of the dynamic response is:

$$\begin{pmatrix} \dot{y}_1 \\ \dot{y}_2 \\ \dot{z}_1 \\ \dot{z}_2 \end{pmatrix} = \begin{pmatrix} y_2 \\ \frac{1}{m}(F_{rad,y} + F_{drag,y}) \\ z_2 \\ \frac{1}{m}(F_{rad,z} + F_{drag,z} + F_{grav}) \end{pmatrix} \quad (6.3)$$

where  $y_1 = y$ ,  $y_2 = \dot{y}$ ,  $z_1 = z$ , and  $z_2 = \dot{z}$ . Instead of utilising the sinusoidal approximation, as in § 4; the acoustic radiation force profile in 2D field ( $y$  and  $z$ ) was approximated as a polynomial function in the form using the data from the Huygens' principle numerical simulation from § 3.4:

$$F_{rad} = f_n(y, z, f_z) = \sum_{n=1}^N \alpha_n (y - y_{off})^{A_{1,n}} (z - z_{off})^{A_{2,n}} (f_z - f_{z,off})^{A_{3,n}} \quad (6.4)$$

where  $A$  is every combination of polynomial orders for 3 variables from 0 to 13 for  $y$  and  $z$  axis and 0 to 12 for  $f_z$ .  $A$  has a size of 559 by 3, and therefore there are 559  $\alpha_n$  coefficients.  $y_{off}$  and  $z_{off}$  were normalising constants representing the focal points and they were 0 and 0.04, respectively. The coefficients are found by matrix operation:

$$\alpha_n = [y^{A_{1,n}} z^{A_{2,n}} f_z^{A_{3,n}}]^{-1} F_{rad} \quad (6.5)$$

As fitting through these data consumes a lot of computer memory, the coordinates are limited by windowing  $\pm 2$  mm and  $\pm 3.5$  mm around the focal point for  $y$  and  $z$  respectively. For this step of the calculation, a large memory node (256 GB) of high computational capabilities at the University of Bristol was used for the calculation.

Similarly to § 4, the drag force was calculated by:

$$F_d = C_d \frac{\pi}{4} d^2 \frac{1}{2} \rho u^2 \quad (6.6)$$

where  $d$  is the diameter of the particle and  $u$  is velocity. The coefficient of drag is approximated by using Flemmer & Banks [162] which is valid for a Reynolds number below  $3 \times 10^5$ :

$$C_d = \frac{24}{Re} 10^E \quad (6.7)$$

where  $E = 0.261\text{Re}^{0.369} - 0.105\text{Re}^{0.431} - \frac{0.124}{1+(\log_{10}(\text{Re}))^2}$ . In the preliminary test, it was identified that solving Equation 6.3 using ODE45 (explicit Runge-Kutta (4,5) formula) in MATLAB require a high tolerance. Therefore, the usage of ODE45 was no longer suitable. Thus, ODE15s which is based on variable-step, variable-order (VSVO) solver [171] on MATLAB was utilised to solve the equation. The result of the dynamic simulation is as shown in Fig. 6.11 (a)-(b). From the result, the  $z$  axis response is predicted accurately, predicting the input and output amplitude to match with minimal difference, before the resonance peak (similarly to experimental results in Fig. 6.10 (a)). Interestingly, the numerically simulation results in Fig. 6.11 (b) does not show the experimentally observed off axis movement in  $y$  direction as observed in Fig. 6.10 (b).

### 6.3.2 Formulation of Hybrid Model

A hypothesis was formulated that the static equilibrium deviation observed in § 5 is causing the unwanted horizontal movement of the particle when the acoustic trap is oscillated sinusoidally in  $z$ -axis. In the numerical simulation, the acoustic trap is moving purely in the  $z$ -axis, however, the static deviation is causing the particle to sway in horizontal direction as

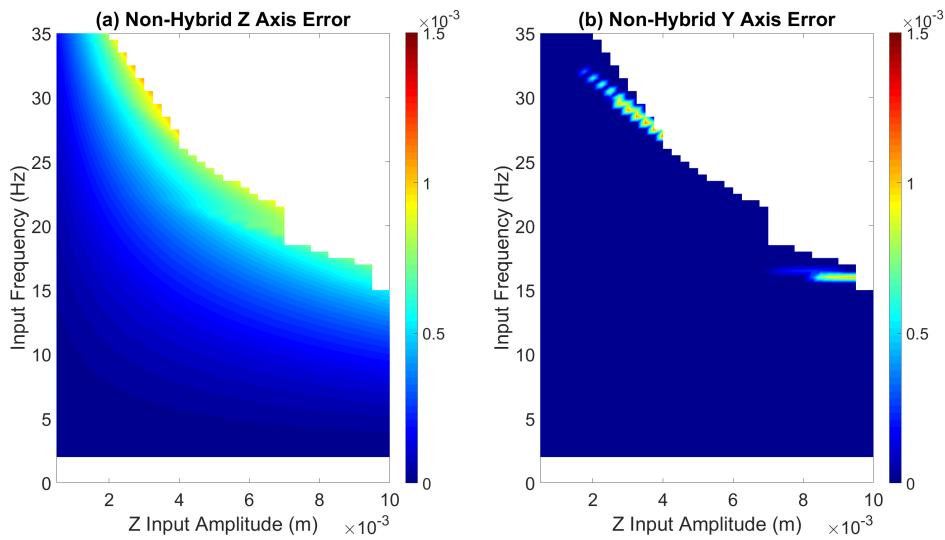


FIG. 6.11. Simulation of the Dynamic Response using a Huygens' Model and the Gor'kov acoustic radiation force model. Reproduced from [29], with the permission of AIP Publishing.



the equilibrium points are shifted from the origin of the  $y$  axis. Therefore, the shift in the equilibrium points were experimentally measured again using the methods in § 5 and the results are as shown in Fig. 6.12.

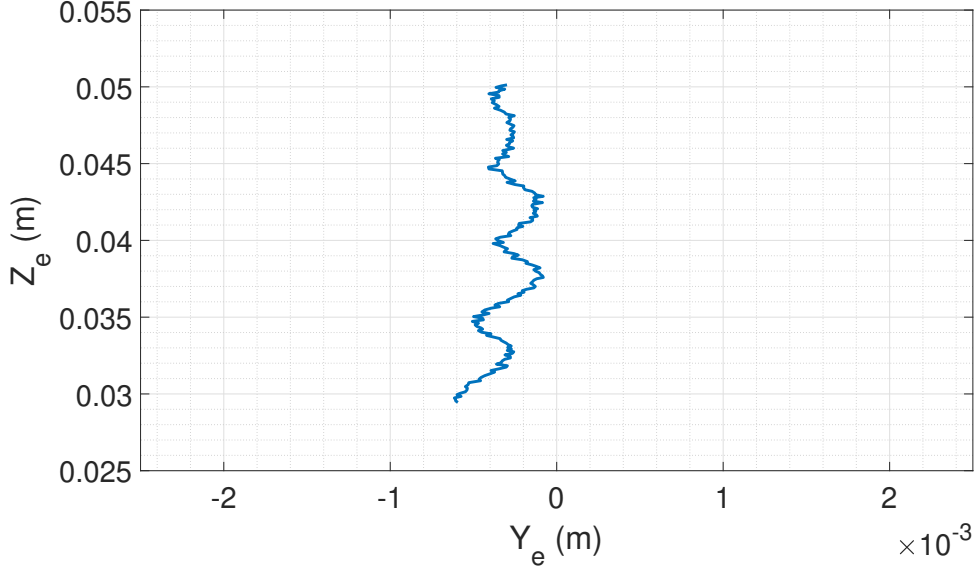


FIG. 6.12. The equilibrium point of the particle as focal point is scanned across  $z_f = 0.03$  to  $0.05$  m.

In order to test this hypothesis, a hybrid model of numerical simulation and experimentally observed static deviation was developed. The first step of constructing the hybrid model was achieved by predicting the acoustic field using Huygens' principle and Gor'kov's potential [40] to extract the forces acting on a small particle (similarly to § 6.3.1). Next, it is assumed that the force amplitude profile remains unchanged (relative to step 1) but that it was shifted spatially by a certain amount. This shift ( $x_\delta$ ) is obtained from the difference between the experimentally obtained equilibrium points ( $\mathbf{x}_{eq,exp}(f_z)$ ) and the numerical prediction of static equilibrium points ( $\mathbf{x}_{eq,sim}(f_z)$ ):

$$\mathbf{x}_\delta = \mathbf{x}_{eq,sim}(f_z) - \mathbf{x}_{eq,exp}(f_z) \quad (6.8)$$

This difference was then fitted into the polynomial approximation of the Gor'kov potential, and generated a hybrid model:

$$F_{rad} = \sum_{n=1}^N \alpha_n (y - (y_{off} + y_\delta(f_z)))^{A_{1,n}} (z - (z_{off} + z_\delta(f_z)))^{A_{2,n}} (f_z - f_{z,off})^{A_{3,n}} \quad (6.9)$$

The result of the hybrid model is as shown in Fig. 6.13 (d)-(f) and it is clear that the off-axis movement of the particle has been recovered. The gaps in the numerical simulation (Fig. 6.13 (d)-(f)) are regions where there is significant particle oscillation, in either axis, that it is out of the region where the numerical model is valid ( $\pm 2$  mm in  $y$  axis and  $\pm 3.5$  mm in  $z$  axis). There exist some discrepancies between the experimental and simulated responses for the

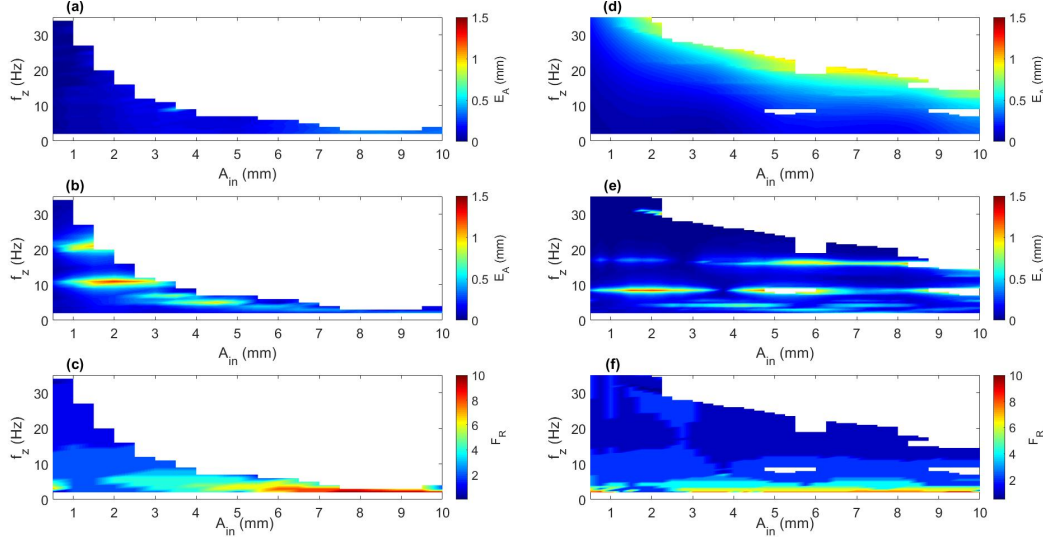


FIG. 6.13. Comparison of experimental and hybrid simulated response to a vertical focal point oscillation of varying amplitude and frequency. (a) shows the experimental  $z$ -axis error, in terms of the absolute difference between the oscillation amplitude of the trap and response amplitude of the particle ( $E_A$ ), (b) shows the experimental  $y$ -axis oscillation, (c) shows the ratio between the  $y$ -axis response frequency and the  $z$ -axis input frequency ( $F_R$ ), (d)-(f) show the numerically simulated  $z$ -axis error,  $y$ -axis error, and  $y$ -axis frequency ratio using the hybrid model, respectively. Reproduced from [29], with the permission of AIP Publishing.

peaks (i.e. resonances) in the off-axis movement, as shown in FIG 6.13 (b) and (e). These differences may be caused by an error in the model of the acoustic radiation force profile, which was not calibrated in the hybrid model (i.e. the hybrid model only corrects for the location of equilibrium point, and not the shape of the force field). However, the good qualitative and reasonable quantitative agreement suggests that this model is capable of explaining the causes of the dynamic observations by the recovery of undesirable off-axis movement. This unwanted off-axis movement will contribute to image degradation of rendered images in the volumetric display. The advantage of utilising this hybrid model is that it simplifies the process of identifying the relevant responses as developing a complete forward model involving, e.g. scattering from each transducer or nearby surfaces, as suggested in § 5.3 was challenging and computationally expensive in comparison to this hybrid model.

The dynamic response for each trajectory will differ with the geometry and output amplitude of the levitator, and the result for the  $z$  (vertical) oscillation does not superimpose with the response for the different shapes in Fig. 6.3.

## 6.4 Performance Limitation in Current Implementation

The direct comparison of experimental results and hybrid simulation results in Fig. 6.13 that the experimental cut-off region (i.e. the frequency and amplitude combinations that result in the particle ejection from the trap) of the results in (a)-(c) occurs earlier, in comparison with the simulated response in (d)-(f). The particle was oscillated until it was ejected from the trap in the experiment, and the operational region of the levitator is significantly smaller

than expected, due to the this early cut-off, in comparison to the hybrid model numerical predictions.

The consistency of the ejection frequency was evaluated for the levitator, and an example of such results are as shown in TABLE 6.1. The maximum standard deviation in the three experiments occurs when the amplitude is 1.0 mm (standard deviation of 3.44 Hz for this condition), and it becomes more consistent as the amplitude of oscillation increases (at 6.0 mm, the standard deviation decreases to 0.83 Hz). In addition, the effects of the opera-

Amplitude (mm)	Expt. 1 (Hz)	Expt. 2 (Hz)	Expt. 3 (Hz)	Mean (Hz)	Standard Deviation
1.0	35.3	42.1	37.7	38.4	3.44
1.5	28.6	30.6	33.0	30.7	2.23
2.0	20.3	24.8	22.1	22.4	2.25
2.5	15.3	19.4	21.0	18.6	2.92
3.0	14.3	13.0	15.5	14.3	1.24
3.5	10.0	9.8	13.0	10.9	1.79
4.0	12.2	12.5	11.9	12.2	0.32
4.5	10.4	12.2	8.71	10.4	1.77
5.0	10.2	10.1	13.4	11.2	1.89
5.5	8.09	9.17	9.18	8.81	0.62
6.0	7.91	9.17	7.61	8.23	0.83

TABLE 6.1: Example showing the variability of the ejection frequency of particle from the acoustic trap. Reproduced from [29], with the permission of AIP Publishing.

tional voltage was also investigated using a similar experiment to Fig. 6.10. Here, instead of stepped-sine excitation, a sine sweep was performed to identify the frequency at which the particle is ejected from the levitator for each amplitude in the range of  $0.5 \text{ mm} \leq A \leq 8 \text{ mm}$ . The result of the experiment is as shown in Fig. 6.14, and contrary to the prediction, the operational voltage does not improve the performance of the acoustic levitator. The invariance of performance with change in operational voltage suggests that there is in some cases, sufficient acoustic radiation force to perform these manipulations, but some other factor is limiting the particle from moving any faster. This is a substantial issue for volumetric display as for an trajectory to be called an image, it requires operational frequency of 10 Hz. This early ejection of the particle signifies that the display can only be operated at a narrow region above 10 Hz in Fig. 6.10.

#### 6.4.1 Transducer Limitation

From these observations, the current performance limit was attributed to the narrow bandwidth of the transducers, which leads to a reduced ability to rapidly change the phase of the ultrasonic signal. As the perturbation frequency and amplitude increase for the focal point, the transducer phases need to vary more rapidly and results in a reduced emitted ultrasonic signal. In a phased array, the signal transmitted to the transducer is assumed to be a periodic function (the FPGA board signal is a square wave, but here, a sine wave is used for

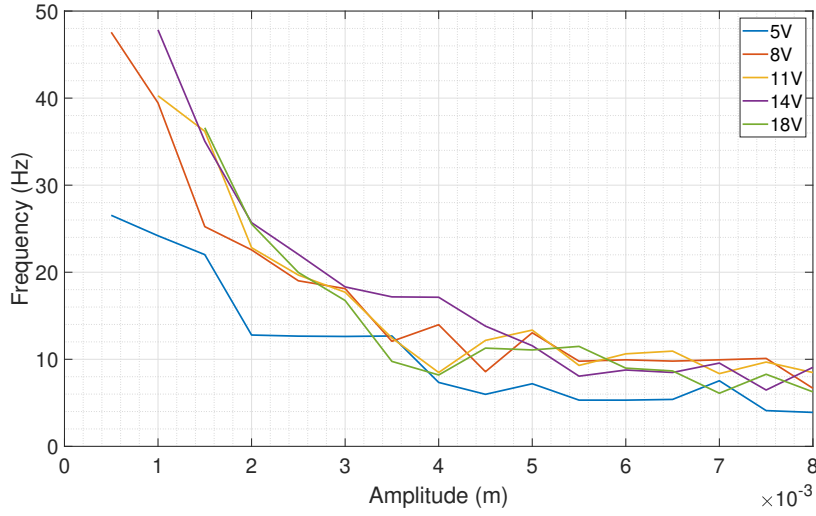


FIG. 6.14. Particle ejection limits for different applied voltages showing that voltage does not significantly affect the ejection frequency of the particle. The experiment for each amplitude starts as a low frequency of oscillation and proceeds until the particle is ejected. Reproduced from [29], with the permission of AIP Publishing.

simplicity):

$$V(t) = V_0 \sin(2\pi ft + \phi) \quad (6.10)$$

Therefore, the instantaneous frequency of this input signal is  $f_i = 2\pi f$ . This assumption that  $\phi$  is constant is relatively true, when the phase of the transducer is not manipulated at a rapid rate. However, as the trap is displaced more rapidly in the space, it demands the acoustic trap to move at a larger displacement at each instance. Therefore, the demand in the ‘change of phase’ increases, and thus the  $\phi$  becomes a function of time:

$$V(t) = V_0 \sin(2\pi ft + \phi(t)) \quad (6.11)$$

This has effect of shifting the instance frequency of the signal to  $f_i = 2\pi f + \frac{\delta\phi}{\delta t}$ . Thus, if the bandwidth of the transducer is narrow, the transducer will not emit signals, as the voltage signal does not hit the resonance of the transducer (off-resonance). In order to test this hypothesis, an experiment, similarly to the measurement of the transducer power in § 3.4.1 was set up. A transducer from the acoustic levitator was taken off from the array, and its acoustic response was recorded using a microphone (4135-A-015) connected to a signal recorder (Handyscope HS3). The pressure microphone was placed 15 mm from the surface of the transducer in a free-space environment. The transducer was connected to the FPGA board, and phase signals for generating a circular trajectory in space with  $r = 0.004742\text{m}$  was selected. The circle’s rendering frequency was increased gradually from  $\approx 1.5$ , 8.0 to 14.8 Hz. The recorded voltage from the microphone was Hilbert transformed to identify the instantaneous amplitude of the signal, and the results are as shown in Fig. 6.15. As the velocity of trap increases, the demanded value of phase changes more rapidly in comparison to when the trap was moving slowly. As a result, it causes the acoustic pressure field generated by the

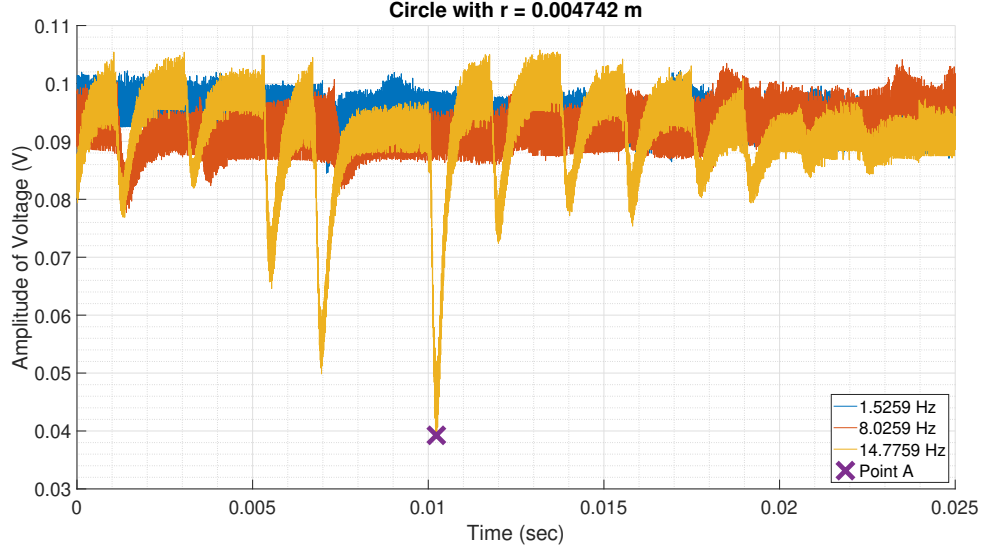


FIG. 6.15. Time domain response (received voltage is proportion to acoustic pressure) for different rates of change of phase. The voltage-time domain signal was Hilbert transformed to identify the amplitude of voltage at instantaneous point.

transducer to drop significantly (Point A in Fig. 6.15 is 41.7 % of the average amplitude of  $\approx 1.5$  Hz signal).

The dynamic response of the narrow band transducer can be modelled, as a single degree of freedom system with empirically-derived parameters.

$$\ddot{x} + \frac{\omega_n}{Q}\dot{x} + \omega_n^2 x = F(t) \quad (6.12)$$

where  $\omega_n$  is the natural frequency,  $Q = \frac{1}{2\zeta}$  is the quality factor  $Q$  in acoustic terms. The acoustic  $Q$  factor of the transducer was measured experimentally using pressure microphone. A function generator (Agilent 3320A) was connected to the transducer instead of the FPGA board to generate a sinusoidal signal in the range of 35000 Hz to 45000 Hz with the increment of 100 Hz. The  $Q$  factor calculated from:

$$Q = \frac{\omega_n}{\Delta\omega_{3dB}} \quad (6.13)$$

where  $\omega_{3dB}$  is the 3dB bandwidth of the acoustic pressure response. For a Murata transducer,  $\omega_n$  and  $\omega_{3dB}$  are 40200 and 3566.2 Hz, respectively. Thus, the  $Q$  factor for this transducer was 11.27. The transfer function for 6.12:

$$P(s) = \frac{1}{s^2 + \frac{\omega_n}{Q}s + \omega_n^2} \quad (6.14)$$

In order to validate this transducer model, two signals (FPGA board signal to the transducer and the acoustic transducer response measured 15 mm from the transducer) were recorded experimentally. The FPGA board signal was fed into the transfer function in 6.14,  $P(s)$  and the comparison of the response is as shown in FIG. 6.16. The simple model of the acoustic

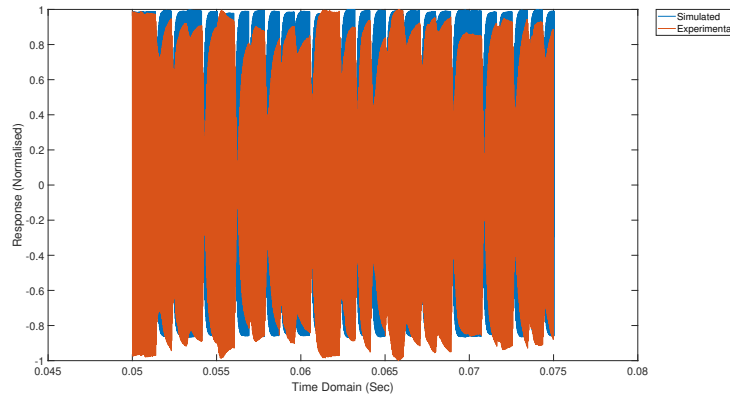


FIG. 6.16. Comparison of transducer model and experimental output. Reproduced from [29], with the permission of AIP Publishing.

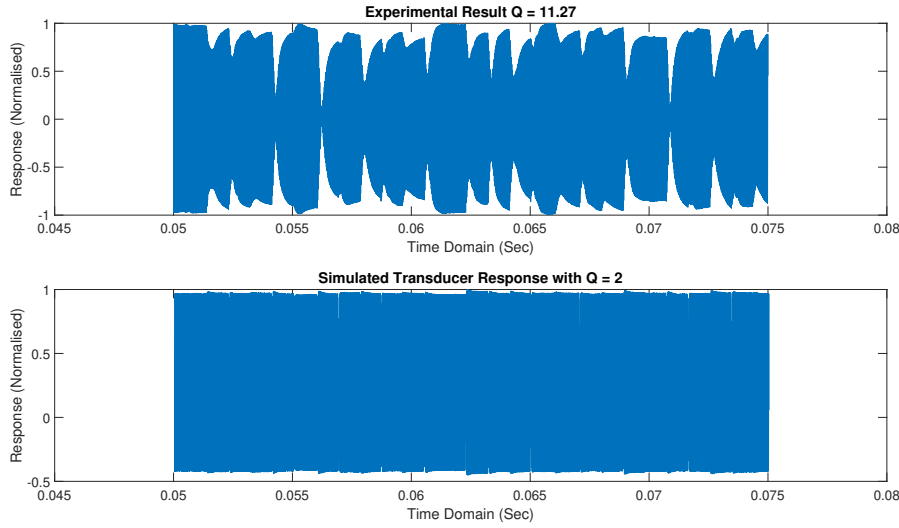


FIG. 6.17. Comparison of experimental result and transducer with wider bandwidth. Reproduced from [29], with the permission of AIP Publishing.

transducer can be seen to capture the dynamic response of interest (i.e. the rapid phase change shifts the frequency: off-resonance of the transducer). The effect of off-resonance on the acoustic radiation force is difficult to assess due to the resultant time-varying pressure field. A method of incorporating the transducer off-resonance is to add a scaling factor that ranges from 0 to 1 on the piston source approximation on 3.12. Here, if the phase is changed rapidly, the output amplitude of the transducer can be reduced accordingly. This, however, requires re-calculation of the total pressure field and is computationally inefficient and hence not pursued.

This off-resonance, however, is recognised as a common cause of the performance limitation, and Marzo et al. [39] and Cox et al. [37] similarly attribute their performance limitation in acoustic levitators to the transducer off-resonance in their literature. This fluctuation in the output acoustic pressure field from the transducer by off-resonance can be bypassed by improving the signal generator or by reducing the Q factor of the transducer, e.g.  $Q = 2$ ,

widening the bandwidth of the transducer. The same FPGA board signal in FIG. 6.16 was sent to the transfer function with lower Q factor, and the response is as shown in FIG. 6.17. Whilst there is still some observable amplitude fluctuation, the transducer more accurately recreates the desired output signal.

## 6.5 Summary

The concept of an acoustophoretic volumetric display in which dynamic acoustic fields are used to rapidly move a levitating particle that traces different 3D graphics was presented. The movement is coordinated with direct illumination of the particle and, due to the persistence of vision effect, the user perceives a free-form floating graphic. It has similar performance as the latest free-space volumetric display using optical traps [183], but it is safe to be used outside of the laboratory. A prototype was developed and evaluated in terms of speed and accuracy. It was identified that the static deviation will continue to effect the trajectory of the particle, and therefore the image quality rendered by the acoustophoretic volumetric display, and the hybrid dynamic model demonstrated that the deviation of static particle equilibrium point will affect the dynamic response of the particle. The implementation was subject to a further limitation due to the narrow bandwidth of the emitting transducers. Despite this limitation, a volumetric image of a 5 – 6 mm sized circle, infinity sign and a square at real-time ( $T_r = 0.1s$ ) was successfully generated. The maximum velocity achieved in the acoustic levitator was  $0.67\text{ ms}^{-1}$  and the maximum acceleration value was  $30.0\text{ ms}^{-2}$ . It is also predicted that better performing (i.e. wider bandwidth) transducers would permit the rendering of raster screens, given the same hardware. The numerical simulation suggests that the acoustic levitator should be able to provide with sufficient amount of acoustic radiation force to move particle at frequency faster than 10 Hz. However, as demonstrated by Fig. 6.3, the effectiveness of the calibration decreases as the velocity of the particle increases. This highlights the need for a dynamic calibration scheme which can effectively avoid the occurrences of undesirable particle movements during the rendering stage. Whilst, the particle dynamics beyond the resonating frequency of the acoustic radiation force have not been evaluated under the current circumstances; it is expected that the nonlinear responses that were identified in the § 4 will have a further role in the quality degradation of the rendered images. For example, if a period-doubling bifurcation occurs during the rendering of an image, the rendering frequency will drop to half of the frequency despite the high excitation frequencies. Therefore, it is a paradigm to continue the further investigation in the dynamics of the acoustic levitation in order to achieve a high performing acoustophoretic volumetric display.

# Chapter 7 Conclusions and future work

In this thesis, the underlying dynamics of a levitated solid particle in a single-axis PAL have been investigated from the numerical equations. The origin of the acoustic radiation force and various methods of calculating and generating acoustic radiation force were revisited in the literature review. In addition, the current and potential application of acoustic levitation was identified, along with the current study of the dynamics of the levitated particle in acoustic levitator in § 2. In § 3, the single-axis PAL that is utilised throughout the thesis was introduced with detailed descriptions of the particle tracking system, along with descriptions of methods of constructing a numerical model for acoustic pressure field and radiation force.

The acoustic radiation force was then utilised to develop one-dimensional nonlinear stiffness models and was validated against experimental results in § 4. The levitated particle was excited by sinusoidally moving the acoustic trap in the axis of gravity, and stepped-sine sweep was performed to identify the system response in experiment. The nonlinear stiffness model correctly predicted the response of the system with an accuracy of  $R^2 = 0.998$  between model and experiment. The commonly employed linear stiffness model was shown to have a small region of validity, and the importance of considering the nonlinear stiffness in the dynamics of the acoustic levitation was highlighted using a one-dimensional model. In particular, the occurrences of bifurcations such as fold bifurcations and period-doubling bifurcations were predicted by numerical simulation and were demonstrated to exist for the first time. The identification of this bifurcation has a significant effect on the development of a closed-loop controller for specimen holding, and will have significant effect on the stability of the system.

In addition, it was identified in § 5, that the equilibrium point of the particle deviates from the numerically simulated position. Whilst the existence of the deviation has been known to exist in the research community; the full picture on the significance of the effect inside the acoustic levitator has not been explored. The static deviation was quantified experimentally, and the RMS error between the specified position and the actual position of the particle was found to be 0.57 and 0.83 mm in  $y$  and  $z$  axis, respectively (compared to numerically simulated RMS with 0.11 and 0.013 mm for  $y$  and  $z$  axis). This deviation was found to be repeatable, and the cause was partially attributed to the reflection from the phased array surfaces. Whilst it requires further investigation, the calibration schemes were proposed to circumvent the effects of static deviation on the trajectory of the particle. Two methods,



online and offline calibration methods, were proposed and its effectiveness was quantitatively and qualitatively validated. The offline calibration methods, in particular, has successfully improved the trajectory accuracy by 79.0 % and 96.3 % for  $y$  and  $z$  axis, respectively. As for online calibration, the RMS error was reduced from 0.309, 0.769 and 1.01 mm to 0.136, 0.114 and 0.210 mm in  $x$ ,  $y$  and  $z$  axis respectively.

The findings from the above work have been applied to the development of practical application of acoustic levitation in § 6: an acoustophoretic volumetric display. It was achieved by rapidly displacing the levitated particle under the illumination of RGB LED light and the persistence of vision effect makes this rapid motion be perceived as a volumetric display, i.e., the particle traces the rendered objects. The proof-of-concept device was utilised to demonstrate two modes of display, vector and raster graphics. It was shown that this approach is able to produce simple vector graphics, such as circles, in real-time (10 frames per second) and raster graphics at a lower frame rate. Trajectories for each mode of volumetric display were calibrated using the developed trajectory calibration methods, and the performance limitations of the first implementation of acoustophoretic volumetric display were identified. Significant movement of the particle in the horizontal movement was experimentally observed, and the static deviation was found to affect the dynamics of particles levitated in the PAL. Therefore, a hybrid model which incorporates the static deviation into the dynamic model has been developed and was quantitatively and qualitatively validated. However, the first implementation of acoustophoretic volumetric display was subject to the limitation of transducer off-resonance which was caused by the rapid shifts in the phase of transducer. This problem needs to be addressed in order to achieve high frequency rendering of images, however, the numerical simulation do suggest that the particle can be moved at a rapid frequency to render images that are visible by eye, upon resolving the “off resonance”.

This process of applying the dynamic models and calibration methods to a practical application demonstrated the relevancy of the findings in the current development of acoustic levitation. Both the numerical models and calibration methods are general results which can be applied to other forms of acoustic levitator, such as resonant single-axis or single-beam acoustic levitators. Therefore, the results presented here will lay the foundation and continue to aid the development of future applications in the field of acoustic levitation.

## **7.1 Future Work**

The investigation into the nonlinear dynamics of particles levitated in the single-axis PAL has opened new avenues of research which can yield a further understanding of the acoustic levitation system. A few examples of such avenues are mentioned below:

### **7.1.1 Increasing the accuracy of the forward model**

It was identified in § 5 that the deviation of the static equilibrium points exists inside the acoustic levitator. The method of calibrating the trajectory were explored in the § 5.4 and method of recovering the predictability of the dynamic responses via the implementation of

hybrid model was explored in § 6.3. Whilst, the cause of static deviation was partially attributed to the reflection from the phased array surfaces in § 5.3; the future work is to develop a forward model that captures more of the physics that contributes the static deviation.

By increasing the accuracy of the forward model; new insights can be obtained in order to reduce the effect of the static deviation via the design of acoustic levitator, or be incorporated into the dynamic model to more accurately predict the causes of image degradation in the acoustophoretic volumetric display.

### 7.1.2 Multi-particle dynamics

The simultaneous manipulation of multiple particles is of substantial interest in the field, as it is an essential component for applications such as additive manufacturing and acoustophoretic volumetric displays. For example, in additive manufacturing applications, parallelization may be made possible by simultaneously employing multiple droplets for manufacturing. As for the acoustophoretic volumetric display, it is possible to reduce the travelling distance of the particle, and therefore improve the screen size and resolution for the volumetric display.

When more than two particles are levitated in close vicinity, it is known to cause secondary acoustic radiation forces due to the scattering from each particle [90]. The multi-particle movement in the HAT system as described by Marzo & Drinkwater [76] is subject to the secondary acoustic radiation force. Dolev et al. has already demonstrated the selected particle movement by exploiting the multi-particle dynamics in experiment [94] and developing dynamic model which can capture motion of multiple particles may yield further understanding of the response of levitated particles and improve the performance of the HAT system.

### 7.1.3 Open / closed-loop controller

The method of improving the static trajectory was discussed in § 5.4, however, as demonstrated by Fig. 6.3, the effectiveness of the calibration decreases with the increase in the velocity of the particle. This overlaps in part with the ‘Increasing the accuracy of the forward model’, but the complete forward model with the static deviation will allow the development of open-loop controller. An open loop control is a method of determining the excitation signals needed to control the particle without feedback signal and this is analogous to the dynamic calibration of the system and is suitable; provided that the external disturbances to the system are minimal. Where the external disturbance is significant, the development of closed-loop control system (with feedback system) will improve the dynamic positioning performance of the levitator; however, as briefly mentioned in § 5, the development of closed-loop control system will require faster and more advanced particle tracking system.

By incorporating such control system to the acoustic levitator, the stability of the levitated objects can be improved during scientific analysis (such as Raman spectroscopy [115], crystallography [115], radar characterisation [115]). In addition, the automation of the liquid droplet handling system (as demonstrated by [75] and [74]) will be made possible. Such an

automated system will help improve the time efficiency of chemical or biological experiments and decrease the risks of contamination via non-contact handling of droplets.

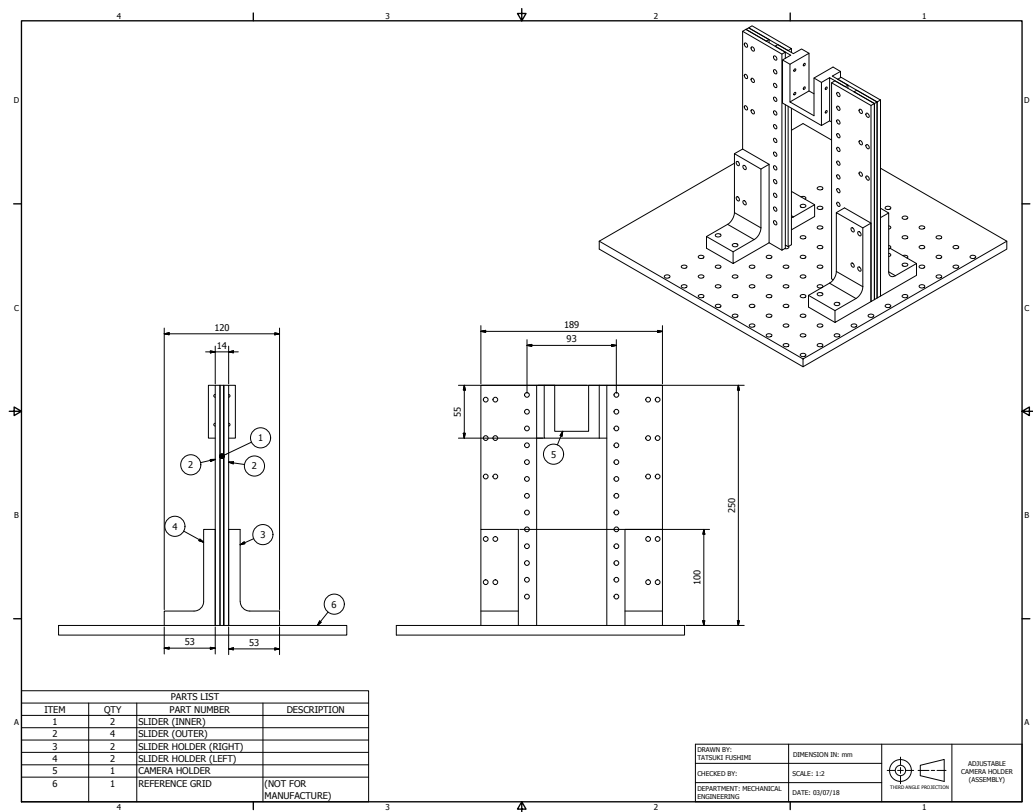
#### **7.1.4 Future of Acoustophoretic Volumetric Display (Transducer Limitation)**

As identified in the § 6, the fundamental limitation in the first implementation of the volumetric display was with the acoustic signal from FPGA board not hitting the resonance of the transducer. This problem needs to be overcome in order to achieve the full acoustophoretic volumetric display, and it may be addressed from the signal generation perspective, or utilising a wider-bandwidth transducer as mentioned in § 6.4.1.

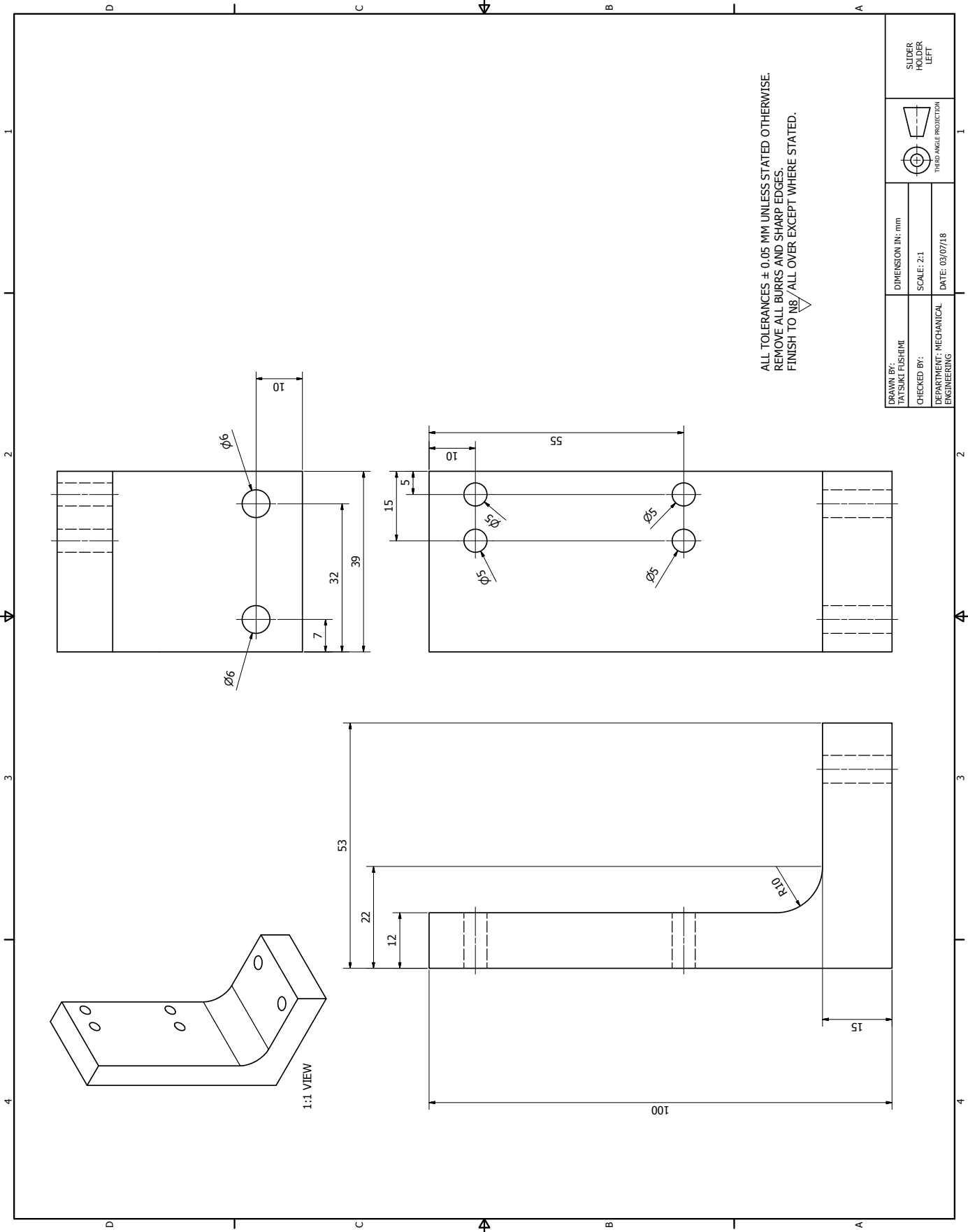
However, there are methods of utilising the current PAL and avoid the particles from falling off due to the “off-resonance”. For example, the single-axis PAL has two phased arrays, and one can utilise single-beam trap such as ‘twin’ trap from one phased-array (either upper or lower) to capture the particle. By multiplexing between each phased array, it may be possible to minimise the time between the transducer being ‘on’ and ‘off’, due to the “off-resonance”. The time gap may further be reduced by utilising more transducer arrays, but will require an advanced particle tracking system to ensure that the generated acoustic trap is appropriate for the motion. Alternative arrangements may be achieved by developing a new acoustic trap which considers the particle motion from the design stage. The current acoustic traps are designed in a quasi-static domain [79], and the performance may be improved by properly considering the motion of the particle. The derivative of phase in time domain can be included for the optimisation function, and therefore minimise the chance of “off-resonance”.

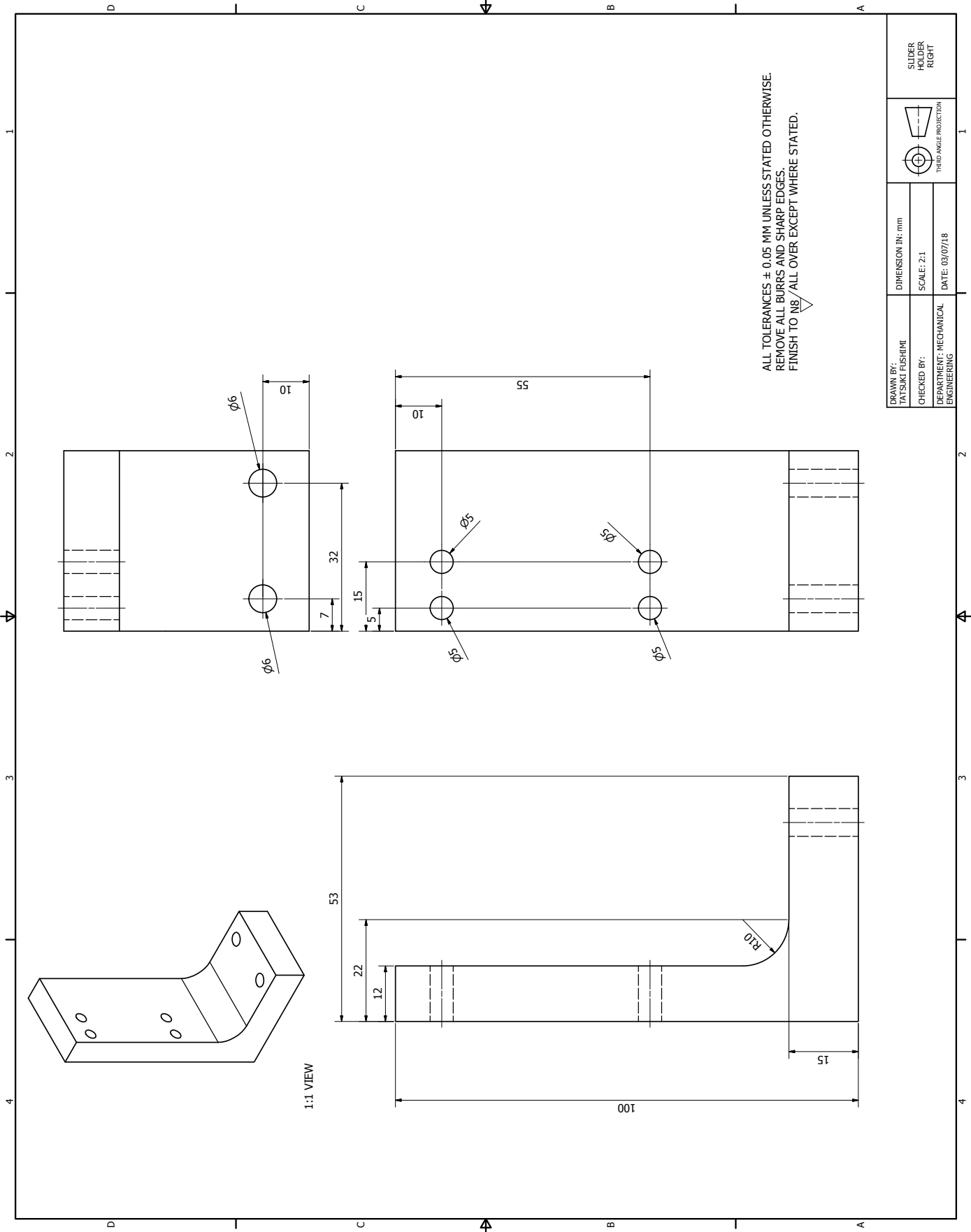
# Appendix A Camera Holder

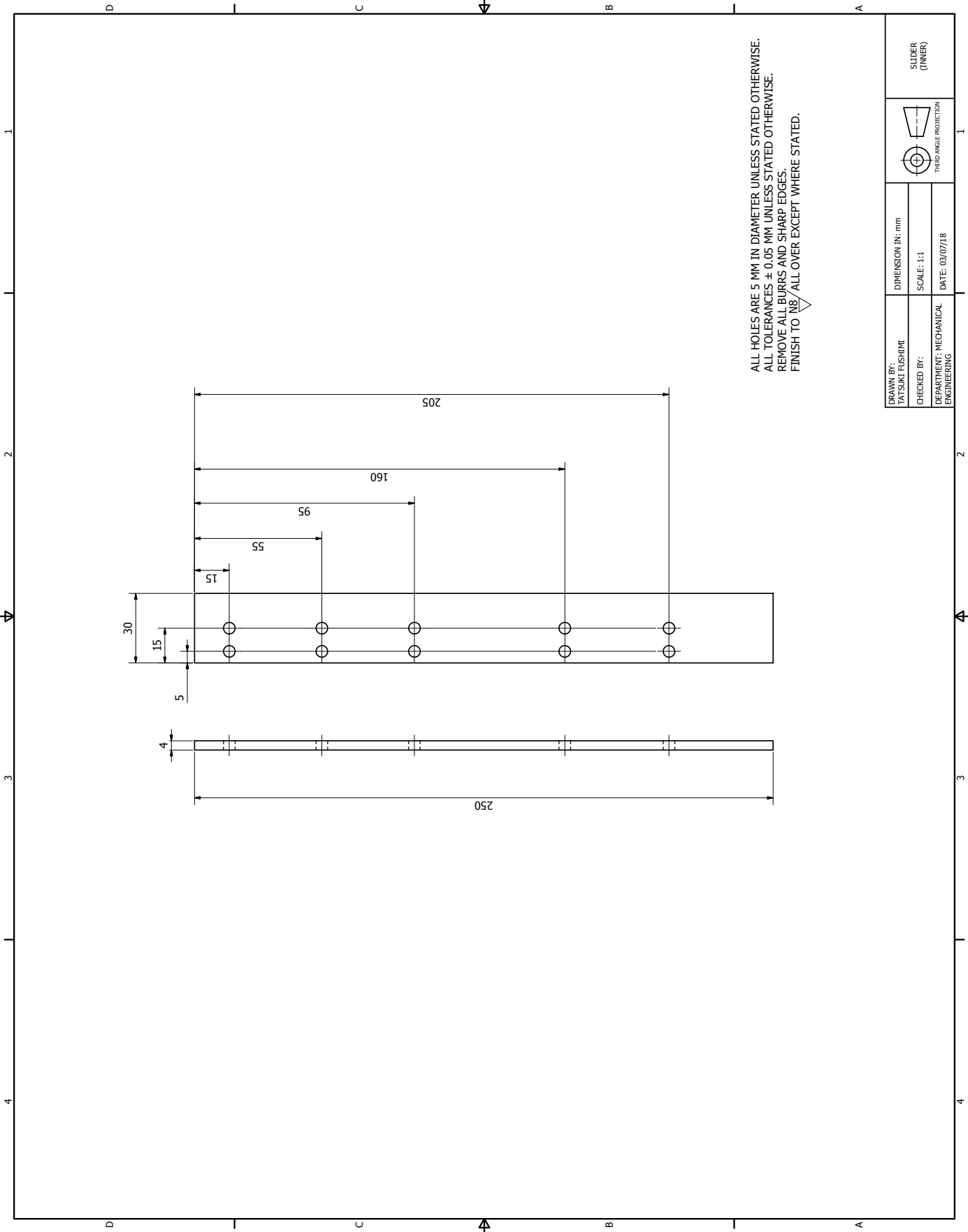
Camera holder was designed by Tatsuki Fushimi, and manufactured by Mr. Stephen Isles.



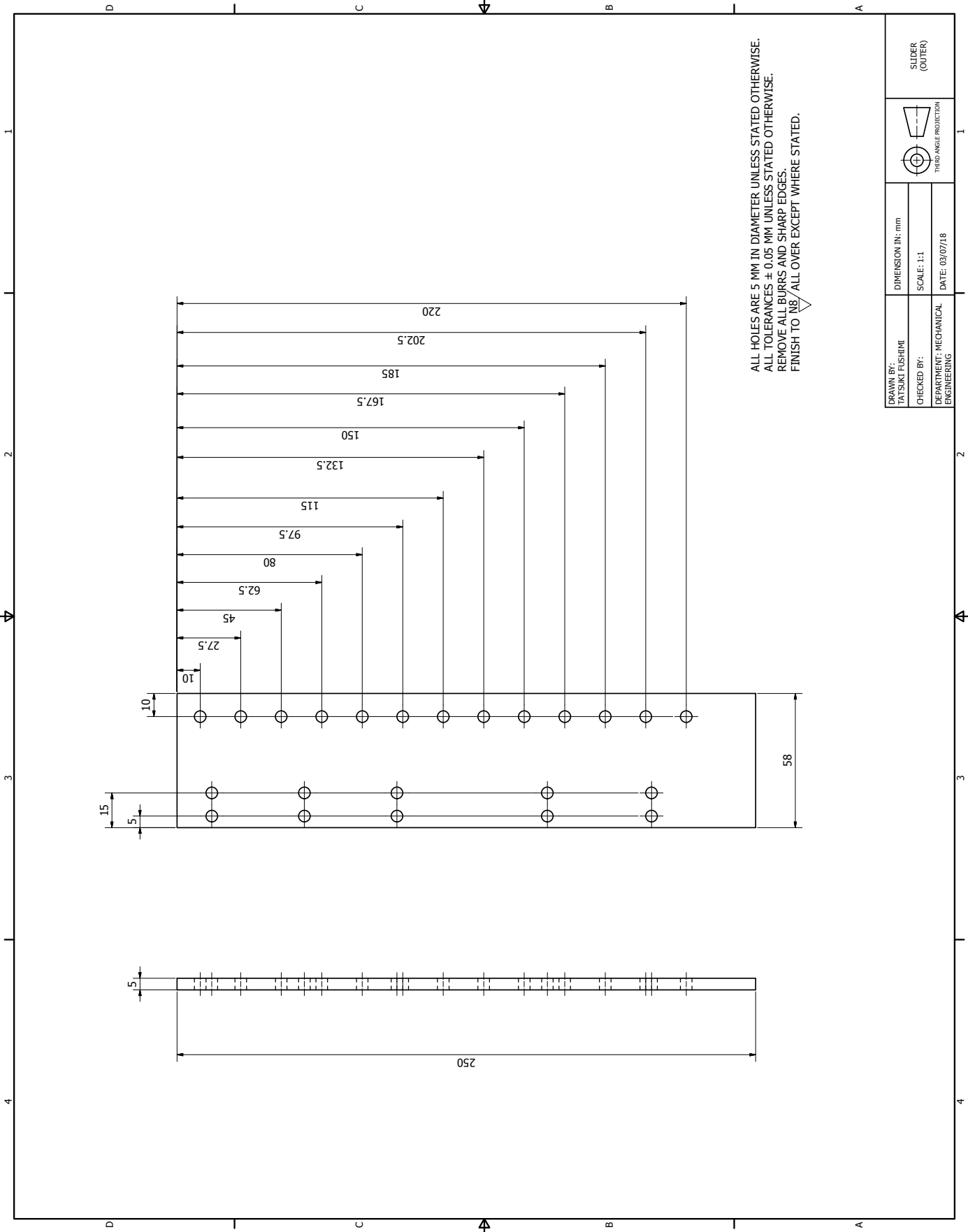






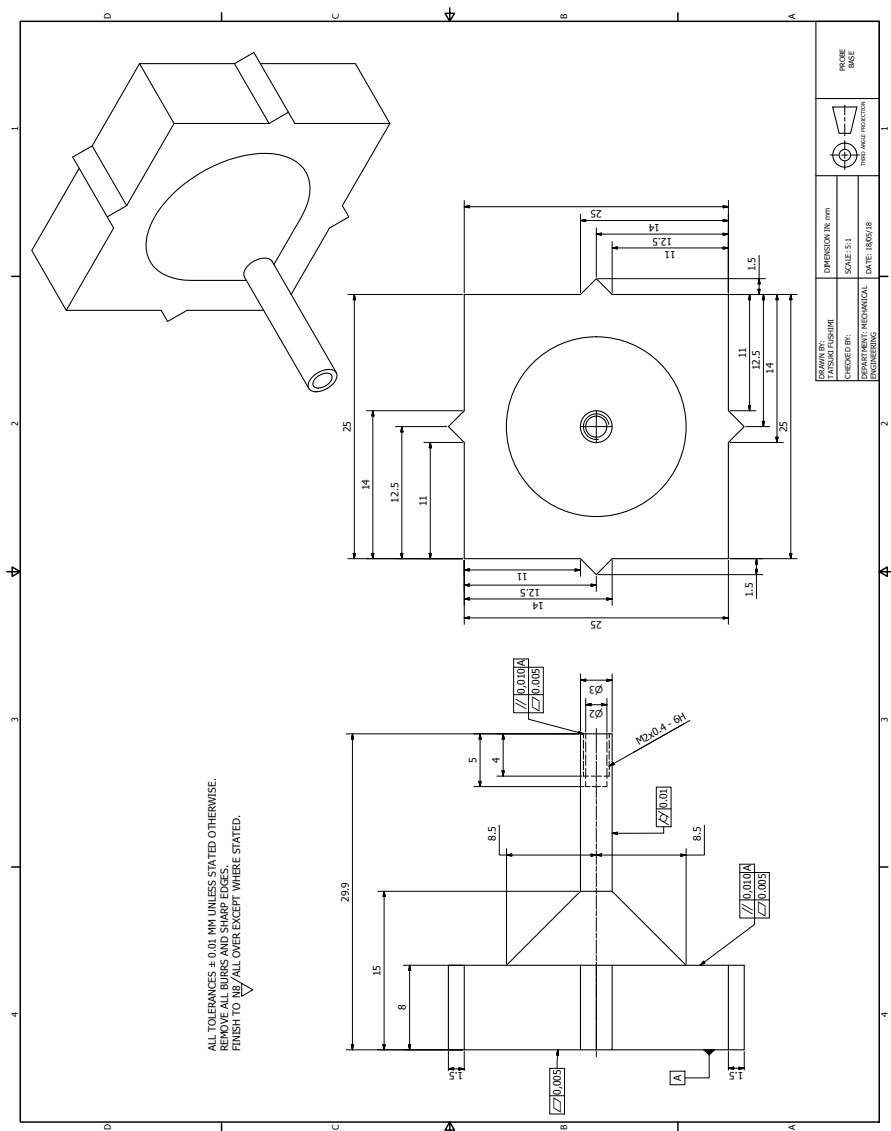






# Appendix B Calibration Probe Holder

Calibration probe was designed by Tatsuki Fushimi, and manufactured by Mr. Stephen Isles.





# Appendix C Calibration Probe Extender

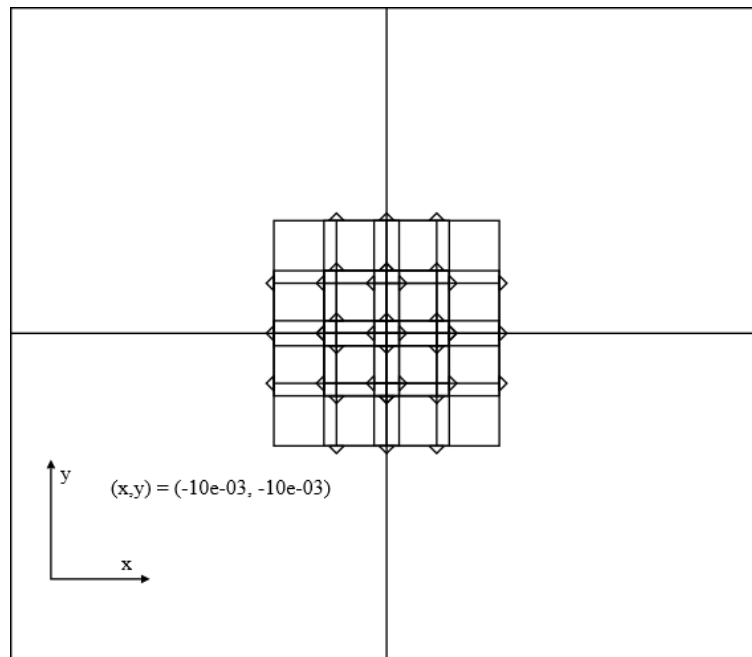
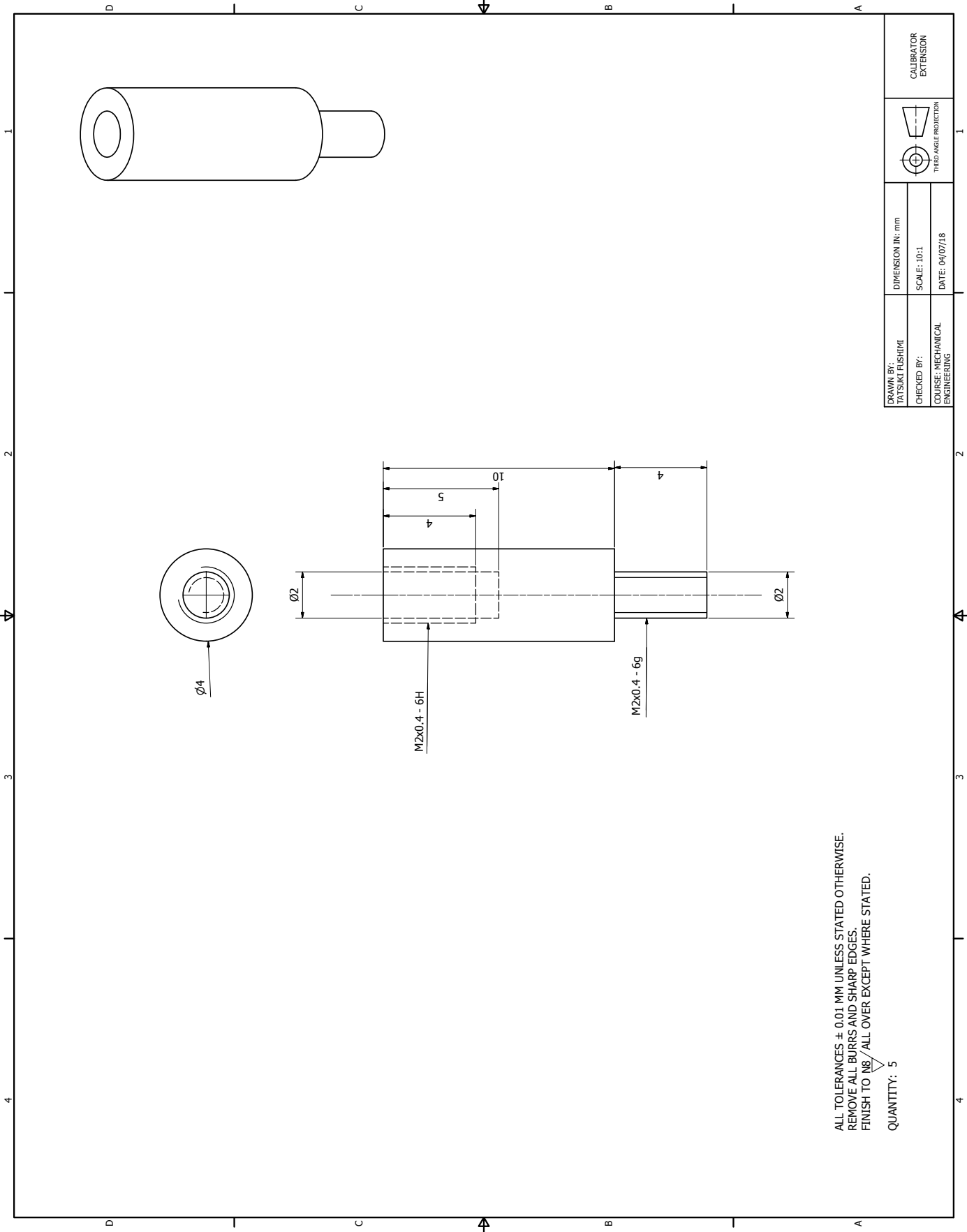
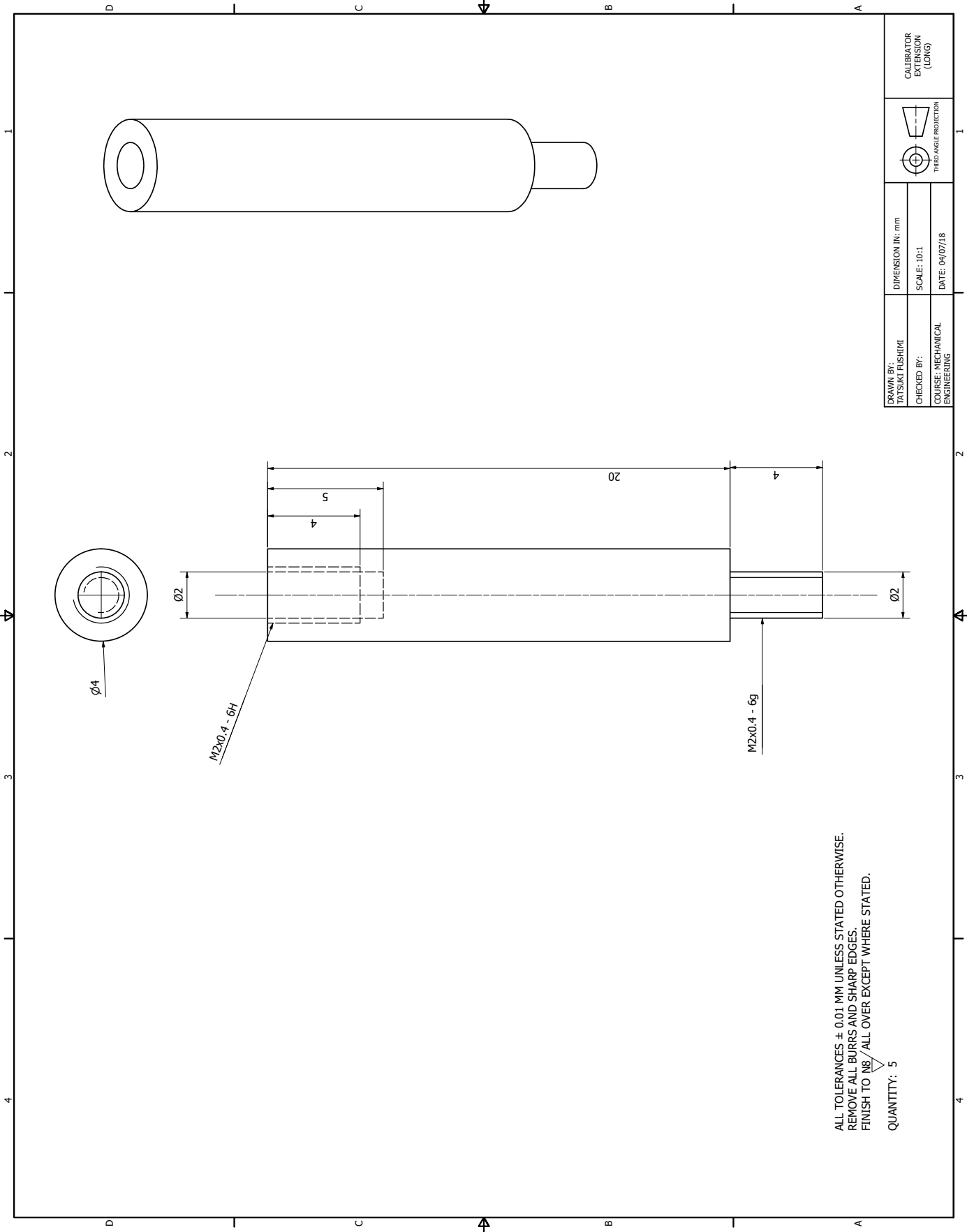


FIG. C.1. Experimental setup for the measurement of the particle in 3D space. The camera assemblies are orthogonal to each other and was calibrated using the CMM-styli.

Calibration probe was designed by Tatsuki Fushimi, and manufactured by Mr. Stephen Isles.







# Bibliography

- [1] A. Kundt. “Über eine neue Art akustischer Staubfiguren und über die Anwendung derselben zur Bestimmung der Schallgeschwindigkeit in festen Körpern und Gasen”. In: *Annalen der Physik* 203.4 (1866), pp. 497–523.
- [2] J. W. S. Rayleigh. “XLII. On the momentum and pressure of gaseous vibrations, and on the connexion with the virial theorem”. In: *Philosophical Magazine Series 6* 10.57 (Sept. 1905), pp. 364–374. ISSN: 1941-5982. DOI: 10.1080/14786440509463381.
- [3] J. W. S. Rayleigh. “XXXI. Investigations in optics, with special reference to the spectroscope”. In: *The London, Edinburgh, and Dublin Philosophical Magazine and Journal of Science* 8.49 (Oct. 1879), pp. 261–274. ISSN: 1941-5982. DOI: 10.1080/14786447908639684.
- [4] K. Bücks and H. Müller. “Über einige Beobachtungen an schwingenden Piezoquarzen und ihrem Schallfeld”. In: *Zeitschrift für Physik* 84.1-2 (Jan. 1933), pp. 75–86. ISSN: 1434-6001. DOI: 10.1007/BF01330275.
- [5] L. V. King. “On the acoustic radiation pressure on spheres”. In: *Proceedings of the Royal Society of London. Series A - Mathematical and Physical Sciences* 147.861 (1934), pp. 212–240. ISSN: 1364-5021. DOI: 10.1098/rspa.1934.0215.
- [6] Y. Hashimoto, Y. Koike, and S. Ueha. “Near-field acoustic levitation using flexural vibration mode”. In: *Ultrasonics World Congress 1995 Proceedings*. 1995, pp. 835–838.
- [7] S. Ueha, Y. Hashimoto, and Y. Koike. “Non-contact transportation using near-field acoustic levitation”. In: *Ultrasonics* 38.1-8 (Mar. 2000), pp. 26–32. ISSN: 0041624X. DOI: 10.1016/S0041-624X(99)00052-9.
- [8] W. J. Xie, C. D. Cao, Y. J. Lü, and B. Wei. “Levitation of Iridium and Liquid Mercury by Ultrasound”. In: *Physical Review Letters* 89.10 (2002), pp. 1–4. ISSN: 10797114. DOI: 10.1103/PhysRevLett.89.104304.
- [9] W. J. Xie and B. Wei. “Dynamics of acoustically levitated disk samples”. In: *Physical Review E - Statistical Physics, Plasmas, Fluids, and Related Interdisciplinary Topics* 70.4 (2004), p. 11. ISSN: 1063651X. DOI: 10.1103/PhysRevE.70.046611.
- [10] R. R. Whymark. “Acoustic field positioning for containerless processing”. In: *Ultrasonics* 13.6 (Nov. 1975), pp. 251–261. ISSN: 0041624X. DOI: 10.1016/0041-624X(75)90072-4.
- [11] J. Rudnick and M. Barmatz. “Oscillational instabilities in single-mode acoustic levitators”. In: *The Journal of the Acoustical Society of America* 87.1 (Jan. 1990), pp. 81–92. ISSN: 0001-4966. DOI: 10.1121/1.398916.



- 
- [12] M. A. B. Andrade, N. Pérez, and J. C. Adamowski. “Review of Progress in Acoustic Levitation”. In: *Brazilian Journal of Physics* (Dec. 2017). ISSN: 0103-9733. DOI: 10.1007/s13538-017-0552-6.
- [13] NASA. *NASA - STS - 50*. 2010. URL: [https://www.nasa.gov/mission\\_pages/shuttle/shuttlemissions/archives/sts-50.html](https://www.nasa.gov/mission_pages/shuttle/shuttlemissions/archives/sts-50.html) (visited on Sept. 18, 2019).
- [14] NASA. *NASA - STS - 51 B*. 2007. URL: [https://www.nasa.gov/mission\\_pages/shuttle/shuttlemissions/archives/sts-51B.html](https://www.nasa.gov/mission_pages/shuttle/shuttlemissions/archives/sts-51B.html) (visited on Sept. 20, 2019).
- [15] C. J. Benmore and J. K. R. R. Weber. “Amorphization of Molecular Liquids of Pharmaceutical Drugs by Acoustic Levitation”. In: *Physical Review X* 1.1 (2011), pp. 1–7. ISSN: 21603308. DOI: 10.1103/PhysRevX.1.011004.
- [16] A. Marzo, A. Barnes, and B. W. Drinkwater. “TinyLev: A multi-emitter single-axis acoustic levitator”. In: *Review of Scientific Instruments* 88.8 (Aug. 2017), p. 085105. ISSN: 0034-6748. DOI: 10.1063/1.4989995.
- [17] R. H. Morris, E. R. Dye, D. Axford, M. I. Newton, J. H. Beale, and P. T. Docker. “Non-Contact Universal Sample Presentation for Room Temperature Macromolecular Crystallography Using Acoustic Levitation”. In: *Scientific Reports* 9.1 (2019), pp. 1–10. ISSN: 2045-2322. DOI: 10.1038/s41598-019-48612-4.
- [18] O. Yurduseven, K. Cooper, and G. Chattopadhyay. “Point-Spread-Function (PSF) Characterization of a 340-GHz Imaging Radar Using Acoustic Levitation”. In: *IEEE Transactions on Terahertz Science and Technology* 9.1 (2019), pp. 20–26. ISSN: 2156342X. DOI: 10.1109/TTHZ.2018.2876418.
- [19] O. Youssefi and E. Diller. “Contactless Robotic Micromanipulation in Air Using a Magneto-Acoustic System”. In: *IEEE Robotics and Automation Letters* 4.2 (Apr. 2019), pp. 1580–1586. ISSN: 2377-3766. DOI: 10.1109/LRA.2019.2896444.
- [20] E. R. Duranty, S. A. Jacoby, and J. H. Davis. “Investigating Processes Occurring in Acoustically Levitated Ionic Liquid Droplets”. In: *ECS Transactions* 86.14 (July 2018), pp. 297–308. ISSN: 1938-6737. DOI: 10.1149/08614.0297ecst.
- [21] A. Marzo, T. Corkett, and B. W. Drinkwater. “Ultraino: An Open Phased-Array System for Narrowband Airborne Ultrasound Transmission”. In: *IEEE Transactions on Ultrasonics, Ferroelectrics, and Frequency Control* 65.1 (Jan. 2018), pp. 102–111. ISSN: 0885-3010. DOI: 10.1109/TUFFC.2017.2769399.
- [22] M. Prisbrey and B. Raeymaekers. “Ultrasound Noncontact Particle Manipulation of Three-dimensional Dynamic User-specified Patterns of Particles in Air”. In: *Physical Review Applied* 10.3 (Sept. 2018), p. 034066. ISSN: 2331-7019. DOI: 10.1103/PhysRevApplied.10.034066.
- [23] D. Foresti, M. Nabavi, M. Klingauf, A. Ferrari, and D. Poulikakos. “Acoustophoretic contactless transport and handling of matter in air”. In: *Proceedings of the National Academy of Sciences* 110.31 (2013), pp. 12549–12554. ISSN: 0027-8424. DOI: 10.1073/pnas.1301860110. arXiv: arXiv:1507.02142v2.
- [24] W. A. Harkness and J. H. Goldschmid. *Free-Form Spatial 3-D Printing Using Part Levitation*. US20160031156A1. 2014.

- [25] D. J. Ryan, A. Kamel, and G. J. Bruck. *Acoustic manipulation and laser processing of particles for repair and manufacture of metallic components*. US20160228991A1. 2016.
- [26] D. P. Stoten and H. Benchaubane. “The minimal control synthesis identification algorithm”. In: *International Journal of Control* 58.3 (Sept. 1993), pp. 685–696. ISSN: 0020-7179. DOI: 10.1080/00207179308923022.
- [27] T. Fushimi, T. L. Hill, A. Marzo, and B. W. Drinkwater. “Nonlinear trapping stiffness of mid-air single-axis acoustic levitators”. In: *Applied Physics Letters* 113.3 (July 2018), p. 034102. ISSN: 0003-6951. DOI: 10.1063/1.5034116.
- [28] T. Fushimi, A. Marzo, T. L. Hill, and B. W. Drinkwater. “Trajectory Optimization of Levitated Particles in Mid-air Ultrasonic Standing Wave Levitators”. In: *2018 IEEE International Ultrasonics Symposium (IUS)* (2018), pp. 1–9. DOI: 10.1109/ULTSYM.2018.8580093.
- [29] T. Fushimi, A. Marzo, B. W. Drinkwater, and T. L. Hill. “Acoustophoretic volumetric displays using a fast-moving levitated particle”. In: *Applied Physics Letters* 115.6 (Aug. 2019), p. 064101. ISSN: 0003-6951. DOI: 10.1063/1.5113467.
- [30] L. E. Kinsler, A. R. Frey, A. B. Coppens, and J. V. Sanders. *Fundamentals of Acoustics: 3rd edition*. Wiley, 1982. ISBN: 978-0471029335.
- [31] R. T. Beyer. “Radiation pressure—the history of a mislabeled tensor”. In: *Journal of the Acoustical Society of America* 63.4 (1978), pp. 1025–1030. DOI: 10.1121/1.381833.
- [32] H. Bruus. “Acoustofluidics 7: The acoustic radiation force on small particles”. In: *Lab on a Chip* 12.6 (2012), pp. 1014–1021. ISSN: 1473-0197. DOI: 10.1039/c2lc21068a.
- [33] P. Glynne-Jones, P. P. Mishra, R. J. Boltryk, and M. Hill. “Efficient finite element modeling of radiation forces on elastic particles of arbitrary size and geometry”. In: *The Journal of the Acoustical Society of America* 133.4 (2013), pp. 1885–1893. ISSN: 0001-4966. DOI: 10.1121/1.4794393.
- [34] K. Yosioka and Y. Kawasima. “Acoustic radiation pressure on a compressible sphere”. In: *Acta Acustica united with Acustica* 5.3 (1955), pp. 167–173. ISSN: 1610-1928.
- [35] G. Maidanik. “Torques Due to Acoustical Radiation Pressure”. In: *The Journal of the Acoustical Society of America* 30.7 (July 1958), pp. 620–623. ISSN: 0001-4966. DOI: 10.1121/1.1909714.
- [36] P. J. Westervelt. “The Theory of Steady Forces Caused by Sound Waves”. In: *The Journal of the Acoustical Society of America* 23.3 (May 1951), pp. 312–315. ISSN: 0001-4966. DOI: 10.1121/1.1906764.
- [37] L. Cox, A. Croxford, B. W. Drinkwater, and A. Marzo. “Acoustic Lock: Position and orientation trapping of non-spherical sub-wavelength particles in mid-air using a single-axis acoustic levitator”. In: *Applied Physics Letters* 113.5 (2018). ISSN: 00036951. DOI: 10.1063/1.5042518.
- [38] S. Inoue, S. Mogami, T. Ichiyama, A. Noda, Y. Makino, and H. Shinoda. “Acoustical boundary hologram for macroscopic rigid-body levitation”. In: *The Journal of the*

- Acoustical Society of America* 145.1 (2019), pp. 328–337. ISSN: 0001-4966. DOI: 10.1121/1.5087130.
- [39] A. Marzo, M. Caleap, and B. W. Drinkwater. “Acoustic Virtual Vortices with Tunable Orbital Angular Momentum for Trapping of Mie Particles”. In: *Physical Review Letters* 120.4 (2018), p. 44301. ISSN: 10797114. DOI: 10.1103/PhysRevLett.120.044301.
  - [40] L. P. Gor’kov. “On the Forces Acting on a Small Particle in an Acoustical Field in an Ideal Fluid”. In: *Soviet Physics Doklady* 6 (1962), p. 773. ISSN: 0002-3264.
  - [41] R. M. Keolian, S. R. Baker, and A. Huffman. “Isadore Rudnick’s spectacular acoustics demonstrations”. In: *The Journal of the Acoustical Society of America* 145.3 (2019), p. 1682. DOI: 10.1121/1.5101167.
  - [42] M. A. B. Andrade, N. Pérez, and J. C. Adamowski. “Experimental study of the oscillation of spheres in an acoustic levitator”. In: *The Journal of the Acoustical Society of America* 136.4 (2014), pp. 1518–1529. ISSN: 0001-4966. DOI: 10.1121/1.4893905.
  - [43] W. J. Xie and B. Wei. “Parametric study of single-axis acoustic levitation”. In: *Applied Physics Letters* 79.6 (2001), pp. 881–883. ISSN: 00036951. DOI: 10.1063/1.1391398.
  - [44] M. A. Andrade, S. Polychronopoulos, G. Memoli, and A. Marzo. “Experimental investigation of the particle oscillation instability in a single-axis acoustic levitator”. In: *AIP Advances* 9.3 (2019). ISSN: 21583226. DOI: 10.1063/1.5078948.
  - [45] Z. Y. Hong, J. F. Yin, W. Zhai, N. Yan, W. L. Wang, J. Zhang, and B. W. Drinkwater. “Dynamics of levitated objects in acoustic vortex fields”. In: *Sci. Rep.* June (2017), pp. 1–7. ISSN: 2045-2322. DOI: 10.1038/s41598-017-07477-1.
  - [46] J. Clough, M. W. Sracic, D. Piombino, J. Braaten, S. Connors, N. Pedigo, V. Prantil, and K. Suthar. “Design and Prototype of a Two-Axis Acoustic Levitator”. In: *Volume 13: Acoustics, Vibration, and Wave Propagation*. American Society of Mechanical Engineers, Nov. 2016, pp. 1–10. ISBN: 978-0-7918-5067-1. DOI: 10.1115/IMECE2016-66193.
  - [47] M. W. Sracic, J. D. Petrie, H. A. Moroder, R. T. Koniecko, A. R. Abramczyk, and K. Suthar. “Acoustic pressure fields generated with a high frequency acoustic levitator”. In: *ASME International Mechanical Engineering Congress and Exposition, Proceedings (IMECE)* 13 (2017), pp. 1–8. DOI: 10.1115/IMECE2017-71849.
  - [48] E. H. Trinh, R. G. Holt, and D. B. Thiessen. “The dynamics of ultrasonically levitated drops in an electric field”. In: *Physics of Fluids* 8.1 (1996), p. 43. ISSN: 10706631. DOI: 10.1063/1.868813.
  - [49] T. G. Wang, E. H. Trinh, A. P. Croonquist, and D. D. Elleman. “Shapes of rotating free drops: Spacelab experimental results”. In: *Physical Review Letters* 56.5 (1986), pp. 452–455. ISSN: 00319007. DOI: 10.1103/PhysRevLett.56.452.
  - [50] E. Trinh, J. Robey, N. Jacobi, and T. Wang. “Dual-temperature acoustic levitation and sample transport apparatus”. In: *Journal of the Acoustical Society of America* 79.3 (1986), pp. 604–612. DOI: 10.1121/1.393450.

- [51] E. H. Trinh and C. J. Hsu. “Acoustic levitation methods for density measurements”. In: *The Journal of the Acoustical Society of America* 80.6 (Dec. 1986), pp. 1757–1761. ISSN: 0001-4966. DOI: 10.1121/1.394290.
- [52] E. H. Trinh and J. L. Robey. “Experimental study of streaming flows associated with ultrasonic levitators”. In: *Physics of Fluids* 6.11 (1994), pp. 3567–3579. ISSN: 00084034. DOI: 10.1063/1.868415.
- [53] T. G. Wang, E. Trinh, W. K. Rhim, D. Kerrisk, M. Barmatz, and D. D. Elleman. “Containerless processing technologies at the Jet Propulsion Laboratory”. In: *Acta Astronautica* 11.3-4 (1984), pp. 233–237. ISSN: 00945765. DOI: 10.1016/0094-5765(84)90113-9.
- [54] M. A. Andrade, N. Pérez, and J. C. Adamowski. “Particle manipulation by a non-resonant acoustic levitator”. In: *Applied Physics Letters* 106.1 (2015). ISSN: 00036951. DOI: 10.1063/1.4905130.
- [55] C. A. Rey. *Acoustic levitation and methods for manipulating levitated objects*. US4284403A. 1978.
- [56] T. Kozuka, K. Yasui, T. Tuziuti, A. Towata, and Y. Iida. “Noncontact acoustic manipulation in air”. In: *Japanese Journal of Applied Physics, Part 1: Regular Papers and Short Notes and Review Papers* 46.7 B (2007), pp. 4948–4950. ISSN: 00214922. DOI: 10.1143/JJAP.46.4948.
- [57] C. H. Hansen. “Fundamentals of acoustics”. In: *Occupational Exposure to Noise: Evaluation, Prevention and Control*. (2001), pp. 23–52.
- [58] Y. Hashimoto, Y. Koike, and S. Ueha. “Acoustic levitation of planar objects using a longitudinal vibration mode.” In: *Journal of the Acoustical Society of Japan (E)* 16.3 (1995), pp. 189–192. ISSN: 0388-2861. DOI: 10.1250/ast.16.189.
- [59] A. Minikes, I. Bucher, and S. Haber. “Levitation force induced by pressure radiation in gas squeeze films”. In: *The Journal of the Acoustical Society of America* 116.1 (2004), pp. 217–226. ISSN: 0001-4966. DOI: 10.1121/1.1760110.
- [60] Y. Hashimoto, Y. Koike, and S. Ueha. “Transporting objects without contact using flexural traveling waves”. In: *The Journal of the Acoustical Society of America* 103.6 (1998), pp. 3230–3233. ISSN: 0001-4966. DOI: 10.1121/1.423039.
- [61] E. Matsuo, Y. Koike, K. Nakamura, S. Ueha, and Y. Hashimoto. “Holding characteristics of planar objects suspended by near-field acoustic levitation”. In: *Ultrasonics* 38.1–8 (2000), pp. 60–63. ISSN: 0041624X. DOI: 10.1016/S0041-624X(99)00046-3.
- [62] G. Reinhart, J. Hoeppner, and J. Zimmermann. “Non-contact wafer handling using high-intensity ultrasonics”. In: *2001 IEEE/SEMI Advanced Semiconductor Manufacturing Conference (IEEE Cat. No.01CH37160)*. 1. IEEE, 2001, pp. 139–140. ISBN: 0-7803-6555-0. DOI: 10.1109/ASMC.2001.925636.
- [63] H. Nomura, T. Kamakura, and K. Matsuda. “Theoretical and experimental examination of near-field acoustic levitation”. In: *The Journal of the Acoustical Society of America* 111.4 (2002), pp. 1578–1583. ISSN: 0001-4966. DOI: 10.1121/1.1453452.

- [64] T. Ide, J. R. Friend, K. Nakamura, and S. Ueha. “A Low-Profile Design for the Non-contact Ultrasonically Levitated Stage”. In: *Japanese Journal of Applied Physics* 44.6B (2005), pp. 4662–4665. ISSN: 0021-4922. DOI: 10.1143/jjap.44.4662.
- [65] Z. Y. Hong, P. Lü, D. L. Geng, W. Zhai, N. Yan, and B. Wei. “The near-field acoustic levitation of high-mass rotors”. In: *Review of Scientific Instruments* 85.10 (2014). ISSN: 10897623. DOI: 10.1063/1.4898120.
- [66] S. Zhao, S. Mojrzisch, and J. Wallaschek. “An ultrasonic levitation journal bearing able to control spindle center position”. In: *Mechanical Systems and Signal Processing* 36 (2013), pp. 168–181. DOI: 10.1016/j.ymssp.2012.05.006.
- [67] M. Takasaki, D. Terada, Y. Kato, Y. Ishino, and T. Mizuno. “Non-contact ultrasonic support of minute objects”. In: *Physics Procedia* 3.1 (2010), pp. 1059–1065. ISSN: 18753884. DOI: 10.1016/j.phpro.2010.01.137.
- [68] M. A. B. Andrade, F. T. A. Okina, A. L. Bernassau, and J. C. Adamowski. “Acoustic levitation of an object larger than the acoustic wavelength”. In: *The Journal of the Acoustical Society of America* 141.6 (June 2017), pp. 4148–4154. ISSN: 0001-4966. DOI: 10.1121/1.4984286.
- [69] H. W. S. Clair. “An electromagnetic sound generator for producing intense high frequency sound”. In: *Review of Scientific Instruments* 12.5 (1941), pp. 250–256. ISSN: 00346748. DOI: 10.1063/1.1769874.
- [70] M. A. Andrade, A. L. Bernassau, and J. C. Adamowski. “Acoustic levitation of a large solid sphere”. In: *Applied Physics Letters* 109.4 (2016), p. 044101. ISSN: 00036951. DOI: 10.1063/1.4959862.
- [71] R. H. Morris, E. R. Dye, P. Docker, and M. I. Newton. “Beyond the Langevin horn: Transducer arrays for the acoustic levitation of liquid drops”. In: *Physics of Fluids* 31.10 (Oct. 2019), p. 101301. ISSN: 1070-6631. DOI: 10.1063/1.5117335.
- [72] Y. Ochiai, T. Hoshi, and J. Rekimoto. “Three-Dimensional Mid-Air Acoustic Manipulation by Ultrasonic Phased Arrays”. In: *PLoS ONE* 9.5 (May 2014). Ed. by Z. D. Deng, e97590. ISSN: 1932-6203. DOI: 10.1371/journal.pone.0097590. arXiv: 1312.4006.
- [73] UpnaLab. *Acoustic Levitator*. 2017. URL: <https://www.instructables.com/id/Acoustic-Levitator/> (visited on Sept. 18, 2019).
- [74] A. Watanabe, K. Hasegawa, and Y. Abe. “Contactless Fluid Manipulation in Air: Droplet Coalescence and Active Mixing by Acoustic Levitation”. In: *Scientific Reports* 8.1 (Dec. 2018), p. 10221. ISSN: 2045-2322. DOI: 10.1038/s41598-018-28451-5.
- [75] M. A. B. Andrade, T. S. A. Camargo, and A. Marzo. “Automatic contactless injection, transportation, merging, and ejection of droplets with a multifocal point acoustic levitator”. In: *Review of Scientific Instruments* 89.12 (2018), p. 125105. ISSN: 0034-6748. DOI: 10.1063/1.5063715.
- [76] A. Marzo and B. W. Drinkwater. “Holographic acoustic tweezers”. In: *Proceedings of the National Academy of Sciences* 116.1 (2018), pp. 84–89. ISSN: 0027-8424. DOI: 10.1073/pnas.1813047115.

- [77] J. Lee, S. Y. Teh, A. Lee, H. H. Kim, C. Lee, and K. K. Shung. “Single beam acoustic trapping”. In: *Applied Physics Letters* 95.7 (2009). ISSN: 00036951. DOI: 10.1063/1.3206910.
- [78] D. Baresch, J.-L. Thomas, and R. Marchiano. “Observation of a single-beam gradient force acoustical trap for elastic particles: acoustical tweezers”. In: *Physical Review Letters* 116.2 (2016), p. 024301. ISSN: 0031-9007. DOI: 10.1103/PhysRevLett.116.024301. arXiv: 1411.1912.
- [79] A. Marzo, S. A. Seah, B. W. Drinkwater, D. R. Sahoo, B. Long, and S. Subramanian. “Holographic acoustic elements for manipulation of levitated objects”. In: *Nature Communications* 6 (Oct. 2015), p. 8661. ISSN: 2041-1723. DOI: 10.1038/ncomms9661.
- [80] M. R. Haberman and A. N. Norris. “Acoustic metamaterials”. In: *Acoustics Today* 12.3 (2016), pp. 31–39. URL: <https://acousticstoday.org/acoustic-metamaterials/>.
- [81] A. Franklin, A. Marzo, R. Malkin, and B. W. Drinkwater. “Three-dimensional ultrasonic trapping of micro-particles in water with a simple and compact two-element transducer”. In: *Applied Physics Letters* 111.9 (2017), p. 094101. ISSN: 00036951. DOI: 10.1063/1.4992092.
- [82] K. Melde, A. G. Mark, T. Qiu, and P. Fischer. “Holograms for acoustics”. In: *Nature* 537.7621 (2016), pp. 518–522. ISSN: 0028-0836. DOI: 10.1038/nature19755.
- [83] G. Memoli, M. Caleap, M. Asakawa, D. R. Sahoo, B. W. Drinkwater, and S. Subramanian. “Metamaterial bricks and quantization of meta-surfaces”. In: *Nature Communications* 8 (2017), pp. 1–8. ISSN: 20411723. DOI: 10.1038/ncomms14608.
- [84] M. A. Norasikin, D. Martinez Plasencia, S. Polychronopoulos, G. Memoli, Y. Tokuda, and S. Subramanian. “SoundBender: Dynamic Acoustic Control Behind Obstacles”. In: *The 31st Annual ACM Symposium on User Interface Software and Technology - UIST '18* (2018), pp. 247–259. DOI: 10.1145/3242587.3242590.
- [85] K. Hasegawa, Y. Abe, A. Fujiwara, Y. Yamamoto, and K. Aoki. “Internal flow of an acoustically levitated droplet”. In: *Microgravity Science and Technology* 20.3–4 (2008), pp. 277–280. ISSN: 09380108. DOI: 10.1007/s12217-008-9070-z.
- [86] H. Kitahata, R. Tanaka, Y. Koyano, S. Matsumoto, K. Nishinari, T. Watanabe, K. Hasegawa, T. Kanagawa, A. Kaneko, and Y. Abe. “Oscillation of a rotating levitated droplet: Analysis with a mechanical model”. In: *Physical Review E - Statistical, Nonlinear, and Soft Matter Physics* 92.6 (2015), p. 062904. ISSN: 15502376. DOI: 10.1103/PhysRevE.92.062904. arXiv: 1507.07741.
- [87] P.-C. Lin and L. I. “Acoustically levitated dancing drops: Self-excited oscillation to chaotic shedding”. In: *Physical Review E* 93.2 (Feb. 2016), 021101(R). ISSN: 2470-0045. DOI: 10.1103/PhysRevE.93.021101.
- [88] D. Ilssar and I. Bucher. “The effect of acoustically levitated objects on the dynamics of ultrasonic actuators”. In: *Journal of Applied Physics* 121.11 (2017), p. 114504. ISSN: 10897550. DOI: 10.1063/1.4978365.

- [89] D. Ilssar, I. Bucher, and H. Flashner. “Modeling and closed loop control of near-field acoustically levitated objects”. In: *Mechanical Systems and Signal Processing* 85 (2017), pp. 367–381. ISSN: 10961216. DOI: 10.1016/j.ymssp.2016.08.011.
- [90] N. Aboobaker, D. Blackmore, and J. Meegoda. “Mathematical modeling of the movement of suspended particles subjected to acoustic and flow fields”. In: *Applied Mathematical Modelling* 29.6 (2005), pp. 515–532. ISSN: 0307904X. DOI: 10.1016/j.apm.2004.09.013.
- [91] J.-H. Xie and J. Vanneste. “Dynamics of a spherical particle in an acoustic field: A multiscale approach”. In: *Physics of Fluids* 26.10 (Oct. 2014), p. 102001. ISSN: 1070-6631. DOI: 10.1063/1.4896523. arXiv: 1406.3006.
- [92] C. T. Crowe, J. D. Schwarzkopf, M. Sommerfeld, and Y. Tsuji. *Multiphase Flows with Droplets and Particles*. CRC Press, 2011. ISBN: 9781439840511.
- [93] A. Nguyen and H. J. Schulze. *Colloidal Science of Flotation*. Surfactant Science. CRC Press, 2003. ISBN: 9781482276411.
- [94] A. Dolev, S. Davis, and I. Bucher. “Noncontact Dynamic Oscillations of Acoustically Levitated Particles by Parametric Excitation”. In: *Physical Review Applied* 12.3 (2019), p. 034031. ISSN: 2331-7019. DOI: 10.1103/PhysRevApplied.12.034031.
- [95] D. Foresti, M. Nabavi, and D. Poulikakos. “On the acoustic levitation stability behaviour of spherical and ellipsoidal particles”. In: *Journal of Fluid Mechanics* 709 (2012), pp. 581–592. ISSN: 0022-1120. DOI: 10.1017/jfm.2012.350.
- [96] N. Pérez, M. A. B. Andrade, R. Canetti, and J. C. Adamowski. “Experimental determination of the dynamics of an acoustically levitated sphere”. In: *Journal of Applied Physics* 116.18 (2014). ISSN: 10897550. DOI: 10.1063/1.4901579.
- [97] B. W. Drinkwater. “Dynamic-field devices for the ultrasonic manipulation of microparticles”. In: *Lab Chip* 16.13 (2016), pp. 2360–2375. ISSN: 1473-0197. DOI: 10.1039/C6LC00502K.
- [98] C. R. P. Courtney, C. E. M. Demore, H. Wu, A. Grinenko, P. D. Wilcox, S. Cochran, and B. W. Drinkwater. “Independent trapping and manipulation of microparticles using dexterous acoustic tweezers”. In: *Applied Physics Letters* 104.15 (2014), p. 154103. ISSN: 00036951. DOI: 10.1063/1.4870489.
- [99] C. R. P. Courtney, B. W. Drinkwater, C. E. M. Demore, S. Cochran, A. Grinenko, and P. D. Wilcox. “Dexterous manipulation of microparticles using Bessel-function acoustic pressure fields”. In: *Applied Physics Letters* 102.12 (2013), p. 123508. ISSN: 00036951. DOI: 10.1063/1.4798584.
- [100] M. Baudoin, J. C. Gerbedoen, A. Riaud, O. B. Matar, N. Smagin, and J. L. Thomas. “Folding a focalized acoustical vortex on a flat holographic transducer: Miniaturized selective acoustical tweezers”. In: *Science Advances* 5.4 (2019), pp. 1–7. ISSN: 23752548. DOI: 10.1126/sciadv.aav1967.
- [101] C. R. P. Courtney, C.-K. Ong, B. W. Drinkwater, P. D. Wilcox, C. Demore, S. Cochran, P. Glynne-Jones, and M. Hill. “Manipulation of microparticles using

- phase-controllable ultrasonic standing waves”. In: *The Journal of the Acoustical Society of America* 128.4 (Oct. 2010), EL195–EL199. ISSN: 0001-4966. DOI: 10.1121/1.3479976.
- [102] L. Meng, F. Cai, F. Li, W. Zhou, L. Niu, and H. Zheng. “Acoustic tweezers”. In: *Journal of Physics D: Applied Physics* 52.27 (2019). ISSN: 13616463. DOI: 10.1088/1361-6463/ab16b5.
- [103] S. N. Limited. *Lab-on-a-chip*. 2019. URL: <https://www.nature.com/subjects/lab-on-a-chip> (visited on Oct. 17, 2019).
- [104] M. Caleap and B. W. Drinkwater. “Acoustically trapped colloidal crystals that are reconfigurable in real time”. In: *Proceedings of the National Academy of Sciences* 111.17 (2014), pp. 6226–6230. ISSN: 0027-8424. DOI: 10.1073/pnas.1323048111.
- [105] J. J. Hawkes and W. T. Coakley. “Force field particle filter, combining ultrasound standing waves and laminar flow”. In: *Sensors and Actuators B: Chemical* 75.3 (May 2001), pp. 213–222. ISSN: 09254005. DOI: 10.1016/S0925-4005(01)00553-6.
- [106] K. Yasuda, S.-i. Umemura, K. Takeda, and T. Kawagoe. *PARTICLE HANDLING METHOD BY ACOUSTIC RADIATION FORCE AND APPARATUS THEREFORE*. US5902489A. 1996.
- [107] G. Simon, Y. Pailhas, M. A. B. Andrade, J. Reboud, J. Marques-Hueso, M. P. Y. Desmulliez, J. M. Cooper, M. O. Riehle, and A. L. Bernassau. “Particle separation in surface acoustic wave microfluidic devices using reprogrammable, pseudo-standing waves”. In: *Applied Physics Letters* 113.4 (2018), p. 044101. ISSN: 00036951. DOI: 10.1063/1.5035261.
- [108] L. Tian, N. Martin, P. G. Bassindale, A. J. Patil, M. Li, A. Barnes, B. W. Drinkwater, and S. Mann. “Spontaneous assembly of chemically encoded two-dimensional coacervate droplet arrays by acoustic wave patterning”. In: *Nature Communications* 7 (2016), p. 13068. ISSN: 20411723. DOI: 10.1038/ncomms13068.
- [109] M. K. Nichols, R. K. Kumar, P. G. Bassindale, L. Tian, A. C. Barnes, B. W. Drinkwater, A. J. Patil, and S. Mann. “Fabrication of Micropatterned Dipeptide Hydrogels by Acoustic Trapping of Stimulus-Responsive Coacervate Droplets”. In: *Small* 14.26 (2018). ISSN: 16136829. DOI: 10.1002/smll.201800739.
- [110] G. T. Silva, J. H. Lopes, J. P. Leão-Neto, M. K. Nichols, and B. W. Drinkwater. “Particle Patterning by Ultrasonic Standing Waves in a Rectangular Cavity”. In: *Physical Review Applied* 11.5 (2019), p. 054044. ISSN: 23317019. DOI: 10.1103/PhysRevApplied.11.054044.
- [111] M. Prisbrey and B. Raeymaekers. “Aligning High-Aspect-Ratio Particles in User-Specified Orientations with Ultrasound-Directed Self-Assembly”. In: *Physical Review Applied* 12.1 (2019), p. 014014. ISSN: 2331-7019. DOI: 10.1103/physrevapplied.12.014014.
- [112] R. Gabai, R. Shaham, S. Davis, N. Cohen, and I. Bucher. “A Contactless Stage Based on Near-Field Acoustic Levitation for Object Handling and Positioning—Concept,



- Design, Modeling, and Experiments”. In: *IEEE/ASME Transactions on Mechatronics* 24.5 (2019), pp. 1954–1963. ISSN: 1083-4435. DOI: 10.1109/tmech.2019.2935428.
- [113] K. T. Chang. “A novel ultrasonic clutch using near-field acoustic levitation”. In: *Ultrasonics* 43.1 (2004), pp. 49–55. ISSN: 0041624X. DOI: 10.1016/j.ultras.2004.02.023.
- [114] T. A. Stolarski, Y. Xue, and S. Yoshimoto. “Air Journal Bearing Utilizing Near-Field Acoustic Levitation Stationary Shaft Case”. In: *Proceedings of the Institution of Mechanical Engineers, Part J: Journal of Engineering Tribology* 225.3 (2011), pp. 120–127. ISSN: 13506501. DOI: 10.1177/2041305X10394956.
- [115] L. Puskar, R. Tuckermann, T. Frosch, J. Popp, V. Ly, D. McNaughton, and B. R. Wood. “Raman acoustic levitation spectroscopy of red blood cells and *Plasmodium falciparum* trophozoites”. In: *Lab on a Chip* 7.9 (2007), p. 1125. ISSN: 1473-0197. DOI: 10.1039/b706997a.
- [116] V. A. Hosseinzadeh, C. Brugnara, and R. G. Holt. “Shape oscillations of single blood drops: applications to human blood and sickle cell disease”. In: *Scientific Reports* 8 (2018), p. 16794. ISSN: 20452322. DOI: 10.1038/s41598-018-34600-7.
- [117] S. Tsujino and T. Tomizaki. “Ultrasonic acoustic levitation for fast frame rate X-ray protein crystallography at room temperature”. In: *Scientific Reports* 6 (2016), p. 25558. ISSN: 20452322. DOI: 10.1038/srep25558.
- [118] A. Bierstedt, U. Panne, and J. Riedel. “Confinement and enhancement of an airborne atmospheric laser-induced plasma using an ultrasonic acoustic resonator”. In: *Journal of Analytical Atomic Spectrometry* 33.1 (2018), pp. 135–140. ISSN: 13645544. DOI: 10.1039/c7ja00297a.
- [119] Y. Ochiai, T. Hoshi, and J. Rekimoto. “Pixie dust: graphics generated by levitated and animated objects in computational acoustic-potential field”. In: *ACM Transactions on Graphics* 33.4 (2014), Article 85. ISSN: 0730-0301. DOI: 10.1145/2601097.2601118.
- [120] D. R. Sahoo, T. Nakamura, A. Marzo, T. Omirou, M. Asakawa, and S. Subramanian. “JOLED: A Mid-air Display based on Electrostatic Rotation of Levitated Janus Objects”. In: *Proceedings of the 29th Annual Symposium on User Interface Software and Technology - UIST '16*. New York, New York, USA: ACM Press, 2016, pp. 437–448. ISBN: 9781450341899. DOI: 10.1145/2984511.2984549.
- [121] Y. Uno, H. Qiu, T. Sai, S. Iguchi, Y. Mizutani, T. Hoshi, Y. Kawahara, Y. Takehi, and M. Takamiya. “Luciola: A Millimeter-Scale Light-Emitting Particle Moving in Mid-Air Based On Acoustic Levitation and Wireless Powering”. In: *Proceedings of the ACM on Interactive, Mobile, Wearable and Ubiquitous Technologies* 1.4 (Jan. 2018), Article 166. ISSN: 24749567. DOI: 10.1145/3161182.
- [122] E. Freeman, J. Williamson, S. Subramanian, and S. Brewster. “Point-and-Shake: Selecting from Levitating Object Displays”. In: *Proceedings of the 2018 CHI Conference on Human Factors in Computing Systems - CHI '18*. New York, New York,

- USA: ACM Press, 2018, pp. 1–10. ISBN: 9781450356206. DOI: 10.1145/3173574.3173592.
- [123] M. Bachynskyi, V. Paneva, and J. Müller. “LeviCursor: Dexterous Interaction with a Levitating Object”. In: *Proceedings of the 2018 ACM International Conference on Interactive Surfaces and Spaces, ISS 2018, Tokyo, Japan, November 25-28, 2018* (2018), pp. 253–262. DOI: 10.1145/3279778.3279802.
  - [124] P. Dallard, A. Fitzpatrick, A. Flint, S. Le Bourva, A. Low, R. Ridsdill Smith, and M. Willford. “The London Millennium Footbridge”. In: *Structural Engineer* 79.22 (2001), pp. 17–21. ISSN: 14665123.
  - [125] K. Y. Billah and R. H. Scanlan. “Resonance, Tacoma Narrows bridge failure, and undergraduate physics textbooks”. In: *American Journal of Physics* 59.2 (Feb. 1991), pp. 118–124. ISSN: 0002-9505. DOI: 10.1119/1.16590.
  - [126] J. Wilkie, M. A. Johnson, and R. Katebi. *Control Engineering: An Introductory Course*. Red Globe Press, 2002. ISBN: 9780333771297.
  - [127] B. Krauskopf, H. M. Osinga, and J. Galán-Vioque. *Numerical continuation methods for dynamical systems*. Path following and boundary value problems. Springer Netherlands, 2007. ISBN: 978-1-4020-6355-8.
  - [128] D. J. Gee. “Numerical continuation applied to panel flutter”. In: *Nonlinear Dynamics* 22.3 (2000), pp. 271–280. ISSN: 0924090X. DOI: 10.1023/A:1008374401581.
  - [129] A. Dhooge, W. Govaerts, and Y. a. Kuznetsov. “MATCONT: A MATLAB package for numerical bifurcation analysis of ODEs”. In: *ACM Transactions on Mathematical Software (TOMS)* 29.2 (June 2003), pp. 141–164. ISSN: 00983500. DOI: 10.1145/779359.779362.
  - [130] F. Schilder and H. Dankowicz. *Continuation Core and Toolboxes (COCO)*. 2016. URL: <https://sourceforge.net/projects/cocotools/files/releases/> (visited on July 17, 2019).
  - [131] P. Kamthan. *AUTO SOFTWARE FOR CONTINUATION AND BIFURCATION PROBLEMS IN ORDINARY DIFFERENTIAL EQUATIONS*. 2010. URL: <http://cmvl.cs.concordia.ca/auto/> (visited on Oct. 2, 2019).
  - [132] T. L. Hill. “Modal interactions in nonlinear systems”. In: March (2016). DOI: 10.13140/rg.2.1.2720.9368.
  - [133] D. J. Wagg and S. A. Neild. *Nonlinear Vibration with Control: For Flexible and Adaptive Structures*. Solid Mechanics and Its Applications. Springer Netherlands, 2010. ISBN: 9789048128372.
  - [134] J. J. Thomsen. *Vibrations and stability: advanced theory, analysis, and tools*. Springer Science & Business Media, 2013. ISBN: 9783662107935.
  - [135] S. H. Strogatz. *Nonlinear Dynamics and Chaos: With Applications to Physics, Biology, Chemistry, and Engineering*. Studies in nonlinearity. Westview Press, 2008. ISBN: 9780786723959.

- [136] A. Pirrera, D. Avitabile, and P. M. Weaver. “Bistable plates for morphing structures: A refined analytical approach with high-order polynomials”. In: *International Journal of Solids and Structures* 47.25-26 (2010), pp. 3412–3425. ISSN: 00207683. DOI: 10.1016/j.ijsolstr.2010.08.019.
- [137] G. Contopoulos. “The genealogy of periodic orbits in a plane rotating galaxy”. In: *Celestial Mechanics* 31.2 (Oct. 1983), pp. 193–211. ISSN: 0008-8714. DOI: 10.1007/BF01686818.
- [138] R. Szabó, Z. Kolláth, L. Molnár, K. Kolenberg, D. W. Kurtz, S. T. Bryson, J. M. Benko, J. Christensen-Dalsgaard, H. Kjeldsen, W. J. Borucki, D. Koch, J. D. Twicken, M. Chadid, M. Di Criscienzo, Y. B. Jeon, P. Moskalik, J. M. Nemec, and J. Nuspl. “Does Kepler unveil the mystery of the Blazhko effect? First detection of period doubling in Kepler Blazhko RR Lyrae stars”. In: *Monthly Notices of the Royal Astronomical Society* 409.3 (2010), pp. 1244–1252. ISSN: 00358711. DOI: 10.1111/j.1365-2966.2010.17386.x.
- [139] M. R. Guevara, L. Glass, and A. Shrier. “Phase locking, period-doubling bifurcations, and irregular dynamics in periodically stimulated cardiac cells”. In: *Science* 214.4527 (Dec. 1981), pp. 1350–1353. ISSN: 0036-8075. DOI: 10.1126/science.7313693.
- [140] T. Geest, C. G. Steinmetz, R. Larter, and L. F. Olsen. “Period-doubling bifurcations and chaos in an enzyme reaction”. In: *Journal of Physical Chemistry* 96.14 (1992), pp. 5678–5680. ISSN: 00223654. DOI: 10.1021/j100193a004.
- [141] T. V. Bronnikova, V. R. Fed’kina, W. M. Schaffer, and L. F. Olsen. “Period-doubling bifurcations and chaos in a detailed model of the peroxidase-oxidase reaction”. In: *Journal of Physical Chemistry* 99.23 (1995), pp. 9309–9312. ISSN: 00223654. DOI: 10.1021/j100023a001.
- [142] C. T. Vi, A. Marzo, D. Ablart, G. Memoli, S. Subramanian, B. Drinkwater, and M. Obrist. “TastyFloats: A Contactless Food Delivery System”. In: *Proceedings of the 2017 ACM International Conference on Interactive Surfaces and Spaces*. New York, New York, USA: ACM Press, 2017, pp. 161–170. ISBN: 9781450346917. DOI: 10.1145/3132272.3134123.
- [143] O. Cramer. “The variation of the specific heat ratio and the speed of sound in air with temperature, pressure, humidity, and CO2 concentration”. In: *The Journal of the Acoustical Society of America* 93.5 (1993), pp. 2510–2516. ISSN: 0001-4966. DOI: 10.1121/1.405827.
- [144] G. F. C. Rogers and Y. R. Mayhew. *Thermodynamic and transport properties of fluids*. Oxford: Wiley, 1995. ISBN: 9780631197034.
- [145] The Engineering ToolBox. *Relative Humidity in Air*. 2004. URL: [https://www.engineeringtoolbox.com/relative-humidity-air-d\\_687.html](https://www.engineeringtoolbox.com/relative-humidity-air-d_687.html) (visited on July 1, 2019).
- [146] The Engineering ToolBox. *Humidity Ratio of Air*. 2004. URL: [https://www.engineeringtoolbox.com/humidity-ratio-air-d\\_686.html](https://www.engineeringtoolbox.com/humidity-ratio-air-d_686.html) (visited on July 1, 2019).

- [147] The Engineering ToolBox. *Density of Moist Humid Air*. 2004. URL: [https://www.engineeringtoolbox.com/density-air-d\\_680.html](https://www.engineeringtoolbox.com/density-air-d_680.html) (visited on July 1, 2019).
- [148] N. Otsu. “A Threshold Selection Method from Gray-Level Histograms”. In: *IEEE Transactions on Systems, Man, and Cybernetics* 9.1 (Jan. 1979), pp. 62–66. ISSN: 0018-9472. DOI: 10.1109/TSMC.1979.4310076.
- [149] Murata Manufacturing Co. Ltd. *MA40S4S*. 2019. URL: <https://www.murata.com/en-us/api/pdfdownloadapi?cate=&partno=MA40S4S> (visited on July 8, 2019).
- [150] A. Marzo, A. Ghobrial, L. Cox, M. Caleap, A. Croxford, and B. W. Drinkwater. “Realization of compact tractor beams using acoustic delay-lines”. In: *Applied Physics Letters* 110.1 (Jan. 2017), p. 014102. ISSN: 0003-6951. DOI: 10.1063/1.4972407.
- [151] M. A. B. Andrade, T. S. Ramos, F. T. A. Okina, and J. C. Adamowski. “Nonlinear characterization of a single-axis acoustic levitator”. In: *Review of Scientific Instruments* 85.4 (Apr. 2014), p. 045125. ISSN: 0034-6748. DOI: 10.1063/1.4872356.
- [152] J. Simon. *DGradient*. 2011. URL: <https://uk.mathworks.com/matlabcentral/fileexchange/29887-dgradient> (visited on July 1, 2019).
- [153] S. Baer, M. A. B. Andrade, C. Esen, J. C. Adamowski, G. Schweiger, and A. Ostendorf. “Analysis of the particle stability in a new designed ultrasonic levitation device”. In: *Review of Scientific Instruments* 82.10 (Oct. 2011), p. 105111. ISSN: 0034-6748. DOI: 10.1063/1.3652976.
- [154] F. Guo, Z. Mao, Y. Chen, Z. Xie, J. P. Lata, P. Li, L. Ren, J. Liu, J. Yang, M. Dao, S. Suresh, and T. J. Huang. “Three-dimensional manipulation of single cells using surface acoustic waves”. In: *Proceedings of the National Academy of Sciences* 113.6 (Feb. 2016), pp. 1522–1527. ISSN: 0027-8424. DOI: 10.1073/pnas.1524813113.
- [155] R. G. Holt and L. A. Crum. “Acoustically forced oscillations of air bubbles in water: Experimental results”. In: *The Journal of the Acoustical Society of America* 91.4 (Apr. 1992), pp. 1924–1932. ISSN: 0001-4966. DOI: 10.1121/1.403703.
- [156] R. Mettin and A. A. Doinikov. “Translational instability of a spherical bubble in a standing ultrasound wave”. In: *Applied Acoustics* 70.10 (2009), pp. 1330–1339. ISSN: 0003682X. DOI: 10.1016/j.apacoust.2008.09.016.
- [157] Z. C. Feng and Y. H. Su. “Numerical simulations of the translational and shape oscillations of a liquid drop in an acoustic field”. In: *Physics of Fluids* 9.3 (Mar. 1997), pp. 519–529. ISSN: 1070-6631. DOI: 10.1063/1.869216.
- [158] K. Jia, D. Mei, J. Meng, and K. Yang. “Dynamic properties of micro-particles in ultrasonic transportation using phase-controllable standing waves”. In: *Journal of Applied Physics* 116.16 (Oct. 2014), p. 164901. ISSN: 0021-8979. DOI: 10.1063/1.4898560.
- [159] M. A. B. Andrade, N. Pérez, and J. C. Adamowski. “Experimental study of the oscillation of spheres in an acoustic levitator”. In: *The Journal of the Acoustical Society of America* 136.4 (2014), pp. 1518–1529. ISSN: 0001-4966. DOI: 10.1121/1.4893905.
- [160] D. Foresti and D. Poulikakos. “Acoustophoretic Contactless Elevation, Orbital Transport and Spinning of Matter in Air”. In: *Physical Review Letters* 112.2 (Jan. 2014),

- p. 024301. ISSN: 0031-9007. DOI: 10.1103/PhysRevLett.112.024301. arXiv: arXiv:1507.02142v2.
- [161] J. Ward-Smith. *Mechanics of Fluids, 9th Edition*. CRC Press, 2012. ISBN: 978-0415602600.
  - [162] R. L. C. Flemmer and C. L. Banks. “On the drag coefficient of a sphere”. In: *Powder Technology* 48.3 (Nov. 1986), pp. 217–221. ISSN: 00325910. DOI: 10.1016/0032-5910(86)80044-4.
  - [163] S Wang, J. S. Allen, and A. M. Ardekani. “Unsteady particle motion in an acoustic standing wave field”. In: *European Journal of Computational Mechanics* 26.1–2 (2017), pp. 115–130. DOI: 10.1080/17797179.2017.1321205.
  - [164] R. Pintelon and J. Schoukens. *System Identification: A Frequency Domain Approach*. John Wiley & Sons, 2012. ISBN: 9781118287392.
  - [165] H. Dankowicz and F. Schilder. *Recipes for Continuation*. Computational Science and Engineering. Society for Industrial and Applied Mathematics, 2013. ISBN: 9781611972573.
  - [166] J. P. Chávez, P. Brzeski, and P. Perlikowski. “Bifurcation analysis of non-linear oscillators interacting via soft impacts”. In: *International Journal of Non-Linear Mechanics* 92. February (2017), pp. 76–83. ISSN: 00207462. DOI: 10.1016/j.ijnonlinmec.2017.02.018. eprint: arXiv:1602.04214.
  - [167] Y. Yan, Y. Liu, J. Páez Chávez, F. Zonta, and A. Yusupov. “Proof-of-concept prototype development of the self-propelled capsule system for pipeline inspection”. In: *Meccanica* 53.8 (2018), pp. 1997–2012. ISSN: 15729648. DOI: 10.1007/s11012-017-0801-3.
  - [168] D. A. W. Barton. “Control-Based Continuation of a Hybrid Numerical/Physical Substructured System”. In: *Nonlinear Dynamics, Volume 1*. Ed. by G. Kerschen. Cham: Springer International Publishing, 2016, pp. 203–207. ISBN: 978-3-319-15221-9.
  - [169] H. Jiang, Y. Liu, L. Zhang, and J. Yu. “Anti-phase synchronization and symmetry-breaking bifurcation of impulsively coupled oscillators”. In: *Communications in Nonlinear Science and Numerical Simulation* 39 (2016), pp. 199–208. ISSN: 10075704. DOI: 10.1016/j.cnsns.2016.02.033.
  - [170] C. J. Cao, T. L. Hill, A. T. Conn, B. Li, and X. Gao. “Nonlinear Dynamics of a Magnetically Coupled Dielectric Elastomer Actuator”. In: *Physical Review Applied* 12.4 (2019), pp. 1–18. ISSN: 23317019. DOI: 10.1103/PhysRevApplied.12.044033.
  - [171] The MathWorks Inc. *Choose an ODE Solver*. 2019. URL: <https://uk.mathworks.com/help/matlab/math/choose-an-ode-solver.html> (visited on July 16, 2019).
  - [172] H. Dankowicz and F. Schilder. *The Periodic Orbit Toolbox*. Tech. rep. 2016, pp. 1–36.
  - [173] J. M. T. Thompson and H. B. Stewart. *Nonlinear dynamics and chaos: geometrical methods for engineers and scientists*. Wiley, 2002, p. 460. ISBN: 9780471876458.

- [174] J. Sieber and B. Krauskopf. “Control based bifurcation analysis for experiments”. In: *Nonlinear Dynamics* 51.3 (2008), pp. 365–377. ISSN: 0924090X. DOI: 10.1007/s11071-007-9217-2.
- [175] S. Tsujino, Y. Sato, Y. Takeda, and T. Tomizaki. “Oscillation resonances and anisotropic damping of the motion of acoustically levitated droplets in single-axis acoustic levitators”. In: *Applied Physics Letters* 115.5 (2019), p. 053702. ISSN: 0003-6951. DOI: 10.1063/1.5112109.
- [176] T. Omirou, A. Marzo, S. A. Seah, and S. Subramanian. “LeviPath: Modular Acoustic Levitation for 3D Path Visualisations”. In: *Proceedings of the 33rd Annual ACM Conference on Human Factors in Computing Systems* 1 (2015), pp. 309–312. ISSN: 00319007. DOI: 10.1145/2702123.2702333.
- [177] S. A. Seah, B. W. Drinkwater, T. Carter, R. Malkin, and S. Subramanian. “Dexterous ultrasonic levitation of millimeter-sized objects in air”. In: *IEEE Transactions on Ultrasonics, Ferroelectrics, and Frequency Control* 61.7 (July 2014), pp. 1233–1236. ISSN: 0885-3010. DOI: 10.1109/TUFFC.2014.3022.
- [178] M. A. B. Andrade, N. Pérez, F. Buiocchi, and J. C. Adamowski. “Matrix method for acoustic levitation simulation”. In: *IEEE Transactions on Ultrasonics, Ferroelectrics, and Frequency Control* 58.8 (2011), pp. 1674–1683. ISSN: 08853010. DOI: 10.1109/TUFFC.2011.1995.
- [179] J. W. S. Rayleigh. “XXXIV. On the pressure of vibrations”. In: *The London, Edinburgh, and Dublin Philosophical Magazine and Journal of Science* 3.15 (Mar. 1902), pp. 338–346. ISSN: 1941-5982. DOI: 10.1080/14786440209462769.
- [180] D. E. Smalley, E. Nygaard, K. Squire, J. Van Wagoner, J. Rasmussen, S. Gneiting, K. Qaderi, J. Goodsell, W. Rogers, M. Lindsey, K. Costner, A. Monk, M. Pearson, B. Haymore, and J. Peatross. “A photophoretic-trap volumetric display”. In: *Nature* 553.7689 (Jan. 2018), pp. 486–490. ISSN: 0028-0836. DOI: 10.1038/nature25176.
- [181] W. Rogers, J. Laney, J. Peatross, and D. Smalley. “Improving Photophoretic Trap Volumetric Displays”. In: (2019).
- [182] J. Berthelot and N. Bonod. “Free-space micro-graphics with electrically driven levitated light scatterers”. In: *Optics Letters* 44.6 (Mar. 2019), pp. 1476–1479. ISSN: 0146-9592. DOI: 10.1364/OL.44.001476.
- [183] D. Smalley, T.-c. Poon, H. Gao, J. Kvavle, and K. Qaderi. “Volumetric Displays: Turning 3-D Inside-Out”. In: *Optics and Photonics News* 29.6 (June 2018), pp. 26–33. URL: [https://www.osa-opn.org/home/articles/volume\\_29/june\\_2018/features/volumetric\\_displays\\_turning\\_3-d\\_inside-out/](https://www.osa-opn.org/home/articles/volume_29/june_2018/features/volumetric_displays_turning_3-d_inside-out/).
- [184] T. G. Leighton. “Are some people suffering as a result of increasing mass exposure of the public to ultrasound in air?” In: *Proceedings of the Royal Society A: Mathematical, Physical and Engineering Science* 472.2185 (Jan. 2016), p. 20150624. ISSN: 1364-5021. DOI: 10.1098/rspa.2015.0624.
- [185] ULTRAHAPTICS. *STRATOS INSPIRE User Manual*. Tech. rep. 2018, pp. 1–7. URL: <https://developer.ultrahaptics.com/wp-content/uploads/2018/09/STRATOS-Inspire-Instruction-Manual-Issue-5-EMAIL.pdf>.

- [186] SonicEnergy. *SonicEnergy Technology*. 2019. URL: <http://sonicenergy.com/technology/> (visited on Jan. 18, 2020).
- [187] B. G. Blundell and A. J. Schwarz. *Volumetric Three-dimensional Display Systems*. John Wiley & Sons, Incorporated, 2000. ISBN: 9780471239284.